

# **ELECTROCHEMICAL STUDIES ON URANIUM AND RARE EARTH ELEMENTS RELATED TO PYROCHEMICAL REPROCESSING**

*By*

**S. VANDARKUZHALI**

**Enrolment No: CHEM02200704010**

**Indira Gandhi Centre for Atomic Research, Kalpakkam**

*A thesis submitted to the*

*Board of Studies in Chemical Sciences*

*In partial fulfillment of requirements*

*for the Degree of*

**DOCTOR OF PHILOSOPHY**

*of*

**HOMI BHABHA NATIONAL INSTITUTE**

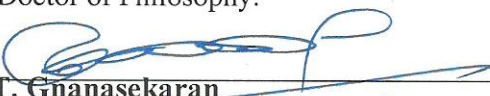


**August, 2014**

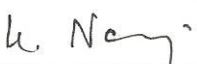
# HOMI BHABHA NATIONAL INSTITUTE

## RECOMMENDATIONS OF THE VIVA VOCE COMMITTEE

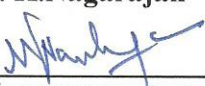
As members of the Viva Voce Committee, we certify that we have read the dissertation prepared by S. VANDARKUZHALI entitled "Electrochemical studies on uranium and rare earth elements related to pyrochemical reprocessing" and recommend that it may be accepted as fulfilling the thesis requirement for the award of Degree of Doctor of Philosophy.

  
Chairman - Prof. T. Gnanasekaran

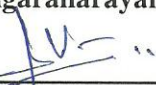
Date: 04-06-2015

  
Guide / Convener - Prof. K. Nagarajan

Date: 04-06-2015

  
Examiner - Prof. M.V. Sangaranarayanan

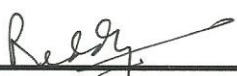
Date: 04-06-2015

  
Member 1- Prof. T.G. Srinivasan

Date: 04-06-2015

  
Member 2- Prof. S. Rangarajan

Date: 04-06-2015

  
Technology Advisor : Dr. B. Prabhakara Reddy

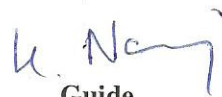
Date: 04-06-2015

Final approval and acceptance of this thesis is contingent upon the candidate's submission of the final copies of the thesis to HBNI.

I/We hereby certify that I/we have read this thesis prepared under my/our direction and recommend that it may be accepted as fulfilling the thesis requirement.

Date: 04-06-2015

Place: IGCAR, Kalpakkam

  
Guide

## **STATEMENT BY AUTHOR**

This dissertation has been submitted in partial fulfillment of requirements for an advanced degree at Homi Bhabha National Institute (HBNI) and is deposited in the Library to be made available to borrowers under rules of the HBNI.

Brief quotations from this dissertation are allowable without special permission, provided that accurate acknowledgement of source is made. Requests for permission for extended quotation from or reproduction of this manuscript in whole or in part may be granted by the Competent Authority of HBNI when in his or her judgment the proposed use of the material is in the interests of scholarship. In all other instances, however, permission must be obtained from the author.

(S. VANDARKUZHALI)

## **DECLARATION**

I, hereby declare that the investigation presented in the thesis has been carried out by me.  
The work is original and has not been submitted earlier as a whole or in part for a degree  
/ diploma at this or any other Institution / University.

(S. VANDARKUZHALI)

## LIST OF PUBLICATIONS

### **Publications in Refereed journals**

1. “Electrochemical behaviour of  $\text{LaCl}_3$  at tungsten and aluminium cathodes in LiCl-KCl eutectic melt”, S. Vandarkuzhali, Nibedita Gogoi, Suddhasattwa Ghosh, B. Prabhakara Reddy, K.Nagarajan, , *Electrochim. Acta* 59 (2012) 245-255.
- 2 “Investigation on the electrochemical behavior of neodymium chloride at W, Al and Cd electrodes in molten LiCl-KCl eutectic”, S. Vandarkuzhali, Manish Chandra, Suddhasattwa Ghosh, Nibedita Samanta, S. Nedumaran, B. Prabhakara Reddy and K. Nagarajan, *Electrochim. Acta* 145 (2014) 86-98.

### **Proceeding and presentations at national/international conference**

1. “Electroanalytical techniques for in-situ measurement of uranium in molten salt electrolyte”, S. Vandarkuzhali, Suddhasattwa Ghosh, B. Prabhakara Reddy and K. Nagarajan presented at “International Pyroprocessing Research Conference, IPRC- 2008” held at Jeju Island, Republic of Korea during Aug 24-27, 2008.
2. “Elucidation of the behaviour of U(III)/U couple at liquid cadmium electrode in LiCl-KCl eutectic melt”, S.Vandarkuzhali, Suddhasattwa Ghosh, Nibedita Gogoi, S. Nedumaran, B.Prabhakara Reddy and K.Nagarajan, *Proc. Int. Conf. on Separation Science and Technology, SESTEC-2010* held at Kalpakkam during March 1-4 2010, SESTEC 2010, pp. 485-486, paper E-2.
3. “Investigation on the electrochemical behaviour of neodymium chloride in molten LiCl-KCl eutectic”, S.Vandarkuzhali, Suddhasattwa Ghosh, S. Nedumaran, Manish Chandra, Nibedita Gogoi, B.Prabhakara Reddy and K.Nagarajan, “CMSNT-2013” held at Mumbai during 9-11 January 2013.

4. “Electrochemical behavior of neodymium chloride on aluminium and cadmium cathodes in LiCl-KCl eutectic melt” , S. Vandarkuzhali, Manish Chandra, S. Nedumaran, B. Prabhakara Reddy and K. Nagarajan, presented in the theme meeting on Recent Trends in Material Chemistry, RTMC-2013 held at VIT, Vellore, Tamilnadu during 25-27 July 2013, paper-28 pp 52.
5. “Feasibility of gallium cathode for separation of uranium from lanthanides in molten LiCl-KCl electrolyte”, S.Vandarkuzhali, P. Venkatesh, Nibedita Samanta, S. Suganthi, K. Perumal, B.Prabhakara Reddy and K. Nagarajan, presented “SESTEC-2014” held at Mumbai during Feb 25-28, 2014.

(S.VANDARKUZHALI)

**Dedicated to my beloved father  
(Late) Shri. A. Thyagarajan**

## ACKNOWLEDGEMENTS

I express my sincere thanks and gratitude to my research guide Dr. K. Nagarajan, Director Chemistry Group, for his wholehearted support, constant encouragement and guidance during the course of the thesis.

I express my sincere thanks to Dr. P. R. Vasudeva Rao, Director, Indira Gandhi Centre for Atomic Research, for granting me permission to carry out this work and allowing me to use the facilities in our laboratory for carrying out the research.

My sincere thanks are due to Dr. T. Gnanasekaran, RRF, IGCAR and chairman of the doctoral committee, for giving me valuable ideas and suggestions during the course of my research. I also express my sincere thanks to the members of my doctoral committee, Dr. T.G. Srinivasan, RRF, IGCAR and Dr. S. Rangarajan, WSCL for their support and encouragement. I am grateful to Dr. B. Prabhakara Reddy, Head PPSS for his constant support and for the technical discussion. I express sincere thanks to Shri. Suddhasattwa Ghosh and Dr. R. Kandan for providing valuable suggestions and input during the course of the research. I would also like to thank my colleagues, Smt. Nibedita Samanta, Dr. Manish Chandra, Shri. P. Venkatesh, Shri. G. Seenivasan, Shri. Gurudas for their support and encouragement. I express my sincere thanks to Shri. Nedumaran, Smt. Suriya Kumari, Smt. Suganthi, Shri Mariappan, Shri Ganapathy, Shri Kakkum Perumal and Smt. Rajeswari for the help rendered. I thank Dr. G. Paneerselvam, Dr. R. Sudha and Dr. Jagadeeswara Rao for characterization of the samples by XRD and SEM-EDAX analysis. I thank colleagues from analytical section for the analytical support.

I express my sincere thanks to my husband Shri. Sivashakar and gratitude to my mother Smt. Lalitha for their constant support and encouragement. My thanks are also due to my sons, Vivek and Sanjeev for their co-operation. I thank all my family members and friends for their encouragement which motivated me to take this work to completion.

# CONTENTS

Sl. No.	TITLE	Page No.
	<b>SYNOPSIS</b>	i
	<b>LIST OF FIGURES</b>	xiii
	<b>LIST OF TABLES</b>	xxiv
	<b>CHAPTER 1 INTRODUCTION</b>	1
1.1	Nuclear energy and nuclear fuel	1
1.2	Types of reactors	2
1.2.1	Fast breeder reactors	3
1.2.2	Metal fuelled fast breeder reactors	3
1.3.	Reprocessing of nuclear fuel	6
1.3.1	Aqueous reprocessing technology	6
1.3.2	Non-aqueous reprocessing technology	8
1.3.3	Development of non-aqueous processes	9
1.3.3.1	Fluoride volatility	9
1.3.3.2	Melt refining	10
1.3.3.3	IFR process	10
1.3.3.4	RIAR process	10
1.4	Molten salt electrorefining process for metallic fuel	11
1.4.1	Overview	11
1.4.2	Challenges of pyrochemical process	14
1.4.3	Research for an alternate to liquid cadmium cathode	15
1.5	Objective of this study	15
1.6	References	19
	<b>CHAPTER 2 Experimental Facilities and Techniques</b>	24
	Section A	24
2.1	Experimental facilities	24
2.1.1	Argon atmosphere glove box facility	24
2.1.2.	Purification of LiCl-KCl mixture	25
2.1.3	Preparation of the electrolytic salt	28

2.1.3.1	Preparation of LiCl-KCl-UCl <sub>3</sub> electrolyte	28
2.1.3.2	Preparation of LiCl-KCl-ReCl <sub>3</sub> electrolyte	29
2.1.3.3	Preparation of LiCl-KCl-AgCl electrolyte	30
2.1.3.4	Preparation of electrolyte for studies by pulse voltammetry	30
2.1.4	Electrochemical apparatus and electrodes	31
2.1.4.1	Electrochemical apparatus	31
2.1.4.2	Electrodes	31
2.1.5	Procedure for electrochemical measurement	33
	Section B	34
2.2	Experimental techniques	35
2.2.1	General Theory	35
2.2.2	Faradaic and non-Faradaic processes	35
2.2.2.1	Charging current and residual current	36
2.2.3	Factors affecting the rate of electrochemical reactions	36
2.2.3.1	Modes of mass transport	36
2.2.3.2	Diffusion layer	37
2.2.4	Single step charge transfer kinetics	39
2.2.5	Shape of voltammograms	41
2.2.6	Cyclic voltammetry	42
2.2.7	Chronopotentiometry	46
2.2.8	Pulse voltammetry	47
2.2.8.1	Normal pulse voltammetry(NPV)	47
2.2.8.2	Differential pulse voltammetry (DPV)	48
2.2.8.3	Square-Wave Voltammetry (SWV)	49
2.2.9	Electrochemical Impedance Spectroscopy (EIS)	51
2.2.10	Open Circuit Potentiometry (OCP)	54
2.3	References	56
<b>CHAPTER 3</b>	<b>Electrochemical behavior of La-, Nd- and U-trivalent ions in LiCl-KCl eutectic melt on inert tungsten electrode</b>	<b>58</b>
3. 1	Introduction	58
3. 2.	Literature survey	59
3.3	Experimental	63
3.4	Results and Discussion	63

3.4.1	Analysis of the cyclic voltammograms	63
3.4.1.1	Redox behavior of $\text{LaCl}_3$	63
3.4.1.2	Redox behavior of $\text{NdCl}_3$	67
3.4.1.3	Redox behavior of $\text{UCl}_3$	71
3.4.2	Kinetic study of the electrode reaction- Reversibility study	73
3.4.2.1	Behavior of $\text{LaCl}_3$	73
3.4.2.2	Behavior of $\text{NdCl}_3$	79
3.4.2.3	Behavior of $\text{UCl}_3$	82
3.4.3	Chronopotentiometry	83
3.4.3.1	Analysis of the chronopotentiograms for $\text{LiCl-KCl-LaCl}_3$ melt	83
3.4.3.2	Analysis of the chronopotentiograms for $\text{LiCl-KCl-NdCl}_3$ melt	84
3.4.4	Square wave voltammetry	86
3.4.4.1	Analysis of the square wave voltammograms for $\text{LiCl-KCl-LaCl}_3$	86
3.4.4.1	Analysis of the square wave voltammograms for $\text{LiCl-KCl-LaCl}_3$	86
3.4.5	Estimation of diffusion coefficient	89
3.4.5.1.	Diffusion coefficient of $\text{La(III)}$ ion	89
3.4.5.2.	Diffusion coefficient of $\text{Nd(III)}$ and $\text{Nd(II)}$ ions	91
3.4.6	Apparent standard potential	95
3.4.6.1	Apparent standard potential of $\text{La(III)/La(0)}$ system in $\text{LiCl-KCl}$ melt	95
3.4.6.2	Estimation of apparent standard potentials for the redox couples $\text{Nd(III)/Nd(II)}$ and $\text{Nd(II)/Nd(0)}$	97
3.4.6.2.1	Stability of $\text{Nd(II)}$ ion	97
3.4.6.2.1	Estimation of apparent standard potentials from cyclic voltammogram	99
3.4.6.2.2	Estimation of apparent standard potentials from open circuit potential transients	101
3.4.6.3	Estimation of apparent standard potentials for the $\text{U(III)/U(0)}$	105

3.4.6.3.1	From cyclic voltammogram	105
3.4.6.3.2	From open circuit potential transients	105
3.4.6.3.3	From emf method	106
3.5	Summary	108
3.6	References	110
<b>CHAPTER 4</b>	<b>Electrochemical behavior of La-, Nd- and U-trivalent ions in LiCl-KCl eutectic melt on cadmium electrode</b>	<b>115</b>
4.1	4.1 Introduction	115
4.2	Literature survey	116
4.3.	Experimental	118
4.3.1.	Chemicals	118
4.3.2.	Preparation of the electrolyte salt	118
4.3.3	Electrochemical apparatus and electrodes	118
4.3.3.1.	Cyclic voltammetry	118
4.3.3.2.	Galvanic cell emf measurement	119
4.4	Results and discussion	121
4.4.1	Reduction behaviour of LaCl <sub>3</sub> and NdCl <sub>3</sub> at the Cd electrode	121
4.4.1.1	Cyclic voltammetry	121
4.4.1.2	Estimation of apparent standard potential for RE(III)/RE(Cd) from cyclic voltammograms	125
4.4.1.3	Open-circuit chronopotentiometry	128
4.4.1.4	Thermodynamic properties of La-Cd and Nd-Cd systems	130
4.4.1.5	Electrodeposition	135
4.4.2	Electrochemical study of uranium at liquid cadmium electrode	135
4.4.2.1	Cyclic voltammetry	135
4.4.2.2	Open-circuit chronopotentiometry-LiCl-KCl-UCl <sub>3</sub>	143
4.4.2.3	Gavanic cell emf measurement	145
4.4.2.4	Potentiostatic electrolysis	150
4.5	Summary	152
4.6	References	155
<b>CHAPTER 5</b>	<b>Electrochemical behavior of La-, Nd- and U-trivalent ions in LiCl-KCl eutectic melt on solid aluminium electrode</b>	<b>159</b>

5.1	Introduction	159
5.2	Literature survey	160
5.3.	Experimental	161
5.3.1.	Chemicals	161
5.3.2.	Preparation of the electrolyte salt	162
5.3.3.	Electrochemical apparatus and electrodes	162
5.4	Results and discussion	162
5.4.1	Electrochemical reduction behaviour of $\text{LaCl}_3$ & $\text{NdCl}_3$ on solid Al electrode	162
5.4.1.1.	Analysis of the cyclic voltammograms	162
5.4.1.2.	Apparent standard potentials of RE(III)/RE(Al) system in LiCl-KCl melt	167
5.4.1.3	Open-circuit chronopotentiometry	169
5.4.1.4	Potentiostatic electrolysis	175
5.4.2	Electrochemical reduction behaviour of $\text{UCl}_3$ on solid aluminium electrode	178
5.4.2.1	Analysis of the cyclic voltammograms	178
5.4.2.2	Open-circuit chronopotentiometry	181
5.4.2.3	Potentiostatic electrolysis	186
5.5	Summary	186
5.6	References	187
<b>CHAPTER 6</b>	<b>Electrochemical behavior of La-, Nd- and U-trivalent ions in LiCl-KCl eutectic melt on gallium cathode</b>	<b>191</b>
6.1	Introduction	191
6.2	Literature survey	191
6.3	Experimental	192
6.3.1	Chemicals	192
6.3.2.	Preparation of the electrolyte salt	192
6.3.3.	Electrochemical apparatus and electrodes	193
6.4	Results and discussion	193

6.4.1	Reduction behavior of $\text{LaCl}_3$ , $\text{NdCl}_3$ and $\text{UCl}_3$ on the Ga surface from cyclic voltammetry	193
6.4.2	Open-circuit chronopotentiometry	201
6.4.3	Electrodeposition	210
6.5	Summary	213
6.6	References	214
<b>CHAPTER 7</b>	<b>Electrochemical pulse techniques for in-situ monitoring the concentration of uranium in molten LiCl-KCl</b>	<b>216</b>
7.1	Introduction	216
7.2	Literature survey	217
7.3.1	Chemicals	217
7.3.2	Preparation of the electrolyte salt	217
7.3.3	Electrochemical apparatus and electrodes	218
7.4	Results and discussion	218
7.4.1	Normal pulse voltammograms	218
7.4.2	Differential pulse voltammograms	221
7.4.3	Square wave voltammograms	222
7.4.4	Influence of the presence of the fission products	224
7.5	Summary	228
7.6	References	228
<b>CHAPTER 8</b>	<b>Conclusions and scope for further studies</b>	<b>230</b>
8.1	Conclusions	230
8.1.1	Challenges encountered during the study	236
8.2	Scope for further studies	237



**Homi Bhabha National Institute**  
**SYNOPSIS OF Ph.D. THESIS**

<b>1. Name of the Student</b>	<b>: Mrs. S. VANDARKUZHALI</b>
<b>2. Name of the Constituent Institution</b>	<b>: Indira Gandhi Centre for Atomic Research</b>
<b>3. Enrolment No.</b>	<b>: CHEM02200704010</b>
<b>4. Title of the Thesis</b>	<b>: <i>Electrochemical studies on uranium and rare earth elements related to pyrochemical reprocessing</i></b>

**SYNOPSIS**

Fast breeder reactors using plutonium based fuels occupy an important place in the Indian nuclear energy programme, as they enable producing more fissile material than that is consumed. The Prototype Fast Breeder Reactor to be commissioned shortly is based on uranium-plutonium mixed oxide fuels whereas the future fast reactors of India will use metallic alloys of U-Pu-Zr or U-Pu as the fuels. Due to the high breeding potential of metallic alloy fuels, they have been chosen to expedite the growth of nuclear energy.

Currently used reprocessing technology is based on PUREX process, a solvent extraction process using tri-butyl phosphate in dodecane as the extractant. But, a high temperature non-aqueous process, known as molten salt electrorefining is more suited for the metallic fuels than the above process, as it offers several advantages such as more compact plant, less criticality problems, less waste volumes etc.

In the molten salt electrorefining process, [1, 2] the spent metallic fuel is anodically dissolved in molten LiCl-KCl eutectic mixture as their chlorides at 773 K. The Gibbs energy of formation of the metal chlorides is the primary determinant of the process. The alkali and alkaline fission products are completely oxidized and they remain in the salt throughout the process. The noble metals are not oxidized and they remain as metal in the anode. The chlorides of rare earths and actinides have intermediate stability. However, the rare earth chlorides are more stable than the actinide chlorides. Two kinds of cathodes are used in the process - a solid iron cathode and a liquid cadmium cathode. In the first stage, uranium is oxidized at the anode (as its chloride) and an equivalent amount of uranium chloride is reduced at the cathode. Plutonium and rare earth metals remain almost entirely in the salt or at the anode because of their relatively negative Gibbs energy of formation of their chlorides. The product obtained at the solid cathode is essentially pure uranium which will be used for fabrication of the blanket fuel. At the cadmium cathode, the activity coefficient of Pu is greatly lowered due to the formation of several intermetallic compounds with Cd. On the contrary, the activity coefficient of U in Cd is about four orders of magnitude larger at the operating temperature. So at the liquid Cd cathode, deposition of Pu is favoured. Similarly, the minor actinides are stabilized due to their very low activity coefficients in cadmium. A small amount of lanthanides also come into the liquid cadmium cathode since their behavior is similar to the trans-uranium metals. The product obtained at the liquid cadmium cathode is a mixture of plutonium, uranium and minor actinides which would be used for making fresh core fuel after blending with uranium and zirconium of required composition.

Minor actinides in the fuel are tolerated as they can be burnt in the reactor. But the lanthanides act as neutron poison and their proportion should be kept as minimum as possible. Under such circumstances, cadmium cannot be considered as the optimum solvent from the perspective of decontamination from the lanthanides. Studies from the liquid-liquid

metal reduction extraction in fluoride melts showed that aluminium has the highest potential for group selective separation of actinides and lanthanides [3]. The process variant being developed at Institute of Transuranium Elements (ITU), Karlsruhe, Germany is based on aluminium cathode. Selective recovery of actinides over lanthanides was achieved in this process [4]. .

Thus it is obvious that knowledge of the electrochemical behavior and the thermochemical properties of actinide and lanthanide chlorides are essential to achieve efficient separation. The basic electrochemical behavior of major elements involved in the electrorefining process, their standard electrode potentials and thermodynamic properties are well studied and reported in the literature. However the kinetics of the reduction process of the metal ions has not been studied to the same extent. The reduction behavior of actinide and rare earth elements at the interface between the LiCl-KCl eutectic melt and liquid Cd are not much studied.

From the perspective of selective separation of actinides from lanthanides, studies under identical conditions would provide inputs for better evaluation of the electrodes. In this thesis, studies on the behavior of an actinide (U) and two rare earth fission product elements (La, Nd) on W, Cd, Al and Ga electrodes in LiCl-KCl eutectic melt in the temperature range 698-773 K were carried out using transient electrochemical techniques. Also, there is need for developing a rapid and reliable method for in-situ monitoring of the composition of the actinides in the electrolyte during the pyrochemical processes. The concentration of uranium would vary to a large extent during the course of the electrorefining process. Hence the method to be selected should be suitable over a large concentration range. Hence studies on different transient techniques, namely, normal pulse voltammetry, square wave voltammetry, differential pulse voltammetry etc. were investigated for monitoring the concentrations of uranium and some lanthanides.

The thesis is divided into 8 chapters. A brief description of the contents of the chapter is given below.

### **Chapter 1: Introduction**

This chapter gives a brief description of the need of nuclear energy to meet the growing energy demand. It discusses about the various types of nuclear fuels and nuclear reactors with an emphasis on the metal fuelled fast breeder reactors for meeting the energy demand. The different non-aqueous processes for reprocessing of spent nuclear fuel are described and the molten salt electrorefining for reprocessing the spent metal fuel is discussed in detail. The need for research on alternate cathodes to cadmium in molten salt electrorefining process and the objective of the thesis are presented.

### **Chapter 2: Experimental facilities and techniques**

The chapter is divided into two sections. The first section gives a brief description of the materials and the equipment used for the studies. The argon atmosphere glove box, purification of the LiCl-KCl salt mixture, preparation of electrolytes, the electrochemical cell, electrodes and the instrumentation are discussed. The second section gives a brief description and theory of the electrochemical techniques used for the studies such as cyclic voltammetry (CV), chronopotentiometry (CP), open circuit potentiometry (OCP), impedance spectroscopy (IS) and pulse techniques such as square wave voltammetry (SWV), normal pulse voltammetry (NPV) and differential pulse voltammetry (DPV).

### **Chapter 3: Electrochemical behavior of LaCl<sub>3</sub>, NdCl<sub>3</sub> and UCl<sub>3</sub> in LiCl-KCl eutectic melt on inert tungsten electrode**

This chapter describes the results of the studies on the redox behavior of LaCl<sub>3</sub>, NdCl<sub>3</sub> and UCl<sub>3</sub> at inert W electrode in LiCl-KCl eutectic melt. The reduction of La(III) ion to La metal and that of U(III) ion to U metal were found to take place in a single step with three electron transfer. On the other hand, reduction of Nd(III) ion to Nd metal on tungsten

electrode takes place in two steps- Nd(III)/ Nd(II) and Nd(II)/ Nd(0). The kinetics of the reduction process was studied by analyzing the semi-integrals of the cyclic voltammograms. The studies showed that the reduction of La(III)/La(0), Nd(II)/Nd(0) and U(III)/U(0) followed the quasi-reversible behavior. The reduction of Nd(III)/Nd(II) showed reversible electrode behavior. The heterogeneous rate constant for the reduction, La(III)/La(0) and Nd(II)/Nd(0) at 798 K were  $4.1 \times 10^{-6}$  and  $7.8 \times 10^{-6} \text{ cms}^{-1}$  respectively and that for U(III)/U(0) at 773 K was  $1.8 \times 10^{-5} \text{ cms}^{-1}$ . The apparent standard electrode potentials,  $E_{La(III)/La(0)}^*$ ,  $E_{Nd(III)/Nd(II)}^*$ ,  $E_{Nd(II)/Nd(0)}^*$ ,  $E_{Nd(III)/Nd(0)}^*$  and  $E_{U(III)/U(0)}^*$  were estimated from the

cyclic voltammograms and open circuit potential measurements. In order to validate our measurements using transient techniques, the equilibrium potential of U(III)/U(0) couple was determined using the emf method also. The electromotive force of the following galvanic cell was measured in the temperature range 680-823 K-  
 $Ag(s) / AgCl \text{ in } LiCl - KCl_{eut} (l) // UCl_3 \text{ in } LiCl - KCl_{eut} (l) / U(s)$

The apparent standard potential values for the redox couple U(III)/U(0) obtained from cyclic voltammetry, OCP and emf measurement are in agreement with each other within  $\pm 10$  mV. The present data are in agreement with the values reported by Masset *et al.* in his critical review of the literature data [5].

#### **Chapter 4: Electrochemical behavior of LaCl<sub>3</sub>, NdCl<sub>3</sub> and UCl<sub>3</sub> in LiCl-KCl eutectic melt on cadmium electrode**

The studies on the reduction behavior of LaCl<sub>3</sub>, NdCl<sub>3</sub> and UCl<sub>3</sub> on liquid cadmium pool and film electrodes in LiCl-KCl eutectic melt are discussed in this chapter. Under potential deposition of the respective lanthanide metal through reduction of their chloride on this reactive due to the formation of the solvent rich intermetallic compound, LaCd<sub>11</sub> and NdCd<sub>11</sub> for the La-Cd and Nd-Cd systems respectively. The apparent standard electrode

potentials,  $E_{La}^* (III)/La(Cd)$  and  $E_{Nd}^* (III)/Nd(Cd)$  at 723 K were  $-2.728 (\pm 0.002)$  and  $-2.721 (\pm 0.002)$  V vs.  $Cl_2/Cl^-$  respectively. The Gibbs energy of formation of the  $LaCd_{11}$  and  $NdCd_{11}$  intermetallic compounds at 723 K determined by OCP were  $-170.6 (\pm 0.9)$  and  $-153.1 (\pm 0.6)$   $kJ\ mol^{-1}$  respectively. The values are in agreement with those reported in the literature.

However, in case of the U-Cd system, the extent of shift in the potential in the cyclic voltammograms did not agree with those expected from the Gibbs energy of formation of the intermetallic  $UCd_{11}$  reported by Johnson *et al.* [6] by molten salt emf measurement. According to the phase diagram of the uranium-cadmium system,  $UCd_{11}$  is the only intermetallic compound and it decomposes peritectically to liquid +  $\alpha$  U beyond 746 K. But we could observe peak in the cyclic voltammograms at positive potentials beyond 746 K. Similar observation was made by Shirai *et al.* also [7]. To understand the anomalous behavior of U on cadmium cathode, we have studied the U-Cd system in the cadmium rich region by galvanic cell emf method in the temperature range 653 to 764 K.



Measurements were made with saturated U-Cd alloy and unsaturated U-Cd alloy. The Gibbs energies of formation of  $UCd_{11}$  in the temperature range 680 to 744 K were evaluated and the values were in good agreement with those reported by Johnson *et al.*[6] The peritectic temperature of  $UCd_{11}$  was evaluated to be 748 K which is consistent with the phase diagram. The discrepancy found in the cyclic voltammograms and OCP transients were fairly understood by comparing the values of the equilibrium potentials obtained from these measurements with those measured in the saturated and unsaturated U-Cd alloy from the galvanic cell.

## **Chapter 5: Electrochemical behavior of $LaCl_3$ , $NdCl_3$ and $UCl_3$ in LiCl-KCl eutectic melt on solid aluminium electrode**

This chapter discusses the reduction behavior of  $\text{LaCl}_3$ ,  $\text{NdCl}_3$  and  $\text{UCl}_3$  on solid aluminium electrode by electrochemical methods in the temperature range 698-773 K. The reduction of  $\text{LaCl}_3$  and  $\text{NdCl}_3$  occurred at more positive potential than that for inert cathode due to the formation of the intermetallic compound  $\text{Al}_{11}\text{RE}_3$ . The apparent standard electrode potential of  $\text{La(III)/La(Al)}$  and  $\text{Nd(III)/Nd(Al)}$  at 723 K were  $-2.539 (\pm 0.002)$  and  $-2.496 (\pm 0.002)$  V vs.  $\text{Cl}_2/\text{Cl}^-$  respectively. The Gibbs energy of formation of the intermetallics estimated from OCP were  $-179.5 (\pm 0.6)$  and  $-168.8 (\pm 0.6)$   $\text{kJ mol}^{-1}$  respectively. Studies on the redox behavior of  $\text{UCl}_3$  on solid aluminium electrode showed the underpotential reduction of  $\text{U(III)}$  ion on aluminium electrode at a potential  $\sim 0.35$  V more anodic than pure uranium metal deposition. The cyclic voltammograms did not show well resolved peaks for the formation and dissolution of the U-Al alloy. The OCP transients showed that the equilibrium potential for the U-Al alloy was very close to the rest potential of the aluminium electrode. From the values of the Gibbs energy of formation of the intermetallics,  $\text{UAl}_4$  and  $\text{UAl}_3$  reported by Chiotti *et al.* [8], it was found that they differ merely by  $1 \text{ kJ mol}^{-1}$  and the difference in the corresponding emf is  $< 10$  mV. Taking this into consideration, it was concluded that the compound formed on the Al surface corresponds to both the intermetallics,  $\text{UAl}_4$  and  $\text{UAl}_3$ . Similar behavior was earlier reported by Cassayre *et al.*[9].

### **Chapter 6: Electrochemical behavior of $\text{LaCl}_3$ , $\text{NdCl}_3$ and $\text{UCl}_3$ in LiCl-KCl eutectic melt on gallium surface**

The feasibility of using gallium cathode for efficient actinide-lanthanide separation in molten LiCl-KCl eutectic is explored in this chapter. Lambertin *et al.* [10] had studied the reduction behavior of  $\text{CeCl}_3$  and  $\text{PuCl}_3$  on gallium cathode in  $\text{CaCl}_2$  and NaCl-KCl melts at 1073 K using electrochemical transient techniques. Their studies showed the feasibility of selective deposition of Pu in gallium cathode. However there is no electrochemical study reported on U-Ga, La-Ga and Nd-Ga systems in the literature to our knowledge. The redox

behavior of  $\text{LaCl}_3$ ,  $\text{NdCl}_3$  and  $\text{UCl}_3$  on Ga surface using CV and OCP is reported in this chapter. The measurements were made using the  $\text{LiCl-KCl-GaCl}_3\text{-MCl}_3$  (M-U, La, Nd) melt in the temperature range 698-785 K at the W electrode using CV and OCP. The metal ions reduced on the pre-deposited gallium surface at more positive potentials forming the Ga-rich intermetallic compounds,  $\text{LaGa}_6$ ,  $\text{NdGa}_6$  and  $\text{UGa}_3$  respectively for La-Ga, Nd-Ga and U-Ga systems. In case of the La-Ga system, there was a change in the trend of the peak potentials in the cyclic voltammograms and the emf values from the OCP transients recorded at temperatures 765 and 785 K. The observation is consistent with the phase diagram of La-Ga system as  $\text{LaGa}_6$  decomposes peritectically to  $\text{Liq.} + \text{LaGa}_2$  beyond 750 K. The apparent standard potentials,  $E_{\text{La(III)/La(Ga)}}^*$ ,  $E_{\text{Nd(III)/Nd(Ga)}}^*$  and  $E_{\text{U(III)/U(Ga)}}^*$  at 723 K were -2.392 ( $\pm 0.001$ ), -2.374 ( $\pm 0.001$ ) and -2.083 ( $\pm 0.001$ ) V vs.  $\text{Cl}_2/\text{Cl}^-$  respectively. The Gibbs energy of formation of the alloys,  $\text{LaGa}_6$ ,  $\text{NdGa}_6$  and  $\text{UGa}_3$  estimated from OCP measurements at 723 K were -217.3 ( $\pm 0.6$ ), -209.3 ( $\pm 0.6$ ) and -129.3 (0.6)  $\text{kJ mol}^{-1}$  respectively. The values for  $\text{UGa}_3$  were in very good agreement with those reported in the literature. However there were no reports to compare the values for  $\text{LaGa}_6$  and  $\text{NdGa}_6$ . Further studies need to be carried out by potentiostatic electrolysis to ascertain the alloys formed.

### **Chapter 7: Electrochemical pulse techniques for in-situ monitoring the concentration of uranium in molten LiCl-KCl**

Electroanalytical pulse techniques could serve quick and reliable methods for in-situ monitoring of the composition of analyte in multi-component systems. Iizuka *et al.* [11] studied the applicability of NPV and SWV for determining the actinide concentration in molten chloride electrolyte. In Argonne National Laboratory, ANL, a semi-quantitative analysis of the SWV was carried out in molten chlorides containing Zr, U, Pu & Dy [12]. In this chapter we discuss the results of NPV, DPV and SWV for determining the concentration of uranium in the concentration range 0.01 to 11 wt %. Linear relationship was observed for

the reduction current with the concentration of  $\text{UCl}_3$  in the electrolyte in the concentration range 0.1 -4 wt % for DPV and fairly a linear relationship was found in the concentration range 0.1 -11 wt % for NPV. The SWV showed higher sensitivity, but a linear relationship for the reduction current was not observed throughout the range. Two different linear dependences, one for lower concentration range and the other for the higher concentration ranges of  $\text{UCl}_3$ . Studies using simulated melt showed that the presence of the lanthanides products does not affect the determination of uranium.

### **Chapter 7: Conclusions and scope for further studies**

This chapter summarizes the major findings of this study

- (1) The apparent standard potentials of various redox couples were obtained under identical conditions from the studies. This serves as a database for our further studies. A brief discussion is made on the selectivity of the electrodes.
- (2) We could estimate the equilibrium potential of the  $\text{Nd(III)/Nd(0)}$  couple from OCP measurement which is not possible by galvanic cell emf method due to the disproportionation reaction of  $\text{Nd(II)}$  ion to  $\text{Nd(III)}$  ion and  $\text{Nd}$  metal
- (3) The discrepancy found in the behavior of  $\text{U}$  on  $\text{Cd}$  cathode was understood by galvanic cell emf measurements using saturated and unsaturated  $\text{U-Cd}$  alloys.
- (4) Studies on the redox behavior of  $\text{LaCl}_3$ ,  $\text{NdCl}_3$  and  $\text{UCl}_3$  on  $\text{Ga}$  surface are reported for first time.
- (5) The pulse parameter for measuring the concentration of uranium over wide concentration range for three electroanalytical pulse techniques was optimized.

#### **Scope for further studies**

- (1) The studies using different cathodes, namely,  $\text{W}$ ,  $\text{Cd}$ ,  $\text{Al}$  and  $\text{Ga}$  can be extended to investigate the redox behavior of the chlorides of  $\text{Pu}$  and minor actinides so as to have a complete database.

- (2) From the difference in potential values of the actinides and lanthanides, their activity coefficient at different substrate, it is possible to model and evaluate the selectivity of the electrodes.
- (3) Studies on the pulse techniques have to be optimized for U, Pu, minor actinides in the presence of major fission products to simulate the process condition.

### **References**

- [1] Y.I. Chang, Nucl. Technol., 88 (1989) 129.
- [2] E. Charles , Y. Till, Y. I. Chang, Plentiful Energy “The Story of Integral Fast Reactor”, ISBN: 978-1466384606, Library of congress control No. 2011918518.
- [3] O. Conocar, N. Douyere, J.P. Glatz, J. Lacquement, R. Malmbeck, J. Serp, Nucl. Sci. Eng. 153 (2006) 253.
- [4] P. Soucek, L. Cassayre, R. Malmbeck, E. Mendes, R. Jardin, J.P. Glatz, Radiochim. Acta 96 (2008) 315.
- [5] P. Masset, D. Bottomley, R. Konings, R. Malmbeck, A. Rodrigues, J. Serp, J.P. Glatz J. Electrochem. Soc. 152 (6) (2005) A1109.
- [6] I. Johnson, H. M. Feder, Trans. Met. Soc. AIME, 224 (1962) 468.
- [7] Osamu Shirai, Koichi Uozumi, Takashi Iwai, Yasuo Arai, Analytical Sciences 2001, vol.17 Suppliment, i959-i962.
- [8] P. Chiotti, V. V. Akhachinskij, I. Ansara, M. H. Rand, “The chemical thermodynamics of actinide elements and compounds, part 5, The Actinide Binary Alloys”.
- [9] L. Cassayre, C. Caravaca, R. Jardin, R. Malmbeck, P. Masset, E. Mendes, J. Serp, P. Soucek, J.P. Glatz, J. Nucl. Mater. 378 (2008) 79.
- [10] D. Lambertin, S. Chedhomme, G. Bourges, S. Sanchez, G.S. Picard, J. Nucl. Mater. 341 (2005) 131.

[11] M. Iizuka, T. Inoue, O. Shirai, T. Iwai, Y. Arai, J. Nucl. Mater. 297 (2001) 43.

[12] Annual Technical Report for 1994, Chemical Technology Division, Argonne National Laboratory Report; ANL-95/24 (1995) p.88.

### **Publications in Refereed journals**

#### ***a. Published***

1. “Electrochemical behaviour of  $\text{LaCl}_3$  at tungsten and aluminium cathodes in LiCl-KCl eutectic melt”, S. Vandarkuzhali, Nibedita Gogoi, Suddhasattwa Ghosh, B. Prabhakara Reddy, K.Nagarajan, , Electrochim. Acta 59 (2012) 245.

#### ***b. Under Review***

1. “Investigation on the electrochemical behavior of neodymium chloride at W, Al and Cd electrodes in molten LiCl-KCl eutectic”, S. Vandarkuzhali, Manish Chandra, Suddhasattwa Ghosh, Nibedita Samanta, S. Nedumaran, B. Prabhakara Reddy and K. Nagarajan, Under review in Electrochim. Acta.

### **Proceeding and presentations at national/international conference**

1. “Electroanalytical techniques for in-situ measurement of uranium in molten salt electrolyte”, S. Vandarkuzhali, Suddhasattwa Ghosh, B. Prabhakara Reddy and K. Nagarajan presented at “International Pyroprocessing Research Conference, IPRC-2008” held at Jeju Island, Republic of Korea during Aug 24-27, 2008.
2. “Elucidation of the behaviour of U(III)/U couple at liquid cadmium electrode in LiCl-KCl eutectic melt”, S.Vandarkuzhali, Suddhasattwa Ghosh, Nibedita Gogoi, S. Nedumaran, B.Prabhakara Reddy and K.Nagarajan, Proc. Int. Conf. on Separation Science and Technology, SESTEC-2010 held at Kalpakkam during March 1-4 2010, SESTEC 2010, pp. 485-486, paper E-2.
3. “Investigation on the electrochemical behaviour of neodymium chloride in molten LiCl-KCl eutectic”, S.Vandarkuzhali, Suddhasattwa Ghosh, S. Nedumaran, Manish

Chandra, Nibedita Gogoi, B.Prabhakara Reddy and K.Nagarajan, “CMSNT-2013” held at Mumbai during 9-11 January 2013.

4. “Electrochemical behavior of neodymium chloride on aluminium and cadmium cathodes in LiCl-KCl eutectic melt” , S. Vandarkuzhali, Manish Chandra, S.

Nedumaran, B. Prabhakara Reddy and K. Nagarajan, presented in the theme meeting on Recent Trends in Material Chemistry, RTMC-2013 held at VIT, Vellore, Tamilnadu during 25-27 July 2013, paper-28 pp 52.

5. “Feasibility of gallium cathode for separation of uranium from lanthanides in molten LiCl-KCl electrolyte”, S.Vandarkuzhali, P. Venkatesh, Nibedita Samanta, S. Suganthi, K. Perumal, B.Prabhakara Reddy and K. Nagarajan, presented “SESTEC-2014” held at Mumbai during Feb 25-28, 2014.

### **Awards**

NA

Signature of Student :

Date :

### **Doctoral Committee**

S. No.	Name	Designation	Signature	Date
1.	Dr. T. Gnanasekaran, RRF, IGCAR	Chairman		
2.	Dr. K.Nagarajan, Director, CG	Guide & Convener		
3.	Dr. T.G. Srinivasan, RRF, IGCAR	Member		
4.	Dr. S. Rangarajan, WSCL	Member		
5.	Dr. B. Prabhakara. Reddy, CG	Technology Advisor		

## LIST OF FIGURES

<b>Figure No.</b>	<b>Figure Caption</b>	<b>Page No.</b>
Fig. 1.1	The IFR fuel cycle	5
Fig. 1.2	Relative radiotoxicity of fission product and transuranium isotopes in spent nuclear fuel relative to the radiotoxicity of natural uranium	7
Fig. 1.3	Schematic of the electrorefiner in IFR process	12
Fig. 2.1	Schematic diagram of the argon atmosphere glove box	26
Fig. 2.2	Schematic diagram of the argon atmosphere glove box	26
Fig. 2.3	Photograph of the chlorination facility	28
Fig. 2.4	Schematic of the electrochemical cell	32
Fig. 2.5	Photograph of the working electrode used for pulse techniques	34
Fig. 2.6	Photograph of the electrochemical cell	34
Fig. 2.7	Concentration profile at the electrode-electrolyte interface	38
Fig. 2.8	Picture showing the diffusion layer and the concentration profile in the electrochemical cell	39
Fig. 2.9	Shape of voltammogram for constant and varying thickness of the diffusion layer	38
Fig. 2.10	Classification of interfacial electrochemical techniques	43
Fig. 2.11	Triangular waveform for the cyclic voltammetry and the corresponding potential current curve	43
Fig. 2.12	The excitation signal and the potential response for chronopotentiometry	46
Fig. 2.13	Potential waveform for normal pulse voltammetry and excitation	48

	signal for the same.	
Fig. 2.14	Potential waveform for differential pulse voltammetry and excitation signal for the same	49
Fig. 2.15	Potential waveform for squarewave voltammetry and excitation signal for the same	50
Fig.2.16	Equivalent circuit for the Randles cell and Nyquist plot for the Randles cell.	52
Fig.2.17	Equivalent circuit for an electrochemical cell and Impedance plot for an electrochemical system showing the regions of mass-transfer and kinetic control at low and high frequencies, respectively	52
Fig. 2.18	Open circuit potential transient after polarizing the electrode at sufficient cathodic potential	55
Fig. 3.1	A comparison of the cyclic voltammogram for pure LiCl–KCl melt and LiCl-KCl-LaCl <sub>3</sub> melt. Working electrode: tungsten, apparent electrode area: 0.301 cm <sup>2</sup> . Temperature: 773 K, scan rate: 0.1 V s <sup>-1</sup> .	65
Fig. 3.2	Cyclic voltammograms for 7.54×10 <sup>-5</sup> mol cm <sup>-3</sup> LaCl <sub>3</sub> in LiCl-KCl melt for a W electrode at various scan rates. Apparent electrode area: 0.347 cm <sup>2</sup> . Temperature: 798 K. Inset: variation of peak potential with logarithm of sweep rate	66
Fig. 3.3	Cyclic voltammograms of LiCl-KCl-NdCl <sub>3</sub> melt on W electrode for different scan rates. Temperature: 723 K; Concentration of NdCl <sub>3</sub> : 6.66 x 10 <sup>-5</sup> mol cm <sup>-3</sup> ; Electrode area: 0.49 cm <sup>2</sup>	69
Fig. 3.4	Cyclic voltammograms of LiCl-KCl-NdCl <sub>3</sub> melt on W electrode obtained at different switching potentials	70
Fig. 3.5	Plot of the cathodic peak potentials as a function of logarithm of the scan rates at 723 and 798 K	71

Fig. 3.6	Cyclic voltammogram of LiCl-KCl-UCl <sub>3</sub> at 748 K; Concentration of UCl <sub>3</sub> : $7.31 \times 10^{-5} \text{ mol cm}^{-3}$ ; Working electrode: W	72
Fig. 3.7	Semi-integral curves of the voltammogram corresponding to La(III)/La(0) at tungsten electrode in LiCl-KCl melt. Concentration of LaCl <sub>3</sub> : $7.54 \times 10^{-5} \text{ mol cm}^{-3}$ , temperature: 798 K, scan rate: $0.025 \text{ V s}^{-1}$	75
Fig. 3.8	Logarithmic analysis of the convoluted data for LaCl <sub>3</sub> in LiCl-KCl melt at a tungsten electrode. Polarization rate: $25 \text{ mV s}^{-1}$ ; apparent electrode area: $0.347 \text{ cm}^2$ ; temperature: 798 K Concentration of LaCl <sub>3</sub> : $7.54 \times 10^{-5} \text{ mol cm}^{-3}$	75
Fig. 3.9	Complex impedance spectra for $7.54 \times 10^{-5} \text{ mol cm}^{-3}$ LaCl <sub>3</sub> in LiCl-KCl melt at 793 K for a W working electrode at rest potential ( $-0.25 \text{ V vs. Ag(I)/Ag}$ ). (a) Nyquist plot; (b and c) Bode plots; (d) corresponding equivalent circuit	77
Fig. 3.10	Cyclic voltammograms of LiCl-KCl-NdCl <sub>3</sub> melt on W electrode at 723 K and corresponding convoluted curve	81
Fig. 3.11	Convoluted curve for cyclic voltammogram recorded in LiCl-KCl-UCl <sub>3</sub> at 748 K at polarization rate $25 \text{ mVs}^{-1}$ ; Concentration of UCl <sub>3</sub> : $7.31 \times 10^{-5} \text{ moles cc}^{-1}$	83
Fig. 3.12	Chronopotentiograms on a tungsten electrode for $7.54 \times 10^{-5} \text{ mol cm}^{-3}$ LaCl <sub>3</sub> in LiCl- KCl melt at 798 K. Apparent area: $0.301 \text{ cm}^2$ . Inset: $i\tau^{1/2}$ against current density. Working electrode: W. Concentration of LaCl <sub>3</sub> : $7.54 \times 10^{-5} \text{ mol cm}^{-3}$ . Temperature: 798 K	85
Fig. 3.13	Chronopotentiograms on a tungsten electrode for LiCl-KCl-NdCl <sub>3</sub> melt. Temperature: 723 K; Concentration of NdCl <sub>3</sub> : $6.66 \times 10^{-5} \text{ mol cm}^{-3}$ ; Electrode area: $0.49 \text{ cm}^2$	85
Fig. 3.14.	Variation of $i\tau^{1/2}$ with different current densities for the redox couples Nd(III)/Nd(0) for the	86

chronopotentiograms shown in Fig. 3.13

- Fig. 3.15 Square wave voltammograms for  $7.54 \times 10^{-5} \text{ mol cm}^{-3}$   $\text{LaCl}_3$  in LiCl-KCl melt at 793 K. Working electrode: tungsten. Apparent electrode area:  $0.347 \text{ cm}^2$ . Frequency: 8 Hz 88
- Fig. 3.16. Square wave voltammograms of  $\text{NdCl}_3$  in LiCl-KCl eutectic at 723 K at various frequencies. Amplitude of pulse: 10 mV. Concentration of  $\text{NdCl}_3$ :  $6.66 \times 10^{-5} \text{ mol cm}^{-3}$ ; Electrode area:  $0.49 \text{ cm}^2$  88
- Fig. 3.17. Plot of peak current density as a function of square root of frequency for LiCl-KCl- $\text{NdCl}_3$  melt. Temperature: 723 K; Concentration of  $\text{NdCl}_3$ :  $6.66 \times 10^{-5} \text{ mol cm}^{-3}$  89
- Fig. 3.18 Plot of current density vs. square root of scan rate for LiCl-KCl- $\text{LaCl}_3$ . Concentration of  $\text{LaCl}_3$ :  $7.54 \times 10^{-5} \text{ mol cm}^{-3}$ . Temperature: 798 K 92
- Fig. 3.19. Plot of current density for peak  $I_c$  vs. square root of scan rate for LiCl-KCl- $\text{NdCl}_3$  melt. Temperature: 723 K; Concentration of  $\text{NdCl}_3$ :  $6.66 \times 10^{-5} \text{ mol cm}^{-3}$  94
- Fig. 3.20. Plot of current density for peak  $II_c$  vs. square root of scan rate for LiCl-KCl- $\text{NdCl}_3$  melt. Temperature: 723 K; Concentration of  $\text{NdCl}_3$ :  $6.66 \times 10^{-5} \text{ mol cm}^{-3}$  94
- Fig. 3.21. Open circuit potential transient curve for  $\text{NdCl}_3$  in LiCl-KCl melt on W electrode. Cathodic polarization: -2.3 V vs. ( $\text{Ag}/\text{Ag}^+$ ) reference electrode. Inset: OCP transient curve showing attainment of open circuit potential for W electrode after long duration 102
- Fig. 3.22 Open circuit potential transient of LiCl-KCl- $\text{UCl}_3$  on W electrode at 798 K; Concentration of  $\text{UCl}_3$ :  $7.31 \times 10^{-5} \text{ moles cc}^{-1}$ ; Applied potential: -1.6 V 106

Fig. 3.23	Apparent standard potential for the redox couple U(III)/U(0) obtained from this study and those reported in literature	108
Fig. 4.1	Photograph of the electrode assembly for liquid cadmium cathode	120
Fig. 4.2	Cyclic voltammograms for LiCl-KCl melt on W and Cd pool cathodes. Temperature: 698 K; Area: 0.314 cm <sup>2</sup> (W) and 0.21 cm <sup>2</sup> (Cd)	122
Fig. 4.3a	Cyclic voltammograms for LaCl <sub>3</sub> in LiCl-KCl melt at cadmium pool electrode. Polarization rate: 10 mVs <sup>-1</sup> ; Concentration of LaCl <sub>3</sub> : 6.66 x 10 <sup>-5</sup> mol cm <sup>-3</sup>	122
Fig. 4.3b	Cyclic voltammograms for NdCl <sub>3</sub> in LiCl-KCl melt at cadmium pool electrode. Polarization rate: 10 mVs <sup>-1</sup> ; Concentration of NdCl <sub>3</sub> : 6.66 x 10 <sup>-5</sup> mol cm <sup>-3</sup>	124
Fig. 4.4	Cd-La phase diagram	124
Fig. 4.5	Cd-Nd phase diagram	125
Fig. 4.6	Comparison of cyclic voltammograms for LiCl-KCl-NdCl <sub>3</sub> melt at Cd pool and film electrode; Polarization rate: 10 mVs <sup>-1</sup> ; Concentration of NdCl <sub>3</sub> : 6.66 x 10 <sup>-5</sup> mol cm <sup>-3</sup> . Inset: Cyclic voltammograms at Cd film electrode at different scan rates; Temperature: 698 K	126
Fig. 4.7	Cyclic voltammograms for LaCl <sub>3</sub> in LiCl-KCl at cadmium film electrode at different scan rates. Temperature: 748 K	126
Fig. 4.8	Open circuit potential transient curve for LaCl <sub>3</sub> in LiCl-KCl melt on Cd film electrode. Cathodic polarization: -1.7 V vs. (Ag/Ag <sup>+</sup> ) reference electrode	131
Fig. 4.9	Open circuit potential transient curve for NdCl <sub>3</sub> in LiCl-KCl melt on Cd film electrode. Cathodic polarization: -1.7 V vs. (Ag/Ag <sup>+</sup> ) reference electrode	131

Fig. 4.10	XRD pattern of Nd-Cd film formed by potentiostatic electrolysis at -1.55V vs. (Ag/Ag <sup>+</sup> ) reference electrode in LiCl-KCl-NdCl <sub>3</sub> -CdCl <sub>3</sub> melt for 5 hrs at 748 K	136
Fig. 4.11	Cyclic voltammogram for LiCl-KCl-UCl <sub>3</sub> melt at different temperatures on cadmium pool cathode; Concentration of UCl <sub>3</sub> : 2.44 x 10 <sup>-5</sup> mol cm <sup>-3</sup> , Ag/AgCl ( <i>X</i> <sub>AgCl</sub> = 0.001)	136
Fig. 4.12	The cadmium- uranium phase diagram in Cd rich side	137
Fig. 4.13	Cyclic voltammograms of LiCl-KCl-UCl <sub>3</sub> on Cd film working electrode at different scan rates; Concentration of UCl <sub>3</sub> : 7.31 x	138
Fig. 4.14	Cyclic voltammograms of LiCl-KCl-UCl <sub>3</sub> on on different working electrodes; Concentration of UCl <sub>3</sub> : 7.31 x 10 <sup>-5</sup> moles cm <sup>-3</sup> ; Temperature: 748 K	138
Fig. 4.15	Cyclic voltammograms of LiCl-KCl-UCl <sub>3</sub> on Cd film working electrode at different switching potentials; Concentration of UCl <sub>3</sub> : 7.31 x 10 <sup>-5</sup> moles cm <sup>-3</sup> ; Temperature: 748 K	139
Fig. 4.16	Electrode potentials for U(III)/U(0) and U(III)/U(Cd) couples from cyclic voltammetry and emf method	142
Fig. 4.17	Open circuit potential transient of LiCl-KCl-UCl <sub>3</sub> on Cd film working electrode at different temperatures; Concentration of UCl <sub>3</sub> : 7.31 x 10 <sup>-5</sup> moles cm <sup>-3</sup> ; Applied potential: -1.5 V	144
Fig. 4.18	Plot of emf as a function of temperature from galvanic cell emf method	147
Fig. 4.19	XRD pattern of the cathode deposit of uranium on cadmium pool cathode formed by potentiostatic electrolysis at -1.3 V vs. Ag/AgCl reference electrode at 723 K	151
Fig. 4.20	SEM micrograph of the cathode deposit of uranium on cadmium pool cathode formed by potentiostatic electrolysis at -1.3 V vs.	151

AgCl/Ag reference electrode at 723 K and the corresponding EDAX analysis

Fig. 4.21	Comparison of cyclic voltammograms for $\text{UCl}_3$ , $\text{LaCl}_3$ and $\text{NdCl}_3$ in LiCl-KCl melt on cadmium pool cathode	152
Fig.5.1	Electroactive domain of pure LiCl-KCl on aluminium electrode as compared to that on a W electrode	163
Fig.5.2	Cyclic voltammograms obtained on the tungsten and aluminium electrodes for LiCl-KCl-NdCl <sub>3</sub> melt	163
Fig. 5.3	Al-La phase diagram	165
Fig. 5.4	Al-Nd phase diagram	165
Fig. 5.5	Cyclic voltammograms for $7.54 \times 10^{-5} \text{ mol cm}^{-3}$ $\text{LaCl}_3$ in LiCl-KCl melt on Al electrode at various scan rates. Electrode area: $0.347 \text{ cm}^2$ . Temperature: 723K	166
Fig. 5.6	Cyclic voltammogram for LiCl-KCl-NdCl <sub>3</sub> melt at Al electrode at 748 K; Concentration of $\text{NdCl}_3$ : $6.66 \times 10^{-5} \text{ mol cm}^{-3}$ . Inset: Cyclic voltammograms at different scan rates	166
Fig.5.7	OCP transient curve for LiCl-KCl-LaCl <sub>3</sub> melt on Al electrode at different temperatures. Cathodic polarization: -1.8 V vs. ( $\text{Ag}/\text{Ag}^+$ , $X_{\text{AgCl}} = 0.001$ ) reference electrode	170
Fig.5.8	OCP transient curve for LiCl-KCl-NdCl <sub>3</sub> melt on Al electrode for different duration. Cathodic polarization: -1.8 V vs. ( $\text{Ag}/\text{Ag}^+$ ) reference electrode. Inset: OCP transient curve at 723 K. Cathodic polarization: -1.8 V for 600 s	170
Fig. 5.9	Enlarged view of the aluminium rich region of Al-La phase diagram	172
Fig. 5.10	Cross-sectional SEM image of La-Al film formed by potentiostatic electrolysis at 773 K. Cathodic polarization: -1.5 V vs. ( $\text{Ag}/\text{Ag}^+$ , $X_{\text{AgCl}} = 0.001$ ) reference electrode and	176

	corresponding EDX analysis confirming the formation of $\text{Al}_{11}\text{La}_3$	
Fig.5.11	XRD pattern of La–Al film formed by potentiostatic electrolysis at 798 K for cathodic polarization of -1.5 V vs. ( $\text{Ag}/\text{Ag}^+$ , $X_{\text{AgCl}} = 0.001$ ) reference electrode for 6 hrs	176
Fig.5.12	Cross-sectional SEM image of Nd–Al film formed by potentiostatic electrolysis at -1.5 V vs. ( $\text{Ag}/\text{Ag}^+$ ) reference electrode at 773 K and and corresponding EDX analysis confirming the formation of $\text{Al}_{11}\text{Nd}_3$	177
Fig.5.13	XRD pattern of Nd–Al film formed by potentiostatic electrolysis at -1.5 V vs. ( $\text{Ag}/\text{Ag}^+$ ) reference electrode for 5 hrs at 773 K	177
Fig.5.14	Cyclic voltammograms obtained on the tungsten and aluminium electrodes for LiCl-KCl- $\text{UCl}_3$ melt at 723 K.	180
Fig.5.15	Cyclic voltammograms obtained on the aluminium electrode for LiCl-KCl- $\text{NdCl}_3$ melt at different temperatures	180
Fig. 5.16	Al-U phase diagram	181
Fig.5.17	Open circuit potential transient curve for $\text{UCl}_3$ in LiCl-KCl melt on Al electrode at different temperatures. Cathodic polarization: -1.3 V vs. ( $\text{Ag}/\text{Ag}^+$ ) reference electrode	182
Fig.5.18	XRD pattern of U–Al film formed by potentiostatic electrolysis at -1.3 V vs. ( $\text{Ag}/\text{Ag}^+$ ) reference electrode for 8 hrs at 723 K	186
Fig.6.1	Cyclic voltammograms for pure LiCl-KCl melt and LiCl-KCl- $\text{GaCl}_3$ melt on W electrode.	194
Fig. 6.2	Cyclic voltammograms for LiCl-KCl- $\text{GaCl}_3$ melt in the presence and absence of $\text{LaCl}_3$ at W electrode. Polarization rate: $50 \text{ mVs}^{-1}$ ; Concentration of $\text{LaCl}_3$ : $6.66 \times 10^{-5} \text{ mol cm}^{-3}$	195
Fig. 6.3	Comparison of cyclic voltammograms for LiCl-KCl- $\text{UCl}_3$ in presence and absence of $\text{GaCl}_3$ on W electrode	196

Fig. 6.4	Cyclic voltammograms for $\text{NdCl}_3$ in $\text{LiCl-KCl-GaCl}_3$ melt at W electrode at different scan rates. Temperature: 748 K. Inset: Comparison of cyclic voltammograms for $\text{LiCl-KCl-NdCl}_3$ in presence and absence of $\text{GaCl}_3$ on W electrode	196
Fig. 6.5	Ga-La phase diagram	198
Fig. 6.6	Ga-Nd phase diagram	198
Fig. 6.7	Ga-U phase diagram	199
Fig. 6.8	Cyclic voltammograms for $\text{LaCl}_3$ in $\text{LiCl-KCl-GaCl}_3$ melt at W electrode at different scan rates at 723 K. Inset: Cyclic voltammograms for the same at different scan rates at 785 K	199
Fig. 6.9	Cyclic voltammograms for $\text{UCl}_3$ in $\text{LiCl-KCl-GaCl}_3$ melt at W electrode at different temperatures. Inset: Cyclic voltammograms for the same at different scan rates at 698 K	200
Fig. 6.10	Cyclic voltammograms for $\text{LaCl}_3$ in $\text{LiCl-KCl-GaCl}_3$ melt at W electrode at different temperatures. Inset: Cyclic voltammograms for the same comparing at 748 and 785 K	200
Fig. 6.11	Cyclic voltammograms for $\text{NdCl}_3$ in $\text{LiCl-KCl-GaCl}_3$ melt at W electrode at different temperatures	201
Fig.6.12	Open circuit potential transient curve for $\text{LiCl-KCl-LaCl}_3\text{-GaCl}_3$ melt on W electrode at different temperatures for cathodic polarization: -1.5 V. Inset: Equilibrium potential of $\text{La(III)/La(Ga)}$ vs. $\text{La(III)/La(0)}$ electrode at different temperatures	203
Fig.6.13	Open circuit potential transient curve for $\text{LiCl-KCl-NdCl}_3\text{-GaCl}_3$ melt on W electrode at different temperatures for cathodic polarization: -1.5 V	205
Fig.6.14	Open circuit potential transient curve for $\text{LiCl-KCl-UCl}_3\text{-GaCl}_3$ melt on W electrode at different temperatures for cathodic	208

polarization: -1.2 V

Fig. 6.15	Cross-sectional SEM image of the cathode deposit formed by potentiostatic electrolysis using LiCl-KCl-LaCl <sub>3</sub> -GaCl <sub>3</sub> melt on Ta sheet at 723 K. Cathodic polarization: -1.45 and the corresponding EDX analysis	211
Fig. 6.16	Cross-sectional SEM image of the cathode deposit formed by potentiostatic electrolysis using LiCl-KCl-UCl <sub>3</sub> -GaCl <sub>3</sub> melt on Ta sheet at 723 K. Cathodic polarization: -1.2 and the corresponding EDX analysis	212
Fig. 7.1a	NPV curves for LiCl-KCl-UCl <sub>3</sub> melt at 773 K for different concentrations of UCl <sub>3</sub> . Working electrode: W; area: 0.154 cm <sup>2</sup>	220
Fig. 7.1b	Plot of differentiated current vs. potential for NPV curves in Fig 7.1a.	220
Fig. 7.2	Dependence of reduction current on concentration of UCl <sub>3</sub> for NPV curves	221
Fig. 7.3	DPV curves for LiCl-KCl-UCl <sub>3</sub> melt at 773 K for different concentrations of UCl <sub>3</sub> . Working electrode: W; Area: 0.154 cm <sup>2</sup> ; Pulse amplitude: 0.01 V	222
Fig. 7.4	Dependence of reduction current on concentration of UCl <sub>3</sub> for DPV curves	222
Fig. 7.5	SWV curves for LiCl-KCl-UCl <sub>3</sub> melt at 773 K for different concentrations of UCl <sub>3</sub> . Working electrode: W; Area: 0.154 cm <sup>2</sup> . Pulse amplitude: 0.01 V; Pulse frequency: 10 Hz	224
Fig. 7.6	Dependence of reduction current on concentration of UCl <sub>3</sub> for SWV curves	224
Fig. 7.7a	NPV curve for LiCl-KCl-1 wt % UCl <sub>3</sub> -0.7 wt % EuCl <sub>3</sub> -1 wt % CeCl <sub>3</sub> -1 wt % LaCl <sub>3</sub> at 773 K on tungsten electrode. Pulse amplitude: 10 mV	226

Fig. 7.7b	Differentiated current for the NPV curve in Fig. 7.7a	226
Fig. 7.8	DPV curves for LiCl-KCl-1 wt % UCl <sub>3</sub> -0.7 wt % EuCl <sub>3</sub> -1 wt % CeCl <sub>3</sub> -1 wt % LaCl <sub>3</sub> at 773 K on tungsten electrode for different modulation amplitudes	227
Fig. 7.9	SWV curve for LiCl-KCl-1 wt % UCl <sub>3</sub> -0.7 wt % EuCl <sub>3</sub> -1 wt % CeCl <sub>3</sub> -1 wt % LaCl <sub>3</sub> at 773 K on tungsten electrode. Pulse amplitude: 10 mV; Pulse frequency: 10 Hz	227
Fig. 8.1	Comparison of apparent standard reduction potentials of actinides and lanthanides from this study and literature	235

## LIST OF TABLES

Table No.	Table Caption	Page No.
Table 1.1	Gibbs energies of formation of chlorides	13
Table 3.1	Cathodic peak analysis of La(III)/La couple at various scan rates and temperatures. Concentration of $\text{LaCl}_3$ : $7.54 \text{ moles cm}^{-3}$	68
Table 3.2	Kinetic parameters of La(III)/La(0) exchange at 798 K	79
Table 3.3	Diffusion coefficient and heterogeneous rate constant at different temperatures. Electrolyte: LiCl-KCl-NdCl <sub>3</sub> , Concentration of NdCl <sub>3</sub> : $6.66 \times 10^{-5} \text{ molcm}^{-3}$	82
Table 3.4	Diffusion coefficient of La(III) ion in LiCl-KCl melt at different temperatures. Concentration of $\text{LaCl}_3$ : $7.54 \times 10^{-5} \text{ mol cm}^{-3}$ . $D$ ( $\text{cm}^2 \text{ s}^{-1} \times 10^5$ )	92
Table 3.5	Apparent standard potentials for La(III)/La(0) and Gibbs free energy of formation of $\text{LaCl}_3$ , Concentration of $\text{LaCl}_3$ : $7.54 \times 10^{-5} \text{ molcm}^{-3}$	96
Table 3.6	Apparent standard potentials ( $\pm 0.003 \text{ V}$ ) and Gibbs free energy formation of $\text{NdCl}_3$ estimated from cyclic voltammograms for LiCl-KCl-NdCl <sub>3</sub> melt at W electrode	101
Table 3.7	Equilibrium potentials ( $\pm 0.002 \text{ V}$ ) on inert W electrode from OCP measurement	104
Table 3.8	Apparent standard potentials obtained from cyclic voltammetry and OCP method	104
Table 3.9	Cathodic peak potential, equilibrium potential and apparent standard potentials of U(III)/ U(0) redox couple from different methods in LiCl-KCl melt at W electrode	107
Table 4.1	Apparent standard potentials ( $\pm 0.002 \text{ V}$ ) for La(III)/La(Cd) estimated from cyclic voltammogram on Cd pool electrode, $X_{\text{LaCl}_3}$	129

= 0.00224

Table 4.2	Apparent standard potentials ( $\pm 0.002$ V) for Nd(III)/Nd(Cd) estimated from cyclic voltammogram on Cd pool, $X_{NdCl_3} = 0.00224$	129
Table 4.3	Gibbs energy of formation of LaCd <sub>11</sub> estimated from OCP measurement on Cd film electrode	133
Table 4.4	Gibbs energy of formation of NdCd <sub>11</sub> estimated from OCP measurement on Cd film electrode	133
Table 4.5	Thermodynamic properties of La in Cd estimated from OCP measurement on Cd film electrode	134
Table 4.6	Thermodynamic properties of Nd in Cd estimated from OCP measurement on Cd film electrode	134
Table 4.7	Apparent standard potentials for U(III)/U(Cd) estimated from cyclic voltammogram on Cd pool, $X_{UCl_3} = 0.00267, Ag/AgCl (X_{AgCl} = 0.0031)$	140
Table 4.8	Equilibrium potentials, $E_{U(III)/U(0)}$ and $E_{U(III)/U(Cd)}$ from open circuit potentials measurement	144
Table 4.9	The emf of unsaturated and saturated U-Cd alloy vs. uranium metal	147
Table 4.10	Thermodynamic properties of U-Cd system – measurements made by galvanic cell emf method	149
Table 5.1	Apparent standard potential ( $\pm 0.002$ V) for La(III)/La(Al) estimated from cyclic voltammogram on Al electrode, $X_{LaCl_3} = 0.00224$	168
Table 5.2	Apparent standard potential ( $\pm 0.002$ V) for Nd(III)/La(Al) estimated from cyclic voltammogram on Al electrode, $X_{NdCl_3} = 0.00224$	169

3

Table 5.3	Gibbs energy of formation of $\text{La}_3\text{Al}_{11}$ estimated from OCP measurement on Al electrode	174
Table 5.4	Gibbs energy of formation of $\text{Nd}_3\text{Al}_{11}$ estimated from OCP measurement on Al electrode	174
Table 5.5	Thermodynamic properties of La-Al intermetallic compound estimated from OCP measurement on Al electrode	174
Table 5.6	Thermodynamic properties of Nd-Al intermetallic compound estimated from OCP measurement on Al electrode	175
Table 5.7	Gibbs energy of formation of $\text{UAl}_n$ estimated from OCP measurement on Al electrode	184
Table 5.8	Gibbs energy formation of $\text{UAl}_n$ from emf measurement	185
Table 5.9	Thermodynamic properties of U-Al intermetallic compound estimated from OCP measurement on Al electrode	185
Table 5.10	Apparent standard potential ( $\pm 0.005$ V) for U(III)/U(Al) estimated from OCP measurement on Al electrode, $X_{\text{UCl}_3} = 0.00268$	185
Table 6.1	Apparent standard potential ( $\pm 0.001$ V) for La(III)/La(Ga) estimated from cyclic voltammogram using LiCl-KCl-LaCl <sub>3</sub> -GaCl <sub>3</sub> melt, $\Lambda_{\text{LaCl}_3}^\Lambda = 0.00224$	202
Table 6.2	Apparent standard potential ( $\pm 0.001$ V) for Nd(III)/Nd(Ga) estimated from cyclic voltammogram using LiCl-KCl-NdCl <sub>3</sub> -GaCl <sub>3</sub> melt, $\Lambda_{\text{NdCl}_3}^\Lambda = 0.00224$	202
Table 6.3	Apparent standard potential ( $\pm 0.001$ V) for U(III)/U(Ga) estimated from cyclic voltammogram using LiCl-KCl-UCl <sub>3</sub> -GaCl <sub>3</sub> melt, $\Lambda_{\text{UCl}_3}^\Lambda = 0.00268$	202
Table 6.4	Gibbs energy of formation of $\text{LaGa}_6$ estimated from OCP measurement	206

Table 6.5	Gibbs energy of formation of NdGa <sub>6</sub> estimated from OCP measurement	206
Table 6.6	Thermodynamic properties of La-Ga system estimated from OCP measurement	206
Table 6.7	Thermodynamic properties of Nd-Ga system estimated from OCP measurement	207
Table 6.8	Equilibrium potentials ( $\pm 0.002$ V) of U(III) ion on Ga surface from OCP measurement	209
Table 6.9	Gibbs energy of formation of UGa <sub>3</sub> from OCP measurement compared with literature values	209
Table 6.10	Thermodynamic properties of U-Ga system estimated from OCP measurement	210
Table 8.1	The difference ( $\Delta E_{An-Ln}$ ) in the reduction potentials of actinides with that of Nd	235

# CHAPTER 1

## INTRODUCTION

### 1.1 Nuclear energy and nuclear fuel

There is growing demand for electric energy worldwide. At present, fossil fuels play a dominant role in energy production. There are two major issues associated with the use of fossil fuels. One is the emission of green-house gases which are detrimental to the environment and the other is the depletion of the fossil fuels. Analysis of global energy resources indicate that oil and natural gas will last for 21<sup>st</sup> century only. Regarding coal, it is estimated that it may not be sufficient even for the next century taking into account of the pattern of usage and the growth rate [1]. Renewable resources like hydro, solar, wind, biomass etc. and nuclear resource are virtually inexhaustible. But for the hydro and nuclear resources, the other resources (namely, solar, wind, biomass etc.) are not suitable for large scale electricity production. Hence, for long term sustainability, it is necessary to go in for nuclear electricity. According to the Indian nuclear program, it has been envisaged to increase the share of nuclear energy to 25% of the total power by 2052 in our country [2, 3].

Nuclear fission is the source of nuclear energy. The fission energy is harnessed in a nuclear reactor. A fissile material forms the essential content of the fuel of a reactor. A 'fissile' material is one that undergoes fission with neutron of any energy, for example,  $^{233}\text{U}$ ,  $^{235}\text{U}$ ,  $^{239}\text{Pu}$ , and  $^{241}\text{Pu}$ .  $^{235}\text{U}$  is the only naturally available fissile nuclide and the rest are produced in the reactor from fertile atoms. A 'fertile' material is one which leads to the production of a fissile nuclide, on absorption of a neutron, for example,  $^{232}\text{Th}$  and  $^{238}\text{U}$ . They produce  $^{233}\text{U}$  and  $^{239}\text{Pu}$ ,  $^{241}\text{Pu}$  respectively. Typical nuclear fuel are uranium oxide,  $\text{UO}_2$ ; uranium plutonium mixed oxide,  $(\text{U}, \text{Pu})\text{O}_2$ ; uranium plutonium mixed carbide,  $(\text{U}, \text{Pu})\text{C}$ ; uranium plutonium mixed nitride,  $(\text{U}, \text{Pu})\text{N}$  and metallic fuel. U, U-5

% Fissium alloy, U-Al alloy, U-20 % Pu-10 % Zr alloys are some of the candidate metallic fuels. Majority of the commercial reactors operating worldwide use the uranium oxide or the uranium-plutonium mixed oxide (MOX) as fuel.

## 1.2 Types of reactors

Based on the energy of the neutron causing fission, nuclear reactors are classified into two types, namely, thermal and fast reactors. In thermal reactors, the energy of the neutrons that cause fission is close to 0.025 eV. Since the neutrons produced during fission reactions have energies about 2 MeV, their energies are reduced, in thermal reactors, by using lighter elements, known as moderators like light water and heavy water which contain lighter elements like hydrogen and deuterium. PHWR (Pressurised Heavy Water Reactor) is a thermal reactor with natural uranium oxide as fuel and heavy water as moderator. The natural uranium contains 0.7 at %  $^{235}\text{U}$  which is responsible for major fission in a thermal reactor. In order to sustain a chain reaction in the reactor the fuel should contain at least the minimum amount of fissile atoms. The majority of uranium is present as  $^{238}\text{U}$  and its main role is to capture a neutron to form  $^{239}\text{Pu}$  which is later used to fuel fast reactor. The maximum burn-up achievable in a thermal reactor is 1 at. % or 10,000 MWd/t. Burn-up is the term used for the amount of fissile material consumed which is in turn related to the amount of power produced.

Thermal reactors such as Pressurized Water Reactor (PWR) and Boiling Water Reactor (BWR) use normal water as moderator. Due to the higher neutron absorption cross-section of hydrogen atom, both these reactors require the fuel to be enriched with  $^{235}\text{U}$  for maintaining the chain reaction. Enrichment process involves enhancing the proportion of  $^{235}\text{U}$  above the 0.7% in natural Uranium.

In a fast reactor, the fission is caused by fast neutrons. Most of the neutrons are in the range around 100 keV. There is no moderator in a fast reactor. The proportion of fissile atoms in the fast reactor is substantially large relative to thermal reactors.

### ***1.2.1 Fast breeder reactors***

With limited uranium resources, it is not possible for our country to meet the growing energy requirement by operating thermal reactors alone. In order to meet the energy demand, Fast Breeder Reactors (FBR) are needed. These reactors generate more fissile material than that are consumed (Breeding). In the fast neutron induced fission, the number of neutrons produced per fission is more than that produced in thermal neutron induced fission. Hence more neutrons are present to cause fission other than that required to maintain the chain reaction. In addition,  $^{238}\text{U}$  also undergoes fission in the fast neutron spectrum, unlike in a thermal reactor. Therefore additional neutrons and energy are produced from the fertile material. Further in the fast neutron spectrum, the absorption cross-section of  $^{238}\text{U}$  is comparable to that of the  $^{239}\text{Pu}$  fission cross-section. Also, the capture cross sections decrease with increase in neutron energy. This gives rise to better neutron economy. All these factors contribute to the high breeding ratio achieved in fast reactors. Hence it becomes possible to extract large amount of power from fast breeder reactors.

### ***1.2.2 Metal fuelled fast breeder reactors***

The early fast breeder reactors to have metallic fuels were EBR-I and EBR-II [4, 5]. Uranium based metal fuel was used for these reactors. The advantages of metal fuel are that it has very high fissile atom density and so it will yield a very high breeding ratio. Also the thermal conductivity is high and hence the linear power rating is high. Some limitation which did not allow high burn-up in the earlier reactors were the swelling due to high smear density (there was not enough gap between fuel and clad to take care of

swelling caused due to accumulation of fission products) and anisotropic expansion of uranium at high temperatures. These shortcomings were addressed by increasing the gap between the fuel and clad and the gap was filled with sodium for better heat transfer. The symmetric cubic structure of the gamma phase of uranium metal was stabilized by alloying with a suitable metal like Zr (10 wt. %) to take care of the anisotropic expansion. This also helped in increasing the solidus temperature of the fuel. These features of metallic fuel helped to achieve high burn-up. Based on these features, the Argonne National Laboratory (ANL), USA developed a new concept called Integral Fast Reactor (IFR) in 1980's [4, 6-7]. IFR is a pool type fast breeder reactor which used 70 wt % U-20 wt % Pu-10 wt % Zr alloy as the fuel and liquid metal sodium as the coolant. The plants for the fabrication of fuel and reprocessing of irradiated fuel and the waste disposal facilities are co-located at the reactor site itself and hence the name IFR. The IFR fuel cycle is shown in Fig. 1.1.

The IFR fuel was fabricated with a low smear density of 75 %. After 1-2 at. % burn up, as the fuel swells to close the fuel-clad gap, the fuel becomes porous due to its lower smear density and the interconnected porosity enables the release of fission gases from the fuel which reduces any further swelling. The fuel being soft, does not stress the clad and thus the fuel could go to burn ups as high as 20 at. %. The reactor is also more effective in burning higher actinides (Neptunium, Americium and Curium) and hence the amount of radio activity released to the environment is significantly low.

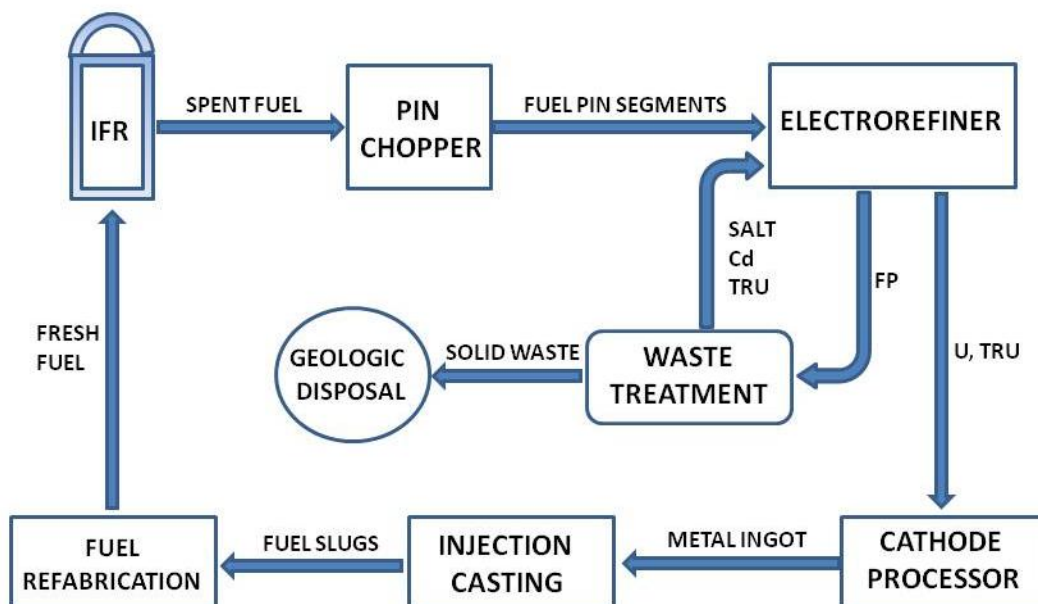


Fig. 1.1 The IFR fuel cycle [14].

U-Pu-Zr alloy is foreseen as the fuel for future fast reactors, because of the characteristics such as, excellent breeding performance, high burn-up potential, ease of fabrication, high thermal conductivity, simple reprocessing, inherent safety benefits etc. U-Pu-Zr fuel coupled with pyrochemical processing of the spent fuel is a promising fuel cycle in the future.

In India, uranium metal was used as fuel for the research reactors, Cirus and Dhruva. Alloys of U-Al were used as fuel in APSARA and is being used in KAMINI research reactor. The first fast reactor in India is the Fast Breeder Test Reactor (FBTR) at Kalpakkam commissioned in 1985. It is sodium cooled, 40 MWt/ 13.2 MWe fast reactor with uranium-plutonium mixed carbide as the fuel. The FBTR has achieved a maximum of 16.5 at % burn-up [8]. A 500 MW(e) fast reactor with uranium –plutonium mixed oxide, Prototype Fast Breeder Reactor (PFBR) is at advanced stage of construction [9]. Due to the high breeding potential of metallic alloy fuel, it has been proposed to convert the core of the FBTR fuel to U-19 wt % Pu- 6 wt % Zr in the coming years. Towards this,

6 test pins of sodium bonded U- 6 wt % Zr has been introduced in the reactor to study the irradiation behavior and gain experience in the reprocessing of the spent metal fuel by pyrochemical processing.

### **1.3. Reprocessing of nuclear fuel**

During the irradiation of the nuclear fuel in the reactor, lot of fission products along with trans-uranic elements like Pu, Np, Am etc. are generated. Some of the fission products like  $^{135}\text{Xe}$  and  $^{145}\text{Sm}$  are good neutron absorbers and are considered as neutron poisons and if the fuel is kept in the reactor for long time, they may result in the reduction of the reactivity. Moreover, prolonged irradiation of the fuel in the reactor causes significant damage to the cladding material due to exposure to intense radiation. After certain irradiation time in the reactor the fuel pins have to be removed from the reactor. The spent fuel contains significant amount of fissile material that has not undergone fission. The process of separating the fuel materials, U and Pu from the fission products so as to recycle them into the reactors for power production is known as the reprocessing. Reprocessing will ensure that the natural uranium resources are available for a longer time. Also closing the fuel cycle (recycling the fuel without storing the spent fuel in geological repositories) will mitigate the problems resulting from the storage of fission products and trans-uranic elements with long half-life (Fig.1.2). The methods used for reprocessing are categorized into two groups, namely, aqueous and non-aqueous reprocessing methods.

#### ***1.3.1 Aqueous reprocessing technology***

Current reprocessing technology is largely based upon solvent extraction although other methods of reprocessing are being developed [10, 11]. There is considerably broad experience available for reprocessing U/Pu oxide fuel since many decades by the PUREX (Plutonium and Uranium Recovery by Extraction) process originally developed by ORNL

in the USA in late 1940s. This aqueous solvent extraction process can be applied to  $\text{UO}_2$ , MOX and metallic fuel. Uranium and plutonium in the spent fuel are separated from the minor actinides and fission products using this method.

In the PUREX process, the de-cladded and chopped spent fuel is dissolved in concentrated nitric acid. The aqueous stream is contacted with the organic stream containing tri-butyl phosphate (TBP) in dodecane. The  $\text{UO}_2^{2+}$  and  $\text{Pu}^{4+}$  present in the aqueous phase are extracted into the organic phase. The plutonium is separated from uranium by selectively reducing the  $\text{Pu}^{4+}$  to  $\text{Pu}^{3+}$  and extract this Pu into a fresh aqueous stream [12]. The plutonium and uranium are then converted to their oxides and are either stored or returned to the fuel cycle. High pure uranium and plutonium oxides are obtained by this process. The aqueous stream contains a large fraction of the radioactive fission

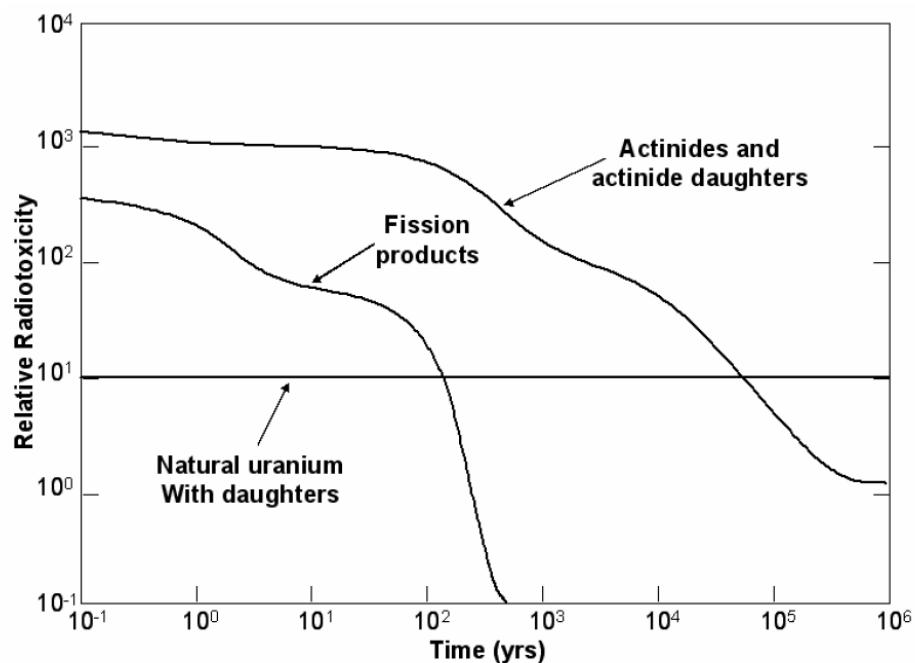


Fig. 1.2 Relative radiotoxicity of fission product and transuranium isotopes in spent nuclear fuel relative to the radiotoxicity of natural uranium [4].

products and long-lived radioactive elements. These are later fixed in suitable solid matrices such as glass and disposed in deep geological repositories. The purex process has the disadvantage of producing large volumes of liquid waste.

### ***1.3.2 Non-aqueous reprocessing technology***

The non- aqueous reprocessing technologies have been used for treatment of spent nuclear fuel since the 1960's [13, 14]. They are still being developed to establish them as economically viable processes. The non-aqueous processes were initially developed by the United States and Russia. They are widely being studied by other countries such as Japan, Germany, France, Korea, United Kingdom, Czech Republic, China and India. Non-aqueous processes typically employ salts or metals in either molten state or gaseous state. The difference in thermodynamic stabilities or vapour pressures at elevated temperatures is the basis of the separation.

The non-aqueous processes offer many advantages compared to the traditional aqueous processes such as compactness of reprocessing plant, resistance to radiation effects, less criticality problem, suitable for reprocessing advanced fuels and easier waste management. The solvents used in non-aqueous process are molten salts and liquid metals. They are not subject to radiation damage. So, relatively short-cooled fuels can be processed. Also the non-aqueous processes can handle large quantities of fissile material since moderator such as water is not present. Hence the criticality concerns are reduced significantly. The reprocessing plant could be more compact and so the reprocessing facility can be set-up in the reactor complex itself. The fuel reprocessed by non-aqueous method is less pure due to incomplete separation of the fission products and trans-uranic elements from the fuel material. This implies that the recovered fuel has to be handled in shielded hot cells for fuel refabrication. But from the perspective of non-proliferation, this feature is considered a benefit. The fast reactor fuels have higher radiation fields due to

high burn-up and significantly higher fissile material concentrations than the light water reactor fuels. The features of the non-aqueous processing technology make them ideal for recycling fast reactor fuel.

### ***1.3.3 Development of non-aqueous processes***

At present most of the non-aqueous separation methods are based on electrochemical technology. Some of the technologies employed successfully in the past are discussed here.

#### ***1.3.3.1 Fluoride volatility process***

Fluoride volatility was one of the important non-aqueous methods used earlier [15, 16]. The basis was that the fluorides can form volatile compounds with the actinides. By converting the spent fuel to fluorides (especially  $\text{UF}_6$ ), the actinides were separated as gases from the bulk of the fission products.

In this method, the spent fuel was dissolved in a non aqueous solvent (like  $\text{N}_2\text{O}_4$ -HF,  $\text{N}_2\text{O}_3$ -HF or NOF-3.1HF) and then fluorinated by using fluorinating agents (such as  $\text{BrF}_3$ ,  $\text{F}_2$ ). U/Pu metal or oxide reacted with NOF to give nitrosyllium hexafluoro uranate/plutonate. Cladding material and fission products also dissolved in a similar manner. The fission products like Kr, Xe and tritium were released to the off-gas during dissolution. The temperature during dissolution was maintained between 90-150°C. The nitrosyllium fluorides were then reacted with liquid bromine trifluoride at 150°C which separates U as volatile  $\text{UF}_6$  (B.P = 56.5°C). Plutonium in the residue was then reacted with  $\text{F}_2$  at 400°C converting it to volatile plutonium hexafluoride (B.P = 62 °C). Purification of  $\text{UF}_6$  stream was achieved by sorption on NaF at 150°C and desorption at 350°C. The plutonium stream was purified by thermal decomposition of  $\text{PuF}_6$  to non-volatile  $\text{PuF}_4$ . Of all non-aqueous processes, fluoride volatility offered high degree of separation and it was the most suited for uranium based fuel.

### ***1.3.3.2 Melt refining***

Another important non-aqueous process for recycling metallic fuel was melt refining [4, 5]. Melt refining was used to recycle fuel from Experimental Breeder Reactor-II (EBR-II). EBR-II was a sodium cooled fast reactor fuelled with uranium- 5 % fission (Nb- 0.01 %, Zr-0.1 %, Pd-0.2 %, Rh-0.3 %, Ru-1.9 %, Mo-2.4 %) alloy. The chopped spent fuel was placed in a ZrO<sub>2</sub> crucible and heated to 1400°C. Volatile and gaseous fission products evolve out, along with sodium that bonded the fuel in the cladding. The reactive gases and vapours were trapped by covering the crucible with a mat of silica-alumina fibers. The chemically reactive fission products (alkali, alkaline earth and rare earths) reacted with the crucible to form oxides. The uranium and noble metals remained in the metallic state and the molten alloy was poured into a graphite mould. The recovered uranium-fission alloy was fabricated using the injection casting technology. The metal fuel was recycled into the EBR-II reactor within 4-6 weeks.

The limitation of the melt refining process was the separation of noble metals and process losses. Eventually this led to the development of a non-aqueous process based on electrochemical separation.

### ***1.3.3.3 IFR process***

Electrochemical process employing molten salts and liquid metals were pursued at the Argonne National Laboratory (ANL) [17-18]. Development of the pyrochemical process was as part of the Integral Fast Reactor Program (IFR) discussed earlier in *section 1.2.2*. Initially the pyrochemical process based on molten salt electrorefining was applied to treat the fuel that was used in EBR-II reactor to validate the technology. The molten salt electrorefining method is discussed in detail in *section 1.4.1*.

### ***1.3.3.4 RIAR process***

Other than United States, a non- aqueous electrochemical process was developed at Russian Institute of Atomic Research (RIAR), Russia for recycling of oxide fuel from fast reactors. The molten salt electrolysis and  $\text{PuO}_2$  volume precipitation in chloride melts were the basis of the RIAR process [19-20]. This process is capable of producing poly-dispersed granules of  $\text{UO}_2$ ,  $\text{PuO}_2$  and MOX with almost their theoretical density and the fuel is re-fabricated by vibro-compaction.

The electrolyte for the process is  $\text{NaCl-2CsCl}$  melt. From electrochemical point, U and Pu oxides behave like metals since  $\text{UO}_2$  and  $\text{PuO}_2$  have electric conduction at high temperature ( $>400^\circ\text{C}$ ). The MOX fuel is introduced in the melt by oxidative dissolution using  $\text{Cl}_2$  gas. The melt is treated with a carefully controlled mixture of  $\text{O}_2$  and  $\text{Cl}_2$  to ensure the dissolution of uranium as uranyl ions, while majority of other elements forms oxygen-free ( $\text{MCl}_n$ ) ions in the melt. Uranium is initially recovered on a graphite cathode as uranium dioxide along with noble metals by partition electrolysis. By changing the oxidation-reduction potential of the system, plutonium is selectively precipitated as  $\text{PuO}_2$ . An additional electrolysis is carried out to recover uranium and plutonium as oxides thereby leaving the fission products in the melt. After removal of salts, the product is crushed and re-fabricated as fuel by vibrocompaction.

## **1.4 Molten salt electrorefining process for metallic fuel**

### ***1.4.1 Overview***

The main step in the pyrochemical reprocessing for the metallic fuel is molten salt electrorefining. Fig. 1.3 shows the schematic of the electrorefining process. The chopped spent metallic fuel is loaded in a steel basket and anodically dissolved (or chemically dissolved using  $\text{CdCl}_2$  as oxidant) in molten  $\text{LiCl-KCl}$  eutectic mixture as their chlorides at 773 K [24, 25]. The Gibbs energy of formation of the metal chlorides is the primary determinant of the process. The alkali and alkaline fission products are completely

oxidized and they remain in the salt throughout the process. The noble metals are not oxidized and they remain as metal in the anode. The chlorides of rare earths and actinides have intermediate stability (Table 1.1). However the rare earth chlorides are more stable than the actinide chlorides. The process is controlled by adjusting the redox state of the electrorefining cell. Two kinds of cathodes are used in the process. A solid iron cathode is used to recover pure uranium metal and a liquid cadmium cathode is used to recover plutonium along with uranium and minor actinides.

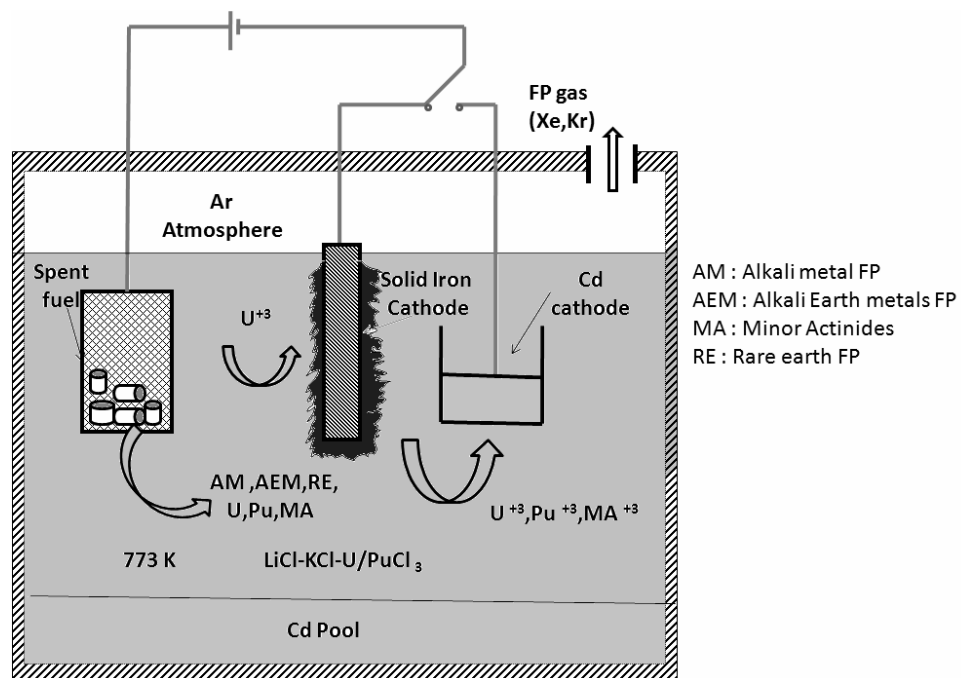


Fig. 1.3 Schematic of the electrorefiner in IFR process [29].

Table 1.1 Gibbs energies of formation of chlorides [18]

(- $\Delta G_f^0$  in kcal/g-mole equiv Cl at 773 K)

Elements that remain in salt (very stable chlorides)		Elements that can be electro-transported		Relatively less stable chlorides (metal phase)	
BaCl <sub>2</sub>	87.9	CmCl <sub>3</sub>	64.0	CdCl <sub>2</sub>	32.2
CsCl	87.8	PuCl <sub>3</sub>	62.4	FeCl <sub>2</sub>	29.2
RbCl	87.0	AmCl <sub>3</sub>	62.1	NbCl <sub>5</sub>	26.7
KCl	86.7	NpCl <sub>3</sub>	58.1	MoCl <sub>4</sub>	16.8
SrCl <sub>2</sub>	84.7	UCl <sub>3</sub>	55.2	TcCl <sub>4</sub>	11.0
LiCl	82.5	ZrCl <sub>4</sub>	46.6	RhCl <sub>3</sub>	10.0
NaCl	81.2			PdCl <sub>2</sub>	9.0
CaCl <sub>2</sub>	80.7			RuCl <sub>4</sub>	6.0
LaCl <sub>3</sub>	70.2				
PrCl <sub>3</sub>	69.0				
CeCl <sub>3</sub>	68.6				
NdCl <sub>3</sub>	67.9				
YCl <sub>2</sub>	65.1				

In the first stage, uranium is oxidized at the anode (as its chloride) and an equivalent amount of uranium chloride is reduced at the cathode. The potential is controlled to give a pure uranium product. Plutonium and rare earth metals remain almost entirely in the salt or at the anode because of their relatively negative Gibbs energy of formation of their chlorides. At the cadmium cathode, the activity of Pu is greatly lowered due to the formation of intermetallic compound with Cd. Reduction of a metal's activity is equivalent to the reduction in the stability of its chloride whereas, the activity of U is not reduced since it does not form intermetallic compound with cadmium at the operating temperature [26-29]. So at the liquid cathode, deposition of Pu is favoured. Similarly, the minor actinides are stabilized due to their very low activity coefficients in cadmium. A

small amount of lanthanides also come into the liquid cadmium cathode, since their activity is also reduced in liquid cadmium. Zirconium which is one of the constituents of the alloy fuel, has the electrode potential close to that of uranium. Hence its behavior is sensitive to the potential applied during the anodic dissolution. The recovery of uranium and plutonium from the respective cathode product is realized through a consolidation step where the salt and cadmium are distilled off. The uranium and plutonium of desired composition are melted using induction heating and cast into fuel pins by injection casting. After some batches are processed, the molten salt is purified from the actinides by reducing the actinides by the reductive extraction process where the actinides are collected in a molten metal phase [30]. The salt is recycled by passing through a zeolite column to trap the lanthanides [31].

#### ***1.4.2 Challenges of pyrochemical process***

The primary drawback of the pyrochemical process is the expensive materials (salts and material of construction) used in the technology. The development of sophisticated technology for remote handling of aggressive media at high temperatures and in inert atmosphere is a challenging task [32]. Presence of oxygen and moisture in the system adversely affects the electrochemistry and the final product obtained. Low separation of actinides from the lanthanides is of concern now and studies are widely being carried out in recent times to look for an alternate to the liquid cadmium cathode.

However, the retention of radioactive fission products and trans-uranium elements in the waste is significantly lower than in the aqueous method. This coupled with the feature such as compact plant with minimum process steps and the final product being resistant to proliferation outweigh the disadvantages of the method. Owing to its advantages, research and development of the metal fuel cycle integrated with electrorefining has been accelerated in the recent years in India.

### ***1.4.3 Research for an alternate to liquid cadmium cathode***

As mentioned earlier, the electrorefining process developed at ANL utilizes two types of cathodes. The product obtained at the solid cathode is essentially pure uranium which will be used for fabrication of the blanket fuel and that obtained at the liquid cadmium cathode which is a mixture of plutonium and uranium would be used for making fresh core fuel after blending with uranium and zirconium of required composition. The minor actinides and some lanthanide also accompany the later product. Minor actinides in the fuel are tolerated as they can be burnt in the fast reactor. But, the lanthanides act as neutron poison and their proportion should be kept as minimum as possible. Under such circumstances, cadmium cannot be considered as the optimum solvent from the perspective of decontamination from the lanthanides. Studies from the liquid-liquid metal reduction extraction in fluoride melts showed that aluminium has the highest potential for group selective separation of actinides and lanthanides [33].

Based on these results, an electrorefining process in molten LiCl-KCl eutectic mixture is being developed in Institute of Transuranium Elements (ITU) to separate the actinides from spent nuclear fuel [34, 35]. In this process, the fuel is electrochemically dissolved into the molten salt and actinides are group-selectively electrodeposited on solid aluminium cathode forming actinide-aluminium (AN-Al) alloys. Selective recovery of actinides over lanthanides was achieved in their studies. Also very high capacity of aluminium to load actinides has been experimentally proved.

### **1.5 Objective of this study**

With the given background for the electrorefining process, it is evident that a favorable thermodynamic property of the actinide chlorides over the fission product chlorides is the basis of the separation. Hence the knowledge of the electrochemical behavior and the thermochemical properties of these chlorides are essential to achieve

efficient separation. The basic electrochemical behavior of major elements involved in the electrorefining process, their standard electrode potentials and thermodynamic properties such as Gibbs energy of formation of the chlorides, their activity coefficient etc. are well studied and reported in the literature [36-40]. A detailed literature survey on the studies is given in chapter 3. However the kinetics of the reduction process is not much reported.

Several studies are reported on electrorefining using cadmium cathode [41-43] and recovery of the actinides by distilling off cadmium [44]. The distribution behavior of actinides and lanthanides between the LiCl-KCl eutectic melt and liquid Cd were reported by equilibrium measurement to evaluate the thermodynamic properties for these elements with cadmium [45-48]. The activities of these elements in liquid cadmium phase and separation factors of actinide elements from rare earth elements were evaluated from the studies. However, the reduction behavior of actinide and rare earth elements at the interface between the LiCl-KCl eutectic melt and liquid Cd are not much studied.

As mentioned earlier, solid aluminium cathode is envisaged for selective recovery of actinides over lanthanides at ITU. Cassayre *et al.* investigated the feasibility of electrorefining of metal alloy fuel (U-Zr and U-Pu-Zr) on solid aluminium cathode [49]. Serp *et al.* had studied the An/Ln separation efficiency in their studies on simulated spent alloy fuel of aluminium cathode [34, 50]. Soucek *et al.* had investigated on the selective reduction of uranium, plutonium and minor actinides on aluminium cathode from simulated An-Ln-Zr alloy fuel and their recovery from An-Al alloy by chlorination route [51-53]. The electrochemical reduction behaviour of actinides and lanthanides on Al electrode and the formation of An-Al and La-Al alloys are reported by their studies. A detailed literature survey is given in chapter 5. Though the behavior of  $\text{LaCl}_3$  and  $\text{UCl}_3$  on Al electrode is reported, studies have not been carried out over a range of temperature. Also, the electrode behavior of  $\text{NdCl}_3$  on Al has not been reported in open literature.

From the perspective of selective separation of actinides from lanthanides, gallium metal also appears to be a suitable solvent. We have not come across any study using gallium cathode in LiCl-KCl melt. However some studies have been reported in the literature on the behavior of Pu and Ce on gallium cathode in NaCl-KCl melt. The details are discussed in the literature survey in chapter 6.

From the above discussion, we believe that a systematic study on different cathodes using identical conditions will give fruitful results for evaluating the electrodes. In this thesis we had chosen to study the behavior of an actinide (U) and two fission products (La, Nd) on W, Cd, Al and Ga electrodes in LiCl-KCl eutectic melt. The studies were carried out using transient electrochemical techniques such as cyclic voltammetry, chronopotentiometry, squarewave voltammetry and open circuit potentiometry. In chapter 3 we have reported the reduction mechanism of the La-, Nd- and U-trivalent ions on inert W electrode in molten LiCl-KCl eutectic mixture with an emphasis on the electrode kinetics for the reduction process. A detailed peak analysis (cyclic voltammograms) for the reduction of Nd(III) ion on W electrode is presented in the manuscript and mechanism is supported by complimentary techniques (chronopotentiometry, squarewave voltammetry) which is done for first time. The kinetics for the reduction of La-, Nd- & U-trivalent ions (by convolution method) is reported for the first time in this study. Apart from examining the reduction mechanism and the electrode kinetics, the aim was to obtain the standard reduction potentials under identical experimental conditions (such as reference electrode, electrode material, experimental technique etc.). The equilibrium potentials for La(III)/La(0), Nd(III)/Nd(0) and U(III)/U(0) redox couples were obtained from open circuit potential (OCP) method and are reported for the first time. These values were used for converting the equilibrium potentials of the intermetallic compound

obtained from the OCP measurement (made with Cd, Al & Ga electrodes) to their respective emf in the studies reported in chapters 4-6.

In chapters 4, 5 and 6 we have discussed the results of the studies on the electrochemical behavior of La-, Nd- and U-trivalent ions on liquid cadmium pool cathode, solid aluminium cathode and on gallium cathode respectively using cyclic voltammetry and open circuit potentiometry in the temperature range 698-773 K. The objective of the work was to study the redox behavior of actinides and lanthanides on different substrates in order to evaluate them for better actinide-lanthanide separation.

Electroanalytical pulse techniques are considered as rapid and reliable methods for in-situ monitoring of the composition of analyte in multi-component systems [54-55]. To our knowledge, we had come across only two reports in the literature on the application of electroanalytical pulse techniques for in-situ monitoring of actinides in molten salt. Iizuka *et al.* [56] had carried out an exhaustive study on the applicability of normal pulse voltammetry and square wave voltammetry as the on-line monitoring method for the actinide concentration in molten chloride electrolyte. The study shows that squarewave voltammetry suffers a disadvantage in the estimation of uranium over a wide concentration range (a linear dependence of the resultant current not found at higher concentrations). Earlier, in the Argonne National Laboratory, the square wave voltammetry was examined as a process monitoring method for pyrometallurgical treatment [57]. In this thesis we had investigated the suitability of three voltammetric techniques namely, normal pulse voltammetry (NPV), differential pulse voltammetry (DPV) and square wave voltammetry (SWV) for determining the concentration of uranium in various concentration ranges and in the presence of rare earth chlorides. The details are presented in chapter 7.

Though there is no relationship between the electrochemical studies and studies on the pulse techniques presented in the manuscript, our intention was to obtain a calibration graph for estimation of uranium in multicomponent system (in the presence of lanthanide FPs) which is not reported earlier.

An evaluation of the selectivity of the electrodes investigated in this study is presented in chapter 8 (Conclusions) for better actinide-lanthanide separation. A true evaluation could be done only by obtaining the standard potentials on all four electrodes under identical conditions.

### 1.6 References

1. R. B. Grover, "Role of Nuclear Power for Green Growth: A Perspective from India", *Energy Strategies Reviews* 1 (2013) 255.
2. A. Kakodkar, World Nuclear Association, Annual Symposium, London, 2002.
3. Baldev Raj, H. S. Kamath, R. Natrajan, P. R. Vasudeva Rao, *Prog. Nucl. Energy*, 47 (2005) 369.
4. Charles E. Till, Y. I. Chang, *Plentiful Energy "The Story of Integral Fast Reactor"*, ISBN: 978-1466384606, Library of congress control No. 2011918518.
5. Charles E. Stevenson, "The EBR-II Fuel Cycle Story", American Nucl. Soc., 1987.
6. Y.I. Chang, *Nucl. Technol.*, 88 (1989) 129.
7. T. Inoue, *Progress in Nuclear Energy*, 40 (3-4) (2002) 547.
8. Baldev Raj, *Int. J. Nucl. Energy Sci. Technol.* 12 (2005) 164.
9. H. S. Kamath, "Fabrication of Mixed Oxide Fuels for Indian Nuclear Power Programme", in: *Nuclear Fuel Cycle Technologies*, (Eds.) Baldev Raj and P. R. Vasudeva Rao, BRNS, DAE, 2006, p. 122.
10. W. D. Bond, *Light Water Reactor Nuclear Fuel Cycle*, Ed. R. G. Waymer and B. L. Vondra (Boca Raton, FL: CRC Press, 1981), p.103.

11. D.E Ferguson, "Chemical Reprocessing of Nuclear Fuel", 24<sup>th</sup> International Congress of Pure and Applied Chemists, Vol. 6 (London: Butterworths, (1974), p.337.
12. J. L. Swanson, Sci. and Tech. of Tributyl Phosphate, Vol.3, Ed. W.W. Schulz, L.L. Burger and J. D.Navaratil (Boca Raton, FL: CRC Press, 1989), pp.55-79.
13. Y. I. Chang, Nucl. Engg, Technol., 39 (2007) 161.
14. J.J. Laidler, Transactions of the American Nuclear Society (USA), 68 (1993) 16-17. Proc. American Nuclear Society (ANS) Annual Meeting, Sang Diego, California, USA, 1993.
15. M. J. Steindler, I. J. Anastasia, I. E. Treverrow and A.A. Chilenskas, Nucl. Mat., 15 (1969) 177.
16. Benedict, Pigford, and Levi. Nuclear Chemical Engineering (New York: McGraw-Hill Book Company, 1981).
17. R. K. Steunenber, R. D. Pierce and I. Johnson, Proc. Symp. On Reprocessing of Nuclear Fuels, Ames, Iowa, 1969, Ed. P. Chiotti, USAEC, 1969, p.325.
18. L. Burries, M. Steindler and W. Miller, Proc. Int. Topl. Mtg. Fuel Reprocessing and Waste Management 2, (1984) 2-257.
19. A. V. Bychkov, S. K. Vavilov, O. V. Skiba, P. T. Porodnov, A. V. Pravdin, G. P. Popkov, K. Suzuki, Y. Shoji, T. Kobayashi, Proceedings of the International Conference Future Nuclear Systems (GLOBAL 97), Yokohama, Japan, October 5-10, 1997, p. 912.
20. S. Vavilov, T. Kobayashi, M. Myyochin, J. Nucl. Sci. Tech. 41 (2004) 1018.
21. Y. Sakamura, M. Kurata, T. Inoue, J. Electrochem.Soc., 153, D31-D39 (2006).
22. M. Kurata, T. Inoue, J. Serp, M. Ougier, J. P. Glatz, J. Nucl. Mater. 328 (2004) 97.
23. T. Usami, M. Kurata, T. Inoue, H. E. Sims, S. A. Beetham, J. A. Jenkins, J. Nucl.

- Mater., 300 (2002) 15.
24. J.L. Willit, W.E. Miller, J.E. Battles, J. Nucl. Mater. 195 (1992) 229.
  25. S.X. Li, ANL/TD/CP-96338, Argonne National Laboratory, 1998, available at <http://www.osti.gov/bridge/>.
  26. T. Inoue, M. Ougier, R. Malmbeck, J.P. Glatz, L. Koch, J. Nucl. Sci. Tech. (Suppl. 3) (2002) 765–768.
  27. J. E. Battles, W. E. Miller, E. C. Gay, ANL/CP-70796.
  28. J. P. Ackerman, Ind. Eng. Chem.. Res. 30 (1) 1991 141.
  29. T. Koyama, M. Iizuka, H. Tanaka, M. Tokiwai, Y. Shoji, R. Fujita and T. Kobayashi, J. Nucl. Sci. Technol., 34 (1997) 384.
  30. T. Koyama, T.R. Johnson and D.F. Fischer, J. Alloys Comp., Vol. 189, 37 (1992).
  31. Y. J. Cho, H. C. Yang, H. C. Eun, H. Kim, J. H. Kim, J. Ind. Eng. Chem. 11 (2005) 707.
  32. J.P. Ackerman, T.T. Johnson, L.S.H. Chow, E.L. Carls, W.H. Hannum, and J.J. Laidler, Treatment of wastes in the IFR Fuel Cycle, *Prog. Nucl. Energ*, **31**(1997) 141.
  33. O. Conocar, N. Douyere, J.P. Glatz, J. Lacquement, R. Malmbeck, J. Serp, Nucl. Sci. Eng. 153 (2006) 253.
  34. J. Serp, M. Allibert, A. Le Terrier, R. Malmbeck, M. Ougier, J. Rebizant, J. P. Glatz, J. Electrochem. Soc. 152 (2005) C167.
  35. P. Soucek, L. Cassayre, R. Malmbeck, E. Mendes, R. Jardin, J.P. Glatz, *Radiochim. Acta* 96 (2008) 315.
  36. S.A. Kuznetsov, M. Gaune-Escard, J. Electroanal. Chem. 595 (2006) 11.
  37. Y. Castrillejo, M.R. Bermejo, E. Barrado, A.M. Martineza, P. Díaz Arocas, J. Electroanal. Chem. 545 (2003) 141.

38. P. Masset, R.J.M. Konings, R. Malmbeck, J. Serp, J. P. Glatz, J. Nucl. Mater. 344 (2005) 173.
39. G. Bourges, D. Lambertin, S. Rochefort, S. Delpech, G. Picard, J. Alloys Compd. 444 (2007) 404.
40. Y. Sakamura, T. Hijikata, K. Kinoshita, T. Inoue, T.S. Storvick, C.L. Krueger, J.J. Roy, D.L. Grimmett, S.P. Fusselman, R.L. Gay, J. Alloys Compds. 271 (1988) 592.
41. J. P. Ackerman and T. R. Johnson, Actinides-93 International Conference on Future Nuclear Systems, Washington, September 12-17, 1993.
42. W. H. Hannum, Ed., Progress in Nuclear Energy, 31, Nos.1/2, Special Issue, 1997.
43. J. P. Ackerman, J. L. Settle, J. Alloys Compd. 199 (1993) 77.
44. T. Kato, T. Inoue, T. Iwai, Y. Arai, J. Nucl. Mater. 357 (2006) 105.
45. L. S. Chow, J. K. Basco, J. P. Ackerman, T. R. Johnson, Int. Conf. Tech. Exhib.- Global – 93, Washington, 1993, Conf-950913-30.
46. M. Kurata, Y. Sakamura, T. Matsui, J. Alloys Compd. 234 (1996) 83.
47. I. Johnson, ANL-01/16, Contract No. W-31-109-Eng-38, 2001.
48. T. Koyama, K. Kinoshita, T. Inoue, M. Ougier, R. Malmbeck, J. P. Glatz, Radiochim. Acta 96 (2008) 311.
49. L. Cassayre, R. Malmbeck, P. Masset, J. Rebizant, J. Serp, P. Soucek, J. P. Glatz, J. Nucl. Mater. 360 (2007) 49.
50. J. Serp, R. Malmbeck, C. Schepller, J. P. Glatz, ATALANTE 2004, 21-24 June 2004.
51. P. Soucek, R. Malmbeck, C. Nourry, J. P. Glatz, Energy Procedia 7 (2011) 396.
52. P. Soucek, R. Malmbeck, E. Mendes, C. Nourry, D. Sedmidubsky, J.-P. Glatz, J. Nucl. Mater. 394 (2009) 26.

53. L. Cassayre, P. Soucek, E. Mendes, R. Malmbeck, C. Nourry, R. Eloirdi, J. P. Glatz  
J. Nucl. Mater. 414 (2011) 12.
54. A.J. Bard, L.R. Faulkner, Electrochemical Methods. Fundamentals and  
Applications, 2<sup>nd</sup> Edition, Wiley New York, 2001, Chapter 7.
55. P. T. Kissinger and W. R. Heineman, Laboratory Techniques in Electroanalytical  
Chemistry, 2<sup>nd</sup> edition, Marcel Dekker, New York, 1996, p.101-105.
56. M. Iizuka, T. Inoue, O. Shirai, T. Iwai, Y. Arai, J. Nucl. Mater. 297 (2001) 43.
57. Annual Technical Report for 1994, Chemical Technology Division, Argonne  
National Laboratory Report; ANL-95/24 (1995) p.88.

## CHAPTER 2

### Experimental Facilities and Techniques

The chapter is divided into two sections-A & B. Section A gives a brief description of the materials and the equipment used for the studies. The argon atmosphere glove box, purification of the LiCl-KCl salt mixture, preparation of electrolytes, the electrochemical cell, electrodes and the instrumentation are discussed. The second section gives a brief description of the general aspects of the electrode-electrolyte interface and the electrochemical techniques used for the studies such as cyclic voltammetry (CV), chronopotentiometry (CP), open circuit potentiometry (OCP), impedance spectroscopy (IS) and pulse techniques such as square wave voltammetry (SWV), normal pulse voltammetry (NPV) and differential pulse voltammetry (DPV).

#### Section A

##### 2.1 Experimental facilities

###### 2.1.1 Argon atmosphere glove box facility

The salts used for the studies such as LiCl, KCl, LaCl<sub>3</sub>, NdCl<sub>3</sub>, UCl<sub>3</sub> etc. are highly sensitive to oxygen and moisture. Further, uranium metal used in the study is sensitive to oxygen and moisture as well as pyrophoric in nature. Hence these materials were handled in an argon atmosphere glove box. The glove box is made of 304 L stainless steel. It is a double module glove box fitted with two safety glass panels on either side and two on the top. Each side panel is fitted with four polypropylene glove ports. The approximate volume of the box is two cubic meters. It has a transfer port (air lock) facility on one side and a bag-out facility on the other to facilitate transfer of materials. To minimize the ingress of oxygen and moisture into the box, butyl rubber

gloves are used in the glove port. A schematic of the glove box with its recirculation system is shown in Fig 2.1.

The argon gas in the box is continuously circulated through a purification tower which contains a mixture of a copper based deoxo-catalyst and molecular sieves grade 4A for removing oxygen and moisture respectively. The copper based deoxo-catalyst and molecular sieves have the advantage that they can get oxygen and moisture at the ambient temperature and also they can be easily regenerated for further use. The moisture and oxygen impurities in the glove box are maintained below 20 vpm each. The pressure inside the box is maintained between 20 and 60 mm of water column above the atmospheric pressure by using an automatic pressure regulatory system. The purity of the glove box atmosphere is monitored periodically using moisture and oxygen analysers. The moisture analyser (supplied by M/s. Systech Inst., UK), is a  $P_2O_5$  based electrolytic type monitor. It works on the principle of the current produced by electrolysis of water, which is absorbed by  $P_2O_5$  coated on the helically coiled platinum electrodes. An oxygen analyser (M/s. Nucon, India) based on the fuel cell principle is used for monitoring the oxygen levels in the box.

Operations such as weighing and mixing of salts, preparation of electrolyte, assembling of electrochemical cell, preparation of the cathode deposits for characterization etc. were performed in the argon atmosphere glove box. The box was used for storing the salts and electrolytes used in the study. A photograph of the glove box is shown in Fig. 2.2.

### ***2.1.2. Purification of LiCl-KCl mixture***

The eutectic mixture of LiCl (58.5 mol. %) and KCl (41.5 mol. %) is used in the preparation of the electrolytes required for the studies. Anhydrous lithium chloride (AR grade, M/s. Chempure Private Ltd, India) and anhydrous potassium chloride (AR grade,

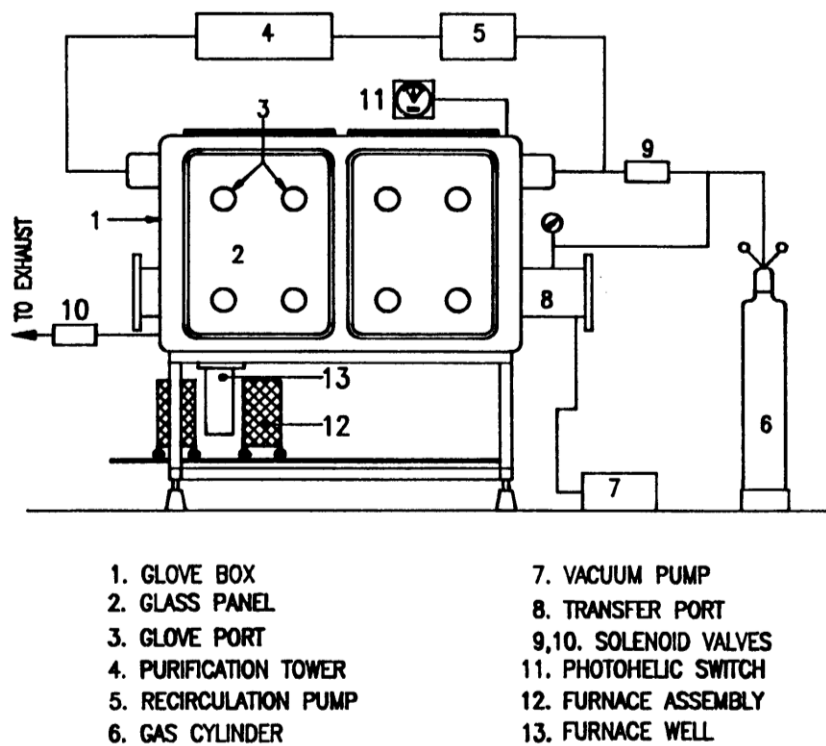


Fig. 2.1 Schematic diagram of the argon atmosphere glove box



Fig. 2.2 Schematic diagram of the argon atmosphere glove box

M/s. Ranbaxy Fine Chemicals, India) were used for the studies. If the moisture present in the salts is not completely removed, it would hydrolyse on fusion forming OH<sup>-</sup> ions. The OH<sup>-</sup> ions precipitate solute metal ions, attack the crucible materials such as alumina, and diminish the available potential span. The salt can be purified from moisture by passing HCl gas or chlorine gas. Maricle and Hume treated the vacuum dried salt mixture with chlorine gas followed by bubbling argon gas to remove the chlorine from the melt. [1]. They found that such a treatment gives a very pure melt. We have adopted this method for purifying the salt mixture. The reaction of chlorine with the metal hydroxide is given as



Initially LiCl and KCl salts were heated separately in a vacuum oven at a vacuum of 1 Pa at 420 K for about 120 hours. The dried salts were stored inside the argon atmosphere glove box until further use. Stoichiometric amounts of LiCl (58.5 mol. %) and KCl (41.5 mol. %) were accurately weighed and loaded in an alumina crucible which in turn was placed inside a quartz tube fitted with Teflon flange. This air tight assembly was then taken out of the glove box and kept in a furnace in the chlorination facility.

The chlorination facility was provided two stainless steel gas lines. One line is for argon gas and the other for chlorine gas. Both these lines are provided with flow meters to adjust the flow of the gas through the quartz vessel. A picture of the chlorination facility is shown in Fig. 2.3. Before the gas enters the purification chamber, it was bubbled through concentrated sulphuric acid to remove any moisture present in the gas before passing through the salt. The salt mixture was initially heated to 473 K under argon atmosphere. Later chlorine gas was passed through the quartz chamber till the salt mixture melted and the gas

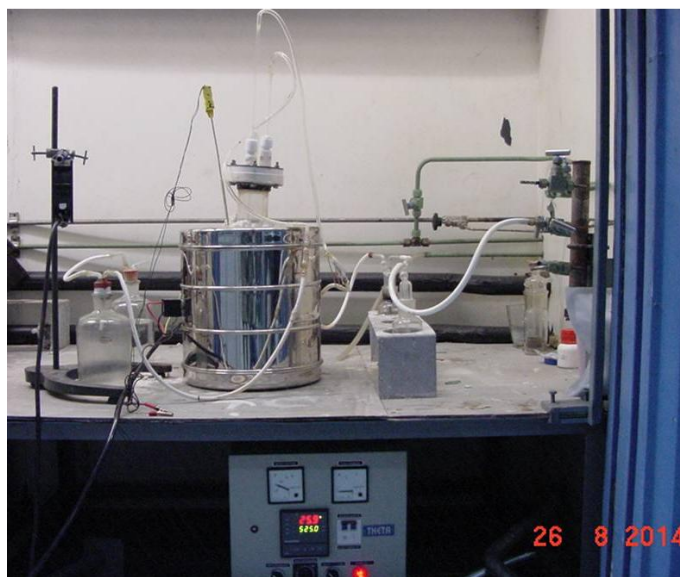


Fig. 2.3 Photograph of the chlorination facility.

was bubbled into the melt for about 30 minutes. The gas that exits from the quartz vessel was bubbled through concentrated sodium hydroxide solution in order to trap the unused chlorine and thereby preventing the corrosion of the fume hood in which the salt purification was done. A chlorine sensor is placed in the room to detect any chlorine leak. Argon gas was later bubbled into the salt melt for about 30 minutes to remove any chlorine adsorbed/dissolved in the salt. The inlet tube was then lifted out of the salt mixture and the salt mixture was cooled up to room temperature gradually. The purified salt mixture was stored in the glove box until further use.

### ***2.1.3 Preparation of the electrolytic salt***

#### ***2.1.3.1 Preparation of LiCl-KCl-UCl<sub>3</sub> electrolyte***

Uranium metal of nuclear grade obtained from BARC, Mumbai and anhydrous cadmium chloride (M/s. Merck, Germany 99 %) were used for the preparation of the electrolyte. Preparation of the electrolyte was carried out in the argon atmosphere glove box. UCl<sub>3</sub> was loaded in the LiCl-KCl eutectic mixture by the following procedure. Purified LiCl-KCl eutectic mixture and cut pieces of uranium metal were taken in a SS 430 crucible and heated in the resistance furnace in the glove box to melt the salt. A

known amount of  $\text{CdCl}_2$  was added to the melt and the latter was equilibrated with uranium metal at 723 K for over 70 hours. The amount of uranium taken was in excess of the stoichiometric amount required as given by Eq. 2.2, thus ensuring that no  $\text{CdCl}_2$  remained in the electrolyte after the equilibration.



The salt loaded with  $\text{UCl}_3$  was decanted leaving behind the unreacted uranium metal and cadmium metal formed during the reaction. Completion of the equilibration was checked by estimating the amount of cadmium in the  $\text{UCl}_3$  loaded salt by Atomic Absorption Spectroscopy (AAS). The concentration of cadmium in the equilibrated salt was measured by dissolving a sample in 1:1  $\text{HNO}_3$ , followed by fuming to dryness. The residue was dissolved in 0.1 M  $\text{HNO}_3$  and Cd was analyzed by AAS. Absence of Cd in the sample indicated the completion of equilibration. The amount of uranium in the electrolyte salt was determined by potentiometric technique based on the Davis and Gray method [2]. The  $\text{UCl}_3$  concentration in the electrolyte salt thus prepared was adjusted to the required concentration by mixing with purified LiCl-KCl mixture.

### ***2.1.3.2 Preparation of LiCl-KCl-RECl<sub>3</sub> electrolyte***

$\text{LaCl}_3$  (Alfa Aesar 99.99 %) and  $\text{NdCl}_3$  (Alfa Aesar 99.99%) were used in our studies. LiCl-KCl- $\text{LaCl}_3$  and LiCl-KCl- $\text{NdCl}_3$  electrolytes were prepared by addition of  $\text{LaCl}_3$  and  $\text{NdCl}_3$  respectively to the purified LiCl-KCl mixture. The mixture was melted and the temperature was held at 723 K for about 1 hour. The molten mixture was stirred using a tantalum rod to obtain uniform concentration of the rare earth chloride. The concentrations of lanthanum and neodymium in the electrolyte were determined by dissolving a sample in 0.1 M  $\text{HNO}_3$  and analyzed by ICP-AES.

### ***2.1.3.3 Preparation of LiCl-KCl-AgCl electrolyte***

The LiCl-KCl-AgCl electrolyte required for the reference electrode was prepared as described. Known amounts of AgCl (Alfa Aesar, 99.99 %) was added to the vacuum dried LiCl-KCl eutectic mixture taken in an alumina crucible. The salt mixture was melted under chlorine atmosphere in the chlorination facility. Chlorine gas was passed through the melt for over 2 hours to ensure complete dissolution of AgCl in the melt. The excess chlorine gas was removed by bubbling high pure argon gas. The melt was later cooled and the LiCl-KCl-AgCl electrolyte thus prepared was stored in air tight container in the argon atmosphere glove box until further use. The amount of silver in the electrolyte was measured by dissolving a sample in dilute ammonia solution and estimated by ICP-AES [3].

### ***2.1.3.4 Preparation of electrolyte for studies by pulse voltammetry (Chapter 7)***

The stock of LiCl-KCl-UCl<sub>3</sub> electrolyte was prepared as described earlier. This salt was diluted with purified LiCl-KCl salt mixture to prepare the electrolyte with required concentration of UCl<sub>3</sub> containing uranium in the range 0.1 – 4 wt. %. The amount of uranium in the electrolyte containing UCl<sub>3</sub> in the concentration 11 wt % -0.5 wt % was estimated by Davis and Gray method. Concentration of uranium in electrolytes containing less than 0.5 wt % UCl<sub>3</sub> was determined by inductively coupled plasma-mass spectrometry (ICP-MS). For simulated studies, the LiCl-KCl-1 wt. % UCl<sub>3</sub>-1 wt. % LaCl<sub>3</sub>-1 wt. % CeCl<sub>3</sub>-0.7 wt. % EuCl<sub>3</sub> was used. The electrolyte was prepared by adding weighed amounts of LaCl<sub>3</sub>, CeCl<sub>3</sub> and EuCl<sub>3</sub> to the LiCl-KCl-UCl<sub>3</sub> electrolyte to obtain the required concentration. The purity of CeCl<sub>3</sub> (Alfa Aesar) and EuCl<sub>3</sub> (Alfa Aesar) used in the preparation of the electrolyte were of AR grade purity.

### ***2.1.4 Electrochemical apparatus and electrodes***

#### ***2.1.4.1 Electrochemical apparatus***

A three electrode assembly was used for all the measurements. The schematic of the electrochemical cell is given in Fig.2.4. The cell consists of a one end closed SS 316 tubular vessel which served as the external vessel. The vessel was sealed with a knife edged flange having provisions for gas inlet and exit, electrode leads and a thermocouple well. The electrolyte was contained in an alumina crucible which was placed inside the stainless steel vessel.

#### ***2.1.4.2 Electrodes***

A 1.5 mm diameter high purity tungsten wire was used as inert working electrode. The tungsten wire was sheathed with an alumina sleeve, exposing the required height of the wire. The area of the working electrode was calculated from the depth of immersion of the wire. A 1mm tungsten wire encased in a glass capsule with a known exposed area was used as the working electrode for studies using pulse techniques discussed in chapter 7. A picture of the electrode used is shown in Fig. 2.5. A tantalum sheet of 1mm thickness was used as the counter electrode for all the electrochemical studies. A 1mm tantalum wire coiled at one end was used as the counter electrode for studies using pulse techniques. The W and Ta surfaces were polished and cleaned with nitric acid before use. The reference electrode used for all the electrochemical measurements involving  $\text{NdCl}_3$  and  $\text{UCl}_3$  consisted of a high pure silver wire (2 mm diameter) dipped in 0.31 mol %  $\text{AgCl-LiCl-KCl}$  mixture contained in a pyrex glass tube. All the potentials involving  $\text{NdCl}_3$  and  $\text{UCl}_3$  mentioned in this thesis were

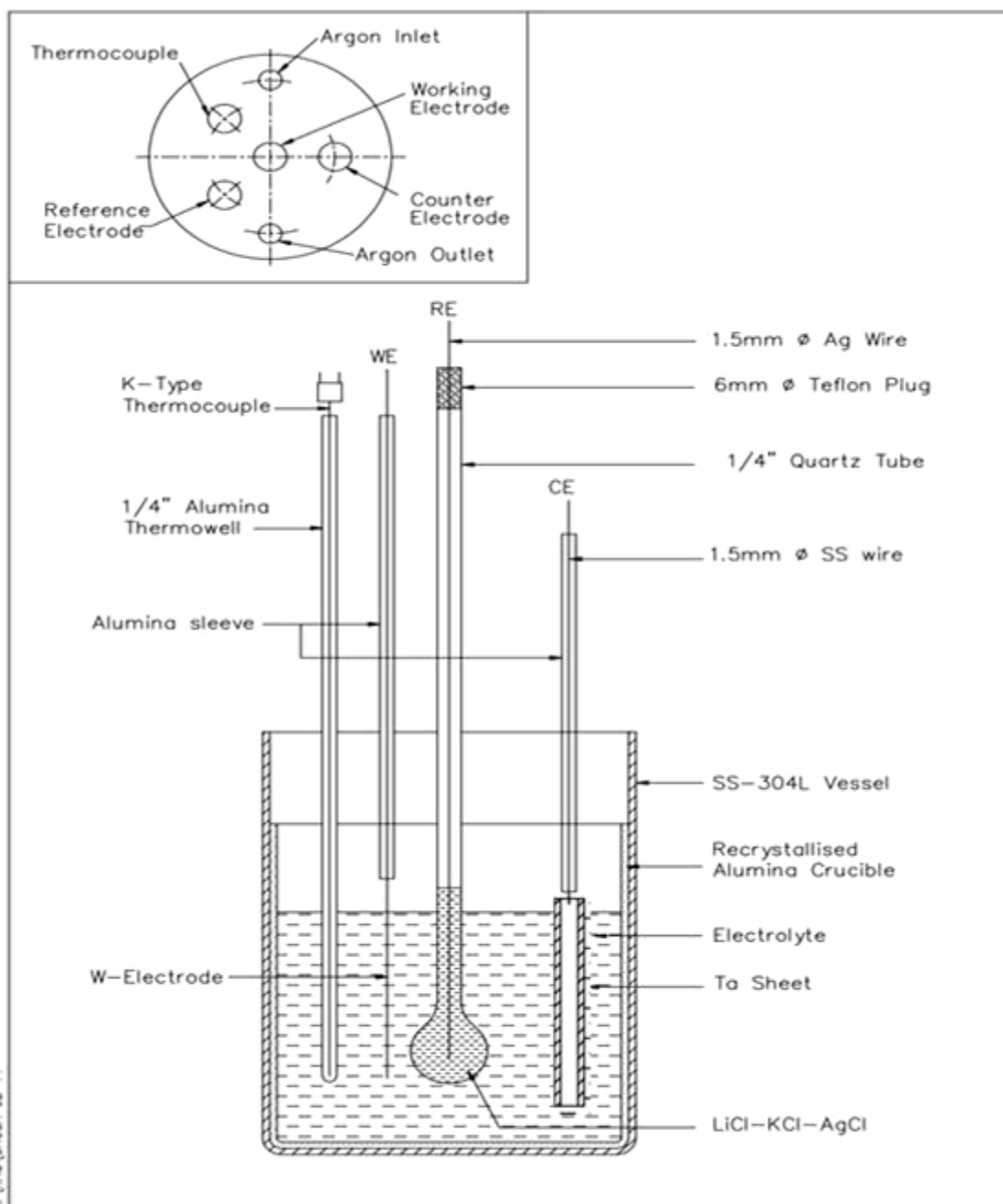


Fig. 2.4 Schematic of the electrochemical cell

measured with respect to this reference electrode. For electrochemical studies involving  $\text{LaCl}_3$  on cadmium and gallium cathodes the same reference electrode was used. For electrochemical studies involving  $\text{LaCl}_3$  on inert tungsten and solid aluminium cathodes and for the measurement on pulse technique (chapter 7), a 1 mm diameter high pure silver wire dipped in 0.1 mol %  $\text{AgCl-LiCl-KCl}$  mixture contained in a pyrex glass tube was used as the reference electrode.

### ***2.1.5 Procedure for electrochemical measurement***

The cleaned SS cell assembly along with the recrystallised alumina crucible was degassed initially without loading the electrolyte and the electrodes. The cell assembly was placed in a Kanthal wire wound resistance furnace which was used for heating the cell. The degassing was done by evacuating the cell assembly using a rotary pump, while gradually raising the temperature of the cell assembly to 773 K. The degassing was continued for about 2 hours at 773 K. The cell assembly was then cooled gradually. The cooled, degassed SS vessel was taken into the argon atmosphere glove box. The electrodes were assembled in their respective feed throughs. The electrolyte salt was loaded in the alumina crucible. The cell was then assembled, taken out of the glove box and kept in the resistance furnace which was used for heating. Argon gas, which was purified by passing through a calcium getter at 823 K, was passed through the cell. The temperature of the cell was controlled by a PID controller with an accuracy  $\pm 1$  K. The temperature of the melt was monitored by a K-type thermocouple kept in thermowell and immersed in the electrolyte. A picture of the cell is shown in Fig. 2.6.

Cyclic voltammograms, square wave voltammograms, chronopotentiograms, open circuit potential measurements and impedance spectrum were obtained using AUTOLAB PGSTAT30 from M/s Eco Chemie, Netherlands equipped with IF 030 interface. The

voltammograms were processed using GPES 4.9 software and the impedance spectrum was processed using FRA 4.9 software.

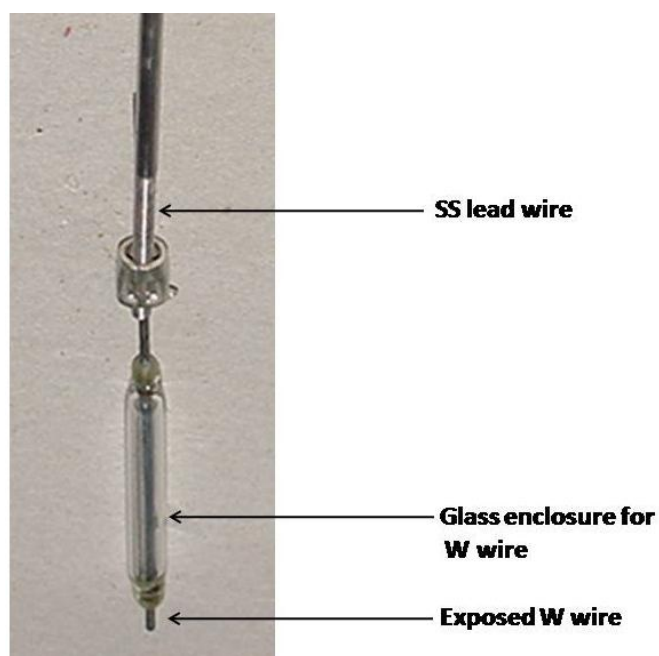


Fig. 2.5 Photograph of the working electrode used for pulse techniques.

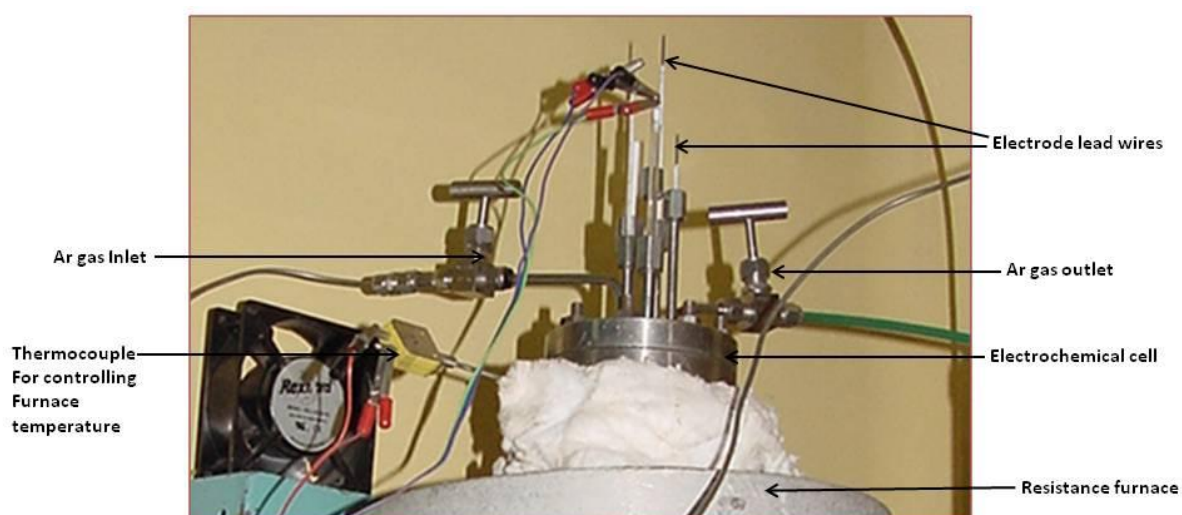


Fig. 2.6 Photograph of the electrochemical cell.

## Section B

### 2.2 Experimental techniques

#### 2.2.1 General Theory

A reversible electrochemical reaction is one in which the reaction is so fast that the equilibrium is always re-established as soon as changes are made. For a reversible reaction described as given in Eq 2.3,



where **O** and **R** are the oxidized and reduced species, the application of a potential  $E$ , forces the respective concentrations of **O** and **R** at the surface of the electrode (that is,  $C_O^0$  and  $C_R^0$ ) to a ratio in compliance with the Nernst equation:

$$E = E^o - \frac{RT}{nF} \ln \frac{C_R^0}{C_O^0} \quad [2.4]$$

where  $R$ , is the molar gas constant ( $8.314 \text{ J mol}^{-1} \text{ K}^{-1}$ ),  $T$ , is the absolute temperature ( $K$ ),  $n$ , is the number of electrons transferred,  $F$ , the Faraday constant ( $96,485 \text{ C/equiv}$ ), and  $E^o$  is the standard reduction potential for the redox couple. If the potential applied to the electrode is changed, the ratio  $c_R^0 / c_O^0$  at the surface will also change so as to satisfy Eq. 2.4. If the potential is made more negative the ratio becomes larger (that is, **O** is reduced) and, conversely, if the potential is made more positive the ratio becomes smaller (that is, **R** is oxidized). The electrochemical equilibrium would result, when the rate constant is very high and such systems obey the Nernst equation [4-6].

#### 2.2.2 Faradaic and non-Faradaic processes

Two types of processes occur at the electrode. One kind comprises of reactions in which electrons are transferred across the metal-solution interface. Electron transfer causes oxidation or reduction to occur. Since such reactions are governed by Faraday's

law (i.e., the amount of chemical reaction caused by the flow of current is proportional to the amount of electricity passed), they are called faradaic processes.

Processes such as adsorption and desorption, change in the structure of electrode-solution interface with change in potential or solution composition are called nonfaradaic processes.

### ***2.2.2.1 Charging current and residual current***

The migration of ions in response to the charge at the electrode's surface leads to the formation of a structured electrode-solution interface, called the electrical double layer. When the potential of the electrode is changed, restructuring of the electrical double layer takes place leading to the charging current. The charging current is non-faradaic, short-lived and decays exponentially. A transient charging current flows, each time when the potential of the electrode is changed.

The residual current has two components- a faradaic current due to the oxidation or reduction of trace impurities and the charging current. Efforts are made to minimize the residual current for electrochemical studies.

### ***2.2.3 Factors affecting the rate of electrochemical reactions***

The two factors that contribute to the rate of the electrochemical reaction are:

- the mass transport (the rate at which the reactants are transported to and from the electrode)
- the kinetics (the rate at which electrons pass between electrode and reactant)

#### ***2.2.3.1 Modes of mass transport***

There are three modes of mass transport that affect the rate at which reactants and products move towards or away from the electrode surface: diffusion, migration and convection [4-5].

(a) Diffusion occurs when the concentration of the ion at the surface of the electrode is different from that in the bulk solution. The resulting concentration gradient and mass transport is described by Fick's law, which states that the flux of matter ( $\phi$ ) is directly proportional to the concentration gradient:

$$\phi = -D_0(\partial C_0 / \partial x) \quad [2.5]$$

where  $D_0$  is the diffusion coefficient of the oxidized species ( $O$ ) and  $x$  is the distance from the electrode surface.

(b) Migration is the movement of a charged ion in the presence of an electric field. In voltammetry, the use of a supporting electrolyte at concentrations 100 times that of the species being determined eliminates the effect of migration.

(c) Convection is the movement of the electroactive species by thermal currents, by density gradients present in the solution, or by stirring the solution or rotating the electrode.

### 2.2.3.2 Diffusion layer

When a potential sufficient to reduce the oxidized species ( $O$ ) is applied at the electrode surface, in the absence of migration and convection, the resultant concentration gradient is shown in Fig. 2.7. Before the potential is applied ( $t=0$ ), the concentration of  $O$  is the same at all distances from the electrode's surface. After applying a potential sufficient to reduce  $O$ , its concentration reduces to zero at the electrode surface. The species  $O$ , diffuses to the electrode surface from the bulk solution. The longer the potential is applied, the greater is the distance over which diffusion occurs. The region of solution over which diffusion occurs is

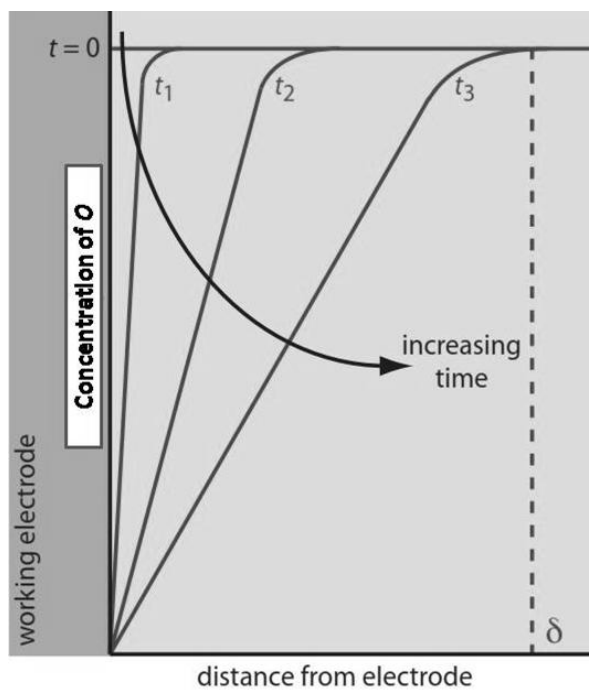


Fig. 2.7 Concentration profile at the electrode-electrolyte interface.

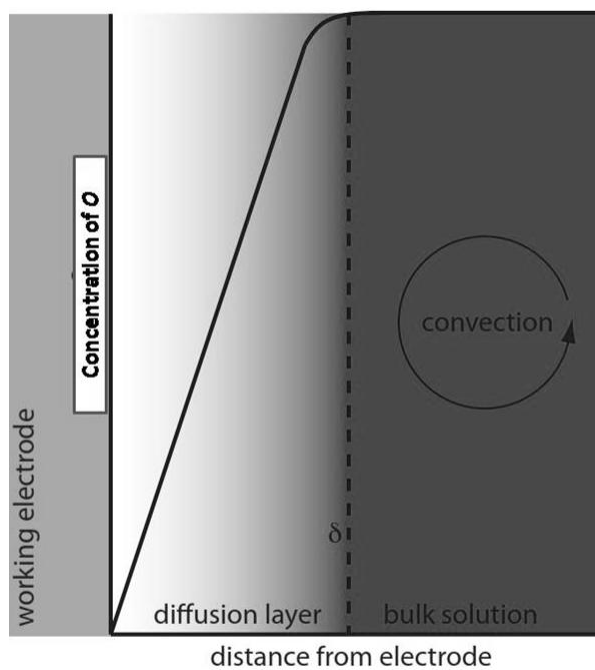


Fig. 2.8 Picture showing the diffusion layer and the concentration profile in the electrochemical cell.

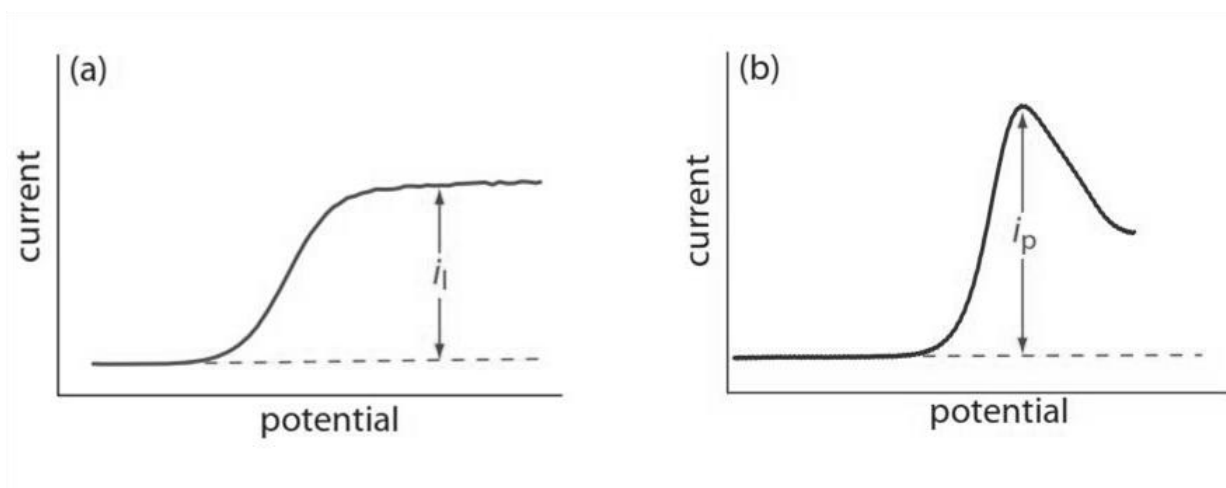


Fig. 2.9 Shape of voltammogram for constant and varying thickness of the diffusion layer.

the diffusion layer. The diffusion layer is depicted in Fig. 2.8. In the absence of other modes of mass transport, the width of the diffusion layer,  $\delta$ , increases with time as  $O$  must diffuse from increasingly greater distances.

The current due to diffusion is given by

$$i = \frac{nFAD_O(C_{bulk} - C_{x=0})}{\delta} \quad [2.6]$$

where  $D_O$  is the diffusion coefficient of the oxidized species,  $C_{bulk}$  and  $C_0$  are the concentration of the oxidized species in the bulk and at the electrode surface and  $\delta$ , is the thickness of the diffusion layer. The thickness of the diffusion layer at any time  $t$ , is related to the diffusion coefficient by the following equation

$$\delta = 2(D_O t)^{1/2} \quad [2.7]$$

#### 2.2.4 Single step charge transfer kinetics

For a general electron transfer reaction considered in Eq.2.3, the rate of the reaction is given as

$$v = k_f C_O(0,t) - k_b C_R(0,t) \quad [2.8]$$

where  $\nu$ , is the rate of the reaction,  $k_f$  and  $k_b$  are the rate constant of the forward and reverse reaction,  $C_O(0, t)$  and  $C_R(0, t)$  are the surface concentration of  $O$  and  $R$  ( $x=0$ ) at time  $t$  respectively. the rate,  $\nu$ , has the unit of  $\text{mol cm}^{-2} \text{s}^{-1}$  and the rate constant  $\text{cm s}^{-1}$ . The electron transfer is a heterogenous process and the kinetics can depend very much on the electrode material. In an electrochemical reaction, the current at any potential is a direct measure of the electron transferred

$$\nu = \frac{i}{nFA} \quad [2.9]$$

$i$ , current in A,  $A$ , area of the electrode surface. The rate of the reaction can be varied by changing the electrode potential  $E$ , then

$$k_f = k_f^0 \exp(-\beta n f E) \quad [2.10]$$

$$k_b = k_b^0 \exp((1 - \beta) n f E) \quad [2.11]$$

$k_f^0$  and  $k_b^0$  are the rate constant when  $E=0$  and  $f=F/RT$  and  $\beta$ , is the symmetry factor.

At the formal electrode potential,  $E^{0'}$ , the forward and reverse rate constant are equal since no net reaction takes place and we get the charge transfer rate constant (at equilibrium) defined as

$$k_f^0 \exp(-\beta n f E) = k_b^0 \exp((1 - \beta) n f E) = k_h^0 \quad [2.12]$$

$k_h^0$  is the standard heterogenous rate constant. For fast processes,  $k_h^0$  may have value upto  $10 \text{ cm s}^{-1}$  and for slow processes,  $k_h^0$  can have value as low as  $10^{-9} \text{ cm s}^{-1}$  (for example hydrogen evolution reaction on mercury electrode). At equilibrium, although there is exchange of electrons in both the directions of the interface, the exchange rate on both the directions are equal and opposite. Hence the net exchange is zero. So at equilibrium,

$$i_{cathodic} = i_{anodic} = i_0 \quad [2.13]$$

where  $i_0$  is the exchange current density. Using high concentrations of  $O$  and  $R$  and assuming that the concentration of  $O$  and  $R$  at the electrode surface is equal to that in the bulk, the popular Butler-Volmer equation is obtained.

$$i = i_0 \{ \exp(-\beta n f \eta) - \exp[(1 - \beta) n f \eta] \} \quad [2.14]$$

$\eta$ , is the over voltage defined as  $(E - E_{eq})$ . For very large values of  $\eta$ , the second term becomes negligible with respect to the first term. We get,

$$i = i_0 \exp(-\beta n f \eta) \quad [2.15]$$

$$\eta = \frac{2.303RT}{\beta n F} \log i_0 - \frac{2.303RT}{n F} \log i \quad [2.16]$$

which is the popular Tafel equation.

To summarize, when the electron transfer is fast, the redox reaction is at equilibrium. Under this condition, the redox reaction is electrochemically reversible and the Nernst equation applies. The mass transport determines the rate of the redox reaction. If the electron transfer kinetics is sufficiently slow, the concentration of the reactant and product at the electrode are not what is predicted by the Nernst equation. In such cases the system is electrochemically irreversible and the rate of the reaction is determined by the electrode kinetics.

### 2.2.5 Shape of voltammograms

The shape of the voltammogram depends upon various experimental factors- such as sampling of the current, quiescent or stirred solution etc. The shape of the voltammogram may be sigmoidal with the current increasing from a background residual current to a limiting current as shown in Fig 2.9a. When the solution is stirred or the diffusion layer remains constant, a limiting current results. It may be recalled that the faradaic current is dependent on the diffusion layer thickness (as given in Eq 2.6). In the

absence of convection, the diffusion layer increases with time. In such case, the resulting voltammogram has a peak current instead of a limited current as shown in Fig 2.9b. In some techniques, the change in current  $\Delta_i$  is measured following a change in potential. The resulting voltammogram also has a peak shape. The general classification of interfacial electrochemical techniques is shown in Fig. 2.10. The techniques have their own unique laws and theoretical relationships. The techniques used in the present study are discussed here.

### ***2.2.6. Cyclic voltammetry***

In cyclic voltammetry, the potential applied to an electrode is changed linearly with time at a particular scan rate till the potential reaches a predetermined switching potential. The direction of the scan is then reversed. The triangular waveform of the potential with time is shown in Fig 2.11a. The typical potential-current curve is shown in Fig 2.11b. The basic feature of the voltammogram is the appearance of a current peak at a potential characteristic of the electrode reaction taking place. The position and shape of a given peak depends on factors such as sweep rate, electrode material, solution composition and the concentration of the reactants. Cyclic voltammetry is suited to identification of steps in the overall reaction and of new species which appear in solution during electrolysis as a result of combined electrochemical and chemical steps. Cyclic voltammetry also provide kinetic data.

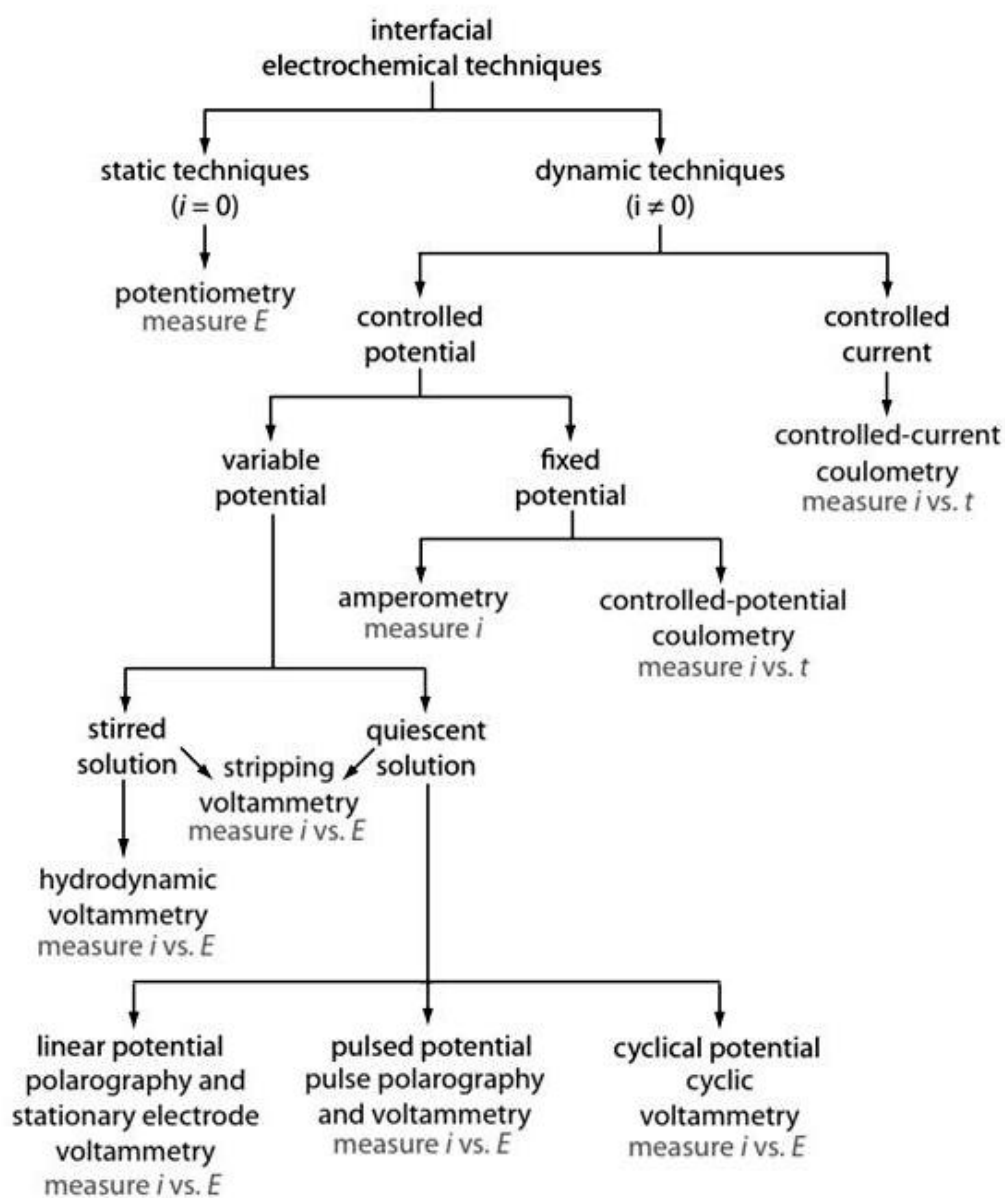


Fig. 2.10 Classification of interfacial electrochemical techniques.

Cyclic voltammetry is carried out in an unstirred solution, and hence has peak current instead of limiting current as the diffusion layer increases progressively with the potential ramp. The important parameters in a cyclic voltammogram are the peak potentials ( $E_{pc}$ ,

$E_{pa}$ ) and peak currents ( $i_{pc}$ ,  $i_{pa}$ ) of the cathodic and anodic peaks, respectively. If the electron transfer process is fast compared with diffusion, the reaction is said to be electrochemically reversible, and the peak separation is given Eq. 2.17 and 2.18 [7].

$$\Delta E_p = |E_{pa} - E_{pc}| = 2.22 \frac{RT}{nF} \quad [2.17]$$

$$|E_p - E_{p/2}| = 2.2 \frac{RT}{nF} \quad [2.18]$$

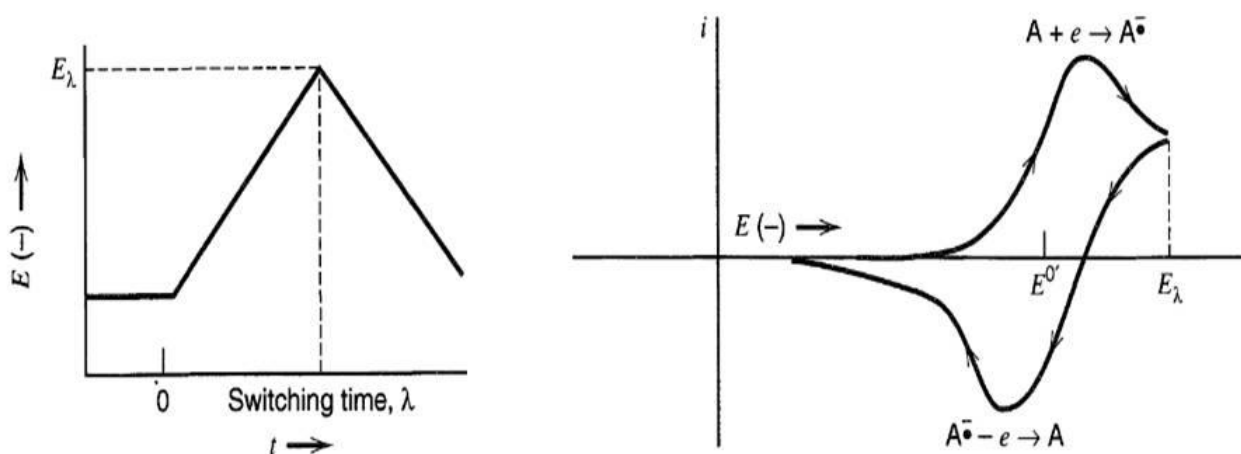


Fig. 2.11 Triangular waveform for the cyclic voltammetry and the corresponding potential current curve.

The formal reduction potential ( $E^o$ ) for a reversible couple is given by

$$E^o = \frac{E_{pc} + E_{pa}}{2} \quad [2.19]$$

Other characteristic features of reversible process are that the ratio of cathodic and anodic peak heights is unity ( $i_{pc}/i_{pa} = 1$ ) and the cathodic peak potential  $E_{pc}$  and the anodic peak potential  $E_{pa}$  does not alter when the scan rates are changed. For a reversible reaction, the concentration is related to peak current by the Randles–Sevcik expression [8]:

$$i_p = 0.44(nF)^{3/2}(RT)^{-1/2} AC^o D^{1/2} \nu^{1/2} \quad [2.20]$$

where  $i_p$ , is the peak current in A,  $n$ , is the number of electrons transferred,  $A$ , is the electrode area ( $\text{cm}^2$ ),  $D$ , is the diffusion coefficient ( $\text{cm}^2 \text{s}^{-1}$ ),  $C^o$ , is the bulk concentration in  $\text{mol cm}^{-3}$ , and  $\nu$ , is the scan rate in  $\text{V s}^{-1}$ .

For an irreversible electrochemical process, the peak current is again directly proportional to the square root of scan rate related by the Delahay equation [9]

$$i_p = 0.496nF(\alpha n_\alpha F)^{1/2}(RT)^{-1/2} AC^o D^{1/2} \nu^{1/2} \quad [2.21]$$

where  $\alpha$ , is the electrochemical transfer coefficient and is a measure of the nature of the transition state ( $0 < \alpha < 1$ ). For an irreversible process, the following relation hold good between the peak potential and the scan rate. The peak potential shift in the negative direction for a reduction reaction with increase in scan rate [10].

$$E_p = E^o - \frac{RT}{\alpha n_\alpha F} \left[ 0.78 + \ln\left(\frac{D^{1/2}}{k^0}\right) + \ln\left(\frac{\alpha n_\alpha F \nu}{RT}\right)^{1/2} \right] \quad [2.22]$$

For a quasi-reversible process, the relationship  $i_p \propto \nu^{1/2}$  does not hold good. The peak separation between  $E_{pa}$  and  $E_{pc}$  increases with increase in scan rate. Also, there is a decrease in peak current  $i_p$  and the peak potential appears at potential cathodic relative to that of a reversible system.

### 2.2.7. Chronopotentiometry

For a simple charge-transfer process as represented by Eq. 2.3, if equilibrium is maintained, the potential of an electrode immersed in a solution containing both species is given by the Nernst equation (Eq. 2.4). When a constant current is applied, the potential varies with time as shown in Fig. 2.12. Although the change in bulk concentrations is negligible during the transient, the concentrations of both reactant and product at the electrode surface vary markedly and the ratio  $c_R^0/c_O^0$  determines the observed potential. This ratio varies rapidly at the beginning of the transient,  $c_R^0$  grows from zero to a finite value. Hence there is rapid change in potential in the beginning (as seen in Fig.2.12). Slowly when concentrations  $c_R^0$  and  $c_O^0$  at the surface are comparable, a plateau appears. If the current is maintained for a longer time, the potential will rise until it reaches another plateau, characteristic of a different reaction.

The Sand's equation gives the relation between the applied current and the transition time for a reversible redox process as [4]

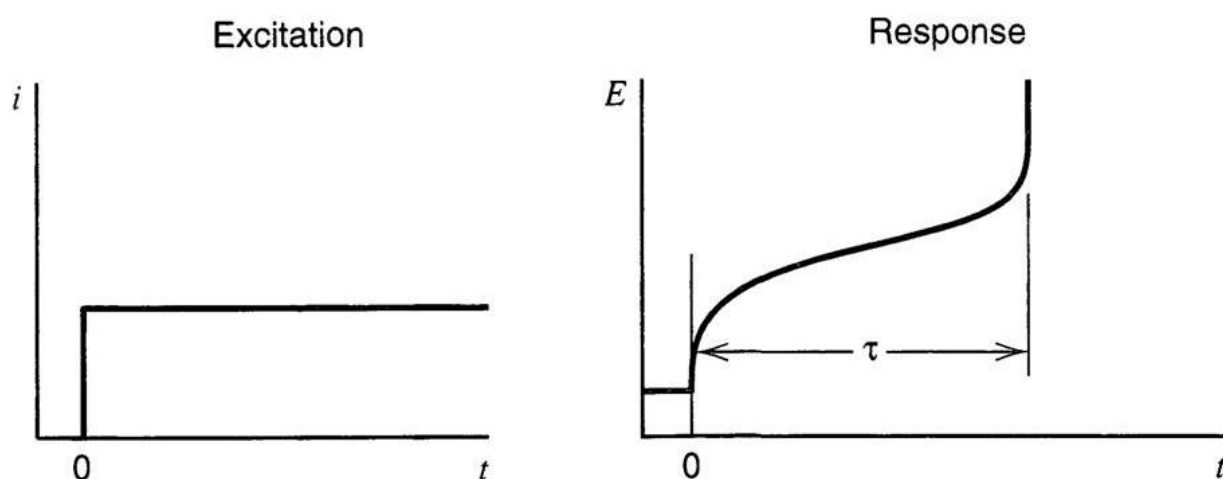


Fig.2.12 The excitation signal and the potential response for chronopotentiometry.

$$\tau^{1/2} = \frac{\pi^{1/2} n F D^{1/2} C_o}{2i} \quad [2.23]$$

where  $C_o$  is the bulk concentration of the reactant and  $i$  is the constant current density applied,  $\tau$ , is the transition time. A common way of testing the reversibility of the redox process is to vary the applied current density and verify that the product ( $i\tau^{1/2}$ ) is constant.

### 2.2.8 Pulse voltammetry

The first important voltammetric technique to be developed was the polarography. This technique uses the dropping mercury as the working electrode. In this method, the current flowing through the electrochemical cell is measured while applying a linear potential ramp. The method had the limitation of contribution from the charging current due to the growing size of the mercury drop. In order to increase the speed and sensitivity, many forms of potential modulation have been tried over years [4,5,10]. Three of these pulse techniques are widely used and are discussed here.

#### 2.2.8.1 Normal pulse voltammetry(NPV)

This technique uses a series of potential pulses of increasing amplitude. The current measurement is made near the end of each pulse, which allows time for the charging current to decay as shown in Fig. 2.13a. The potential is pulsed from an initial potential,  $E_i$ . The duration of pulse,  $\tau$ , is usually 1 to 100 ms and the interval between pulses is typically 0.1 to 5 s. The resulting sampled current is plotted against the potential to which the pulse is stepped (Fig. 2.13b). Since the electrode is held at the base potential (here the base potential is such that no faradaic current flows) for long time and also the

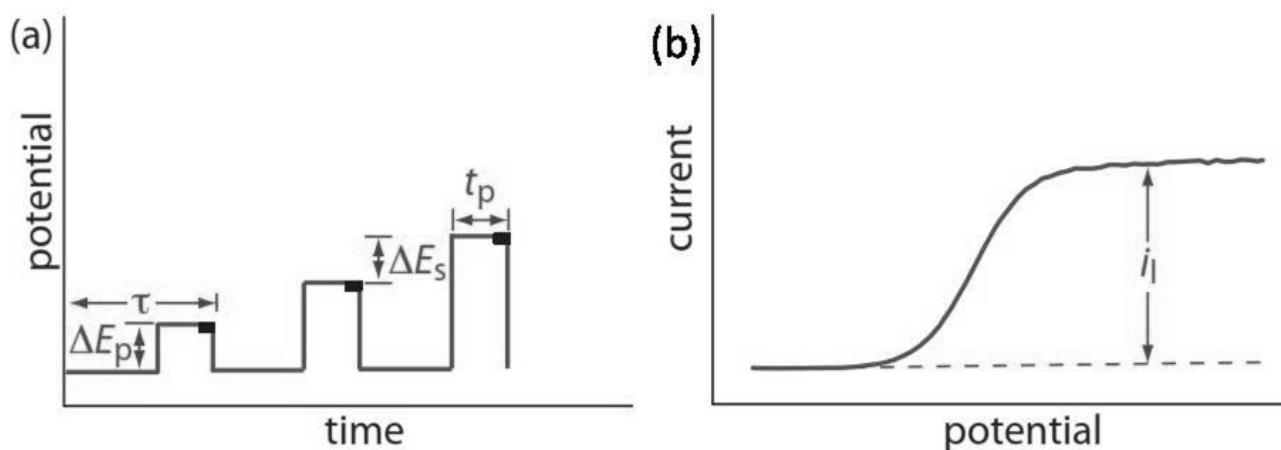


Fig. 2.13 (a) Potential waveform for normal pulse voltammetry. (b) Excitation signal for the same. The current is sampled at the time intervals shown by black rectangles.  $\tau$ , is the cycle time;  $\Delta E_p$  is the pulse potential;  $\Delta E_s$  is the fixed change in potential per cycle and  $t_p$  is the pulse time.

potential pulse is applied for short period, there is less time for the analyte to undergo oxidation or reduction and hence the diffusion layer is small. As a result, the faradaic current in normal pulse polarography is greater than in the conventional polarography, resulting in better sensitivity and lower detection limits ( $10^{-6}$ - $10^{-7}$  M).

#### 2.2.8.2 Differential pulse voltammetry (DPV)

This technique is comparable to the normal pulse voltammetry in the sense that the potential is scanned with a series of pulses. However, it differs from the NPV because each potential pulse is fixed, of small amplitude (10 to 100 mV), and is superimposed on a slowly changing base pulse as shown in Fig. 2.14a. Current is sampled at two points for each pulse, the first point just before the application of the pulse and second the end of the pulse.

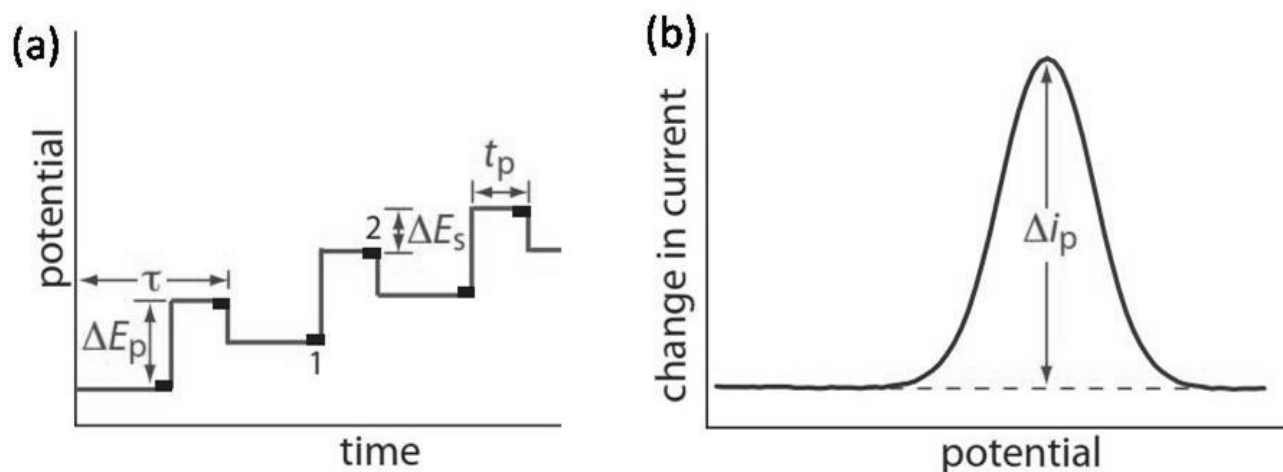


Fig. 2.14 (a) Potential waveform for differential pulse voltammetry. (b) Excitation signal for the same.  $\tau$ , is the cycle time;  $\Delta E_p$  is the pulse potential;  $\Delta E_s$  is the fixed change in potential per cycle and  $t_p$  is the pulse time. When measuring the change in current,  $\Delta I$ , the current at point 1 is subtracted from current at point 2.

These sampling points are selected to allow for the decay of the nonfaradaic (charging) current. The difference between the sampled current for each pulse is determined and plotted against the base potential. The difference in the two currents give rise to the peak-shaped voltammogram

(Fig. 2.14b). Since the differential current is measured by this technique, the contribution of the residual current is minimised and hence the sensitivity is better than the NPV.

### 2.2.8.3 Square-Wave Voltammetry (SWV)

This technique was described in detail by Osteryoung and Osteryoung [11] and Ramaley [12]. The excitation signal in SWV consists of a symmetrical square-wave pulse

of amplitude  $E_{sw}$  superimposed on a staircase waveform of step height  $\Delta E$ , where the forward pulse of the square wave coincides with the staircase step as shown in Fig. 2.15a. The net current,  $i_{net}$ , is obtained by taking the difference between the forward and reverse currents ( $i_{for} - i_{rev}$ ) and is centered on the redox potential (Fig. 2.15b). The peak height is directly proportional to the concentration of the electroactive species and direct detection limits as low as  $10^{-8} M$  is possible.

Square-wave voltammetry is slightly more sensitive than DPV, since the anodic current produced in the reverse pulse will enhance the  $\Delta i$ . Square-wave voltammetry has several advantages. Among these are its excellent sensitivity and the rejection of background currents. Applications of square-wave voltammetry include the study of electrode kinetics with regard to preceding, following, or catalytic homogeneous chemical reactions, determination of some species at trace levels.

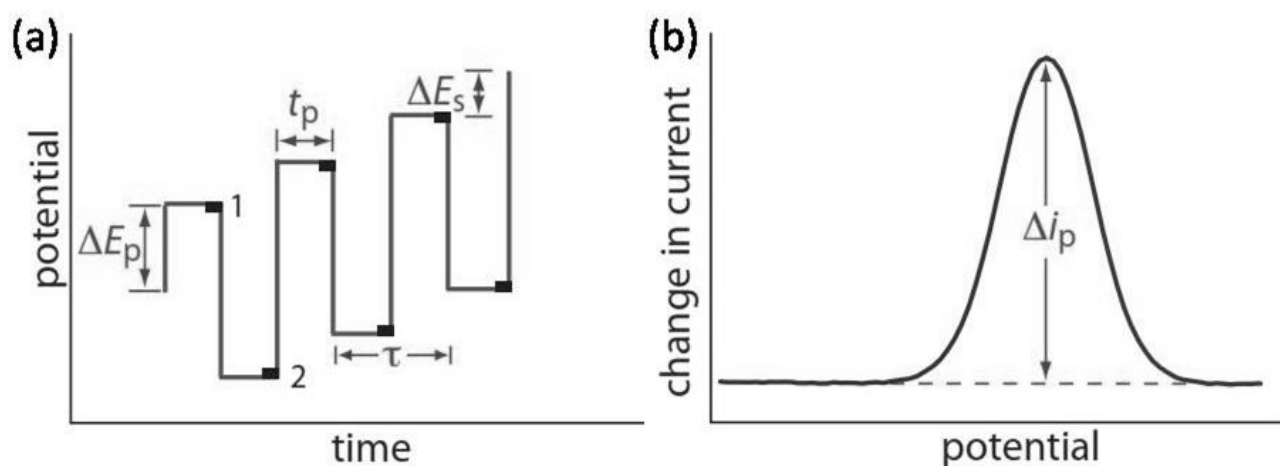


Fig. 2.15 (a) Potential waveform for squarewave voltammetry. (b) Excitation signal for the same. When measuring the change in current,  $\Delta I$ , the current at point 1 is subtracted from current at point 2.

### 2.2.9 Electrochemical Impedance Spectroscopy (EIS)

In electrochemical impedance spectroscopy, the system under investigation is excited by a small amplitude ac sinusoidal signal of potential or current in a wide range of frequencies and the response of the current or voltage is measured. By sweeping the frequency in a wide range from high-to-low, the reaction steps with different time constants, such as mass transport, charge transfer and chemical reaction can be separated [4, 13-14].

The excitation input and the resulting current output are described as

$$E(t) = E_0 \exp(j\omega t) \quad [2.24]$$

where  $E(t)$  is the applied potential at time  $t$  and  $E_0$ , is the potential amplitude,  $\omega$  and  $\phi$  are the angular frequency and phase shift respectively. The output current signal  $I(t)$  has amplitude  $I_0$  and is shifted in phase by  $\phi$

$$I(t) = I_0 \exp[j(\omega t - \phi)] \quad [2.25]$$

The impedance of the system is expressed as a complex function as

$$Z(\omega) = Z_0 \exp(j\phi) = Z_0 (\cos \phi + j \sin \phi) \quad [2.26]$$

When the real part of the impedance is plotted on the abscissa and the imaginary part is plotted on the ordinate, we get the “Nyquist plot”.

The Randles circuit is the simplest and most common electrical representation of an electrochemical cell. It includes a resistor (with a resistance of  $R_{ct}$ ; an interfacial charge-transfer resistance) connected in parallel with a capacitor (with a capacitance of  $C_{dl}$ ; double layer capacitance). This RC electrical unit is connected in series with another resistor (with a resistance of  $R_s$ ; solution resistance) as shown in Fig. 2.16a. The total impedance is given by

$$Z = R_s + (R_{ct}^{-1} + j\omega C_{dl})^{-1} \quad [2.27]$$

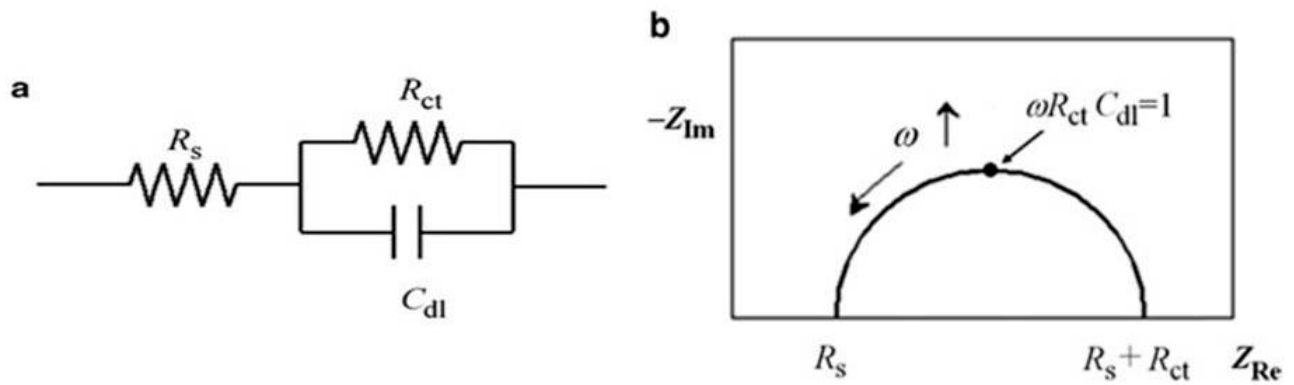


Fig.2. 16 (a) Equivalent circuit for the Randles cell. (b) Nyquist plot for the Randles cell.

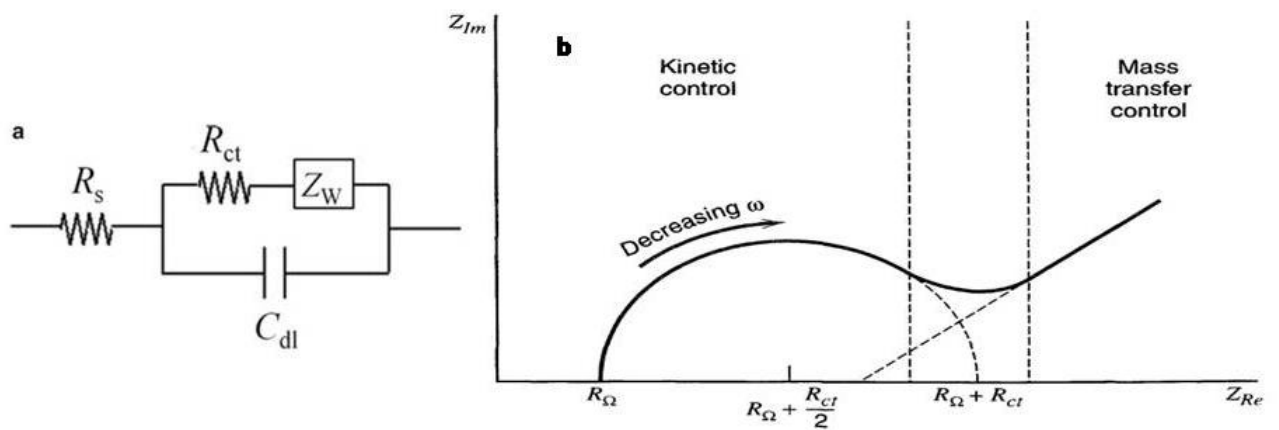


Fig.2.17 (a) Equivalent circuit for an electrochemical cell. (b) Impedance plot for an electrochemical system showing the regions of mass-transfer and kinetic control at low and high frequencies, respectively.

The Randles cell and the corresponding Nyquist plot are shown in Fig. 2.16b. The Nyquist plot for a Randles cell is a semi-circle with two intercepts on the real axis in the high and low frequency regions. The former is the solution resistance and the latter is the sum of solution resistance and charge transfer resistance. The diameter of the circle is therefore the charge transfer resistance. The variation of impedance with frequency is also of interest. In a Bode plot,  $\log|Z|$  and  $\phi$  are both plotted against  $\log\omega$ .

The double layer capacitor in the Randles cell does not show an ideal capacitor behavior. Instead it acts like an electrical element with constant phase called constant phase element (CPE). Its impedance has the form

$$Z = A(j\omega)^{-\alpha} \quad (0.5 < \alpha \leq 1) \quad [2.28]$$

The electrochemical cell also has the contribution from diffusion of the electro-active species. Hence the equivalent circuit also includes the diffusion impedance. Its equivalent circuit element, Warburg impedance,  $Z_w$  is connected in series with the resistor representing the interfacial charge transfer,  $R_{ct}$ . The behaviour of Warburg impedance is midway between that of a resistor (0 degree phase shift) and a capacitor (90 degree phase shift) and hence has a 45 degree phase shift.

Therefore on the Nyquist plot the Warburg impedance appears as a diagonal slope of  $45^\circ$ . The Randle cell incorporating the Warburg impedance and its corresponding Nyquist plot are shown in Fig 2.17.

The measured impedance spectra can be modeled in a simplified equivalent circuit. The values of the resistance, capacitance and the diffusion element, can be determined from the complex nonlinear least squares (CNLS) fitting method, by fitting the impedance spectra to the equivalent circuit. The kinetic parameter exchange current density,  $i_0$  can be derived from the charge transfer resistance by the following equation

$$R_{ct} = \frac{RT}{nFi_o} \quad [2.29]$$

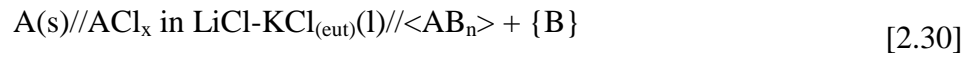
### 2.2.10 Open Circuit Potentiometry (OCP)

Open-circuit potentiometry is a suitable technique to estimate the equilibrium potential of the redox species, investigate the formation of intermetallic compounds in molten salt systems [15, 16]. To obtain the equilibrium potential of the redox couple  $A(x)/A$ , a thin film of the metal is formed on an inert electrode by depositing the metal at sufficient cathodic potential for a short period (30-300 sec). The polarization is stopped and the open-circuit potential is monitored as a function of time when no current flows. The electrode potential gradually shifts to more positive values and a potential plateau appears at the equilibrium potential of the redox couple  $A(x)/A$ . The potential shifts further towards anodic direction and stabilizes at the equilibrium potential of the inert electrode.

To study the formation of intermetallic compounds, the substrate material is used as the cathode. A thin film of the intermetallic compound is prepared on the substrate (which is a reactive cathode) by depositing the metal of interest at sufficient cathodic potential for a short period. The polarization is stopped and the open-circuit potential is monitored as a function of time at zero current. The deposited metal reacts with the substrate and diffuses into the bulk of the electrode. The electrode potential gradually shifts to more positive values evolving a series of potential plateaus as shown in Fig. 2.18. The potential plateaus appear when two phases are in equilibrium at the electrode surface. The potential shifts further towards anodic direction and stabilizes at the equilibrium potential of the substrate electrode.

Let us consider a system A-B where B is the substrate material (reactive cathode here). If we consider there are three intermetallic compounds in the system, then the

potential of the plateau 3 shown in the Fig 2.18, referred to the equilibrium potential of the metal electrode (A) is equivalent to the *emf* of the galvanic cell represented by



Where A is the metal electrode and the co-existing phases are, alloy rich in B saturated with A and the solid intermetallic compound  $AB_n$ .  $AB_n$  is the intermetallic compound most rich in B for the A-B system. The cell reaction can be written as



The *emf*,  $E$ , the partial molar free energy of A in the alloy and Gibbs free energy of formation of  $AB_n$  from solid A and pure liquid B are related by the following equations:

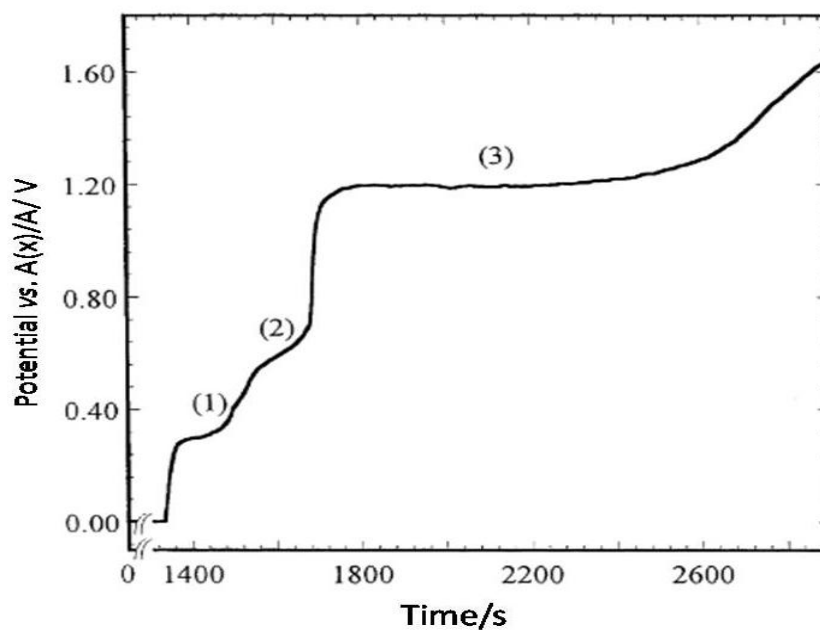


Fig. 2.18 Open circuit potential transient after polarizing the electrode at sufficient cathodic potential.

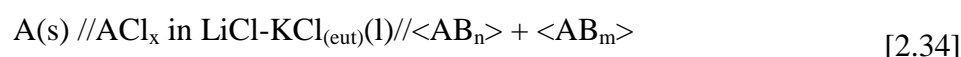
$$\bar{G}_A - G_A^0 = -zFE \quad [2.32]$$

and

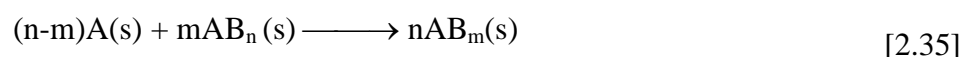
$$\Delta G_f^o(AB_n) = -zFE + nRT \ln a_B \quad [2.33]$$

From the potential measured from plateau 3 and assuming the solutions are ideal with respect to B, the Gibbs free energy of formation of  $AB_n$  can be derived.

The potential of the plateau 2, referred to the equilibrium potential of the metal electrode is equivalent to the emf of the cell represented by



The two phases that are coexisting corresponding to plateau 2 are the intermetallic compounds,  $AB_n$  and  $AB_m$ . The reaction for formation of the intermetallic compound  $AB_m$  can be written as



The Gibbs free energy of formation of the intermetallic compound  $AB_m$  can be calculated from the potential of plateau 2 and the Gibbs free energy of formation of the co-existing intermetallic compound,  $AB_n$  by using the following expressions.

$$-zFE = n\Delta G_f^0(AB_m) - m\Delta G_f^0(AB_n) \quad [2.36]$$

$$\Delta G_f^0(AB_m) = \frac{-zFE + m\Delta G_f^0(AB_n)}{n} \quad [2.37]$$

### 2.3 References

1. D. L. Maricle and D. N. Hume, J. Electrochem. Soc. 107 (1960) 354.
2. W. Davies, W. Gray, Talanta 11 (1964) 1203.
3. S. Vijayalakshmi, S. Annapoorani, R. Uma Maheswari, Theme Meeting on Recent trends in Analytical Chemistry-TRAC-2012, Aug. 30-31. Chennai, India, 2012.
4. A.J. Bard, L.R. Faulkner, Electrochemical Methods. Fundamentals and

- Applications, 2<sup>nd</sup> Edition, Wiley New York, 2001, Chapters 1, 5, 6.
5. Saylor, [URL:http://www.saylor.org/courses/chem108](http://www.saylor.org/courses/chem108)
  6. M. Noel, K.I. Vasu, Cyclic Voltammetry and the Frontiers of Electrochemistry, Oxford & IBH Publishing Co. Pvt. Ltd., New Delhi, 1990. Chapters 3-4.
  7. Z. Galus, Fundamentals of Electrochemical Analysis, Ellis Horwood, London, 1994.
  8. P. Delahay, J. Amer. Chem. Soc. 75 (1953) 1190.
  9. P. Delahay, New Instrumental Methods in Electrochemistry: Theory, Instrumentation and Application to Analytical and Physical Chemistry, Interscience, New York, 1954, Chapter 6.
  10. P. T. Kissinger and W. R. Heineman, Laboratory Techniques in Electroanalytical Chemistry, 2<sup>nd</sup> edition, Marcel Dekker, New York, 1996, p.101.
  11. J. Osteryoung and R. A. Osteryoung, Anal. Chem., 57 (1985) 101.
  12. L. Ramaley and M. S. Krasue, Anal. Chem. 41 (1969) 1362.
  13. J. Ross Macdonald, Impedance Spectroscopy: Emphasizing Solid Materials and Systems, John Wiley and Sons Inc., New York, 1980, p. 285.
  14. A. R. West, Solid State Chemistry, Wiley India, 2012, Chapter 13.
  15. Y. Castrillejo, M.R. Bermejo, E. Barrado, A.M. Martinez, Electrochim. Acta 51 (2006) 1941.
  16. P. Soucek, R. Malmbeck, E. Mendes, C. Nourry, D. Sedmidubsky, J. P. Glatz, J. Nucl. Mater. 394 (2009) 26.

## CHAPTER 3

### **Electrochemical behavior of La-, Nd- and U-trivalent ions in LiCl-KCl eutectic melt on inert tungsten electrode**

#### **3.1 Introduction**

As discussed earlier in chapter 1, during the electrorefining of spent metallic fuel, high pure uranium metal is deposited on the steel cathode. The chlorides of Pu, minor actinides (MA) and lanthanide fission products are more stable than  $UCl_3$ . During the recovery of uranium, the rare earth elements remain in the salt phase, plutonium and minor actinides are distributed between the salt phase and the alloy phase (spent fuel) in the anode basket. Later, plutonium and MA are recovered along with uranium metal on liquid cadmium cathode due to their lower activity in cadmium. Hence the knowledge of the electrochemical behavior and the thermochemical properties of these chlorides are essential for efficient separation.

In order to maximize the efficiency of the electrorefiner, it is necessary to understand the electrode kinetics of the actinide and fission product chlorides. Chauvin and Boisdé were the first to emphasize the importance of facile redox kinetics in combination with favorable thermodynamics to obtain high-purity uranium by the electrorefining process [1, 2]. The kinetics of the reaction play a vital role since a slow electrode kinetics would result in large overpotential and this could affect the purity of the uranium deposit.

Rare earth elements are among the major fission products formed during irradiation of fuel in a nuclear reactor. They are the most difficult elements to separate from actinides due to similar chemical properties. Therefore, one aims to study the electrochemical behavior and electrode kinetics of actinides and rare earth elements. Though the electrochemical behavior of actinide and lanthanide chlorides and their redox

potentials in LiCl-KCl on inert electrodes are reported in literature, we consider that measurements carried out under identical condition would provide more reliable data for our future work. In the present study we have investigated the electrochemical behavior of  $\text{LaCl}_3$ ,  $\text{NdCl}_3$  and  $\text{UCl}_3$  at inert W electrode in LiCl-KCl eutectic melt using transient electrochemical techniques. The electrode behavior of these chlorides and their redox potentials on inert electrode were evaluated.

Electrochemical transient techniques are powerful method to determine the thermodynamic properties in molten salt. In recent days electrochemical transient techniques are widely used to estimate the formal standard potential, Gibbs energy formation of chlorides, their activity coefficient etc [3-5]. In this study we have used cyclic voltammetry, chronopotentiometry, squarewave voltammetry, convolution voltammetry and open circuit chronopotentiometry to study the redox behavior, electrode kinetics and estimate the apparent standard electrode potentials,  $E_{\text{La(III)/La(0)}}^*$ ,  $E_{\text{Nd(III)/Nd(II)}}^*$ ,  $E_{\text{Nd(II)/Nd(0)}}^*$ ,  $E_{\text{Nd(III)/Nd(0)}}^*$ ,  $E_{\text{U(III)/U(0)}}^*$  and Gibbs energy formation of  $\text{LaCl}_3$  and  $\text{NdCl}_3$ .

### 3. 2. Literature survey

The redox potentials and thermodynamic properties of the actinides and lanthanides in molten salt media have been reported in the literature using both transient electrochemical methods and equilibrium potential measurement. The studies are of interest from the standpoint of the electrolytic separation of these elements.

#### *a. Electrochemical transient method*

Masset *et al.* had studied the electrochemical reduction of actinide (U, Pu, Np & Am) and lanthanide (La & Nd) chlorides at a tungsten working electrode in LiCl-KCl melt using cyclic voltammetry and chronopotentiometry [5]. They had derived the thermochemical data from their measurements. Castrillojo *et al.* had studied the stable

oxidation states of La, Ce, Nd and Y using cyclic voltammetry and derived the standard potentials of the redox couples in LiCl-KCl and CaCl<sub>2</sub>-NaCl molten salts and obtained the activity coefficient of the ions in these melts [4, 7]. The electroreduction of lanthanum trichloride at 773 K on a tungsten electrode, at low concentrations in LiCl-KCl and LiCl-KCl-NaCl eutectic was reported by Lantelme *et.al* [8]. Fukusawa *et al.* and Yamana *et al.* had studied the electrochemical and spectrophotometric behavior of neodymium in chloride media and studied its stable oxidation state [9, 10]. Yamamura *et al.* had studied the electrochemical behavior of the chlorides of La, Ce, Nd, Sm and Dy in LiCl-KCl and NaCl-KCl media and reported their reduction mechanism [11]. Taxil *et al.* have reported the reduction behavior of lanthanide ions (Ce, Gd, Sm and Nd) on molybdenum electrode and co-reduction of lanthanide ions along with aluminium ions on tantalum electrode in LiF-CaF<sub>2</sub> melt [12-13]. Novoselova *et al.* had studied the electrochemical behavior of NdCl<sub>3</sub> in LiCl-KCl-CsCl eutectic in the temperature range 573-943 K by cyclic voltammetry and linear sweep voltammetry. They had estimated the apparent standard redox potential of the Nd(III)/Nd(II) couple by direct potentiometric method [14]. Osipenko *et al.* had investigated the reduction mechanism of ytterbium (III) ions in fused NaCl-KCl-CsCl eutectic in the temperature range 723-1073 K [15]. Transient electrochemical techniques such as linear sweep, cyclic, semi-integral and square wave voltammetry and potentiometry at zero current were used to investigate the reduction mechanism and derive the standard potential, transport parameters and thermodynamics properties. Kuznetsov *et al.* had investigated the electroreduction of EuCl<sub>3</sub> in alkali chloride melts (NaCl-KCl, KCl, CsCl) in the temperature range 973-1173 K by different electrochemical methods [16]. The formal standard potentials  $E_{Eu(III)/Eu(II)}^*$ ,  $E_{Eu(III)/Eu(0)}^*$  were determined from open-circuit potentiometry and linear sweep voltammetry data.

Some thermodynamic properties relative to the formation of europium di- and trichloride in dilute solutions in alkali chloride melts were obtained.

A number of studies have been reported on the electrochemical behavior of uranium in chloride melts by transient electrochemical method. *Poa et al.* have studied the reduction of U(III) in LiCl–NaCl–CaCl<sub>2</sub>–BaCl<sub>2</sub> by cyclic voltammetry [17]. The reduction was determined to be a single step, three-electron transfer reversible process. *Serrano et al.* have investigated the reduction of U(III) in NaCl–KCl eutectic by cyclic voltammetry, chronopotentiometry and square wave voltammetry [18]. They observed that the reduction was a three-electron transfer, reversible process and found the reduction of adsorbed uranium to compete with metal deposition. *Shirai et al.* had studied the electrochemical behavior of actinide ions in LiCl–KCl eutectic and have made similar observations as *Serrano et al.* [19]. *Kuznetsov et al.* had studied the electrochemical behavior of UCl<sub>3</sub> and LaCl<sub>3</sub> in LiCl–KCl eutectic melt and derived the apparent standard potentials and separation coefficient of uranium from lanthanum [20]. The electrode kinetics of the reduction of UCl<sub>3</sub> was done using impedance spectroscopy. In our earlier work reported by *Reddy et al.*, we had investigated the reduction and oxidation processes of UCl<sub>3</sub> in molten LiCl–KCl eutectic on platinum and glassy carbon electrodes by cyclic voltammetry, chronopotentiometry and electrochemical impedance spectroscopy in the temperature range 660–780 K [21]. However we had not derived the standard potentials for the redox couples over a range of temperature and also had not carried out a detailed study on the electrode kinetics. *Masset et al.* had studied the electrochemical behavior of UCl<sub>4</sub> and UCl<sub>3</sub> in LiCl–KCl melt and derived the apparent standard potentials for the reduction for U(IV)/U(III) and U(III)/U(0) from cyclic voltammetry, their semi-integrals and chronopotentiometry [22].

*b. Equilibrium potential measurements*

Plembeck and co workers have measured the standard electrode potentials for a number of rare earths in LiCl-KCl melt at 773 K [23]. Fusselman *et al.* had reported standard electrode potential data for Y, La, Ce, Pr and Gd in molten LiCl-KCl in the temperature range 673-723 K by equilibrium potential measurements [24]. Hill *et al.* had measured the standard potential of U(III)/U(0) and U(IV)/U(III) couples in LiCl-KCl and MgCl<sub>2</sub>-NaCl-KCl eutectic [25]. Roy *et al.* had measured the equilibrium potentials of actinides (U, Np, Pu & Am) in LiCl-KCl melt [26]. They had obtained their standard electrode potentials and the thermodynamic properties of their chlorides. Sakamura *et al.* have estimated the standard potential of actinides (U, Pu, Np & Am) from galvanic cell emf method and used the data to study the separation of actinides from lanthanides [27]. The emf values of U(III)/ U(0) couple in NaCl-KCl eutectic were measured by Flengas [28]. Shirai *et al.* had obtained the standard electrode potential of U(III)/U(0) redox couple in LiCl-KCl melt by equilibrium measurement [29]. They had obtained the values as part of their studies on the electrode behavior of U(III) ion on cadmium and bismuth electrodes. The values were used to derive the Gibbs energy formation of the intermetallics of U-Cd and U-Bi Systems.

Though a number of data are available in the literature, there is disagreement in the values of the standard potentials reported due to different experimental conditions used. For instance, Masset *et al.* have done a critical review on the reported values of electrode potentials for U(III)/U(0) redox couple both by emf measurement and transient techniques [22]. They had derived a mean empirical equation from the literature values for the apparent standard potential,  $E_{U(III)/U(0)}^*$  and reported a scatter of  $\pm 35$  mV. In order to have our database with measurements carried out under identical conditions, we have investigated the electrochemical behavior of LaCl<sub>3</sub>, NdCl<sub>3</sub> and UCl<sub>3</sub> in this study using different electrochemical methods. The equilibrium potentials measured in this study

were used for the estimation of Gibbs energy formation of intermetallics formed between La, Nd and U with Cd, Al and Ga which are discussed in the chapters that follow. Also the electrode kinetics for the redox process for  $\text{LaCl}_3$  and  $\text{NdCl}_3$  are not much studied. In this paper we have reported a detailed elucidation on the electrode kinetics for the reduction of  $\text{LaCl}_3$ ,  $\text{NdCl}_3$  and  $\text{UCl}_3$  on W inert electrode.

### 3.3. Experimental

The purity of chemicals used is the same as discussed in Chapter 2. Purification of LiCl-KCl eutectic mixture, preparation of the electrolytes, LiCl-KCl- $\text{LaCl}_3$ , LiCl-KCl- $\text{NdCl}_3$  and LiCl-KCl- $\text{UCl}_3$  were as discussed in Chapter 2. The electrochemical cell used for the studies, experimental procedures and instrumentation were as discussed in Chapter 2. The working electrode used for the studies was the inert W electrode. The counter and reference electrodes are the same as discussed in Chapter 2. Cyclic voltammograms were obtained using the electrolytes, LiCl-KCl- $\text{LaCl}_3$ , LiCl-KCl- $\text{NdCl}_3$  and LiCl-KCl- $\text{UCl}_3$  at different polarization rates in the temperature range 698- 798 K. Open circuit chronopotentiograms were obtained using the electrolytes, LiCl-KCl- $\text{LaCl}_3$ , LiCl-KCl- $\text{NdCl}_3$  and LiCl-KCl- $\text{UCl}_3$  for different cathodic polarization for short duration (30-300 s). Chronopotentiograms were recorded for different current densities and square wave voltammograms were recorded for different pulse frequencies at pulse amplitude of 10 mV using LiCl-KCl- $\text{LaCl}_3$  and LiCl-KCl- $\text{NdCl}_3$  at different temperatures. The electrochemical impedance spectrum was recorded at 798 K for LiCl-KCl- $\text{LaCl}_3$  melt at the rest potential -0.25 V in the frequency range 1Hz to 1 MHz with applied amplitude of 10mV on the W working electrode.

### 3.4 Results and Discussion

#### 3.4.1 Analysis of the cyclic voltammograms

##### 3.4.1.1. Redox behavior of $\text{LaCl}_3$

The cyclic voltammogram obtained at the W working electrode in molten salt containing  $1.64 \times 10^{-4} \text{ mol cm}^{-3}$   $\text{LaCl}_3$  in LiCl-KCl eutectic melt at 773 K is shown in Fig. 3.1. Reduction of  $\text{LaCl}_3$  was found to take place in a single step. The cathodic peak,  $I_c$  and the associated anodic peak,  $I_a$  are characteristic of a soluble-insoluble exchange. Peak  $I_c$  lies close to -1.95 V and this potential is in agreement with that reported by Plembeck and co-workers [23] for La(III) /La(0) couple. Hence peak  $I_c$  in Fig. 3.1 corresponds to the reduction of La(III) to La metal and the corresponding anodic peak  $I_a$  to the dissolution of La metal that had been deposited during the cathodic sweep. The electrode reaction for reduction of La(III) ion at W electrode is



An electrochemical reaction is considered to follow a reversible exchange when the electron transfer is fast and the rate of the reaction is controlled by mass transfer by diffusion. An electrochemical reaction is considered to follow an irreversible exchange, when the electron transfer is not facile and the rate of the reaction is controlled by the electrode kinetics. An electrochemical reaction is considered to follow quasi-reversible exchange, when both the mass transfer and electrode kinetics compete for the control of the rate of the electrode reaction.

Cyclic voltammograms recorded in LiCl-KCl eutectic melt containing  $\text{LaCl}_3$  ( $7.54 \times 10^{-5} \text{ mol cm}^{-3}$ ) at 798 K at different scan rates are shown in Fig. 3.2. We had investigated the dependence of the peak potential and peak current on the polarization rates for the reduction process. Eq. 3.2 gives the relationship among the peak potential ( $E_p$ ), the half peak potential ( $E_{p/2}$ ) and the number of electrons transferred ( $n$ ) for a reversible electrochemical reaction involving soluble-insoluble species [30]:

$$E_p - E_{p/2} = -0.77 \frac{RT}{nF} \quad (3.2)$$

For a reversible electrochemical process, the peak potential,  $E_p$  and the magnitude of the peak width,  $E_p - E_{p/2}$ , remain the same for all scan rates. It was observed that the cathodic peak potential shifted to more cathodic values at higher scan rates as seen in the inset of Fig. 3.2. Also the magnitude of  $E_p - E_{p/2}$  increased with increase in scan rates and it is much larger than that expected for a reversible process. The value of  $n$  estimated using Eq. 3.2 is much less than the expected value 3. Table 3.1 shows the cathodic peak analysis at various scan rates and temperatures.

As mentioned earlier, the cathodic peak potential shifted to more cathodic values at higher scan rates. However we did not observe a gradual shift in the peak potentials within the scan interval studied. Eq. 3.3 is applicable for an electrochemical reaction considered to follow irreversible exchange i.e. reactions which are controlled by charge transfer [31]

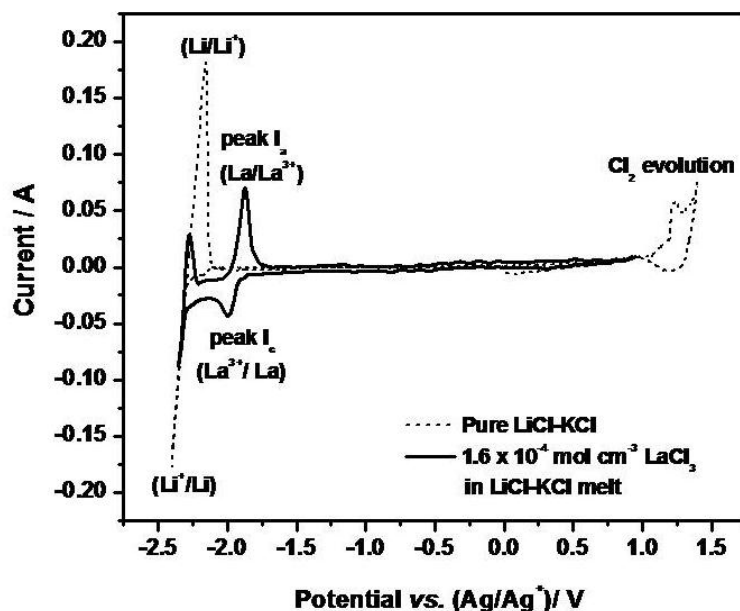


Fig. 3.1 A comparison of the cyclic voltammogram for pure LiCl–KCl melt and LiCl–KCl–LaCl<sub>3</sub> melt. Working electrode: tungsten, apparent electrode area: 0.301 cm<sup>2</sup>. Temperature: 773 K, scan rate: 0.1 V s<sup>-1</sup>.

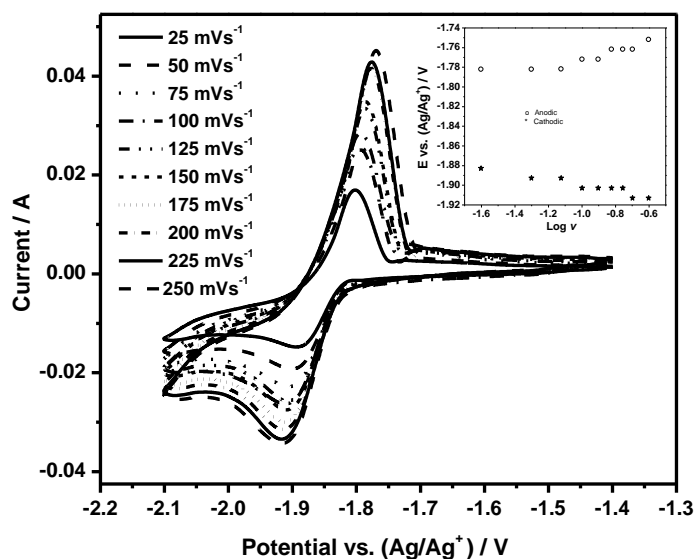


Fig. 3.2 Cyclic voltammograms for  $7.54 \times 10^{-5} \text{ mol cm}^{-3}$   $\text{LaCl}_3$  in  $\text{LiCl-KCl}$  melt for a W electrode at various scan rates. Apparent electrode area:  $0.347 \text{ cm}^2$ . Temperature: 798 K. Inset: variation of peak potential with logarithm of sweep rate.

$$E_p - E_{p/2} = -1.857 \frac{RT}{\alpha n_\alpha F} \quad (3.3)$$

where ' $\alpha$ ' is the charge transfer coefficient and  $n_\alpha$  is the number of electrons transferred in the rate determining step. The value of ' $\alpha n_\alpha$ ' calculated using Eq. 3.3 is shown in Table 3.1. It may be noted that the values obtained are not consistent and the values do not have any significance for scan rates between 25 and 150  $\text{mVs}^{-1}$ , since the value of ' $\alpha$ ' is more than 1 in this scan range. The value of ' $\alpha$ ' should lie between 0 and 1 for any electrochemical process. The observations suggest that the electrode process is not totally irreversible. It is necessary to estimate the value of ' $\alpha$ ' to evaluate the reversibility of the electrode process. Eq. 3.4 was used for estimating the charge transfer coefficient, since it incorporates the variation of cathodic peak potential for a range of scan rates [32-33].

$$\frac{\Delta E_p}{\Delta \log v} = \frac{2.303RT}{2\alpha n_\alpha F} \quad (3.4)$$

The value of ' $\alpha n_\alpha$ ' was obtained from the slope of the plot of  $E_p$  vs.  $\log v$  for scan rates 75, 150 and 200  $\text{mVs}^{-1}$  at 798 K and was found to be 1.77. Considering the value of  $n$  to be 3, the value of ' $\alpha$ ' is 0.59. A detailed analysis on the reversibility of the reduction process is done in section 3.4.2.1.

### 3.4.1.2. Redox behavior of $\text{NdCl}_3$

Cyclic voltammograms were recorded using tungsten as working electrode in molten LiCl-KCl mixture containing  $\text{NdCl}_3$ , ( $6.66 \times 10^{-5} \text{ mol cm}^{-3}$ ) in the temperature range 723-798 K. Cyclic voltammograms at 723 K for different scan rates are shown in Fig. 3.3. It may be seen that there are two peaks in the cathodic cycle and two corresponding peaks in the anodic cycle. Castrillejo *et al.*, Masset *et al.* and Fukusawa *et al.* have also made similar observation in their studies involving the redox behavior of  $\text{NdCl}_3$  in chloride media at inert electrode [4, 5, 9]. They had deduced that the reduction of Nd(III) ion to Nd metal takes place in two steps with the formation of Nd(II) ion in the intermediate step. We have carried out a detailed analysis of the voltammograms to elucidate the redox behavior of  $\text{NdCl}_3$  in LiCl-KCl.

#### a. Analysis of peak I

Cyclic voltammograms were obtained by switching the potential before peak  $\text{II}_c$  appeared as shown in Fig. 3.4. It may be observed that peak  $\text{I}_a$  is the corresponding anodic peak for peak  $\text{I}_c$ . The shape of the voltammogram for the redox couple  $\text{I}_c$  and  $\text{I}_a$  resemble closely those of reversible soluble-soluble system. Fig. 3.5 (a) shows the plot of the cathodic peak potentials,  $E_{p\text{I}_c}$ , as a function of logarithm of the scan rates at 723 and 798 K. The peak potentials do not vary appreciably in the scan rate range 10 - 200  $\text{mVs}^{-1}$  indicating that the electrode process is facile. For a reversible electrochemical process

Table 3.1 Cathodic peak analysis of La(III)/La couple at various scan rates and temperatures. Concentration of  $\text{LaCl}_3$  :  $7.54 \text{ moles cm}^{-3}$ .

Scan rate, $\text{Vs}^{-1}$	Temperature, K	Cathodic peak potential, $E_{p,c}$ , V	$E_p - E_{p/2}$ , V	n value using Eq. 3.2	$\alpha n_\alpha$ using Eq. 3.3
0.025	798	-1.883	0.033	1.61	3.88
0.050		-1.893	0.040	1.33	3.22
0.075		-1.893	0.036	1.47	3.55
0.100		-1.903	0.042	1.24	3.01
0.125		-1.903	0.044	1.21	2.92
0.150		-1.903	0.042	1.24	2.99
0.175		-0.903	0.041	1.29	3.13
0.200		-1.913	0.049	1.062	2.56
0.250		-1.913	0.049	1.08	2.59
0.025	773	-1.943	0.034	1.49	3.61
0.050		-1.943	0.031	1.63	3.92
0.075		-1.953	0.041	1.26	3.05
0.100		-1.953	0.033	1.53	3.68
0.125		-1.953	0.035	1.44	3.47
0.150		-1.953	0.035	1.44	3.48
0.175		-1.963	0.045	1.14	2.74
0.200		-1.963	0.043	1.18	2.85
0.250		-1.963	0.041	1.24	2.98
0.025	748	-1.953	0.022	2.26	5.46
0.050		-1.953	0.029	1.71	4.12
0.075		-1.953	0.036	1.36	3.27
0.100		-1.973	0.050	0.99	2.38
0.125		-1.983	0.054	0.92	2.22
0.150		-1.983	0.047	1.04	2.51
0.175		-1.993	0.062	0.81	1.94
0.200		-1.993	0.058	0.95	2.31
0.250		-2.003	0.066	0.74	1.79
0.025	723	-1.973	0.033	1.44	3.47
0.030		-1.973	0.030	1.59	3.63
0.040		-1.973	0.028	1.71	4.13
0.050		-1.973	0.029	1.66	4.01
0.060		-1.983	0.032	1.47	3.55
0.075		-1.983	0.035	1.36	3.29
0.100		-1.983	0.033	1.44	3.46
0.125		-1.993	0.041	1.16	2.80
0.150		-1.993	0.039	1.22	2.93

involving soluble-soluble species, the anodic and cathodic peak potentials and the number of electron transferred are related as [34]

$$E_p^A - E_p^C = 2.22 \frac{RT}{nF} \quad (3.5)$$

Value of  $n$  estimated using the Eq. 3.5 is close to 1 suggesting that peak  $I_c$  and  $I_a$  correspond to the redox couple Nd(III)/Nd(II).

*b. Analysis of peak II*

The shapes of peak II in Fig. 3.3 during the cathodic and anodic cycles are suggestive of soluble-insoluble couple, Nd(II)/Nd(0). The value of  $n$  estimated from the cathodic peak  $II_c$  using Eq. 3.2 was not about 2 for all scan rates which is expected for the reduction, Nd(II)/Nd(0) [22, 30]. The value of  $n$  was about 1.7 for scan range 10 - 30 mVs<sup>-1</sup>.

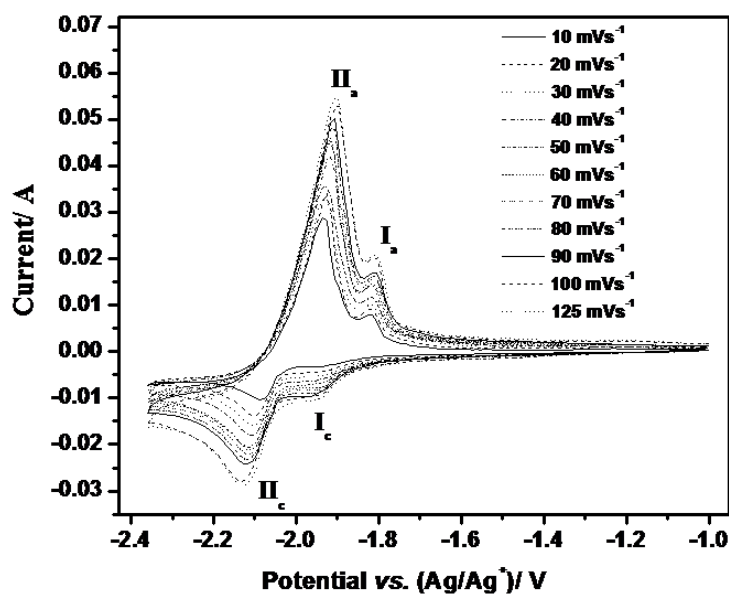


Fig. 3.3 Cyclic voltammograms of LiCl-KCl-NdCl<sub>3</sub> melt on W electrode for different scan rates. Temperature: 723 K; Concentration of NdCl<sub>3</sub>: 6.66 x 10<sup>-5</sup> mol cm<sup>-3</sup>; Electrode area: 0.49 cm<sup>2</sup>.

It was found that the peak width,  $E_p - E_{p/2}$  increased with increase in scan rate. Also the ratio of anodic peak current ( $i_{pIIa}$ ) to cathodic peak current ( $i_{pIIC}$ ) is greater than 1 for all scan rates. Fig. 3.5 (b) shows the plot of the cathodic peak potentials,  $E_{pIIC}$ , as a function of logarithm of the scan rates at 723 and 798 K. It was observed that the peak potential varies with increasing scan rate. These observations suggest that the reduction of Nd(II) ion to Nd metal on W electrode does not involve a perfect reversible exchange with the rate of reduction controlled by mass transfer for all scan rates. The reduction of Nd(II)/Nd(0) at the electrode was influenced by the charge transfer process also. Eq. 3.3 which is applicable for an irreversible electrochemical process was used for the peak analysis. It was observed that the values of ' $\alpha n_a$ ' obtained from Eq. 3.3 at various scan rates and at different temperatures ranged between 2.4 to 3.6 and did not have any significant meaning for an electrode reaction

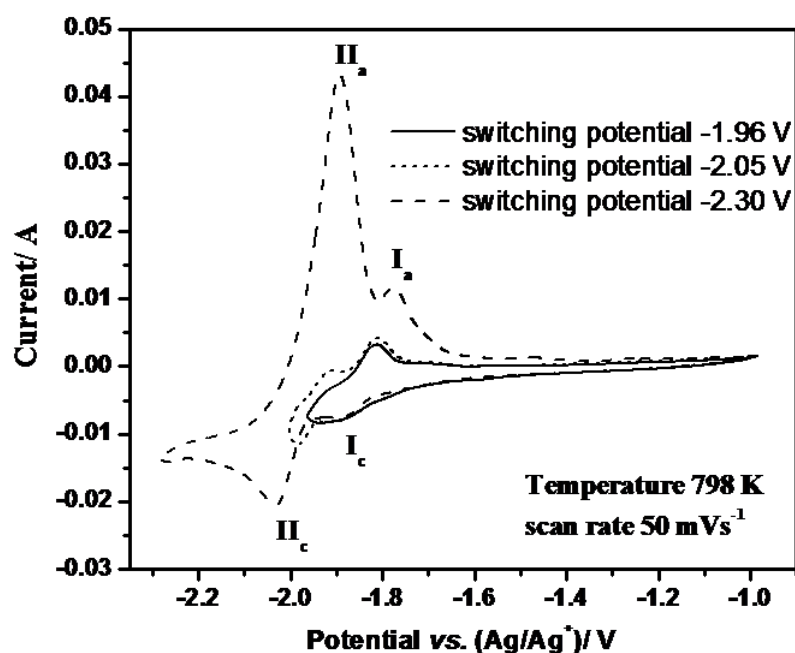


Fig. 3.4 Cyclic voltammograms of LiCl-KCl-NdCl<sub>3</sub> melt on W electrode obtained at different switching potentials.

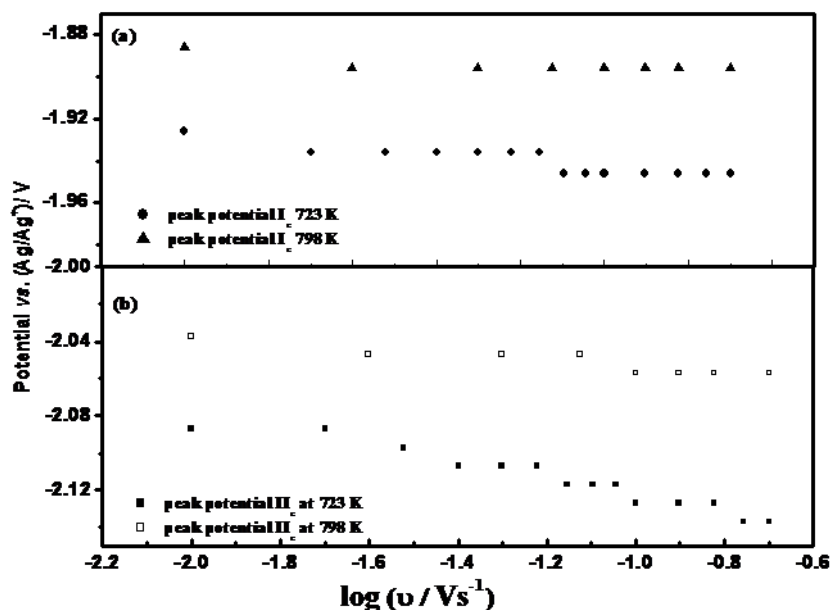


Fig. 3.5 Plot of the cathodic peak potentials as a function of logarithm of the scan rates at 723 and 798 K.

with two electron transfer. This fact suggests that the reduction of Nd(II)/Nd(0) is not controlled by the charge transfer process alone. Hence we had carried out a detailed study on the electrode kinetics from the convoluted curves obtained from semi-integration of the cyclic voltammetry data and the results are discussed in section 3.4.2.2.

### 3.4.1.3. Redox behavior of $\text{UCl}_3$

Cyclic voltammogram recorded for LiCl-KCl- $\text{UCl}_3$  melt (concentration of  $\text{UCl}_3$ :  $6.36 \times 10^{-5} \text{ mol.cm}^{-3}$ ) at tungsten is shown in Fig. 3.6. Three redox couples were found in the potential window studied. A detailed analysis of the peaks in the voltammograms was carried out in our earlier work [21]. It was found that peak  $\text{I}_c$  corresponds to the reduction of U(III) ion to uranium metal in a single step with three electron transfer. The pre-peak,  $\text{II}_c$ , corresponds to reduction of monolayer U(III) ion adsorbed on the W surface to sub-

chloride of uranium. Peak current for the reduction of monolayer U(III) ion did not increase with increase in concentration of  $\text{UCl}_3$  in the melt. At higher concentrations, the pre-peak was negligible compared to peak  $I_c$  which was attributed to reduction of the U(III) ion that arrived at the electrode surface by diffusion from the bulk. From the peak positions, peak width and peak current for peak  $I_c$  at different scan rates, it was concluded that the reduction of  $\text{UCl}_3$  at the electrode surface was predominantly controlled by diffusion at lower scan rates as observed in case of La(III)/La(0) and Nd(II)/Nd(0).

Peak  $\text{III}_c$  was attributed to the reduction of U(IV) ion (which was formed in the anodic cycle) to U(III) ion. Similar observations were made by other authors also [18, 19, 22]. In the present work we are not discussing the peak analysis in detail as it had been discussed in our previous paper [21] and in the literature. The reduction of U(III) ion to U(0) was reported to follow quasi-reversible behavior in our earlier work. However a

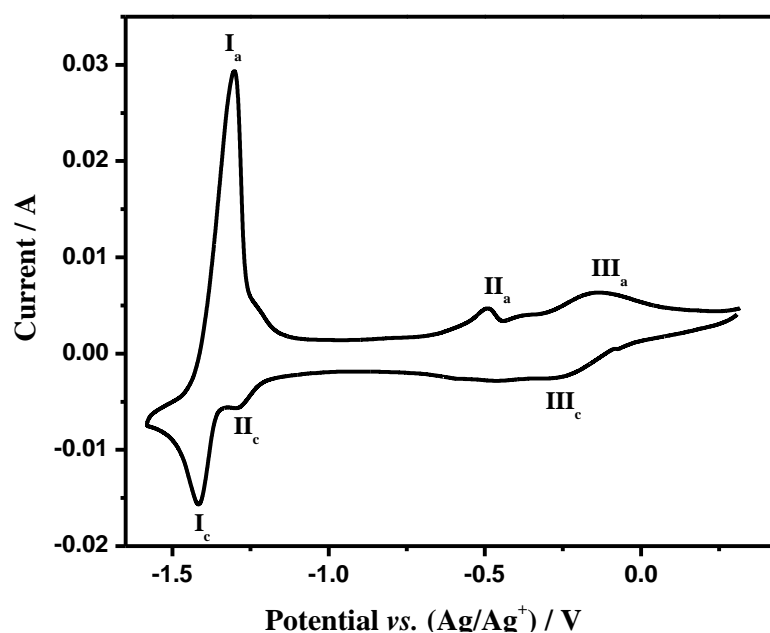


Fig. 3.6 Cyclic voltammogram of LiCl-KCl- $\text{UCl}_3$  at 748 K; Concentration of  $\text{UCl}_3$ :  $7.31 \times 10^{-5} \text{ mol cm}^{-3}$ ; Working electrode: W.

detailed study on the electrode kinetics was not done earlier. In this study cyclic voltammograms were recorded at W electrode in the potential window -0.7 to -1.7 V for higher concentration of  $\text{UCl}_3$  in LiCl-KCl (concentration of  $\text{UCl}_3$ :  $1.45 \times 10^{-4} \text{ mol cm}^{-3}$ ). In this work, a detailed study on the electrode kinetics for the reduction of U(III) ion to U metal by convolution method has been carried out and the results are discussed in section 3.4.2.3.

### 3.4.2. Kinetic study of the electrode reaction- Reversibility study

Semi-integral of the cyclic voltammograms give the convoluted curves, a form resembling a steady-state voltammetric curve which may be given by the Eq. 3.6 [35, 36]

$$m(t) = \left[ \frac{d^{-1/2} I(t)}{dt^{-1/2}} \right] = \frac{1}{\sqrt{\pi}} \int_0^t \frac{i(\tau)}{t-\tau} d\tau \quad (3.6)$$

where  $i(\tau)$  is the current measured at the time  $\tau$  of the  $I(t)$  transients. A potential plateau,  $m^*$ , occurs in the region of cathodic peak potentials which indicates that the rate transfer is limited by diffusion. The forward and backward waves of the convoluted curve superimpose for an electrode reaction that is controlled by diffusion.

#### 3.4.2.1. Behavior of $\text{LaCl}_3$

Fig. 3.7 shows the convoluted curves obtained for LiCl-KCl- $\text{LaCl}_3$  melt. It may be observed that the cathodic and anodic waves more or less superimpose with some hysteresis. The hysteresis could be attributed to the non-reversibility of the electrode process or the existence of nucleation overpotential or a combination of both. However the occurrence of the plateau suggests that the rate of electron transfer is controlled mostly by diffusion.

For a reversible charge transfer process, the convoluted curve should obey the relation given by Equation 3.7 [37]

$$E = E_{\text{La(III)/La(0)}}^0 + \frac{RT}{nF} \ln \frac{a_{\text{LaCl}_3}}{a_{\text{La(0)}}} + \frac{RT}{nF} \ln \left( \frac{m^* - m}{m^*} \right) \quad (3.7)$$

where  $E_{\text{La(III)/La(0)}}^0$  is the standard potential of the La(III)/La(0) redox couple,  $a_{\text{LaCl}_3}$  and  $a_{\text{La(0)}}$  are the activities of  $\text{LaCl}_3$  and pure lanthanum metal, respectively,  $m$  is the semi-integral of the current density and  $m^*$  the cathodic limiting value of these functions. The plot of  $E$  vs.  $\ln((m^* - m)/m^*)$  was a straight line as seen in Fig. 3.8 and slope of the plot corresponds to three electron transfer. The convoluted curves obtained at various scan rates appeared similar. However, we observed that the plot  $E$  vs.  $\ln((m^* - m)/m^*)$  corresponding to convoluted curves obtained at  $25 \text{ mVs}^{-1}$  and  $50 \text{ mVs}^{-1}$  alone yielded a slope close to that corresponding to three electron transfer.

Though there was no indication of large overpotential from the cyclic voltammograms and convoluted curves such as cross over in the cathodic branch, the cathodic peak potential was found to shift cathodically with increasing scan rates and the peak potential difference,  $E_p - E_{p/2}$  increased with increasing scan rates. It is necessary to evaluate the kinetic parameter- the heterogeneous rate constant,  $k_s$ , of the electrode reaction in order to determine the scan rates at which the reduction showed reversible, quasi-reversible and irreversible behavior. The following relationship is valid for a quasi-reversible exchange with formation of an insoluble product [7, 38].

$$E = E^0 + 2.3 \frac{RT}{\alpha n_\alpha F} \log k_s + 2.3 \frac{RT}{\alpha n_\alpha F} \log B \quad (3.8)$$

$$B = \frac{(m^* - m)D^{-1/2} + nFA \exp\left[\left(\frac{nF}{RT}\right)(E - E^0)\right]}{I} \quad (3.9)$$

where  $k_s$  and  $\alpha$  are the charge-transfer rate constant and the transfer coefficient, respectively, Plots of  $E$  vs.  $\log B$  were obtained for polarization rates 75, 100, 125 and  $150 \text{ mV s}^{-1}$  using values of  $m$  from 10% to 90% of  $m^*$  and they were found to be linear. The value of apparent standard potential calculated in section 3.3.5.1 was used for  $E^0$ . The transfer coefficient,  $\alpha$ , was obtained from the slope and the charge-transfer rate constant,

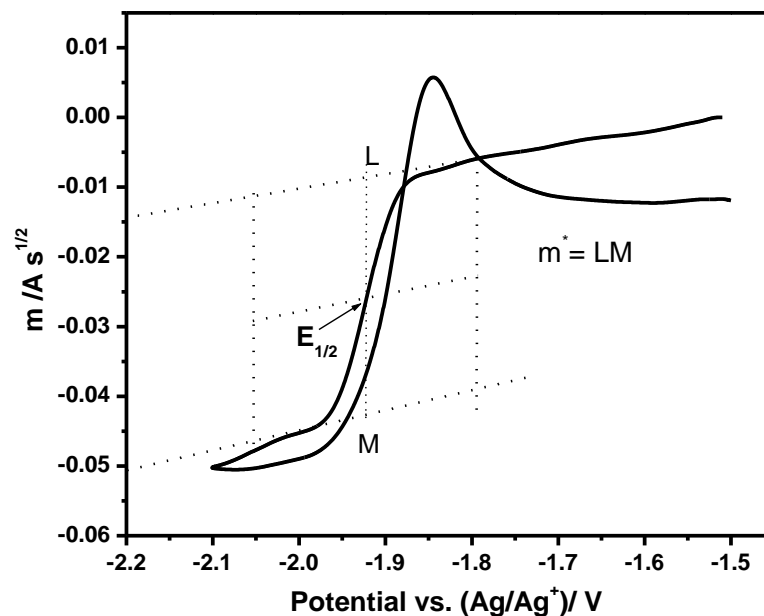


Fig. 3.7 Semi-integral curves of the voltammogram corresponding to La(III)/La(0) at tungsten electrode in LiCl–KCl melt. Concentration of  $\text{LaCl}_3$ :  $7.54 \times 10^{-5} \text{ mol cm}^{-3}$ , temperature: 798 K, scan rate:  $0.025 \text{ V s}^{-1}$ .

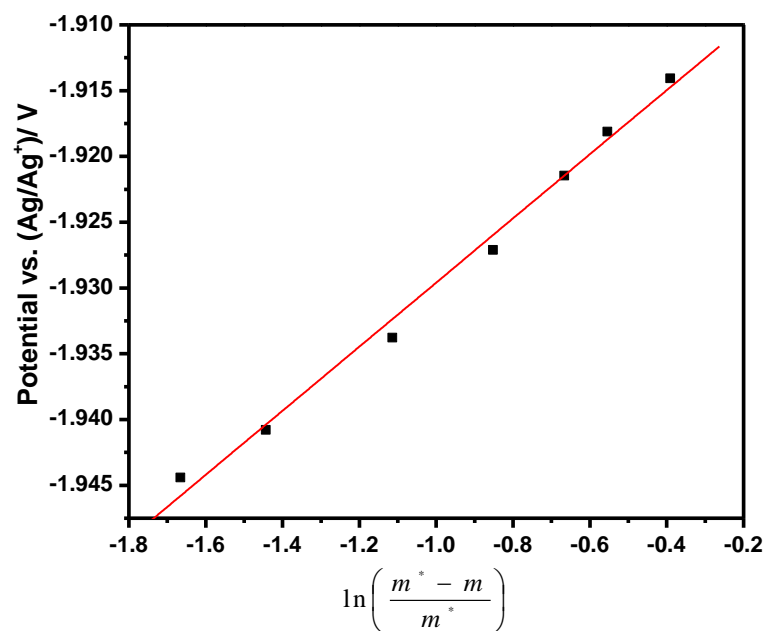


Fig. 3.8 Logarithmic analysis of the convoluted data for  $\text{LaCl}_3$  in LiCl–KCl melt at a tungsten electrode. Polarization rate:  $25 \text{ mV s}^{-1}$ ; apparent electrode area:  $0.347 \text{ cm}^2$ ; temperature: 798 K. Concentration of  $\text{LaCl}_3$ :  $7.54 \times 10^{-5} \text{ mol cm}^{-3}$ .

$k_s$ , was obtained from the intercept. The results are shown in Table 2 and the average value of ' $\alpha$ ' and  $k_s$  were found to be  $0.71 \pm 0.09$  and  $4.1 \pm 0.6 \times 10^{-6} \text{ cm s}^{-1}$  respectively at 798 K. However we did not observe a linear trend for the plots of  $E$  vs.  $\log B$  for scan rates 25 and 50  $\text{mVs}^{-1}$  which indicates that the reduction  $\text{La(III)/La(0)}$  showed reversible behavior for low polarization rates.

Electrochemical impedance spectroscopy is a suitable method for the estimation of heterogeneous rate constant. In order to validate the value of  $k_s$  obtained by convolution technique, we had studied the electrode kinetics using impedance spectroscopy. The electrochemical impedance spectrum was recorded at 798 K for  $7.54 \times 10^{-5} \text{ mol cm}^{-3}$   $\text{LaCl}_3$  in  $\text{LiCl-KCl}$  melt at the rest potential  $-0.25 \text{ V}$  in the frequency range 1 Hz to 1 MHz with an applied amplitude of 10 mV on the W working electrode. The impedance data between 100 Hz to 50 kHz were fitted into an equivalent circuit containing a general diffusion related element, known as Warburg impedance ( $W$ ), a resistor element ( $R1$ ), corresponding to the electrolyte resistance, another resistor element ( $R2$ ) corresponding to the charge transfer resistance and the diffuse double layer capacitance ( $C$ ). This circuit, called the Randles cell was used to simulate the impedance data [39]. The measured and simulated impedance data are shown in Fig. 3.9. It is observed that the complex impedance diagram consists of two parts, one a capacitance loop in the higher frequency region which corresponds to the electrochemical charge transfer at the electrode/electrolyte interface and a straight line with a slope of about  $45^\circ$  in the lower frequency attributed to the diffusion of the  $\text{La(III)}$  ions. The resistance of the molten salt electrolyte was found to be  $0.72 \Omega$ . The charge transfer resistance, Warburg impedance and the capacitance values were  $0.78 \Omega$ ,  $0.016$  and  $20.77 \mu\text{F}$ , respectively. The conceived Randles cell is able to

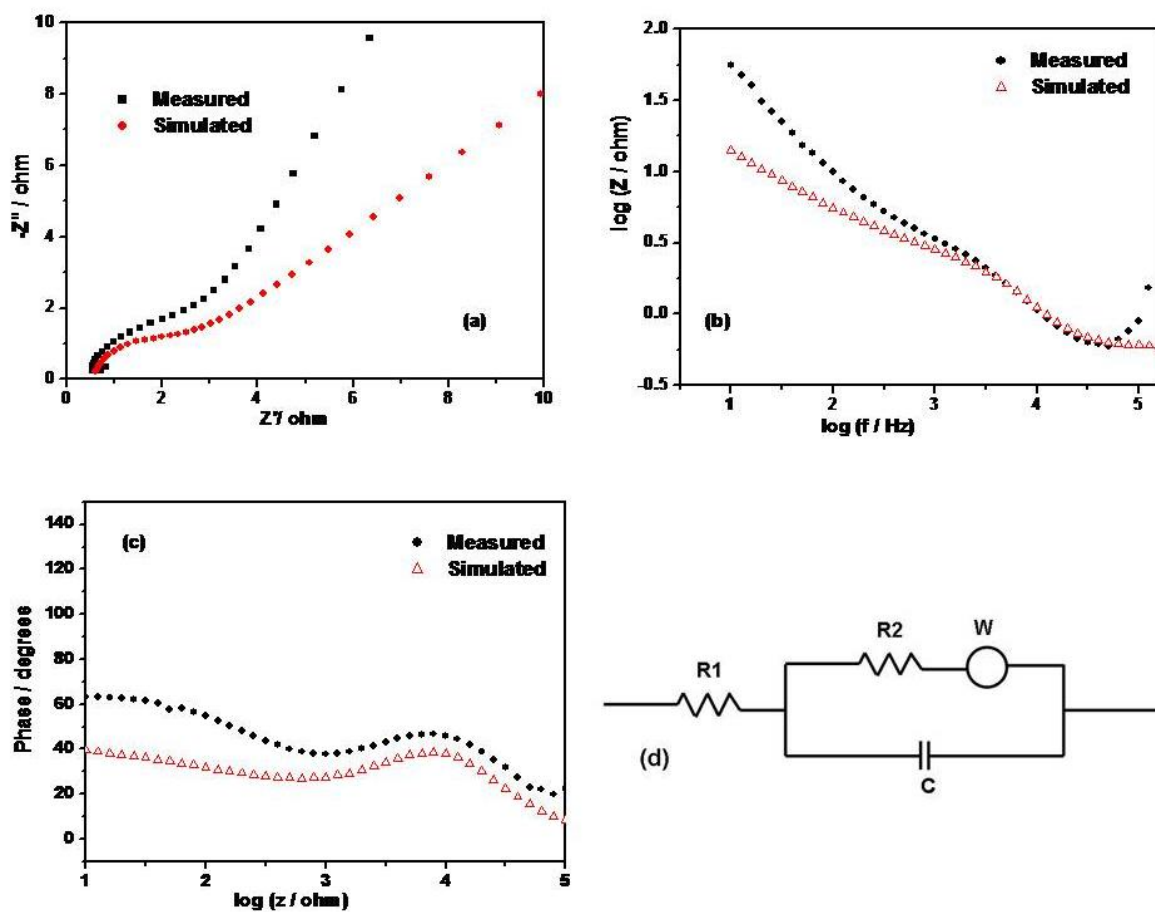


Fig. 3.9 Complex impedance spectra for  $7.54 \times 10^{-5} \text{ mol cm}^{-3}$   $\text{LaCl}_3$  in  $\text{LiCl-KCl}$  melt at 793 K for a W working electrode at rest potential ( $-0.25 \text{ V}$  vs.  $\text{Ag(I)/Ag}$ ). (a) Nyquist plot; (b and c) Bode plots; (d) corresponding equivalent circuit.

simulate the measured data fairly well. The charge transfer resistance,  $R_{CT}$  at the rest potential is given by the following equation [39, 20]:

$$R_{CT} = \frac{RT}{nFi_o} = \frac{RT}{n^2 F^2 k_s C_{La(III)}^{1-\alpha}} \quad (3.10)$$

where  $i_o$  is the exchange current density. This expression allows us to calculate the rate constant of charge transfer. The value of the rate constant  $k_s$  was estimated to be  $5.05 \times 10^{-6} \text{ cm s}^{-1}$ . It may be noted that the value of  $k_s$  depends largely on the value of ' $\alpha$ '. The value of ' $\alpha$ ' used was that obtained from the slope of the plot of  $E_p$  vs.  $\log \nu$  for scan rates 75, 150 and 200  $\text{mVs}^{-1}$  according to Eq. 3.4. The value of  $k_s$  obtained from impedance spectroscopy was found to be close to that obtained from convolution technique as shown in Table 2.

According to Matsuda and Ayabe, the following criteria is applicable for an electrochemical process [31].

For Reversible (Nernstian) process:

$$\frac{k_s}{(Dn\nu F/RT)^{1/2}} \geq 15 \quad (3.11)$$

For Quasi-reversible process:

$$10^{-2(1+\alpha)} < \frac{k_s}{(Dn\nu F/RT)^{1/2}} < 15 \quad (3.12)$$

Totally irreversible process:

$$\frac{k_s}{(Dn\nu F/RT)^{1/2}} \leq 10^{-2(1+\alpha)} \quad (3.13)$$

The following observations were made for  $7.54 \times 10^{-5} \text{ mol cm}^{-3}$   $\text{LaCl}_3$  in  $\text{LiCl-KCl}$  melt at 798 K at various scan rates using the value of 0.71 for  $\alpha$  and  $4.1 \times 10^{-6} \text{ cm s}^{-1}$  for  $k_s$  as obtained from the convoluted curves:

$k_s < 5.31 \times 10^{-6}$  for scan rate  $250 \text{ mVs}^{-1}$

Table 3.2 Kinetic parameters of La(III)/La(0) exchange at 798 K.

Technique	Scan rate (Vs <sup>-1</sup> )	$\alpha$	$k_s (x 10^6 \text{ cms}^{-1})$
Convolution	0.075	0.68	2.5
	0.100	0.79	6.2
	0.125	0.77	1.9
	0.150	0.60	5.9
<i>Impedance spectroscopy</i>			5.05

$k_s < 4.75 \times 10^{-6}$  for scan rate 175 mVs<sup>-1</sup>

$3.9 \times 10^{-6} < k_s < 0.16$  for scan rate 150 mVs<sup>-1</sup>

$3.36 \times 10^{-6} < k_s < 0.13$  for scan rate 100 mVs<sup>-1</sup>

$2.91 \times 10^{-6} < k_s < 0.12$  for scan rate 75 mVs<sup>-1</sup>

Hence it may be concluded that the reduction of La(III) ion on W electrode shows quasi-reversible behavior for scan rates up to 150 mVs<sup>-1</sup> and irreversible behavior for scan rates higher than this. The reduction of La(III) ion is predominantly controlled by charge transfer for scan rates higher than 75 mVs<sup>-1</sup>.

#### 3.4.2.2 Behavior of NdCl<sub>3</sub>

Fig. 3.10 shows the convoluted curves obtained for LiCl-KCl-NdCl<sub>3</sub> melt. Curve c of Fig 3.10 shows the convoluted curve for the voltammogram obtained by switching the potential before appearance of peak II<sub>c</sub>. It may be observed that the forward and backward waves more or less superimpose indicating that the electrode process for Nd(III)/Nd(II) may be considered as reversible [40]. Curve b of Fig.4 shows the convoluted curve for the cyclic voltammogram involving both the redox couples. A potential plateau appears about the cathodic peak potential for Nd(II)/Nd(0). However, there is some hysteresis between the cathodic and the anodic cycles. The hysteresis could be attributed to the non-

reversibility of the electrode process and indicates that the rate of the reduction is not limited by diffusion of Nd(II) ions alone.

The behavior of Nd(II)/Nd(0) on W cathode is similar to our observation for La(III)/La(0). Analysis of the convoluted data in the region corresponding to reduction of Nd(II)/Nd(0) showed that the reduction followed the quasi-reversible hypothesis in the scan range 75-250 mVs<sup>-1</sup> as per Eq. 3.8 and 3.9. Plots of E vs. log B were obtained for polarization rates 75, 100, 200 and 250 mV s<sup>-1</sup> using values of m from 10% to 90% of m\* and they were found to be linear. The half wave potential, E<sub>1/2</sub>, is considered close to the standard potential, E<sup>0</sup>. The half wave potential seen in Fig. 3.10 was obtained graphically from the convoluted curves as described by Goto *et al.* [41] and as discussed above for LaCl<sub>3</sub>. The value of E<sub>1/2</sub> thus obtained was used for E<sup>0</sup> in Eq. 3.8. The transfer coefficient, α, was obtained from the slope and the charge-transfer rate constant, k<sub>s</sub>, was obtained from the intercept. The average value of 'αn<sub>α</sub>' was found to be 1.78 ± 0.1 and this value was used for calculation of the charge-transfer rate constant, k<sub>s</sub>. The results are shown in Table 3.3. However, the value of 'αn<sub>α</sub>' obtained from the slope of the plots of E vs. log B for scan rates 25 and 50 mVs<sup>-1</sup> were above 2 and did not have any significance for a two electron transfer process. So we consider that the redox couple did not show quasi-reversible behavior for scan rates below 50 mVs<sup>-1</sup>.

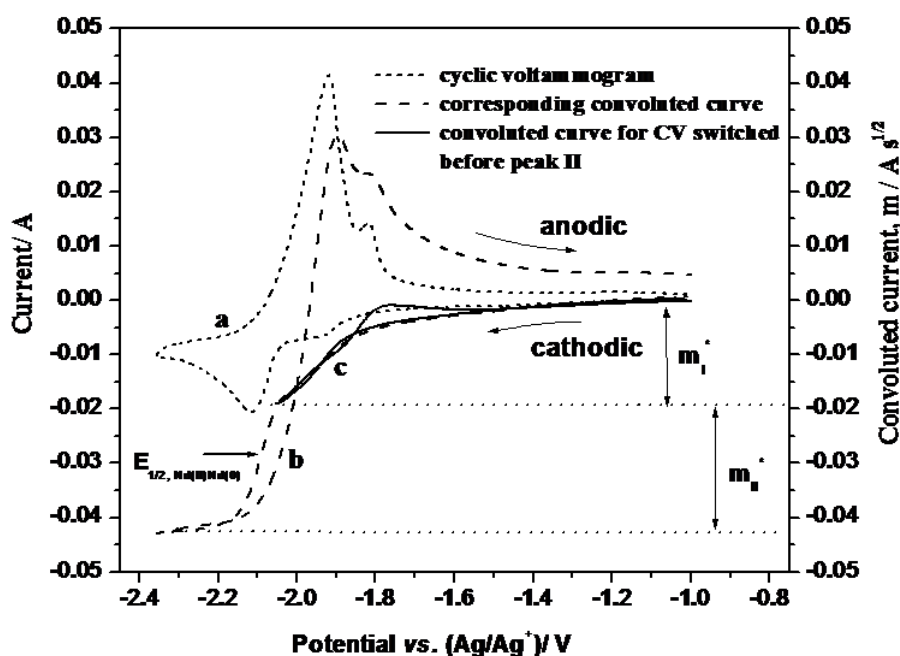


Fig. 3.10 Cyclic voltammograms of LiCl-KCl-NdCl<sub>3</sub> melt on W electrode at 723 K and corresponding convoluted curve.

Using the Matsuda-Ayabe criteria discussed above, it was found that  $k_s$  obeyed the quasi reversible hypothesis for the scan rates in the range 75 mVs<sup>-1</sup> to 250 mVs<sup>-1</sup> in this study.

The following observations were made for  $6.66 \times 10^{-5}$  mol cm<sup>-3</sup> NdCl<sub>3</sub> in LiCl-KCl melt at 773 K at various scan rates using the value of 1.78 for ' $\alpha n_\alpha$ ' and  $5.01 \times 10^{-6}$  cm s<sup>-1</sup> for  $k_s$  obtained from the convolution method:

$$1.87 \times 10^{-6} < k_s < 0.169 \text{ for scan rate } 250 \text{ mVs}^{-1}$$

$$1.68 \times 10^{-6} < k_s < 0.152 \text{ for scan rate } 200 \text{ mVs}^{-1}$$

$$1.19 \times 10^{-6} < k_s < 0.107 \text{ for scan rate } 100 \text{ mVs}^{-1}$$

$$1.03 \times 10^{-6} < k_s < 0.092 \text{ for scan rate } 75 \text{ mVs}^{-1}$$

Hence it may be concluded that the reduction of Nd(II) ion to Nd metal on W electrode shows quasi-reversible behavior for polarization rates in the range 75 - 250mVs<sup>-1</sup>.

Table 3.3. Diffusion coefficient and heterogeneous rate constant at different temperatures.

Electrolyte: LiCl-KCl-NdCl<sub>3</sub>, Concentration of NdCl<sub>3</sub>:  $6.66 \times 10^{-5} \text{ mol cm}^{-3}$ .

Temperature, K	723	748	773	798
$D_{\text{Nd(III)}} (\pm 0.05 \times 10^5, \text{ cm}^2 \text{ s}^{-1})$	0.28	0.45	0.54	0.76
$D_{\text{Nd(II)}} (\pm 0.05 \times 10^5, \text{ cm}^2 \text{ s}^{-1})$	0.98	1.38	1.69	2.03
$k_s, \text{Nd(II)/Nd(0)} (x 10^6, \text{ cm s}^{-1})$	2.95	3.23	5.01	7.76

 $D_{\text{Nd(III)}}$  and  $D_{\text{Nd(II)}} (x 10^5, \text{ cm}^2 \text{ s}^{-1})$ : 0.95 and 1.25 respectively at 733 K [49].

### 3.4.2.3. Behavior of UCl<sub>3</sub>

Fig. 3.11 shows the convoluted curves obtained for LiCl-KCl-UCl<sub>3</sub> melt. It may be observed that the convoluted curve resembles those obtained for LiCl-KCl-LaCl<sub>3</sub> melt. Analysis of the convoluted data for reduction of U(III)/U(0) showed that the reduction followed the quasi-reversible hypothesis for the scan rates,  $100 \text{ mVs}^{-1}$  and  $150 \text{ mVs}^{-1}$  complying with Eq. 3.8 and 3.9. Plot of E vs. log B were obtained for polarization rates  $100$  and  $150 \text{ mV s}^{-1}$  using values of m from 10% to 90% of  $m^*$  and they were found to be linear. The value of half wave potential,  $E_{1/2}$ , was used for the value of standard potential,  $E^0$  in Eq. 3.8. The half wave potential was obtained graphically from the convoluted curves as discussed earlier. The average value of ' $\alpha n_\alpha$ ' was found to be  $2.67 \pm 0.1$  and the charge-transfer rate constant,  $k_s$  was estimated to be  $1.77 \times 10^{-5} \text{ cm s}^{-1}$  at 773 K. Using the Matsuda-Ayabe criteria discussed above, it was found that  $k_s$  obeyed the quasi reversible hypothesis for the scan rates  $100 \text{ mVs}^{-1}$  and  $150 \text{ mVs}^{-1}$  in this study. The following observations were made for  $1.45 \times 10^{-4} \text{ mol cm}^{-3}$  UCl<sub>3</sub> in LiCl-KCl melt at 773 K for  $k_s$ ,  $1.77 \times 10^{-5} \text{ cm s}^{-1}$ :

$$1.35 \times 10^{-6} < k_s < 0.122 \text{ for scan rate } 150 \text{ mVs}^{-1}$$

$$1.1 \times 10^{-6} < k_s < 0.099 \text{ for scan rate } 100 \text{ mVs}^{-1}$$

Hence it may be concluded that the reduction of U(III) ion to U metal on W electrode shows quasi-reversible behavior for polarization rates above  $100 \text{ mVs}^{-1}$ . Kuznetsov *et al.* have reported the value of  $k_s$  to be  $2.6 \times 10^{-4} \text{ cms}^{-1}$  at 773 K estimated from impedance measurement and showed from the Matsuda-Ayabe criteria that the reduction followed quasi-reversible behavior [33]. The difference in the values is not understood.

### 3.4.3 Chronopotentiometry

#### 3.4.3.1 Analysis of the chronopotentiograms for LiCl-KCl-LaCl<sub>3</sub> melt

Fig. 3.12 shows the chronopotentiograms at various current densities for LiCl-KCl melt containing  $7.54 \times 10^{-5} \text{ mol cm}^{-3} \text{ LaCl}_3$  at 798 K at the W electrode. There is only one

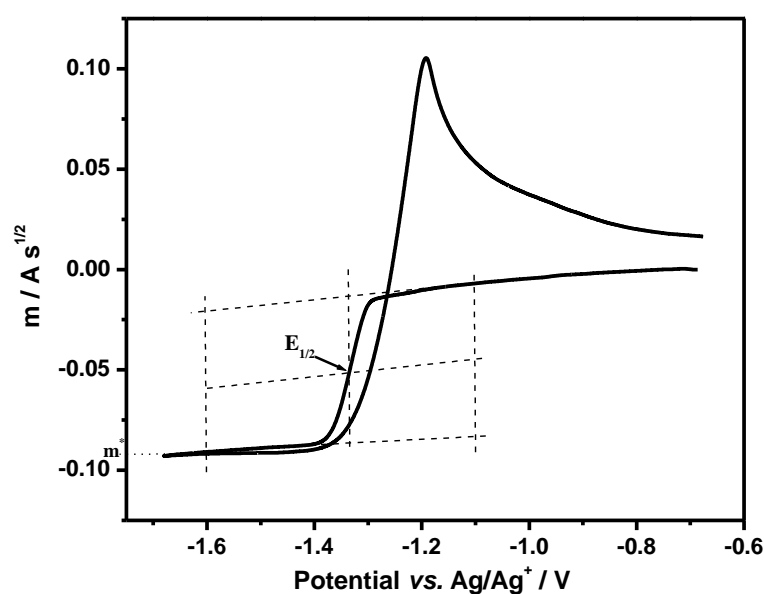


Fig. 3.11: Convoltuted curve for cyclic voltammogram recorded in LiCl-KCl-UCl<sub>3</sub> at 748 K at polarization rate  $25 \text{ mVs}^{-1}$ ; Concentration of UCl<sub>3</sub>:  $7.31 \times 10^{-5} \text{ moles cc}^{-1}$ ;

plateau corresponding to the reduction of the La(III) to La(0) as observed in the cyclic voltammograms. The Sand's relation for a reversible process is given as [42].

$$i\tau_c^{1/2} = 0.5nFD_{M(x)}^{1/2}\pi^{1/2}C_{M(x)}^0 \quad (3.14)$$

where  $i$  is the current density,  $\text{Acm}^{-2}$  and  $\tau_c$  is the transition time, sec. The product  $i\tau_c^{1/2}$  should remain constant for different current densities, according to the Sand's equation. Inset of Fig. 4 shows the plot of  $i\tau_c^{1/2}$  for various cathodic polarizations. It may be observed that the value of the product  $i\tau_c^{1/2}$  remained almost constant in the current density range investigated indicating that the reduction followed reversible behavior for low polarization value. Hence, Sand's equation was used to estimate the diffusion coefficient of La(III) ion which is described in section 3.3.6.

#### 3.4.3.2 Analysis of the chronopotentiograms for LiCl-KCl-NdCl<sub>3</sub> melt

Fig. 3.13 shows the chronopotentiograms of NdCl<sub>3</sub> in LiCl-KCl eutectic at different current densities at 773 K. The chronopotentiograms showed two plateaus which correspond to reduction of Nd(III) to Nd(II) and Nd(II) to Nd(0). Fig. 3.14 shows the plot of the product  $i\tau_c^{1/2}$  as a function of the current density for the redox couples Nd(III)/Nd(II) and Nd(II)/Nd(0) at 773 K. It may be observed that the value of  $i\tau_c^{1/2}$  was constant for the current density range studied for the first redox couple whereas the same was not constant for the redox couple Nd(II)/Nd(0). Hence Sand's equation cannot be used for evaluating the diffusion coefficient of Nd(II) ion. We have not used chronopotentiometry for evaluation of apparent standard potentials and diffusion coefficient of the redox couples in this study. The data were used for qualitative purpose only.

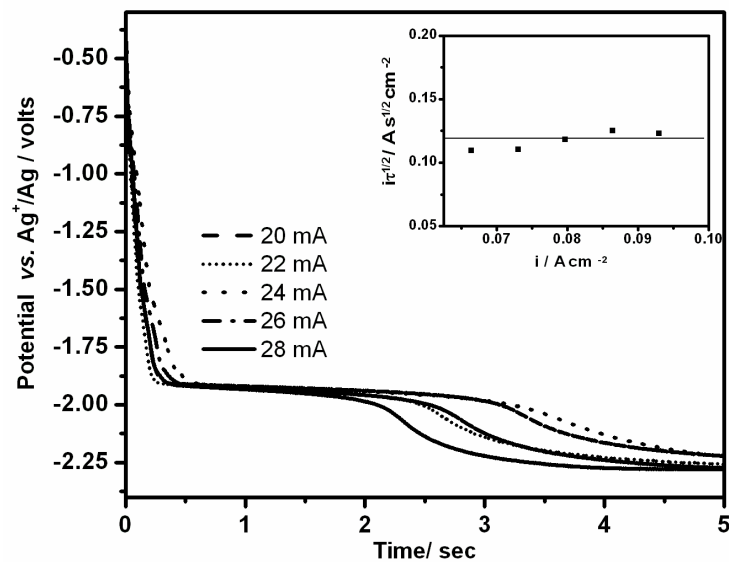


Fig. 3.12 Chronopotentiograms on a tungsten electrode for  $7.54 \times 10^{-5} \text{ mol cm}^{-3}$   $\text{LaCl}_3$  in  $\text{LiCl-KCl}$  melt at 798 K. Apparent area:  $0.301 \text{ cm}^{-2}$ . Inset:  $i\tau^{1/2}$  against current density. Working electrode: W. Concentration of  $\text{LaCl}_3$ :  $7.54 \times 10^{-5} \text{ mol cm}^{-3}$ . Temperature: 798 K.

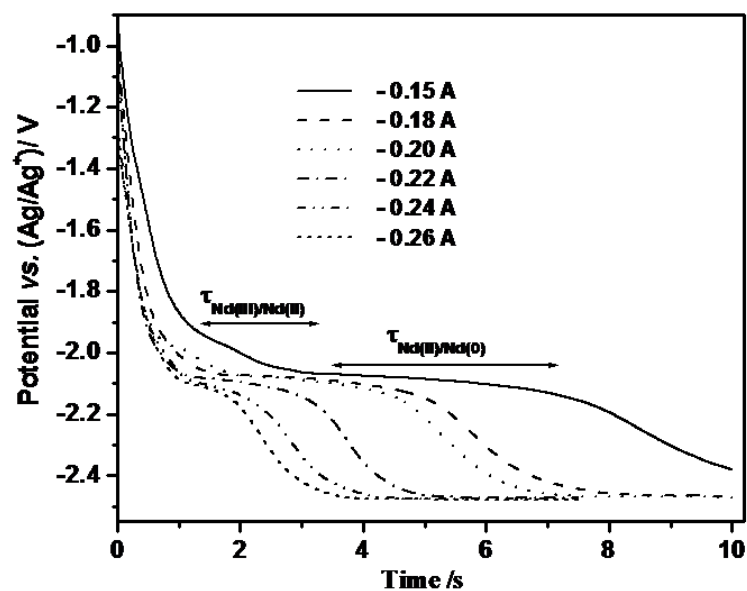


Fig. 3.13 Chronopotentiograms on a tungsten electrode for  $\text{LiCl-KCl-NdCl}_3$  melt. Temperature: 723 K; Concentration of  $\text{NdCl}_3$ :  $6.66 \times 10^{-5} \text{ mol cm}^{-3}$ ; Electrode area:  $0.49 \text{ cm}^2$ .

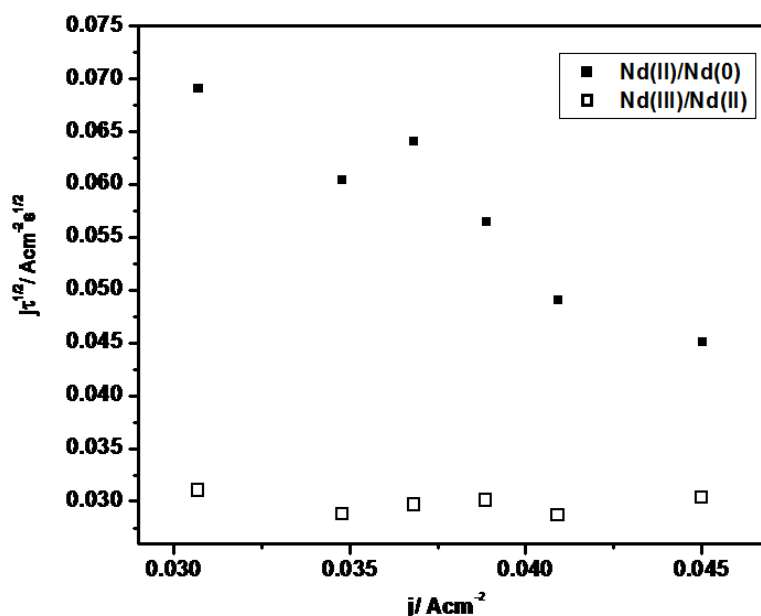


Fig. 3.14. Variation of  $i_p^{1/2}$  with different current densities for the redox couples Nd(III)/Nd(II) and Nd(II)/Nd(0) for the chronopotentiograms shown in Fig. 3.13.

### 3.4.4 Square wave voltammetry

#### 3.4.4.1 Analysis of the square wave voltammograms for LiCl-KCl-LaCl<sub>3</sub>

Fig. 3.15 shows the square wave voltammograms of  $7.54 \times 10^{-5} \text{ mol cm}^{-3}$  LaCl<sub>3</sub> in LiCl-KCl melt at 793 K at 8 Hz. It was observed that only a single redox species is present in the potential range studied. For a reversible electrochemical reaction, the net current-potential curve is bell shaped and the width  $W_{1/2}$ , of the peak at half of its height is given by Eq. (21) [43, 44]

$$W_{1/2} = 3.52 \frac{RT}{nF} \quad (3.15)$$

The peak should be purely Gaussian in nature for a perfect reversible system. But it may be observed from Fig. 3.15 that the peak is asymmetric due to nucleation phenomena.

Limited fitting was done considering only the left part of the voltammogram. The value of  $n$  using the above relation for the Gaussian fit was evaluated to be  $2.93 \pm 0.08$ . The square wave voltammograms substantiate our earlier findings from cyclic voltammetry and chronopotentiometry that the La(III) ion reduces to La metal in a single step.

#### ***3.4.4.2 Analysis of the square wave voltammograms for LiCl-KCl-NdCl<sub>3</sub>***

Fig. 3.16 shows the square wave voltammograms of NdCl<sub>3</sub> in LiCl-KCl eutectic at 723 K at various frequencies. The voltammograms indicate the presence of a two step process for the reduction of Nd(III) ion to Nd metal. The peak should be purely Gaussian in nature for a reversible system with the plot of the peak current density against square root of frequency being linear [45]. Fig. 3.17 shows the plot of peak current density as a function of square root of frequency for the redox couple Nd(III)/Nd(II) and that for Nd(II)/Nd(0). It may be observed that a linear dependence is seen in case of the first redox couple only. This indicates that the reduction of Nd(III) to Nd(II) shows reversible behavior and that for Nd(II)/Nd(0) does not obey a perfect reversible electrode process. The observations are in agreement with the results obtained from cyclic voltammograms and chronopotentiograms.

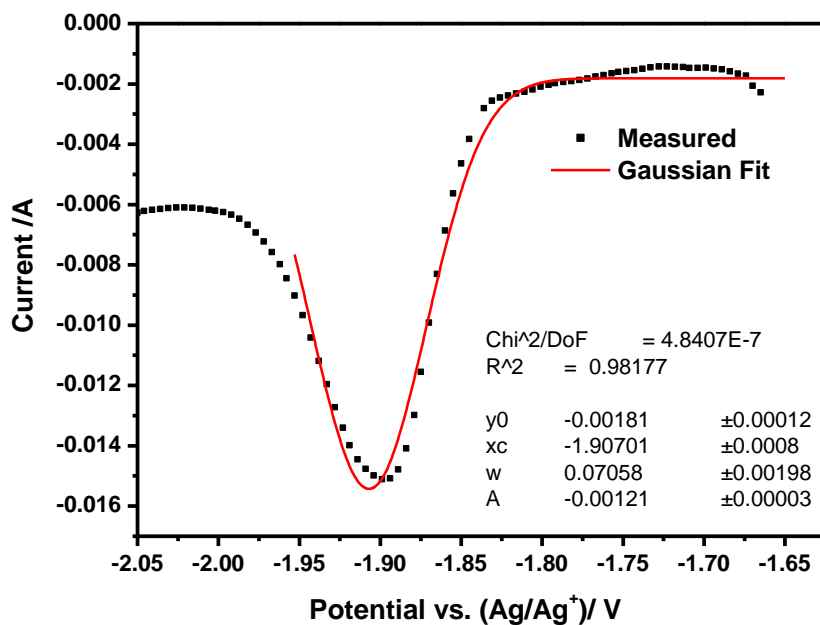


Fig. 3.15 Square wave voltammograms for  $7.54 \times 10^{-5} \text{ mol cm}^{-3}$   $\text{LaCl}_3$  in LiCl-KCl melt at 793 K. Working electrode: tungsten. Apparent electrode area:  $0.347 \text{ cm}^2$ . Frequency: 8 Hz.

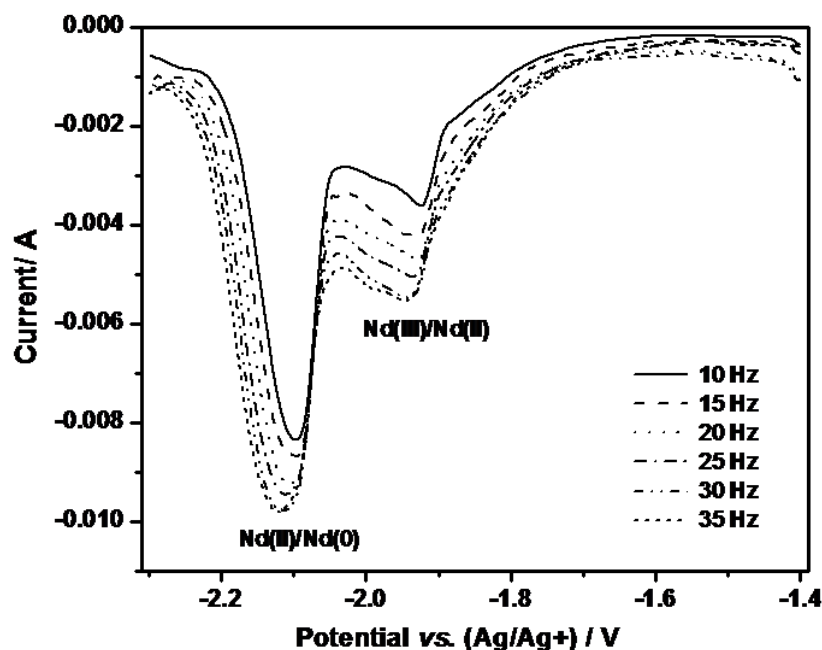


Fig. 3.16. Square wave voltammograms of  $\text{NdCl}_3$  in LiCl-KCl eutectic at 723 K at various frequencies. Amplitude of pulse: 10 mV. Concentration of  $\text{NdCl}_3$ :  $6.66 \times 10^{-5} \text{ mol cm}^{-3}$ ; Electrode area:  $0.49 \text{ cm}^2$ .

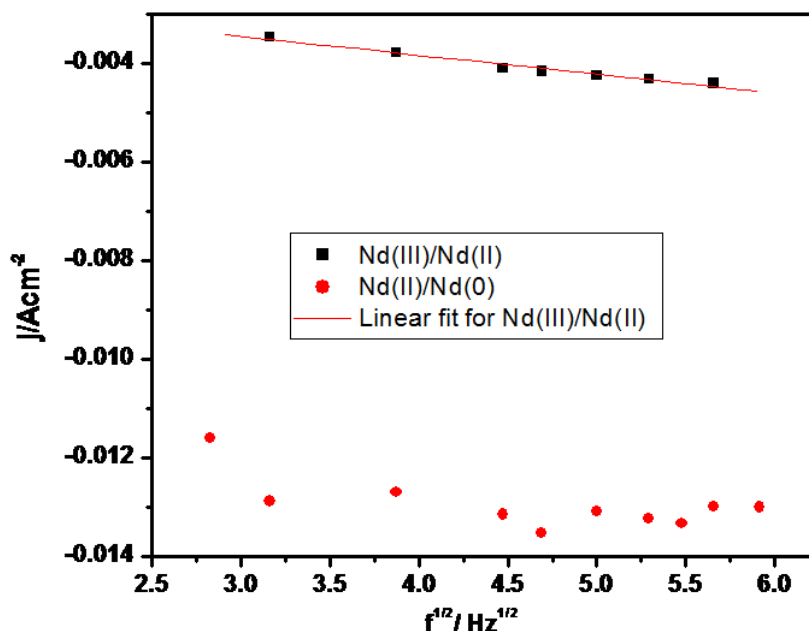


Fig. 3.17. Plot of peak current density as a function of square root of frequency for LiCl-KCl-NdCl<sub>3</sub> melt. Temperature: 723 K; Concentration of NdCl<sub>3</sub>:  $6.66 \times 10^{-5} \text{ mol cm}^{-3}$ .

### 3.4.5 Estimation of diffusion coefficient

#### 3.4.5.1. Diffusion coefficient of La(III) ion

The diffusion coefficient of La(III) ion was estimated by three methods, namely, cyclic voltammetry, chronopotentiometry and convolution voltammetry. The cathodic peak currents of the cyclic voltammograms obtained at different scan rates were plotted against square root of the scan rate. Linear dependence of peak current,  $i_{pc}$ , on the square root of scan rate,  $\nu^{1/2}$  was observed for low scan rates only, namely in the scan range  $25 \leq \nu \leq 150 \text{ mVs}^{-1}$  as seen in Fig. 3.18. The Berzins-Delahay equation gives the relation between the peak current and the scan rate, for a diffusion controlled process with the formation of an insoluble product as given in Eq. 3.16 [46]

$$i_{pc} = 0.61(nF)^{3/2}(RT)^{-1/2} AC_{M(x)}^0 D_{M(x)}^{1/2} \nu^{1/2} \quad (3.16)$$

where  $i_{pc}$  is the cathodic peak current corresponding to peak I<sub>c</sub>,  $n$ , number of electron transferred,  $F$ , Faraday's constant,  $R$ , the universal gas constant (8.314 Jmol<sup>-1</sup>K<sup>-1</sup>),  $T$ , the absolute temperature,  $A$ , the electrode area (cm<sup>2</sup>),  $C_{M(x)}^0$ , the bulk concentration (mol cm<sup>-3</sup>),  $D_{M(x)}$  the diffusion coefficient (cm<sup>2</sup> s<sup>-1</sup>) of the electroactive species M(x) and  $\nu$ , the potential sweep rate (Vs<sup>-1</sup>). Linear dependence of peak current, on the square root of scan rate at low polarization rates suggest that the reduction is predominantly controlled by diffusion in this scan range. We have earlier discussed about the convoluted curves at different scan rates and deduced that the reduction process shows reversible behavior for polarization rates less than 50 mVs<sup>-1</sup>. Also we have verified the validation of Sand's equation for a diffusion controlled process from the chronopotentiograms for the current densities studied. Hence we consider it is more appropriate to use the Berzins-Delachay relation which is applicable for a diffusion controlled process with the formation of an insoluble product for calculation of the diffusion coefficient in this case as has been adopted by many authors earlier [47].

The diffusion coefficient of La(III) ion was calculated from the slope of the plot,  $i_{pc}$  vs.  $\nu^{1/2}$ , in the scan range  $25 \leq \nu \leq 150$  mVs<sup>-1</sup> using Eq.3.16.

According to the theory of convolution [40], the diffusion coefficient of La(III) ion can be obtained using Equation 3.17

$$m^* = -nFAC_{La(III)} D_{La(III)}^{1/2} \quad (3.17)$$

$m^*$  was obtained from cyclic voltammograms at 25 mVs<sup>-1</sup> graphically as mentioned earlier. The diffusion coefficient of La(III) ion was estimated using Eq. 3.17 from the convoluted curve for cyclic voltammograms recorded at 25 mVs<sup>-1</sup> for temperatures in the range 698-798 K. The diffusion coefficient was also obtained from the chronopotentiograms using the Sand's relation (Eq. 3.14) from the slope of the plot of

the current density against  $\tau_c^{-1/2}$ . The diffusion coefficients of La(III) ion in LiCl-KCl melt estimated by the three methods are reported in Table 3.4. The diffusion coefficient of La(III) ion at 723 K reported by Castrillejo *et al.* [7], Masset *et al.* [5] and 748 K by Lantelme *et al.* [8] are also listed in the table and it may be seen that our values are in agreement with the reported values.

#### 3.4.5.2. Diffusion coefficient of Nd (III) and Nd(II) ions

The diffusion coefficients of Nd(III) and Nd(II) ions were estimated from the cyclic voltammograms. The cathodic peak current for the reduction of Nd(III)/Nd(II) and that for Nd(II)/Nd(0) were plotted against square root of the scan rate. Linear dependence of peak current,  $i_{pc}$ , on the square root of scan rate,  $v^{1/2}$  was observed for the scan rate in the scan range  $25 \leq v \leq 150 \text{ mV s}^{-1}$  for Nd(III)/Nd(II) redox couple and in the scan range  $10 \leq v \leq 50 \text{ mV s}^{-1}$  for Nd(II)/Nd(0) couple as seen in Fig. 3.19 and Fig. 3.20 respectively. Based on our contention that the reduction of Nd(III)/Nd(II) is a reversible electrochemical process, the diffusion coefficient, of Nd(III) ion was evaluated using the Randle-Sevick equation for a diffusion controlled process involving soluble-soluble couple [42]

$$i_{pc} = 0.446(nF)^{3/2}(RT)^{-1/2} AC_{M(x)}^0 D_{M(x)}^{1/2} v^{1/2} \quad (3.18)$$

where  $i_{pc}$  is the cathodic peak current corresponding to peak I<sub>c</sub> (A) Fig. 3.3, A is the electrode area (cm<sup>2</sup>),  $C_{M(x)}^0$ , is the concentration of Nd(III) ion in the bulk (mol cm<sup>-3</sup>) and  $D_{M(x)}$  is the diffusion coefficient of Nd(III) ion (cm<sup>2</sup>s<sup>-1</sup>) and v is the scan rate (Vs<sup>-1</sup>). Fig. 3.20 shows the plot of current densities as a function of square root of scan rate for the redox couple Nd(II)/Nd(0). It was observed that a linear dependence is found only for a limited scan range studied. Inset of Fig. 3.20 shows the plot of current densities as a function of square root of

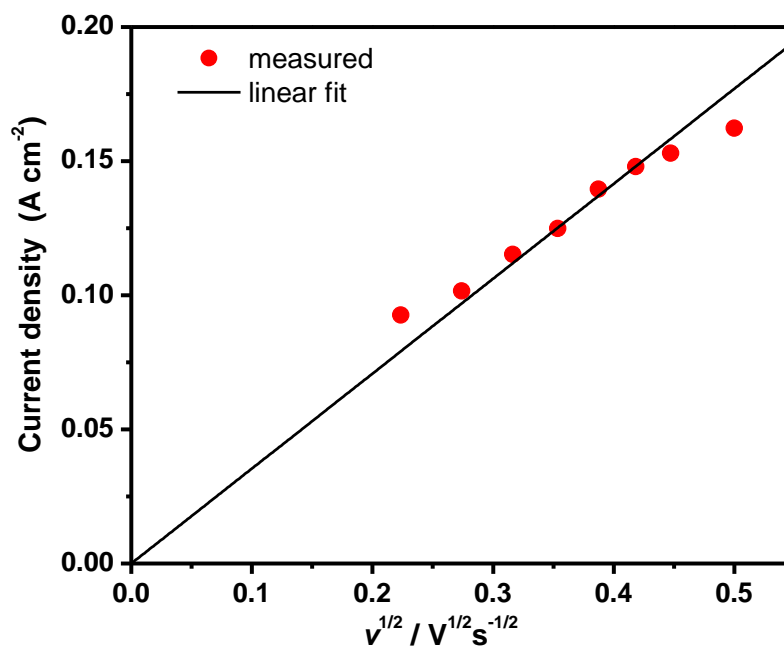


Fig. 3.18 Plot of current density vs. square root of scan rate for LiCl-KCl-LaCl<sub>3</sub>. Concentration of LaCl<sub>3</sub>:  $7.54 \times 10^{-5}$  mol cm<sup>-3</sup>. Temperature: 798 K.

Table 3.4. Diffusion coefficient of La(III) ion in LiCl-KCl melt at different temperatures. Concentration of LaCl<sub>3</sub>:  $7.54 \times 10^{-5}$  mol cm<sup>-3</sup>. D (cm<sup>2</sup>s<sup>-1</sup> x 10<sup>5</sup>)

Temperature, K	698	723	748	798
Cyclic Voltammetry	0.74±0.05	0.91±0.10	1.31±0.07	1.52±0.07
Convolution	1.02±0.05	1.16±0.06	1.38±0.07	1.79±0.09
Chronopotentiometry (using Sand's equation for reversible system)	1.52±0.07	-	2.75±0.13	3.2±0.35
(Literature value)		1.17 [7] 0.80 [5]	1.76 [8]	

scan rate in the range  $10\text{-}50\text{ mVs}^{-1}$ . Since the plot of peak current against square root of scan rate was found to be linear for the electrode reaction  $\text{Nd(II)/Nd(0)}$  at low polarization rates and also from our discussion in the previous section, it is presumed that the electrode reaction shows reversible behavior in the scan range  $10 \leq \nu \leq 50\text{ mVs}^{-1}$ . The diffusion coefficient, of  $\text{Nd(II)}$  ion was evaluated using the Berzins-Delahay equation, Eq. 3.16 applicable for a diffusion controlled process involving soluble-insoluble species. Since the  $\text{Nd(II)}$  ion is formed from  $\text{Nd(III)}$  ion, it is assumed that  $C_{\text{Nd(II)}} = C_{\text{Nd(III)}}$  for calculation of diffusion coefficient of  $\text{Nd(II)}$  [48]. Similar assumption was made by Glatz *et al.* for estimating  $D_{\text{Nd(II)}}$  [49]. Estimation of the diffusion coefficient using the melt  $\text{LiCl-KCl-NdCl}_2$  should yield more accurate values for the diffusion coefficient of  $\text{Nd(II)}$  ion. Since we had not carried out any studies using  $\text{LiCl-KCl-NdCl}_2$  melt, we have adopted the procedure used by Glatz *et al.* The values of diffusion coefficient of  $\text{Nd(III)}$  and  $\text{Nd(II)}$  ions calculated at different temperatures are shown in Table 3.3. The diffusion coefficient value at 733 K reported by Glatz *et al.* is close with that of ours [49]. Kuznetsov *et al.* had estimated the diffusion coefficient of  $\text{Eu(III)}$  ion using  $\text{LiCl-KCl-EuCl}_3$  melt and that for  $\text{Eu(II)}$  ion using  $\text{LiCl-KCl-EuCl}_2$  melt [16]. It was found that the order of the values of  $D_{\text{Eu(III)}}$  and  $D_{\text{Eu(II)}}$  obtained by Kuznetsov *et al.* are similar to the values of  $D_{\text{Nd(III)}}$  and  $D_{\text{Nd(II)}}$  in this study indicating that the assumption may not result in large error in the value of  $D_{\text{Nd(II)}}$ .

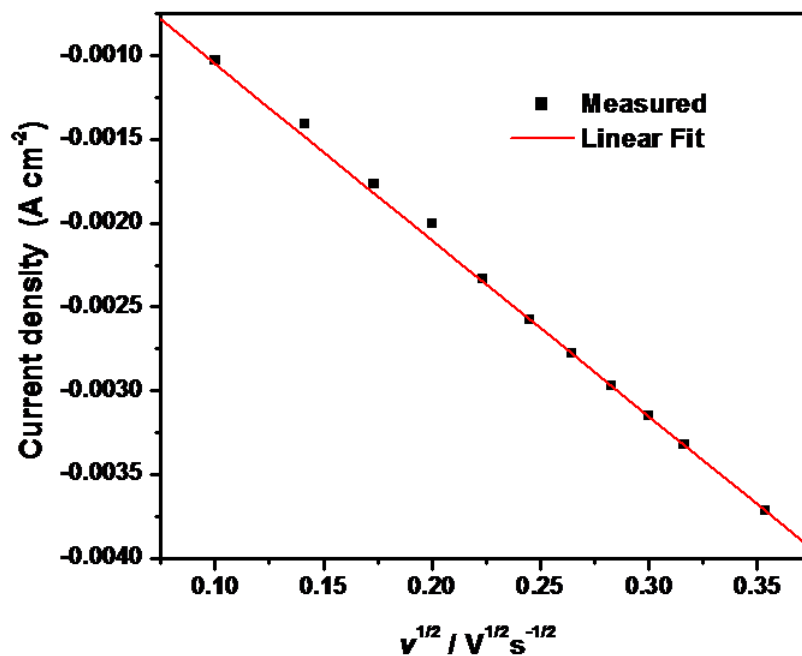


Fig. 3.19. Plot of current density for peak  $I_c$  vs. square root of scan rate for LiCl-KCl-NdCl<sub>3</sub> melt. Temperature: 723 K; Concentration of NdCl<sub>3</sub>:  $6.66 \times 10^{-5} \text{ mol cm}^{-3}$ .

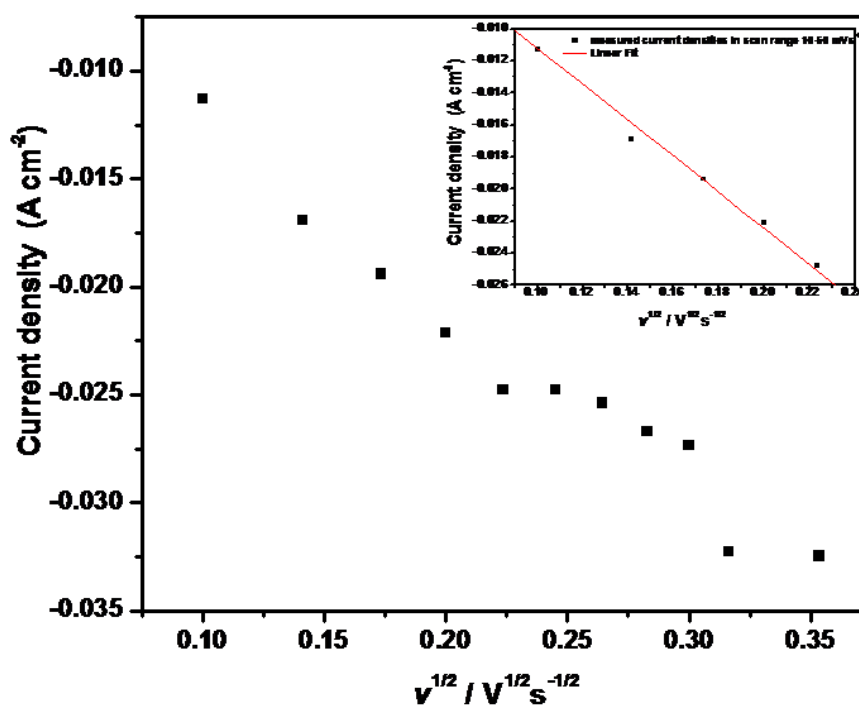


Fig. 3.20. Plot of current density for peak  $II_c$  vs. square root of scan rate for LiCl-KCl-NdCl<sub>3</sub> melt. Temperature: 723 K; Concentration of NdCl<sub>3</sub>:  $6.66 \times 10^{-5} \text{ mol cm}^{-3}$ .

### 3.4.6 Apparent standard potential

#### 3.4.6.1 Apparent standard potential of La(III)/La(0) system in LiCl-KCl melt

The apparent standard potential of La(III)/La(0) redox couple was estimated from the convoluted curves obtained at  $25 \text{ mV s}^{-1}$  and from chronopotentiograms using the relations applicable for a reversible electrode process.

##### a. Convolution method

As stated in Section 3.4.2.1 the convoluted curves obtained at low polarization rates obeyed the relation for a reversible charge transfer process given by Eq. (3.7) which may be used for deriving the apparent standard potential of the La(III)/La redox couple as follows.

The apparent standard potential  $E^*$  for the redox couple La(III)/La is defined as

$$E_{La(III)/La(0)}^* = E_{La(III)/La(0)}^0 + \frac{RT}{nF} \ln \gamma_{LaCl_3} \quad (3.19)$$

where  $\gamma_{LaCl_3} = a_{LaCl_3} / X_{LaCl_3}$  is the activity coefficient of  $LaCl_3$ .

Equation (3.7) may be rewritten as

$$E = E_{La(III)/La(0)}^* + \frac{RT}{nF} \ln(X_{LaCl_3}) + \frac{RT}{nF} \ln\left(\frac{m^* - m}{m^*}\right) \quad (3.20)$$

We had seen earlier that the plots of the electrode potential versus  $\ln[(m^* - m)/m^*]$  were linear as seen in Fig. 3.8 and the number of electrons transferred computed from the slope of the plot was close to three. The apparent standard potential was obtained from the intercept of the plot for the concentration of  $LaCl_3$ ,  $X_{LaCl_3} = 0.0022$ . The apparent standard potential thus obtained versus the Ag/AgCl ( $X_{AgCl} = 0.001$ ) was converted to the scale of  $Cl_2/Cl^-$  reference electrode. Assuming unit activity of the pure metal and unit activity coefficient for AgCl at low concentration of AgCl as reported by Flengas and Ingraham [50], the potential of the Ag/AgCl reference electrode is defined as

$$E_{AgCl} = E_{AgCl}^0 + \frac{RT}{nF} \ln X_{AgCl} \quad (3.21)$$

The value of  $E_{AgCl}^0$  relative to the  $Cl_2/Cl^-$  is given by Yang et. al. [51]

$$E_{AgCl}^0 = -1.0910 + 0.0002924 * T (K) \quad (3.22)$$

The potentials  $E_{AgCl}^0$  vs.  $Cl_2/Cl^-$  and  $E_{AgCl(X_{AgCl}=0.001)}$  vs.  $Cl_2/Cl^-$  at various temperatures were evaluated using Eq. 3.22 and Eq. 3.21 respectively. The apparent standard potentials of La(III)/La(0) vs.  $Cl_2/Cl^-$  reference electrode at different temperatures were thus evaluated and are shown in Table 3.5.

The apparent standard potentials were also obtained from the chronopotentiograms as discussed below. The potential-time relation of the chronopotentiometric curve for a

Table 3.5 Apparent standard potentials for La(III)/La(0) and Gibbs free energy of formation of  $LaCl_3$ , Concentration of  $LaCl_3: 7.54 \times 10^{-5} \text{ molcm}^{-3}$

	Temperature, K	$E_{La(III)/La(0)}^{*0}$ vs. $Cl_2/Cl^-$ , V	$\Delta G_{LaCl_3}^\infty$ , KJ $mol^{-1}$
Convolution	723	-3.152 (-3.146)*	-912.5
Convolution	748	-3.138	-908.3
Chronopotentiometry		-3.140	-909.1
Convolution	773	-3.116	-902.1
Convolution	798	-3.105	-898.7
Chronopotentiometry		-3.098	-896.7

\*Fusselman *et.al* [24]

# At 733  $E_{La(III)/La(0)}^{*0}$  vs.  $Cl_2/Cl^- = -3.126$  V,  $\Delta G_{LaCl_3}^\infty = -904.9$  KJ  $mol^{-1}$  [49]

b. Chronopotentiometry

reversible redox couple with the formation of an insoluble metallic deposit is given by the following equation [11]

$$E(t) = E_{La(III)/La(0)}^0 + \frac{RT}{nF} \ln(a_{LaCl_3}) + \frac{RT}{nF} \ln\left(\frac{\tau^{1/2} - t^{1/2}}{\tau^{1/2}}\right) \quad (3.23)$$

Introducing the relation for apparent standard potential from Eq. 3.19, Eq. 3.23 may be rewritten as

$$E(t) = E_{La(III)/La(0)}^* + \frac{RT}{nF} \ln(X_{LaCl_3}) + \frac{RT}{nF} \ln\left(\frac{\tau^{1/2} - t^{1/2}}{\tau^{1/2}}\right) \quad (3.24)$$

The plots of cathodic potential of the chronopotentiograms versus  $\ln[(\tau^{1/2} - t^{1/2})/\tau^{1/2}]$  were also found to be linear. The apparent standard potential was obtained from the intercept. The apparent standard potential obtained for temperatures 748 and 798 K are shown in Table 3.5.

### 3.4.6.2 Estimation of apparent standard potentials for the redox couples Nd(III)/Nd(II) and Nd(II)/Nd(0)

#### 3.4.6.2.1 Stability of Nd(II) ion

A short discussion on the stability of the Nd(II) ion reported in the literature is given here. Yamana *et al.* have studied the stability of Nd(II) ion by spectroscopic method. Nd(II) ions were formed in-situ by applying a cathodic potential sufficient to reduce Nd(III) ion without forming metallic Nd [10]. They had observed the peaks for Nd(II) ion in their spectroscopic studies as long as the potential was applied and the peak intensity for Nd(II) ion gradually fell down with time once the potential was switched off. This showed that NdCl<sub>2</sub> is unstable and disproportionate to Nd(III) and Nd metal as given by Eq. 3.25.



However, we have observed peak for formation of Nd(II) ion at about -1.85 V and its subsequent oxidation to Nd(III) during the anodic cycle in the cyclic voltammograms in the concentration range studied. This could be due to the short time scale of our transient measurement. Novoselova *et al.*[14] had estimated the apparent standard redox potential of Nd(III)/Nd(II) couple by direct potentiometric method in LiCl-KCl-CsCl melt containing NdCl<sub>3</sub> and NdCl<sub>2</sub>. They had reported that NdCl<sub>2</sub> is unstable above 798 K and disproportionate to Nd(III) and Nd metal. Hence they observed that the potential of the electrode stabilized at the rest potential of Mo electrode in their studies above 798 K. But they were able to obtain the equilibrium potential of the Nd(III)/Nd(II) couple in the temperature range 573-723 K. This suggests that the disproportionation reaction is not significant in LiCl-KCl-CsCl melt for temperatures below 798 K. Fukusawa *et al.* had studied the thermodynamic stability of the Nd(III) complex in different molten alkali chloride melts at 923 K [9]. The Nd(Cl<sub>6</sub>)<sup>3-</sup> complex was more stable in an alkali chloride mixture with larger averaged cationic radius which implies that the stability is controlled by the polarizing power of solvent cations. The stability of Nd(III) and Nd(II) complex in the study of Novoselova *et al.* may be due to the presence of Cs(I) ions. Apart from the disproportionation reaction, corrosive reaction due to the interaction of Nd(II) ions with the materials used in the cell such as alumina and pyrex glass has been reported leading to the formation of oxychlorides [3]. However from our studies we found that it became significant only when the same electrolyte was used for repeated measurement and the duration of the measurement were too long. We did not intend to study this reaction in the present work. Hence we had made measurements with fresh electrolyte and electrode set-up for each set of measurement. Nd metal in contact with Nd(III) ions in the melt forms Nd(II) ions as shown in Eq. 3.25. This prevents the attainment of stable equilibrium potential for the Nd(III)/Nd couple by emf method as reported by Fusselman *et al.* [24].

But the cyclic voltammograms and open circuit potential measurements allowed us to estimate the equilibrium potentials of Nd(III)/Nd(II), Nd(II)/Nd(0) and Nd(III)/Nd(0) redox couples which is discussed in the following section. Since our measurement are by transient technique with short time period of perturbation, significant amount of Nd(II) ions will not form in the system. The Nd(II) ions is generated in-situ at the electrode surface alone.

### 3.4.6.2.1 Estimation of apparent standard potentials from cyclic voltammogram

#### a. For soluble-soluble couple

For soluble-soluble species, the half wave potential,  $E_{1/2}$ , is related to the standard potential and apparent standard potential by the following relation [3, 16, 42]

$$E_p^C = E_{1/2} - 1.11(RT/F) \quad (3.26)$$

$$E_p^A = E_{1/2} + 1.11(RT/F) \quad (3.27)$$

$$E_{1/2} = (E_p^C + E_p^A)/2 \quad (3.28)$$

Where

$$E_{1/2} = E_{Nd(III)/Nd(II)}^0 + \frac{RT}{F} \ln \frac{\sqrt{D_{Nd(II)}}}{\sqrt{D_{Nd(III)}}} + \frac{RT}{F} \ln \left( \frac{\gamma_{Nd(III)}}{\gamma_{Nd(II)}} \right) \quad (3.29)$$

And the apparent standard potential is described as

$$E_{Nd(III)/Nd(II)}^* = E_{Nd(III)/Nd(II)}^0 + \frac{RT}{F} \ln \left( \frac{\gamma_{Nd(III)}}{\gamma_{Nd(II)}} \right) \quad (3.30)$$

Hence we get,

$$E_{Nd(III)/Nd(II)}^* = E_{1/2} + \frac{RT}{F} \ln \frac{\sqrt{D_{Nd(III)}}}{\sqrt{D_{Nd(II)}}} \quad (3.31)$$

Where  $E_{Nd(III)/Nd(II)}^0$  and  $E_{Nd(III)/Nd(II)}^*$  are the standard potential and apparent standard potential of the Nd(III)/Nd(II) redox couple. The apparent standard potential for

reduction of Nd(III)/Nd(II) was obtained from the cyclic voltammograms using Eq. 3.26 and Eq. 3.31. The value of diffusion coefficients obtained from this study was used for the calculations.

*b. For soluble - insoluble couple*

Taking into account only the voltammograms recorded at low scan rate,  $25 \text{ mVs}^{-1}$ , for which the reduction of Nd(II)/Nd(0) is being considered reversible, the apparent standard potential was evaluated using Eq. 3.32 [4, 5].

$$E_{p,c} = E_{Nd(II)/Nd(0)}^* + \frac{RT}{2F} \ln(X_{Nd(II)}) - 0.854 \frac{RT}{2F} \quad (3.32)$$

where  $X_{Nd(II)}$  is the mole fraction of the electroactive species Nd(II) ion and it is considered that the mole fraction of  $\text{NdCl}_2$  is the same as the mole fraction of  $\text{NdCl}_3$  added [48].

The apparent standard potential thus obtained versus the Ag/AgCl (0.31 mole %) was converted to the scale of  $\text{Cl}_2/\text{Cl}^-$  reference electrode using Eq.3.22 and Eq. 3.21. The apparent standard potentials of the redox couples Nd(III)/Nd(II), Nd(II)/Nd(0) vs.  $\text{Cl}_2/\text{Cl}^-$  reference electrode at different temperatures were thus evaluated and are shown in Table 3.6. The apparent standard potential for the redox couple Nd(III)/Nd(0) was obtained by combining the reactions for the two redox couples, Nd(III)/Nd(II) and Nd(II)/Nd(0), using the Luter equation given below [52]

$$E_{Nd(III)/Nd(0)}^* = \frac{E_{Nd(III)/Nd(II)}^* + 2E_{Nd(II)/Nd(0)}^*}{3} \quad (3.33)$$

Table 3.6. Apparent standard potentials ( $\pm 0.003$  V) and Gibbs free energy formation of  $\text{NdCl}_3$  estimated from cyclic voltammograms for  $\text{LiCl-KCl-NdCl}_3$  melt at W electrode.

Temperature, K	$E_{\text{Nd(III)/Nd(II)}}^*$ vs. $\text{Cl}_2/\text{Cl}^-$ , V	$E_{\text{Nd(II)/Nd(0)}}^*$ vs. $\text{Cl}_2/\text{Cl}^-$ , V	$E_{\text{Nd(III)/Nd(0)}}^*$ vs. $\text{Cl}_2/\text{Cl}^-$ , V	$\Delta G_{\text{NdCl}_3}^\infty$ $\pm 0.9 \text{ kJ mol}^{-1}$
723	-3.058	-3.110	-3.093	-895.4
748	-3.049	-3.094	-3.079	-891.3
773	-3.039	-3.078	-3.065	-887.2
798	-3.029	-3.061	-3.050	-883.1

#### 3.4.6.2.2 Estimation of apparent standard potentials from open circuit potential transients

Open-circuit chronopotentiometry is a suitable technique to investigate the formation of intermetallic compounds in molten salt systems and to calculate their Gibbs energies of formation as was discussed in Chapter 2. In this study we have used the open circuit potentiometry method to estimate the equilibrium potential of the redox species. A thin film of the metal was formed at the inert W electrode by depositing the metal at sufficient cathodic potential for a short period (30-120 sec). The polarization is stopped and the open-circuit potential is monitored as a function of time when no current flows. It was observed that the electrode potential gradually shifted to more positive values. A series of potential plateau appeared when two phases were in equilibrium at the electrode surface and the potential shifted further towards anodic direction and stabilizes at the equilibrium potential of the inert electrode.

Open-circuit chronopotentiograms were obtained with a solution of  $\text{NdCl}_3$  in  $\text{LiCl-KCl}$  melt at W electrode by applying a cathodic polarization (-2.3 V) for a short

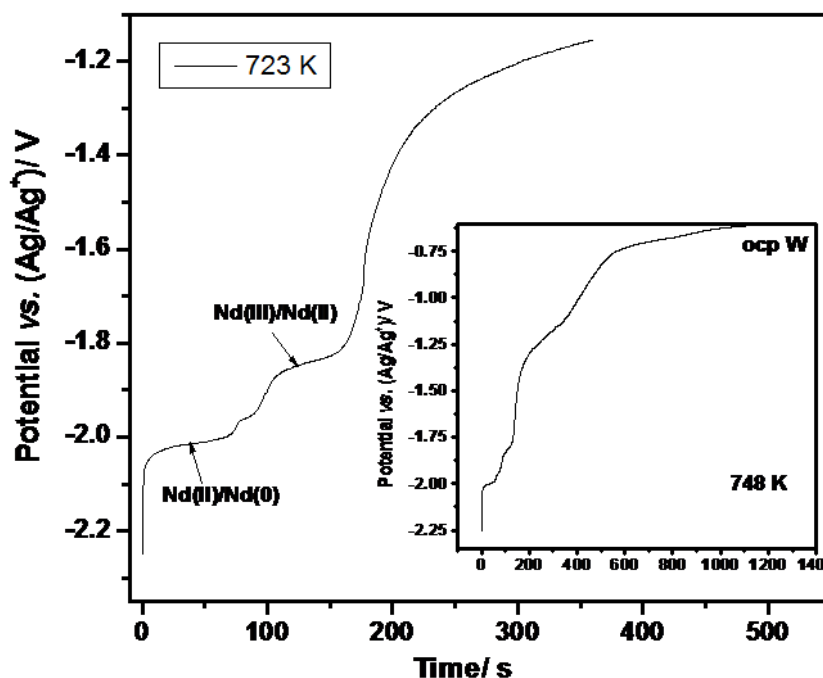


Fig. 3.21. Open circuit potential transient curve for  $\text{NdCl}_3$  in  $\text{LiCl-KCl}$  melt on W electrode. Cathodic polarization:  $-2.3 \text{ V}$  vs.  $(\text{Ag}/\text{Ag}^+)$  reference electrode. Inset: OCP transient curve showing attainment of open circuit potential for W electrode after long duration.

period (60-300 s) to form metallic Nd on the W surface. The open circuit potential was monitored as a function of time. The Nd metal coated on W undergoes the reaction shown in Eq. 3.25. Fig. 3.21 shows the open circuit potential after depositing Nd metal on W electrode at  $-2.3 \text{ V}$  for 120 s at 723 K. Considering the above mentioned reaction, it is deduced that the potential plateau at  $\sim -2.02 \text{ V}$  corresponds to the redox couple  $\text{Nd(II)}/\text{Nd(0)}$  and is the equilibrium potential for the redox couple. This potential is close to the potential of peak  $\text{II}_c$  in the cyclic voltammogram. Similar behavior was observed by Cordoba *et al.* for their studies on  $\text{NdCl}_3$  in  $\text{CaCl}_2\text{-NaCl}$  melt and they have used the potential values of the plateau to estimate the apparent standard potential of the  $\text{Nd(II)}/\text{Nd(0)}$  couple from OCP measurement [53]. Estimating apparent standard potential

from OCP measurement has been earlier used by Osipenko *et al.* [15]. They had estimated the apparent standard potential of the Cm(III)/Cm(0) couple from OCP measurement. The potential plateau at  $\sim -1.84$  V in Fig. 3.18 is attributed to the redox couple Nd(III)/Nd(II) from the peak potentials in the cyclic voltammograms. The equilibrium potential for the redox couple Nd(III)/Nd(0) was estimated using  $E_{\text{Nd(II)/Nd(0)}}$  and  $E_{\text{Nd(III)/Nd(II)}}$  using the Luter equation given in Eq. 3.33. The  $E_{\text{Nd(III)/Nd(0)}}$  estimated was  $\sim -1.957$  V. Hence the plateau  $\sim -1.96$  V seen in Fig. 3.21 could be attributed to equilibrium potential of Nd(III)/Nd(0). The equilibrium potentials for Nd(III)/Nd(II) and Nd(II)/Nd(0) estimated from open circuit potential measurements at various temperatures are listed in Table 3.7. The equilibrium potentials for Nd(III)/Nd(0) calculated using Eq. 3.33 are also shown in Table 3.7. As stated earlier, estimation of equilibrium potential for the redox couple Nd(III)/Nd(0) using equilibrium technique such as emf method is prevented by the formation of Nd(II) ion by Eq. 3.33. From our study, we find that open circuit potential measurement could be a suitable method for estimation of the equilibrium potentials of redox species such as Nd(III)/Nd(0), Am(III)/Am(0) etc whose stable equilibrium potentials cannot be obtained from emf measurement due to corrosive reaction [24, 53].

From the equilibrium potential of the redox couple Nd(III)/Nd(0) thus measured, the apparent standard potential,  $E_{\text{Nd(III)/Nd(0)}}^*$ , was determined using the Nernst equation :

$$E_{\text{Nd(III)/Nd(0)}}^{eq} = E_{\text{Nd(III)/Nd(0)}}^0 + \frac{RT}{3F} \ln \frac{a_{\text{Nd(III)}}}{a_{\text{Nd(0)}}} \quad (3.34)$$

Defining the apparent standard potential as

$$E_{\text{Nd(III)/Nd(0)}}^* = E_{\text{Nd(III)/Nd(0)}}^0 + \frac{RT}{3F} \ln \gamma_{\text{Nd(III)}} \quad (3.35)$$

We get ,

Table 3.7. Equilibrium potentials ( $\pm 0.002$  V) on inert W electrode from OCP measurement.

Temperature, K	$E_{Nd(III)/Nd(II)}$ vs. Ag/Ag <sup>+</sup> , V	$E_{Nd(II)/Nd(0)}$ vs. Ag/Ag <sup>+</sup> , V	$E_{Nd(III)/Nd(0)}$ vs. Ag/Ag <sup>+</sup> , V	$E_{Nd(III)/Nd(II)}$ vs. Cl <sub>2</sub> /Cl <sup>-</sup> , V	$E_{Nd(II)/Nd(0)}$ vs. Cl <sub>2</sub> /Cl <sup>-</sup> , V	$E_{Nd(III)/Nd(0)}$ vs. Cl <sub>2</sub> /Cl <sup>-</sup> , V
698	-1.858	-2.030	-1.973	-3.093	-3.264	-3.207
723	-1.842	-2.015	-1.957	-3.082	-3.254	-3.197
748	-1.825	-2.001	-1.942	-3.069	-3.245	-3.186
773	-1.807	-1.986	-1.926	-3.057	-3.235	-3.176

Table 3.8. Apparent standard potentials obtained from cyclic voltammetry and OCP method

Temperature, K	$E_{Nd(III)/Nd(0)}^*$ vs. Cl <sub>2</sub> /Cl <sup>-</sup> , V (Cyclic voltammetry)	$E_{Nd(III)/Nd(0)}^*$ vs. Cl <sub>2</sub> /Cl <sup>-</sup> , V (OCP)	Literature
723	-3.093	-3.070	-3.105 [4]
748	-3.079	-3.055	-3.113 at 733 K [5]
773	-3.065	-3.040	-3.079 [4]; -3.25 [9]
798	-3.050	-3.025	

$$E_{Nd(III)/Nd(0)}^{eq} = E_{Nd(III)/Nd(0)}^* + \frac{RT}{3F} \ln X_{Nd(III)} \quad (3.36)$$

The apparent standard potential for the redox couple Nd(III)/Nd(0) obtained from cyclic voltammetry and OCP method are listed in Table 3.8. The values are compared with those reported in literature. Our values are in agreement to those reported by Castrillejo *et al.*[10].

### 3.4.6.3 Estimation of apparent standard potentials for the U(III)/U(0)

#### 3.4.6.3.1 From cyclic voltammogram

Taking into account only the voltammograms recorded at low scan rate,  $25 \text{ mVs}^{-1}$ , for which the reduction of U(III)/U(0) is being considered reversible, the apparent standard potential was evaluated using Eq. 3.32. The apparent standard potential thus obtained versus the Ag/AgCl ( $X_{\text{AgCl}_3} = 0.0031$ ) was converted to the scale of  $\text{Cl}_2/\text{Cl}^-$  reference electrode using Eq.3.22 and Eq. 3.21. The apparent standard potentials of the redox couples U(III)/U(0) vs.  $\text{Cl}_2/\text{Cl}^-$  reference electrode at different temperatures were thus evaluated and are shown in Table 3.9.

#### 3.4.6.3.2 From open circuit potential transients

Open-circuit chronopotentiograms were obtained with a solution of  $\text{UCl}_3$  in LiCl-KCl melt at W electrode by applying a cathodic polarization ( $-1.6 \text{ V}$ ) for a short period (60-300 s) to form metallic U on the W surface. The open circuit potential was monitored as a function of time. Fig. 3.22 shows the open circuit potential transient obtained after depositing U metal on W electrode at  $-1.6 \text{ V}$  for 120 s at 723 K. A potential plateau at  $\sim -1.4 \text{ V}$  corresponding to the redox couple U(III)/U(0) may be seen in the figure which is the equilibrium potential for the redox couple. This potential is close to the potential of peak  $I_c$  in the cyclic voltammogram in Fig. 3.6. The apparent standard potential,  $E_{\text{U(III)/U(0)}}^*$ , was determined using the Nernst equation as done in case of Nd(III)/Nd(0) couple using Eq. 3.36. The equilibrium potentials and apparent standard potentials for U(III)/U(0) estimated from open circuit potential measurements at various temperatures are listed in Table 3.9.

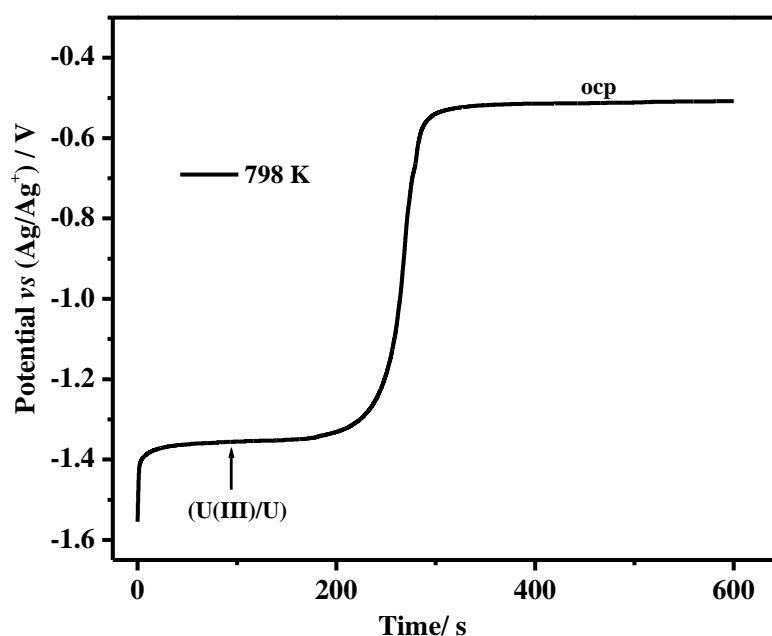
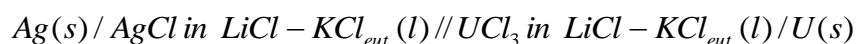


Fig. 3.22 Open circuit potential transient of LiCl-KCl-UCl<sub>3</sub> on W electrode at 798 K; Concentration of UCl<sub>3</sub>:  $7.31 \times 10^{-5}$  moles cc<sup>-1</sup>; Applied potential: -1.6 V.

#### 3.4.6.3.3 From emf method

In order to validate our measurement using transient techniques, the equilibrium potential of U(III)/U(0) was estimated from emf method also. These measurement were part of the studies carried out to investigate the U-Cd system by galvanic cell emf method which is more fully discussed in Chapter 4. The electromotive force of the following galvanic cell was measured in the temperature range 680-823 K.



A 4 mm diameter uranium metal electrode was held on a Ta strip using 1mm Ta wire. The Ta strip was welded to 1.5 mm Ta wire and the wire was sheathed in an alumina sleeve. The Ta wire served as lead electrode. The uranium rod was dipped in a solution of LiCl-KCl-UCl<sub>3</sub> melt contained in an alumina crucible. The temperature of the cell was monitored using a K-type thermocouple sheathed with an alumina sleeve and dipped in the melt. The equilibrium potential of U(III)/U(0) was measured against

Ag/AgCl reference electrode using a high impedance electrometer, Agilent 34970A and the data were acquired using Data Logger. The apparent standard potential,  $E_{U(III)/U(0)}^*$  was estimated using the Nernst equation using Eq. 3.32 for  $X_{UCl_3} = 0.0027$

The values of the equilibrium potential and apparent standard potentials for the redox couple U(III)/U(0) at different temperatures are shown in Table 3.9.

The apparent standard potential for the redox couple U(III)/U(0) obtained from cyclic voltammetry, OCP and emf measurement are compared with those reported in literature in Fig. 3.23. Our values measured by the three techniques are in agreement with each other with a standard deviation of  $\pm 10$  mV. It may be seen that apparent potentials values reported by different authors taken from the literature lie within  $\pm 35$  mV from the mean values as estimated by Masset *et al.* [22]. Our values lie close to the mean values given by Masset *et al.* We would like to emphasize that the values obtained from the open circuit potential measurement are very much in agreement with those obtained from the emf method. The present study has helped to reduce the uncertainty in the value of apparent standard potential of U(III)/U(0).

Table 3.9. Cathodic peak potential, equilibrium potential and apparent standard potentials of U(III)/ U(0) redox couple from different methods in LiCl-KCl melt at W electrode.

Temperatur e, K	$E_{pc_{U(III)/U(0)}}$ ( $\pm 0.003$ V) vs. Ag/Ag <sup>+</sup> , V (CV)	$E_{U(III)/U(0)}$ ( $\pm 0.003$ V) vs. Ag/Ag <sup>+</sup> , V (OCP)	$E_{U(III)/U(0)}$ ( $\pm 0.002$ V) vs. Ag/Ag <sup>+</sup> , V (emf)	$E_{U(III)/U(0)}^*$ ( $\pm 0.003$ V) vs. Cl <sub>2</sub> /Cl <sup>-</sup> , V (CV)	$E_{U(III)/U(0)}^*$ ( $\pm 0.003$ V) vs. Cl <sub>2</sub> /Cl <sup>-</sup> , V (OCP)	$E_{U(III)/U(0)}^*$ ( $\pm 0.002$ V) vs. Cl <sub>2</sub> /Cl <sup>-</sup> , V (emf)
673	-1.466	-1.453	-1.431	-2.565	-2.564	-2.546
723	-1.439	-1.417	-1.402	-2.537	-2.529	-2.518
748	-1.426	-1.399	-1.388	-2.522	-2.512	-2.505
773	-1.412	-1.381	-1.373	-2.508	-2.494	-2.496

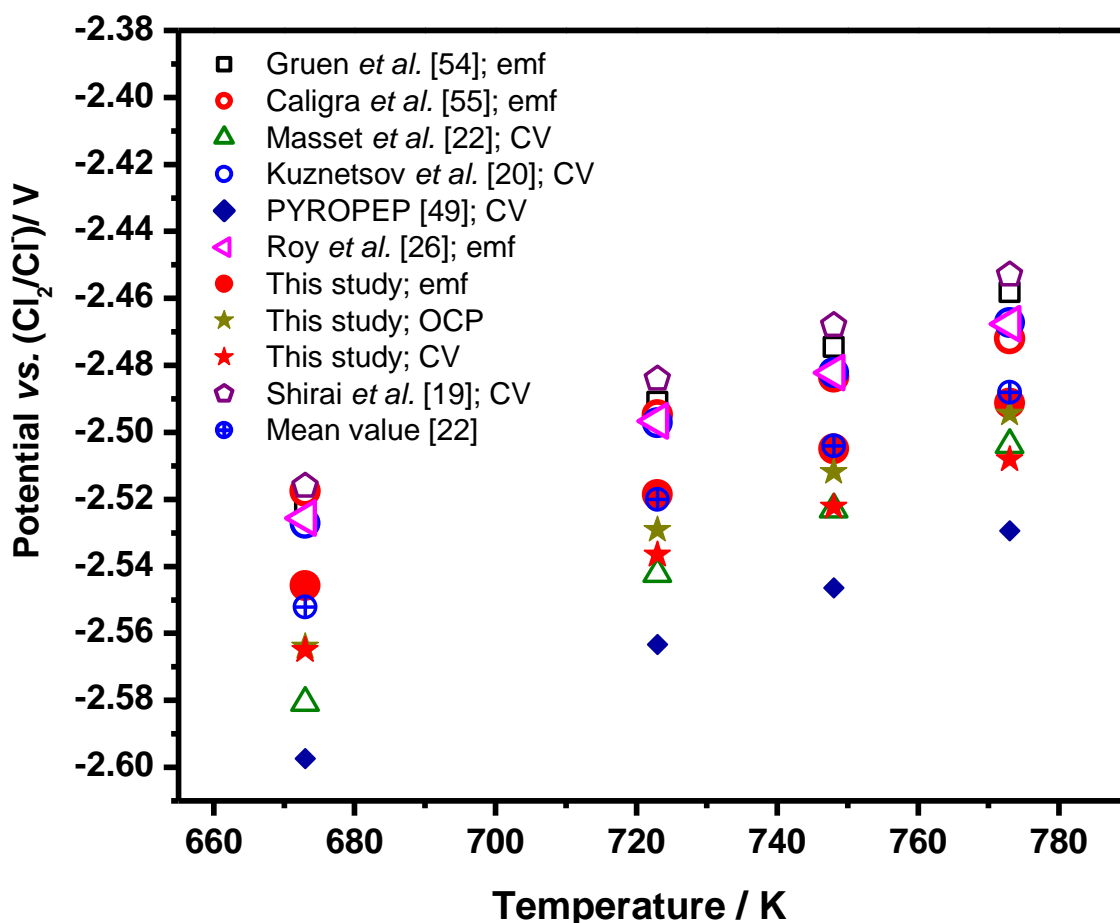


Fig. 3.23 Apparent standard potential for the redox couple U(III)/U(0) obtained from this study and those reported in literature.

### 3.5 Summary

The redox behavior and electrode kinetics for reduction of  $\text{LaCl}_3$  and  $\text{NdCl}_3$  at inert W electrode in LiCl-KCl eutectic melt were investigated by transient electrochemical techniques such as cyclic voltammetry, convolution method, chronopotentiometry and squarewave voltammetry and that for  $\text{UCl}_3$  by cyclic voltammetry and convolution method. The reduction of La(III) ion to La metal takes

place in a single step with three electron transfer. The reduction of Nd(III) ion to Nd metal on tungsten electrode takes place in two steps- Nd(III)/ Nd(II) and Nd(II)/ Nd(0). The reduction behavior of La(III) and Nd(III) ions on W electrode reported in literature show the single step and two step reduction process respectively. However, a detailed peak analysis (cyclic voltammograms) for the reduction of La(III) and Nd(III) ions on W electrode is presented in the chapter and the mechanism is supported by complimentary techniques (chronopotentiometry, squarewave voltammetry) in this study. The reduction of U(III) ion to U metal takes place in a single step with three electron transfer. The diffusion coefficient of La(III), Nd(III) and Nd (II) ions were determined. The kinetics for the reduction of La-, Nd- & U- trichlorides (by convolution method) is reported for the first time in this study. Analysis of the semi-integrals showed that the reduction of La(III)/La(0), Nd(II)/Nd(0) and U(III)/U(0) followed the quasi-reversible behavior. The reduction of Nd(III)/Nd(II) showed reversible electrode behavior. Heterogeneous rate constant for the reduction, La(III)/La(0), Nd(II)/Nd(0) and U(III)/U(0) were estimated from the convoluted voltammograms. The apparent standard electrode potentials,  $E_{La(III)/La(0)}^*$ ,  $E_{Nd(III)/Nd(II)}^*$ ,  $E_{Nd(II)/Nd(0)}^*$ ,  $E_{Nd(III)/Nd(0)}^*$  and  $E_{U(III)/U(0)}^*$  were estimated from the cyclic voltammograms and open circuit potential measurement.

The equilibrium potentials for La(III)/La(0), Nd(III)/Nd(0) and U(III)/U(0) redox couples obtained from the open circuit potential transient is reported for the first time. These values were used for converting the equilibrium potentials of the intermetallic compound obtained from the OCP measurement (made with Cd, Al & Ga electrodes) to their respective emf in the studies reported in chapters 4-6.

Estimation of the standard potential of the redox couple Nd(III)/Nd(0) is not possible by emf method due to the presence of Nd(II) ions in the melt. In the present study we could estimate the equilibrium potential of Nd(III)/Nd(0) from the open circuit

potential transients. This method allows the estimation of equilibrium potentials of redox couples such as Nd(III)/Nd(0), Am(III)/Am(0) etc. which is not possible by emf method due to the presence of the divalent ion.

A compilation of the values of the apparent standard potential reported from emf measurement and cyclic voltammetry reported by seven different authors and this work (from emf measurement, cyclic voltammetry and OCP ) is given in the chapter. The value from OCP method is within  $\pm 10$  mV from the methods used in this study. Also our values lie within the mean value of the literature values. This compilation shows that OCP method is suitable for deriving the standard potentials of redox species, M(X)/M(0).

### 3.6 References

1. G. Chauvin, M. Coriou, P. Jabot, A. Laroche, J. Nucl. Mater. 11 (1964) 183.
2. G. Boisdé, G. Chauvin, H. Coriou and J. Hure, Electrochim. Acta 5 (1961) 54-71.
3. S. A. Kuznetsov, M. Gaune-Escard, J. Nucl. Mater. 389 (2009) 108.
4. Y. Castrillejo, M.R. Bermejo, E. Barrado, A.M. Martinez, P. Diaz Arocas, J. Electroanal. Chem. 545 (2003) 141.
5. P. Masset, R.J.M. Konings, R. Malmbeck, J. Serp, J. P. Glatz, J. Nucl. Mater. 344 (2005) 173.
6. G. Bourges, D. Lambertin, S. Rochefort, S. Delpech, G. Picard, J. Alloys Compd. 444 (2007) 404.
7. Y. Castrillejo, M. R. bermejo, a. M. Martinez and P. Diaz arcas, J. Mining and Metallurgy, 39 (1-2) B (2003) 109.
8. Frederic Lantelme, Thierry Cartaller, Youssef Berghoute and Mohamed Hamdani, J. Electrochem Soc, 148 (9) (2001) C604.
9. K. Fukasawa, A. Uehara, T. Nagai, T. Fujii, H. Yamana, J. Alloys Compd. 509

- (2011) 5112.
10. H. Yamana, B. G. Park, O. Shirai, T. Fujii, A. Uehara, H. Moriyama, J. Alloys Compd. 66 (2006) 408.
  11. T. Yamamura, M. Mehmood, H. Maekawa, Y. Sato, Chem. Sustainable Development 12 (2004) 105.
  12. P. Taxil, L. Massot, C. Nourry, M. Gibilaro, P. Chamelot, L. Cassayre, J. Fluorine Chem. 130 (2009) 94.
  13. M. Gibilaro, L. Massot, P. Chamelot, P. Taxil, Electrochim. Acta 55 (2009) 281.
  14. A. Novoselova, V. Smolenski, Electrochim. Acta 87 (2013) 657.
  15. A. Osipenko, A. Maershin, V. Smolenski, A. Novoselova, M. Kormilitsyn, A. Bychkov J. Electroanal. Chem. 651 (2011) 67.
  16. S.A. Kuznetsov, M. Gaune-Escard, Electrochimica Acta 46 (2001) 1101.
  17. D. S. Poa, Z. Tomczuk, and R. K. Steunenber, J. Electrochem. Soc., **135**, (1988) 1161.
  18. K. Serrano and P. Taxil, J. Appl. Electrochem., **29** (1999) 497.
  19. O. Shirai., T. Iwai, Y. Suzuki, Y. Sakamura, H. Tanaka, J. Alloys Compd. 271 (1998) 685.
  20. S.A. Kuznetsov, H. Hayashi, K. Minato, M. Gaune-Escard, Electrochim. Acta 51(2006) 2463.
  21. B. Prabhakara Reddy, S. Vandarkuzhali, T. Subramanian, P. Venkatesh, Electrochim. Acta 49 (2004) 2471.
  22. P. Masset, D. Bottomley, R. Konings, R. Malmbeck, A. Rodrigues, J. Serp, J.P. Glatz J. Electrochem. Soc. 152 (6) (2005) A1109.
  23. J. A. Plambeck, in Encyclopaedia of Electrochemistry of the elements, vol X: “

- Fused Salt Systems” ,A. J. Bard (ed.), chapter 2, Marcel Dekker, New York, 1976.
24. S. P. Fusselman, J. J. Roy, D. L. Grimmitt, I. F. Grantham, C. L. Krueger, C. R. Nabelek, T. S. Storvick, T. Inoue, T. Hijikata, K. Kinoshita, Y. Sakamura, K. Uozumi, T. Kawai, N. Takahashi, *J. Electrochem. Soc.* 146 (7) (1999) 2573.
  25. D. L. Hill, J. Perano, and R. A. Osteryoung, *J. Electrochem. Soc.* 107 (1960) 698.
  26. J. J. Roy, L. F. Grantham, D. L. Grimmitt, S. P. Fusselman, C. L. Krueger, T. S. Storvick, T. Inoue, Y. Sakamura, and N. Takahashi, *J. Electrochem. Soc.* 143 (1996) 2487.
  27. Y. Sakamura, T. Hijikata, K. Kinoshita, T. Inoue, T.S. Storvick, C.L. Krueger, J.J. Roy, D.L. Grimmitt, S.P. Fusselman , R.L. Gay, *J. Alloys and Compds* 271–273 (1998) 592.
  28. S. N. Flengas, *Can. J. Chem.*, 39 (1961) 773.
  29. O. Shirai, K. Uozumi. T. Awai, Y. Arai, *Anal. Sci.* 17 (2001) i959.
  30. G. Mamantov, D.L. Manning, J.M. Dale, *J. Electroanal. Chem.* 9 (1965) 253.
  31. H. Matsuda, Y. Ayabe, *Z. Elektrochem.* 59 (1955) 494.
  32. S.A. Kuznetsov, H. Hayashi, K. Minato, M. Gaune-Escard, *J. Electrochem. Soc.* 152 (2005) C203.
  33. S.A. Kuznetsov, H. Hayashi, K. Minato, M. Gaune-Escard, *Electrochim. Acta* 51 (2006) 2463.
  34. Z. Galus, *Fundamentals of Electrochemical Analysis*, Ellis Horwood, London, 1994.
  35. K.B. Oldham, G.D. Zoski, *Anal. Chem.* 52 (13) (1980) 2116.
  36. L. Nadio, J.M. Saveant, D. Tessier, *J. Electroanal. Chem.* 52 (1974) 403.
  37. J. Serp, R.J.M. Konings, R. Malmbeck, J. Rebizant, C. Scheppler, J.P. Glatz, *J. Electroanal. Chem.* 561 (2004) 143.
  38. Y. Castrillejo, S. Palmero, M.A. Garcia, L. Deban, P. Sanchez Batanero,

- Electrochim. Acta 41 (15) (1996) 2461.
39. J. Ross Macdonald, Impedance Spectroscopy: Emphasizing Solid Materials and Systems, John Wiley and Sons Inc., New York, 1980, p. 285.
  40. M. Mohamedi, S. Martimet, J. Bouteillon, J.C. Poignet, Electrochem. Acta 44 (1998) 797.
  41. M Goto, K. B. Oldham, Analytical Chem., 45 (12) (1973) 2043.
  42. A.J. Bard, L.R. Faulkner, Electrochemical Methods. Fundamentals and Applications, 2<sup>nd</sup> Edition, Wiley New York, 2001, p. 310.
  43. J. Osteryoung, R.A. Osteryoung, Anal. Chem. 57 (1985) 101.
  44. L. Ramaley, M.S. Krasue, Anal. Chem. 41 (1969) 1362.
  45. A. Saila, M. Gibilaro, L. Massot, P. Chamelot, P. Taxil, A. M. Affoune, J. Electroanal. Chem. 642 (2010) 150.
  46. T. Store, G.M. Haarberg, R. Tunold, J. Appl. Electrochem. 30 (2000) 1351.
  47. Y. Castrillejo, S. Palmero, M.A. Garcia, L. Deban, P. Sanchez Batanero, Electrochim. Acta 41 (15) (1996) 2461.
  48. P. Delahay (Ed.), New Instrumental Methods in Electrochemistry. Theory, Instrumentation, and Applications to Analytical and Physical Chemistry, Interscience, New York, 1954, Chapter 6.
  49. J. P. Glatz, R. Malmbeck, C. Pernel, C. Scheppler, J. Serp, PYROREP Contract No. FIKW- CT-2000-00049, Project No. FIS5-1999-00199.
  50. S.N. Flengas, T.R. Ingraham, J. Electrochem. Soc. 106 (8) (1959) 714.
  51. L. Yang, R.G. Hudson, J. Electrochem. Soc. 106 (11) (1959) 986.
  52. S.A. Kuznetsov, L. Rycerz, M. Gaune-Escard, J.Nucl. Mater. 344 (1-3) (2005) 152.
  53. G. De Cordoba, A. Laplace, O. Conocar, J. Lacquement, C. Caravaca, Electrochim. Acta 54 (2008) 280.

54. D. M. Gruen, R. A. Osteryoung, *Ann. N.Y. Acad. Sci.* 79 (1960) 897.
55. F. Caligara, L. Martinot, G. Duyckaerts, *Bull. Soc. Chim. Belg.*, 76 (1967) 210.

## CHAPTER 4

### Electrochemical behavior of La-, Nd- and U-trivalent ions in LiCl-

### KCl eutectic melt on cadmium electrode

#### 4.1 Introduction

As discussed earlier, in the electrorefining process, liquid cadmium cathode is used to recover the trans-uranium metals. The activities of Pu and MA are reduced at the cadmium cathode and they co-deposit along with small amounts of U [1, 2]. The product will contain small amounts of rare earth metals also [3, 4]. Cd is considered to be a typical liquid metal cathode since the activities of Pu and MAs in the Cd phase are very small. Cd has a low melting point and sufficiently low boiling point. This property enables the distillation of Cd for the recovery of the actinides [5, 6]. Therefore, several studies were conducted on electrorefining using cadmium cathode and recovery of the actinides by distilling off cadmium [7]. The distribution behavior of actinides and lanthanides between the LiCl-KCl eutectic melt and liquid Cd were studied by equilibrium measurements to evaluate the thermodynamic properties for these elements with cadmium [8-12]. The activities of these elements in the liquid Cd phase and separation factors of actinide elements from rare earth elements were evaluated from the studies. However, the reduction behaviour of actinide and rare earth chlorides at the interface between the LiCl-KCl eutectic melt and liquid Cd are not much studied.

In the present work we had investigated the electrochemical behavior of  $\text{LaCl}_3$ ,  $\text{NdCl}_3$  and  $\text{UCl}_3$  on liquid cadmium pool cathode using cyclic voltammetry. The Gibbs energy formation of the intermetallics,  $\text{LaCd}_{11}$  and  $\text{NdCd}_{11}$  were estimated from the open circuit potential measurement on Cd film electrode.

The reduction behaviour of  $\text{UCl}_3$  in LiCl-KCl eutectic melt was studied on cadmium electrode in the temperature range 698-798 K using cyclic voltammetry. Gibbs

energy formation of  $UCd_{11}$  and the activity coefficient of uranium in the solvent rich region were computed from molten salt galvanic cell emf method.

## 4.2 Literature survey

Many studies have been reported on the reduction behaviour of lanthanides on cadmium cathode. Castrillejo *et al.* had investigated the electrochemical behaviour of some rare earths ions (Ce, La, Pr, Gd, Er, Ho) and Y in the LiCl–KCl eutectic at various reactive electrodes, namely, liquid Cd and Bi and solid Al electrodes. They had obtained the redox potentials for the rare earth metals and yttrium on these cathodes [13, 14]. They had derived the thermodynamic properties of their intermetallics using open circuit potential measurement. Shirai *et al.* had studied the reaction of  $LaCl_3$  on cadmium film cathode in LiCl-KCl- $LaCl_3$ - $CdCl_2$  melt by cyclic voltammetry. They had evaluated the Gibbs energy formation of the five intermetallic compounds of the La-Cd system using open circuit chronopotentiometry [15]. The work of Castrillejo *et al.* and Caravaca *et al.* had been compiled in the project report PYROREP [16]. The electrochemical behaviour of uranium on W electrode, lanthanides (La, Ce, Pr, Nd ) and Y on W, Cd, Bi and Al electrodes has been reported in the study. The standard reduction potentials of lanthanides on cadmium electrode were estimated from the cyclic voltammograms. The Gibbs energy formation of the various intermetallics of lanthanides with cadmium was estimated from the open circuit potential measurements. The activity coefficients of lanthanides in cadmium and other thermodynamic properties were evaluated from the electrochemical studies. Shibata *et al.* had studied the Ce-Cd system using electrochemical techniques. They had derived the Gibbs energy formation of six intermetallic compounds of the system [17]. Other than PYROREP [16], we have not come across any study on the behavior of  $NdCl_3$  on cadmium cathode in LiCl-KCl melt.

There have been many studies on the recovery of uranium, plutonium and minor actinides on liquid cadmium cathode at laboratory scale and engineering scale [18-20]. However, there are not many reports on the electrode reaction of the actinides on liquid cadmium pool cathode. Shirai *et al.* had studied the reduction behaviour of  $\text{PuCl}_3$  on cadmium cathode in LiCl-KCl melt by cyclic voltammetry and open circuit potentiometry [21]. They had derived the Gibbs energy formation of the intermetallics of Pu-Cd system. Iizuka *et al.* had studied the behaviour of Pu and Am in liquid Cd cathode and evaluated their redox potentials on Cd cathode [22]. To our knowledge, the reaction mechanism of uranium chloride on liquid cadmium electrode has been reported by Shirai *et al.* alone [23]. They had studied the reduction behaviour of  $\text{UCl}_3$  on cadmium cathode in LiCl-KCl melt using cyclic voltammetry and had observed underpotential deposition of uranium on cadmium due to formation of the intermetallic,  $\text{UCd}_{11}$ .

According to the phase diagram of the uranium-cadmium system,  $\text{UCd}_{11}$  is the only intermetallic compound and it decomposes peritectically to liquid +  $\alpha$  U beyond 746 K [24, 25]. Martin *et al.* [24] have constructed the phase diagram of the U-Cd system. They had studied the U-Cd system by thermal, metallographic, X-ray and sampling techniques. They had identified a single intermetallic compound,  $\text{UCd}_{11}$  which melts peritectically at 746 K to form  $\alpha$ -uranium and melt containing 2.5 wt % uranium in the cadmium rich region. A unique feature of the U-Cd system was the retrograde solubility of uranium in the temperature region 746-873 K. Shirai *et al.* [23] have reported the appearance of a peak in cyclic voltammograms recorded at temperatures above 746 K and had attributed the peak to  $\text{UCd}_{11}$  which is not consistent with the phase diagram. Also there is disagreement in value of the Gibbs energy of formation of the intermetallic,  $\text{UCd}_{11}$ , reported by Shirai *et al.* using cyclic voltammetry and those reported by Johnson *et al.* [25] by molten salt emf measurement and Veleckis *et al.* [26] using vapour pressure

measurement. To understand the anomalous behavior of U on cadmium cathode, we have studied the reduction behavior of uranium in liquid cadmium cathode using cyclic voltammetry and open circuit potential measurement in LiCl-KCl melt. The U-Cd system was also studied in the cadmium rich region by galvanic cell emf method in the temperature range 653 to 764 K.

### **4.3. Experimental**

#### **4.3.1. Chemicals**

Anhydrous lithium chloride (AR grade, M/s. Chempure Private Ltd, India), anhydrous potassium chloride (AR grade, M/s. Ranbaxy Fine Chemicals, India),  $\text{LaCl}_3$  (Alfa Aesar 99.99 %),  $\text{NdCl}_3$  (Alfa Aesar 99.99 %) and anhydrous cadmium chloride (M/s. Merck, Germany 99%) were used for the studies. High purity cadmium metal shots (Alfa Aesar 99.99%) were used for preparing the cadmium working electrode. Uranium metal of nuclear grade obtained from BARC, Mumbai was used for making uranium metal electrode, for preparation of  $\text{UCl}_3$  and uranium-cadmium alloys.

#### **4.3.2. Preparation of the electrolyte salt**

Purification of LiCl-KCl salt mixture was as described earlier in chapter 2. Preparation of LiCl-KCl- $\text{LaCl}_3$ , LiCl-KCl- $\text{NdCl}_3$  and LiCl-KCl- $\text{UCl}_3$  electrolytes was also carried out as discussed earlier in Chapter 2.

#### **4.3.3. Electrochemical apparatus and electrodes**

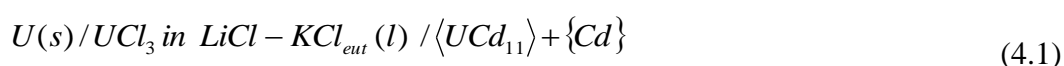
##### **4.3.3.1. Cyclic voltammetry**

A three electrode cell assembly was used for all the electrochemical measurements. The schematic of the electrochemical cell and the electrode assembly were as discussed in Chapter 2. The reference electrode consisting of a silver wire (2 mm dia) dipped in 0.31 mol % AgCl-LiCl-KCl mixture contained in a pyrex glass tube was used for all the measurements. All the potentials reported in this chapter are with respect to this

reference electrode unless otherwise specified. Different working electrodes were used for the studies: (a) 1.5 mm diameter tungsten wire, (b) cadmium pool electrode, (c) cadmium film electrode. The tungsten working electrode was sheathed with an alumina sleeve exposing 40 mm of the wire and the area of working electrode was calculated from the depth of immersion. The cadmium pool electrode was prepared by placing cadmium granules in an alumina crucible which was in turn placed in an SS 430 holder assembly. The crucible was immersed in molten LiCl-KCl to melt cadmium. A 1mm diameter tungsten wire covered with an alumina sheath was immersed in the cadmium melt through the SS assembly and this served as the lead wire. Photograph of the electrode assembly used for liquid cadmium cathode is shown in Fig. 4.1. The Cd film electrode were prepared in-situ by electrodepositing Cd on a W wire of 1.5 mm in diameter as working electrode from melt containing LiCl-KCl-CdCl<sub>2</sub>-UCl<sub>3</sub>. The electrodeposition was carried out at about -1 V vs. reference electrode for a period of 300 s. A tantalum wire of 1mm in diameter, coiled at one end was used as the counter electrode. The instrumentation, assembling of cell and other experimental procedures are the same as described in Chapter 2.

#### 4.3.3.2. Galvanic cell emf measurement

The electromotive force of the following galvanic cell was measured in the temperature range 653 to 764 K.



The uranium metal electrode was tied on to a Ta strip using 1mm Ta wire. The Ta strip was welded to 1.5 mm Ta wire and the wire was sheathed in an alumina sleeve. The Ta wire served the as lead electrode. The alloy electrode was prepared by taking stoichiometric amounts of uranium metal and cadmium shots in an alumina crucible which was placed in an SS 430 assembly similar to that used for cadmium pool cathode.

The crucible was immersed in molten LiCl-KCl to melt the cadmium. The reaction was allowed to proceed for completion by equilibrating for several hours. A 1mm diameter tungsten wire covered with an alumina sheath was immersed in the alloy melt and this served as the lead wire. Alternately, the alloy was also prepared by electrotransport of uranium from uranium electrode to a liquid cadmium electrode in a cell containing LiCl-KCl-UCl<sub>3</sub> electrolyte. Assembling of the cell and positioning of the set-up in the furnace are the same as described in Chapter 2. The cell was heated to the desired temperature and the emf values were allowed to stabilize for several hours. The emf of the cell was measured using a high impedance electrometer, Agilent 34970A and the data were acquired using a Data Logger.

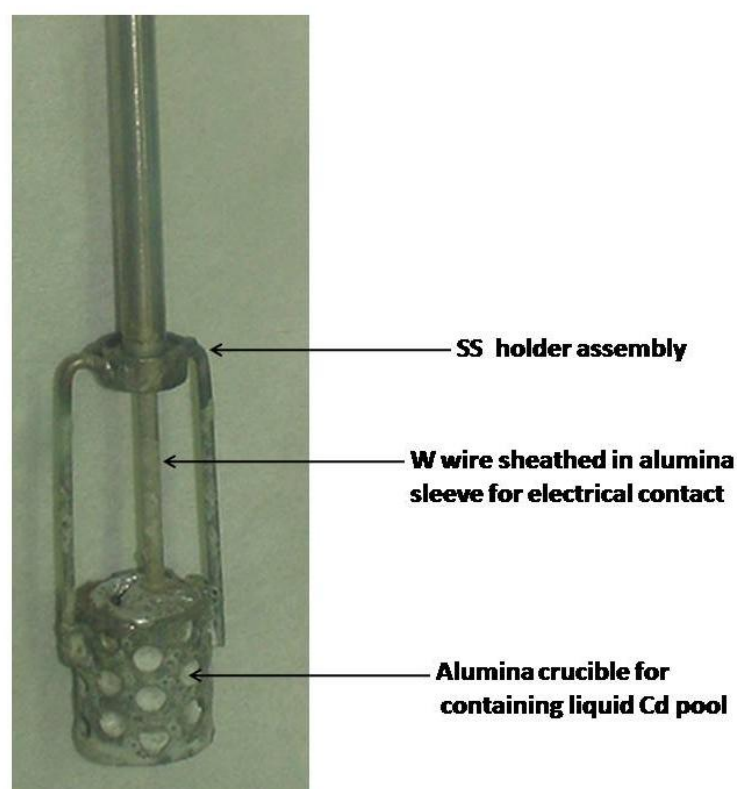


Fig. 4.1 Photograph of the electrode assembly for liquid cadmium cathode.

## 4.4 Results and discussion

### 4.4.1 Reduction behaviour of $\text{LaCl}_3$ and $\text{NdCl}_3$ at the Cd electrode

#### 4.4.1.1 Cyclic voltammetry

Fig. 4.2 compares the cyclic voltammogram recorded for molten LiCl-KCl on tungsten inert electrode with that on liquid cadmium pool electrode. It may be observed that the electrochemical window of the LiCl-KCl melt is limited by the dissolution of Cd at  $\sim -0.5$  V in the anodic side and under-potential deposition of lithium on cadmium surface forming Li-Cd alloy ( $\sim -1.6$ V) on the cathodic side, when cadmium was used as the cathode. Behavior of  $\text{LaCl}_3$  and  $\text{NdCl}_3$  on cadmium pool and film electrodes were studied in LiCl-KCl melt at various temperatures using cyclic voltammetry. Fig. 4.3a and Fig. 4.3b show the cyclic voltammograms of  $\text{LaCl}_3$  and  $\text{NdCl}_3$  in LiCl-KCl melt at 748 K on liquid cadmium pool cathode, respectively. Reduction of  $\text{LaCl}_3$  and  $\text{NdCl}_3$  on these electrodes takes place at much positive potential than on the W electrode. The behavior is attributed to the reduced activity of La and Nd on Cd surface due to formation of the intermetallic compounds of La-Cd and

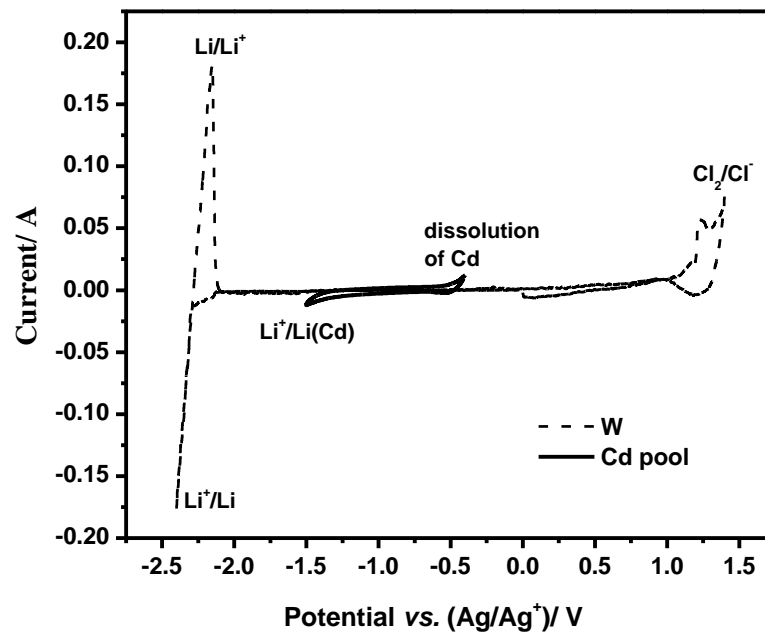


Fig. 4.2 Cyclic voltammograms for LiCl-KCl melt on W and Cd pool cathodes.

Temperature: 698 K; Area: 0.314 cm<sup>2</sup> (W) and 0.21 cm<sup>2</sup> (Cd)

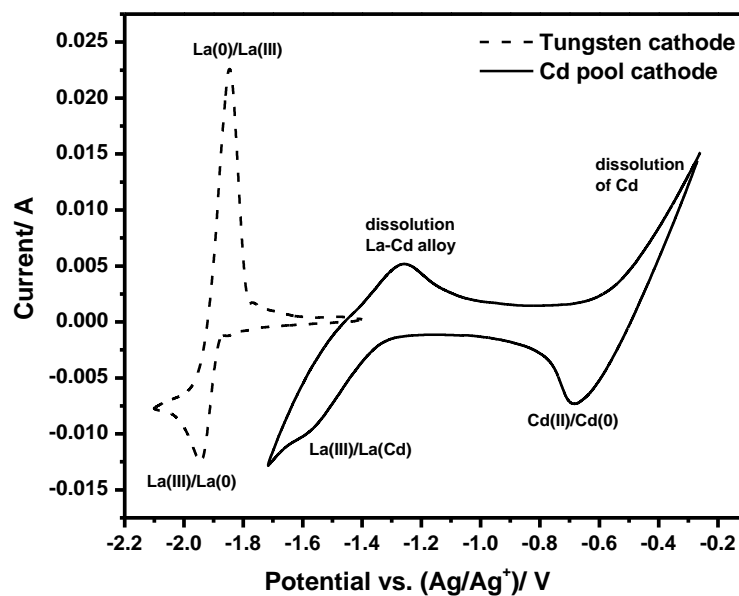


Fig. 4.3a Cyclic voltammograms for LaCl<sub>3</sub> in LiCl-KCl melt at cadmium pool electrode.

Polarization rate: 10 mVs<sup>-1</sup>; Concentration of LaCl<sub>3</sub>: 6.66 × 10<sup>-5</sup> mol cm<sup>-3</sup>.

Nd-Cd systems. Thus underpotential deposition of lanthanum and neodymium occur on cadmium electrode. The reduction of La(III) and Nd(III) ions on Cd surface takes place in a single step with three electron transfer. It may be recalled that reduction of Nd(III) ion to Nd metal takes place in two steps on W electrode with the formation of Nd(II) ion as the intermediate which was discussed in Chapter 3, whereas the reduction of Nd(III) ion takes place in a single step with three electron transfer on cadmium electrode forming intermetallic compound during the cathodic cycle and dissolution of the alloy during the anodic cycle.

Fig. 4.4 and Fig. 4.5 show the phase diagrams of the La-Cd system and Nd-Cd systems respectively [27, 28]. Lanthanum and neodymium form various intermetallic compounds with cadmium. However we have observed only one redox peak predominantly for both the electrodes. It may be envisaged from the phase diagram and also from the extent of potential shift towards the anodic direction that the substrate rich intermetallic is formed in both the cases. The electrode reaction for the reduction of La(III) and Nd(III) ions on Cd electrode is given by,



Formation of  $\text{RECD}_{11}$  has been reported for other lanthanides in the literature [14, 15, 29]. Further, the fact that the compounds formed are  $\text{LaCd}_{11}$  and  $\text{NdCd}_{11}$  has been supported by the XRD pattern of the electrodeposits, details of which will be discussed in *section 4.4.1.5*.

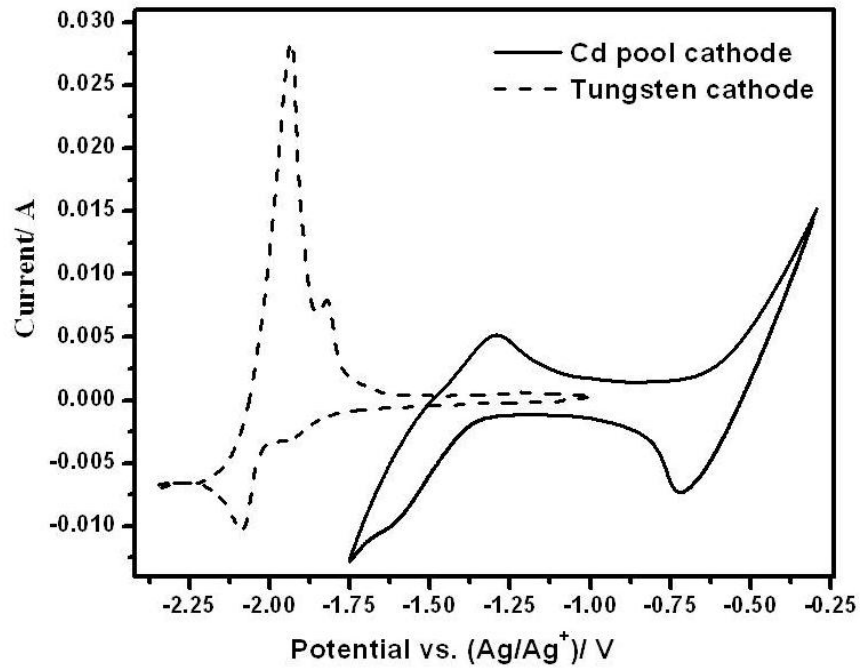
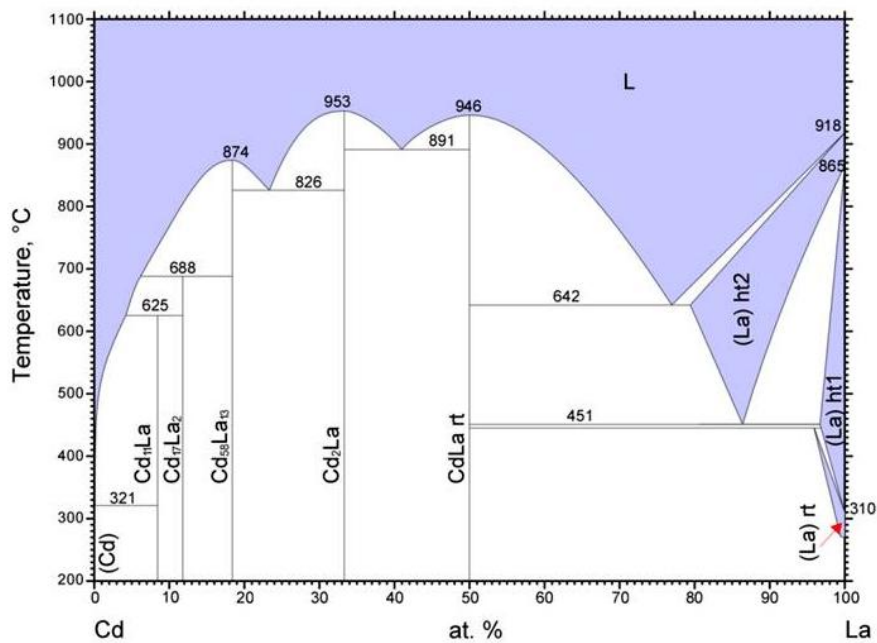


Fig. 4.3b Cyclic voltammograms for  $\text{NdCl}_3$  in  $\text{LiCl-KCl}$  melt at cadmium pool electrode.

Polarization rate:  $10 \text{ mVs}^{-1}$ ; Concentration of  $\text{NdCl}_3$ :  $6.66 \times 10^{-5} \text{ mol cm}^{-3}$ .



© ASM International 2006. Diagram No. 900586

Fig. 4.4 Cd-La phase diagram [27].

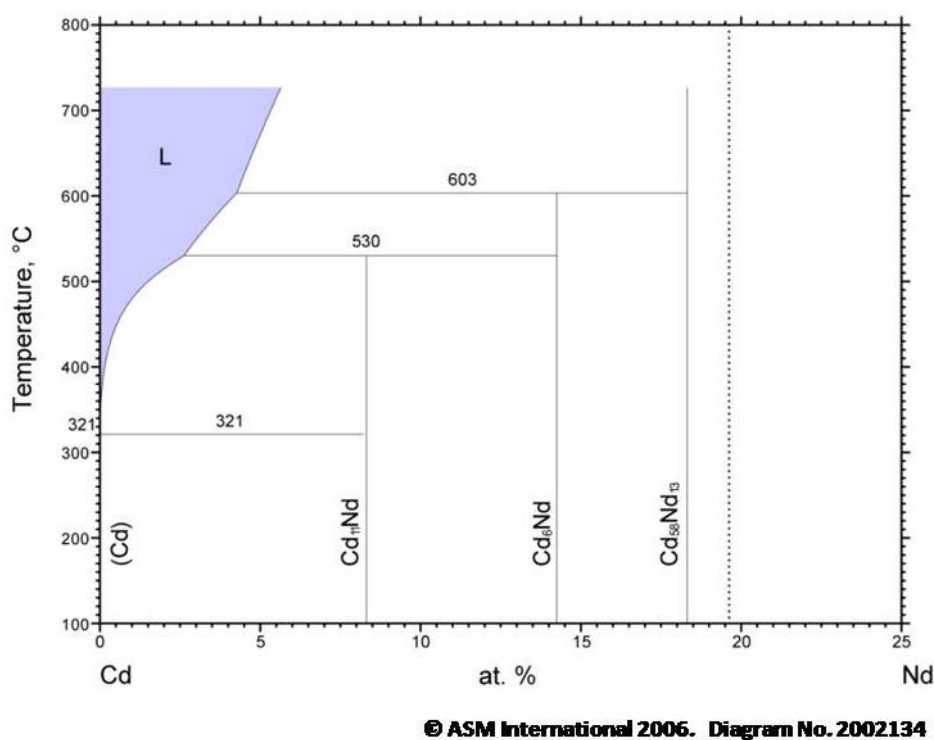


Fig. 4.5 Cd-Nd phase diagram [28].

#### 4.4.1.2 Estimation of apparent standard potential for $RE(III)/RE(Cd)$ from cyclic voltammograms

Fig. 4.6 compares the cyclic voltammograms recorded for a solution of  $NdCl_3$  in  $LiCl-KCl$  at 723 K on cadmium pool and cadmium film electrodes and the inset of Fig. 4.6 shows the cyclic voltammogram on cadmium film electrode at different scan rates at 698 K. Fig. 4.7 shows the cyclic voltammograms recorded for a solution of  $LaCl_3$  in  $LiCl-KCl$  at 748 K on cadmium film electrode at different scan rates. The reduction peak and the oxidation peak currents appeared at much positive potentials than those on tungsten inert electrode. On the cadmium pool electrode, the cathodic and anodic peaks are similar to those for soluble-soluble reversible system. The cathodic peak potentials do not shift appreciably

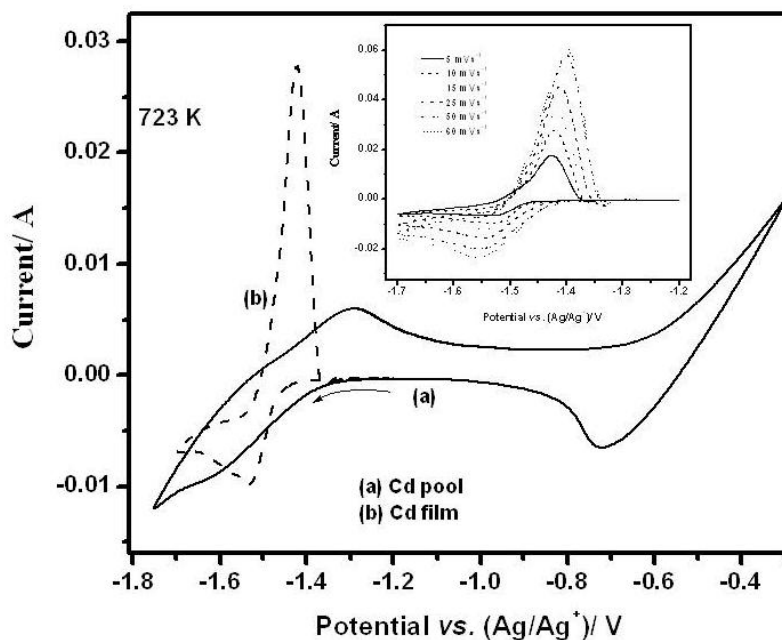


Fig. 4.6 Comparison of cyclic voltammograms for LiCl-KCl-NdCl<sub>3</sub> melt at Cd pool and film electrode; Polarization rate: 10 mVs<sup>-1</sup>; Concentration of NdCl<sub>3</sub>: 6.66 × 10<sup>-5</sup> mol cm<sup>-3</sup>. Inset: Cyclic voltammograms at Cd film electrode at different scan rates; Temperature: 698 K.

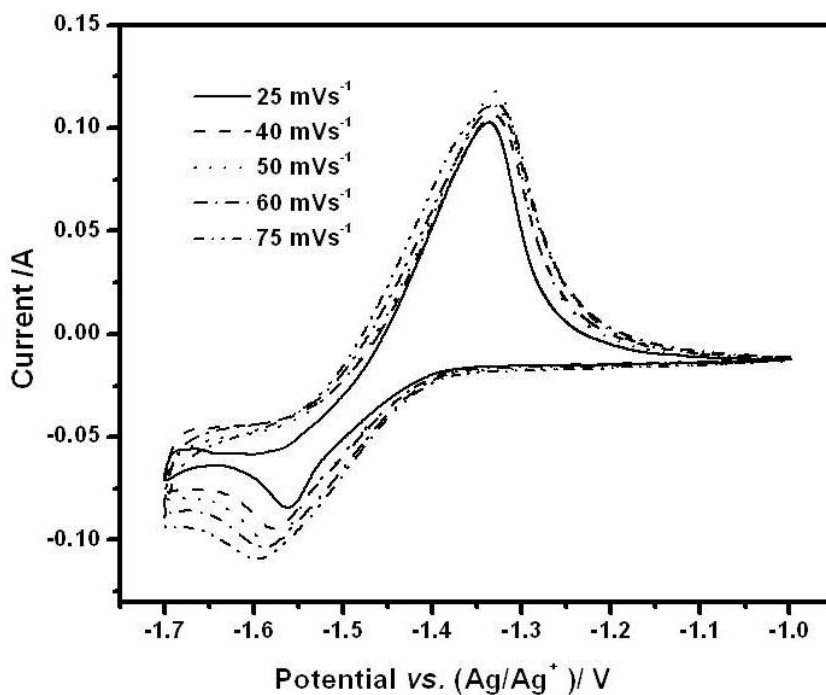


Fig. 4.7 Cyclic voltammograms for LaCl<sub>3</sub> in LiCl-KCl at cadmium film electrode at different scan rates. Temperature: 748 K.

with increase in the polarization rates. The magnitude of  $E_{p_c} - E_{p_c/2}$  is in agreement with the one expected for soluble-soluble couple (Eq. 4.3) for a three electron transfer [30]. Thus, the reduction is presumed to show Nernstian behavior.

$$E_p - E_{p/2} = -2.2 \frac{RT}{nF} \quad (4.3)$$

Assuming that the concentration of RE(III) ions is very less than that required for exceeding saturation, we have used the voltammetric curves to derive the half wave potential, using Eq. (4.4) for a soluble-soluble reversible system. For soluble-soluble species, the half wave potential,  $E_{1/2}$ , is related to the standard potential and apparent standard potential by the following relation [21, 31, 32]

$$E_{1/2} = (E_p^C + E_p^A)/2 \quad (4.4)$$

Where

$$E_{1/2} = E_{RE(III)/RE(Cd)}^0 + \frac{RT}{3F} \ln \frac{\sqrt{D_{RE(Cd)}}}{\sqrt{D_{RE(III)}}} + \frac{RT}{3F} \ln \left( \frac{\gamma_{RE(III)}}{\gamma_{RE(Cd)}} \right) \quad (4.5)$$

And the apparent standard potential is described as

$$E_{RE(III)/RE(Cd)}^* = E_{RE(III)/RE(Cd)}^0 + \frac{RT}{3F} \ln \left( \frac{\gamma_{RE(III)}}{\gamma_{RE(Cd)}} \right) \quad (4.6)$$

Hence we get,

$$E_{RE(III)/RE(Cd)}^* = E_{1/2} + \frac{RT}{3F} \ln \frac{\sqrt{D_{RE(III)}}}{\sqrt{D_{RE(Cd)}}} \quad (4.7)$$

where  $E_{RE(III)/RE(Cd)}^0$  and  $E_{RE(III)/RE(Cd)}^*$  are the standard potential and apparent standard potential of the RE(III)/RE(Cd) redox couple. The apparent standard potentials,  $E_{La(III)/La(Cd)}^*$  and  $E_{Nd(III)/Nd(Cd)}^*$  were obtained from the cyclic voltammograms using Eq. 4.4 and Eq.4.7. Since cadmium is a liquid at the temperature of study, it is assumed that the diffusion coefficient of RE in the salt phase and cadmium phase are identical. Similar

assumption has been made by other authors earlier [14, 15, 23]. The potentials thus obtained versus the reference electrode, Ag/AgCl ( $X_{AgCl} = 0.0031$ ), were converted to the scale of  $Cl_2/Cl^-$  reference electrode using the relation given by Yang and Hudson (Eq. 3.21 and Eq. 3.22) discussed in chapter 3. The values of apparent standard potentials,  $E_{La(III)/La(Cd)}^*$  and  $E_{Nd(III)/Nd(Cd)}^*$  are shown in Table 1 and 2 respectively. The apparent standard potentials obtained from this study are compared to those reported in the project report PYROREP in the Tables [16]. The present data of  $NdCl_3$  on cadmium electrode are comparable to those of PYROREP but those for  $LaCl_3$  differ from those of PYROREP by about 30 mV.

The difference between the cadmium pool electrode and film electrode is that the amount of Cd in the film electrode is limited. So the deposited metal exceeds its solubility in Cd and the electrode loses its homogeneity. Appearance of separate solid phase makes the voltammograms on cadmium film electrode less accurate for estimating the half wave potential than those obtained from cadmium pool electrode. It may be observed in Fig. 4.6 that the onset potential for the reduction on film electrode is more cathodic than that on pool electrode. The half wave potentials on Cd film electrode are shifted cathodically by  $\sim 30$  mV. Hence we have estimated the apparent standard potentials from the cyclic voltammograms recorded on cadmium pool electrode.

#### ***4.4.1.3 Open-circuit chronopotentiometry***

Open-circuit potential measurements were recorded after depositing the RE on cadmium film electrode by polarizing the electrode at -1.7 V using LiCl-KCl- $RECl_3$  melt. Fig.4.8 shows the open circuit potential transient curve on the cadmium film cathode

Table 4.1 Apparent standard potentials ( $\pm 0.002$  V) for La(III)/La(Cd) estimated from cyclic voltammogram on Cd pool electrode,  $X_{LaCl_3} = 0.00224$ .

Temperature, K	$E_{La(III)/La(Cd)}^*$ vs. Ag/Ag <sup>+</sup> , V	$E_{La(III)/La(Cd)}^*$ vs. Cl <sub>2</sub> /Cl <sup>-</sup> , V	$E_{La(III)/La(Cd)}^*$ vs. Cl <sub>2</sub> /Cl <sup>-</sup> , V [16]
698	-1.471	-2.705	-2.730 (693 K)
723	-1.453	-2.693	-2.728
748	-1.436	-2.681	-
773	-1.419	-2.668	-2.707

Table 4.2 Apparent standard potentials ( $\pm 0.002$  V) for Nd(III)/Nd(Cd) estimated from cyclic voltammogram on Cd pool,  $X_{NdCl_3} = 0.00224$ .

Temperature, K	$E_{Nd(III)/Nd(Cd)}^*$ vs. Ag/Ag <sup>+</sup> , V	$E_{Nd(III)/Nd(Cd)}^*$ vs. Cl <sub>2</sub> /Cl <sup>-</sup> , V	$E_{Nd(III)/Nd(Cd)}^*$ vs. Cl <sub>2</sub> /Cl <sup>-</sup> , V [16]
698	-1.499	-2.733	-2.736 (673)
723	-1.487	-2.726	-2.721
733	-1.482	-2.723	-
758	-1.469	-2.716	-
773	-1.462	-2.711	-2.703

monitored at different temperatures for LiCl-KCl-LaCl<sub>3</sub> melt and Fig. 4.9 that for LiCl-KCl-NdCl<sub>3</sub> melt. A distinct potential plateau is seen in both the cases. The presence of the plateau indicates that there is equilibrium between two co-existing phases. From the phase diagram and our observations from the cyclic voltammograms, it may be concluded that the plateau corresponds to the coexistence of the phases, RECd<sub>11</sub> and (Cd). Though

La and Nd forms various intermetallic compounds with Cd, only one intermetallic is predominantly formed under our experimental condition.

#### 4.4.1.4 Thermodynamic properties of La-Cd and Nd-Cd systems

The measurement of equilibrium potential for Nd(III)/Nd(0) redox couple by OCP method was described in *section 3.4.6.2.2* in chapter 3. The equilibrium potential of the La(III)/La(0) couple was obtained from the open-circuit chronopotentiograms recorded with a solution of LaCl<sub>3</sub> in LiCl-KCl melt at W electrode. The OCP transient curves were obtained by applying a cathodic polarization (-2.1 V) for a period 300 s to deposit La metal on the W surface. The open circuit potential was monitored as a function of time. A potential plateau at ~ -2 V corresponding to the redox couple La(III)/La(0) was observed in the transient which is the equilibrium potential for the redox couple. The potentials of the plateaus that were measured with respect to the reference electrode, Ag/AgCl ( $X_{AgCl} = 0.0031$ ), in LiCl-KCl-RECl<sub>3</sub> melt on cadmium film electrode using the OCP method were converted to the equilibrium potentials of the RE(III)/RE(0) couple obtained as described above. The potential of the plateau referred to the rare earth metal electrode is the emf of the cell represented by



The emf was evaluated for different temperatures for La-Cd and Nd-Cd systems. The Gibbs energy formation of the intermetallics, LaCd<sub>11</sub> and NdCd<sub>11</sub> at different temperatures

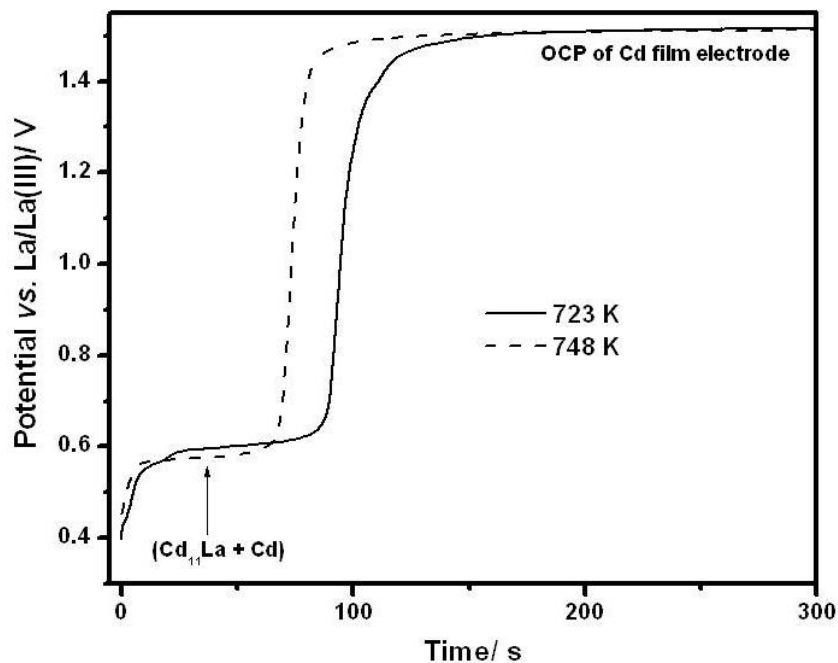


Fig. 4.8 Open circuit potential transient curve for LaCl<sub>3</sub> in LiCl-KCl melt on Cd film electrode. Cathodic polarization: -1.7 V vs. (Ag/Ag<sup>+</sup>) reference electrode.

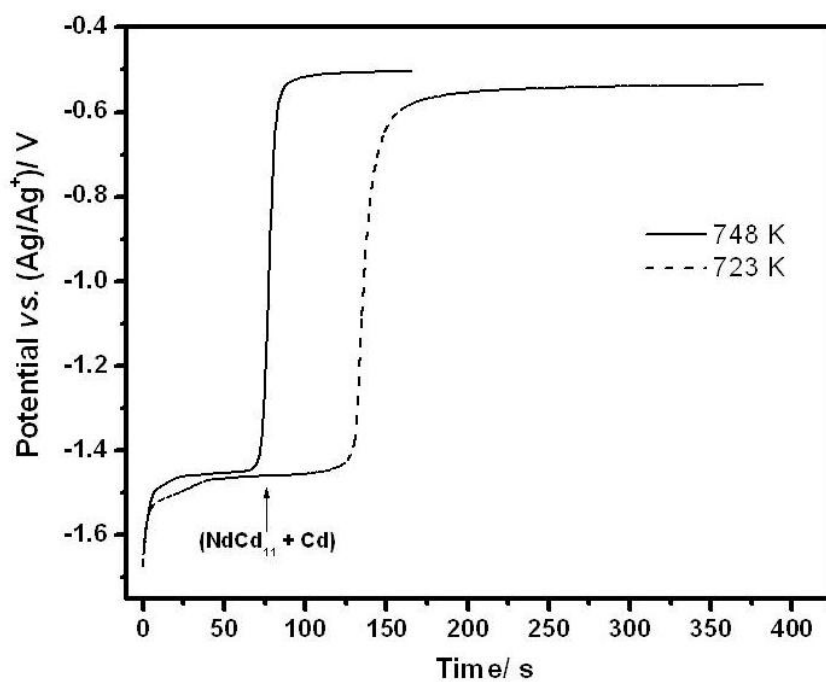


Fig. 4.9 Open circuit potential transient curve for NdCl<sub>3</sub> in LiCl-KCl melt on Cd film electrode. Cathodic polarization: -1.7 V vs. (Ag/Ag<sup>+</sup>) reference electrode.

were estimated from the emf values and are shown in Table 3 and Table 4 respectively. The activity of RE in cadmium was calculated from Eq. 4.9 and the values are given in Table 3 and 4.

$$emf = -\frac{RT}{3F} \ln a_{RE(Cd)} \quad (4.9)$$

The excess Gibbs energy of RE in cadmium,  $\Delta G_{RE(Cd)}^{exc}$  was evaluated using Eq. 4.10 [35-36]

$$\Delta \bar{G}_{RE}^{xs} = RT \ln \gamma_{RE(Cd)} = -3F\Delta E - RT \ln X_{RE(Cd)} \quad (4.10)$$

The mole fraction of RE in cadmium,  $X_{RE(Cd)}$  was taken from the solubility data reported in the literature [37, 38].

Solubility (La-Cd system),  $X$  (mol %)

$$593-899 \text{ K } \text{Log}(X) = 7.350 - 6061/T \quad (4.12)$$

Solubility (Nd-Cd system),  $X$  (mol %)

$$593-803 \text{ K } \text{Log}(X) = 6.909 - 5211/T \quad (4.13)$$

The thermodynamic properties for RE-Cd system estimated from OCP measurements are shown in Table 5 and 6. The low activity coefficient values show the strong interaction between the rare earth metal with cadmium. The values of Gibbs energy of formation of  $\text{LaCd}_{11}$  obtained from the OCP measurement is compared to those reported in literature. Our values are in good agreement with those reported by Johnson *et al.* [39]. The value of Gibbs energy formation of  $\text{NdCd}_{11}$  obtained from the OCP measurement is compared to those reported in the project report PYROREP [16] and it may be seen that the values are in agreement. The activity coefficients of the lanthanides in cadmium reported by Sakamura *et al.* and Johnson *et al.* are also shown in the table [40, 41]. The activity coefficients of the lanthanides in cadmium are in good agreement with those reported by Sakamura *et al.*

Table 4.3 Gibbs energy of formation of  $\text{LaCd}_{11}$  estimated from OCP measurement on Cd film electrode.

Temperature, K	emf ( $\pm 0.003$ ) V	$\Delta_f G_{\text{LaCd}_{11}}$ , $\text{kJ mol}^{-1}$			
		This study OCP	Johnson <i>et al.</i> [39] emf	Shirai <i>et al.</i> [15] OCP	PYROREP [16] OCP
698	0.608	-176.2	-175.2	-156.4	-
723	0.596	-172.7	-170.6	-152.3	-164.7
748	0.585	-169.2	-166.1	-148.1	-
762	0.578	-167.3	-163.5	-145.8	-

Table 4.4 Gibbs energy of formation of  $\text{NdCd}_{11}$  estimated from OCP measurement on Cd film electrode.

Temperature, K	emf ( $\pm 0.002$ ) V	$\Delta_f G_{\text{Cd}_{11}\text{Nd}}$ , $\text{kJ mol}^{-1}$	
		This study OCP	PYROREP [16] OCP
698	0.531	-153.6	-
723	0.529	-153.1	-157.2
733	0.527	-152.5	-
773	0.521	-150.7	-

Table 4.5 Thermodynamic properties of La in Cd estimated from OCP measurement on Cd film electrode

Temperature, K	$\log a_{La(Cd)}$	$\Delta\bar{G}_{La}^{xs}$ kJ mol <sup>-1</sup>	$\log \gamma_{La(Cd)}$			
			This study (OCP)	PYROREP [16] (CV)	Sakamura <i>et al.</i> [40] (emf)	Johnson <i>et al.</i> [41] (emf)
698	-13.2	-131.5	-9.8	-9.3	-9.7	-10.6
723	-12.5	-130.5	-9.4	-8.7	-9.3	-10.0
748	-11.8	-129.9	-9.1	-	-8.9	-9.3
773	-11.5	-129.3	-8.9	-7.8	-8.4	-8.7

Table 4.6 Thermodynamic properties of Nd in Cd estimated from OCP measurement on Cd film electrode

Temperature, K	$\log a_{Nd(Cd)}$	$\Delta\bar{G}_{Nd}^{xs}$ kJ mol <sup>-1</sup>	$\log \gamma_{Nd(Cd)}$		
			This study (OCP)	PYROREP [16] (CV)	Sakamura <i>et al.</i> [40] (emf)
698	-11.5	-119.4	-8.9	-9.4 (673 K)	-9.1
723	-11.1	-121.3	-8.8	-8.5	-8.7
733	-10.9	-121.6	-8.6	-	-8.5
773	-10.2	-123.6	-8.4	-7.6	-7.92

#### **4.4.1.5 Electrodeposition**

To examine the alloy formed on the cadmium surface, potentiostatic electrolysis was carried out using LiCl-KCl-RECl<sub>3</sub>-CdCl<sub>2</sub> melt (RE- La, Nd). A Ta sheet was polarized at -1.55 V vs. Ag/AgCl reference electrode for 5 hours. This potential is slightly cathodic to the potential plateau observed in the OCP measurement for the La-Cd and Nd-Cd systems. Co-deposition of Cd and the rare earth metal (La, Nd) occurs to form the stable intermetallic compound on the W surface. The cathode deposit adhered with salt was powdered, placed in a glass slide and sealed thoroughly to ensure it was air tight for characterization by XRD analysis. Fig. 4.10 shows the XRD pattern of the cathode deposit obtained using LiCl-KCl-RECl<sub>3</sub>-CdCl<sub>2</sub>. The XRD pattern shows the formation of the intermetallic NdCd<sub>11</sub>.

#### **4.4.2 Electrochemical study of uranium at liquid cadmium electrode**

##### **4.4.2.1 Cyclic voltammetry**

Cyclic voltammograms were recorded for LiCl-KCl-UCl<sub>3</sub> melt at cadmium pool and cadmium film electrodes. Fig. 4.11 shows the cyclic voltammograms of LiCl-KCl containing  $2.44 \times 10^{-5}$  moles cm<sup>-3</sup> UCl<sub>3</sub> on a cadmium pool cathode at different temperatures. Reduction of UCl<sub>3</sub> on a cadmium cathode takes place at a less cathodic potential than that observed on the inert W electrode. Only a single peak couple is observed for the redox process on cadmium pool electrode. The reduction peak is attributed to under potential deposition of uranium metal on the cadmium electrode due to lowering of activity of uranium in cadmium. A shift of about 150 mV in the peak potential towards positive direction was observed. Similar observation was made by Shirai *et al.* [23] in their study on electrode reaction of UCl<sub>3</sub> in cadmium pool cathode in LiCl-KCl melt. Fig. 4.12 shows the phase diagram of the

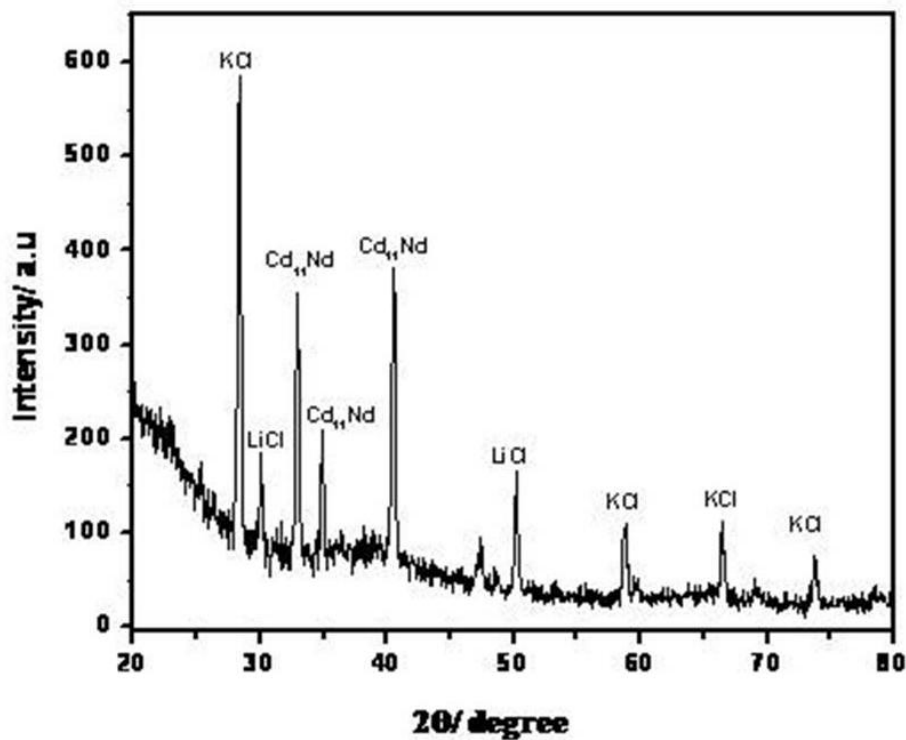


Fig. 4.10 XRD pattern of Nd-Cd film formed by potentiostatic electrolysis at  $-1.55\text{V}$  vs.  $(\text{Ag}/\text{Ag}^+)$  reference electrode in  $\text{LiCl-KCl-NdCl}_3\text{-CdCl}_3$  melt for 5 hrs at 748 K.

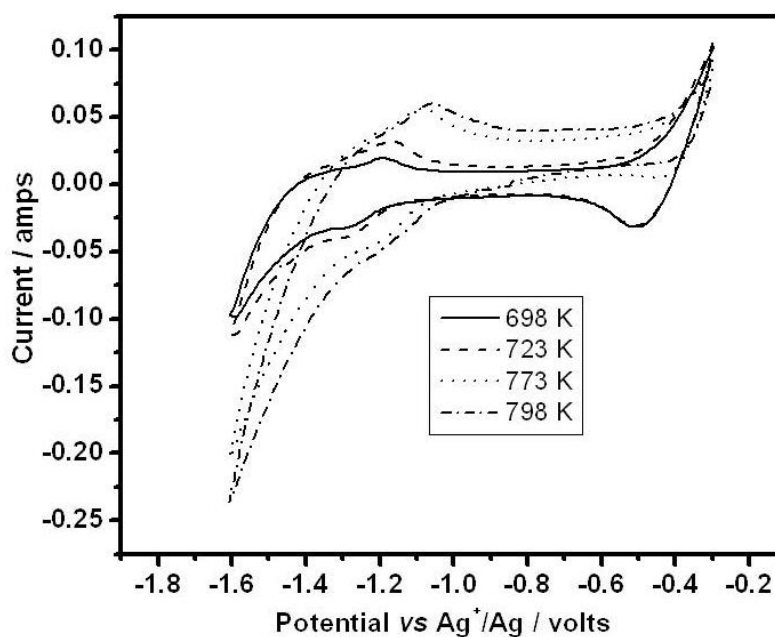


Fig. 4.11 Cyclic voltammogram for  $\text{LiCl-KCl-UCl}_3$  melt at different temperatures on cadmium pool cathode; Concentration of  $\text{UCl}_3$ :  $2.44 \times 10^{-5}$  moles  $\text{cm}^{-3}$ ;  $\text{Ag}/\text{AgCl}$  ( $X_{\text{AgCl}} = 0.001$ ).

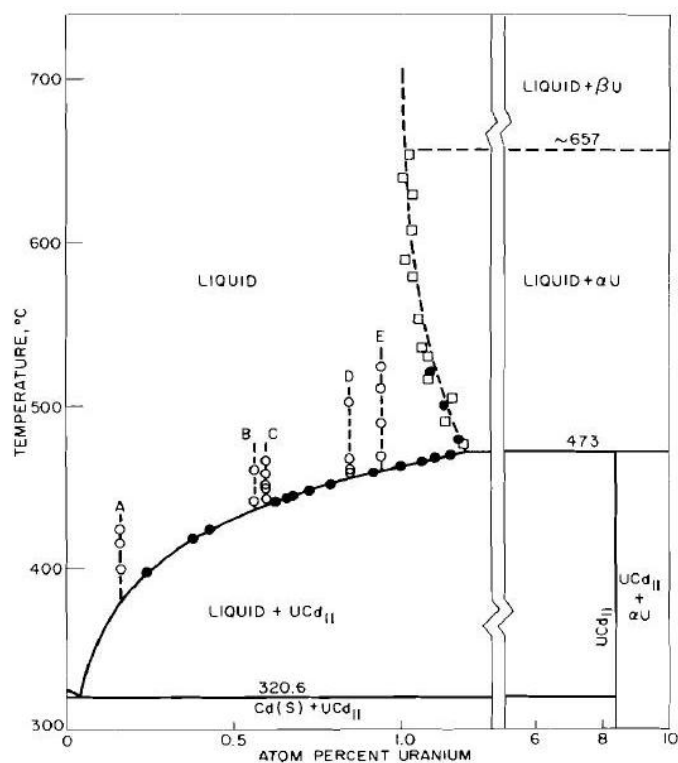


Fig. 4.12 The cadmium- uranium phase diagram in Cd rich side [25].

U-Cd system in the cadmium rich region [25]. It is deduced that uranium deposits as  $\text{UCd}_{11}$  as it is the only stable intermetallic compound for this system.



Fig. 4.13 shows the cyclic voltammograms of  $\text{LiCl-KCl-UCl}_3$  on a cadmium film electrode at various polarization rates. Unlike the cyclic voltammograms on the cadmium pool, two distinct peaks were seen on a cadmium film electrode. Fig. 4.14 compares the cyclic voltammograms obtained on W, cadmium pool and cadmium film electrodes. It may be seen that peak  $\text{II}_c$  appears at a potential close to that for  $\text{U(III)/U(0)}$  on inert W electrode. Peak  $\text{II}_c$  in Fig. 4.13 is attributed to the reduction of  $\text{U(III)}$  to uranium metal

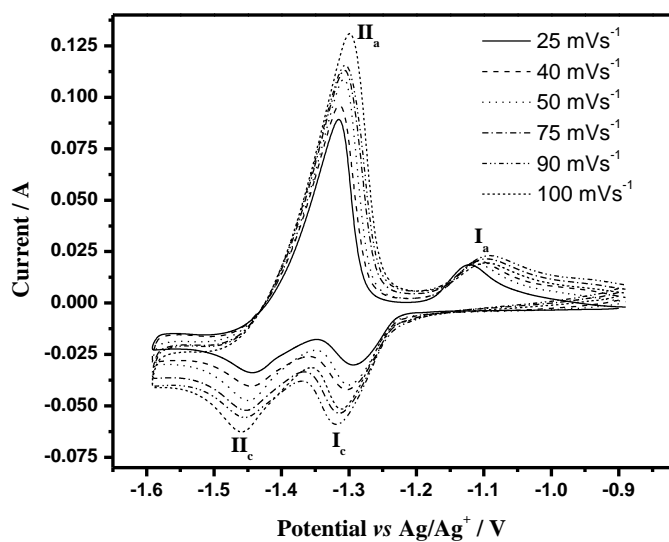


Fig. 4.13 Cyclic voltammograms of LiCl-KCl-UCl<sub>3</sub> on Cd film working electrode at different scan rates; Concentration of UCl<sub>3</sub>:  $7.31 \times 10^{-5}$  moles cm<sup>-3</sup>; Temperature: 723 K.

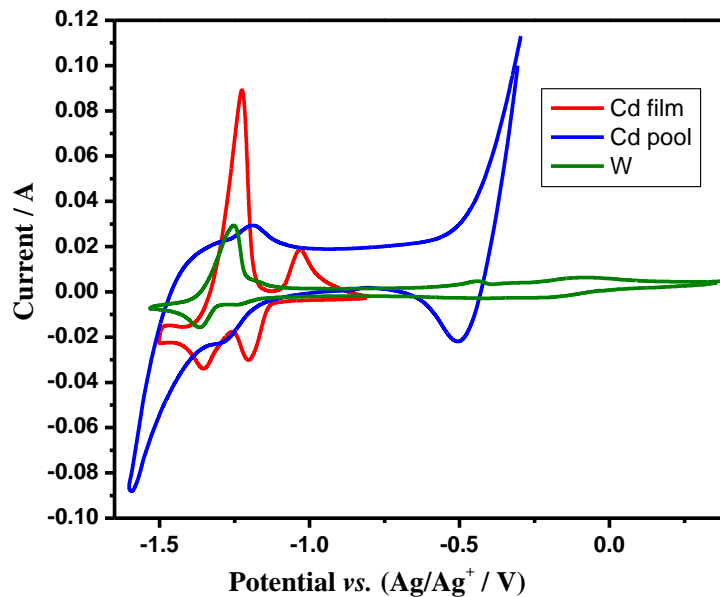


Fig. 4.14 Cyclic voltammograms of LiCl-KCl-UCl<sub>3</sub> on on different working electrodes; Concentration of UCl<sub>3</sub>:  $7.31 \times 10^{-5}$  moles cm<sup>-3</sup>; Temperature: 748 K.

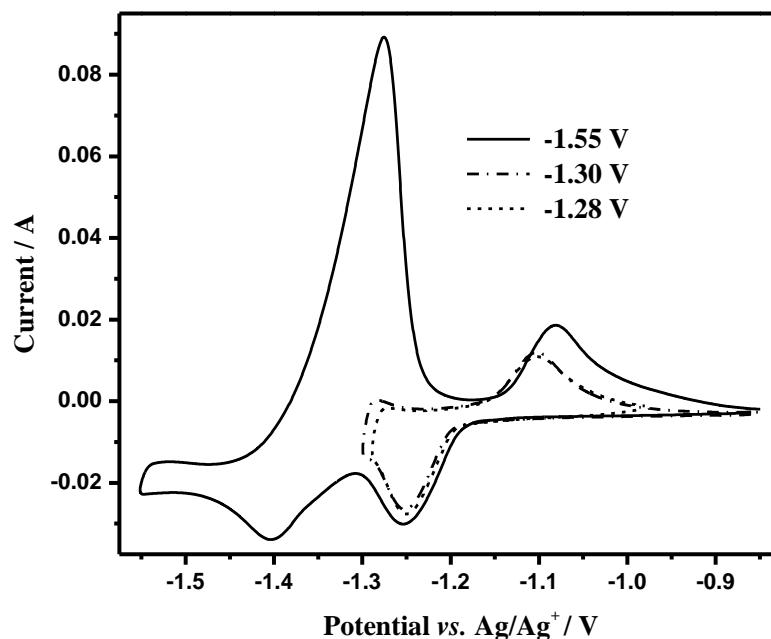


Fig. 4.15 Cyclic voltammograms of LiCl-KCl-UCl<sub>3</sub> on Cd film working electrode at different switching potentials; Concentration of UCl<sub>3</sub>:  $7.31 \times 10^{-5}$  moles cm<sup>-3</sup>; Temperature: 748 K.

from the peak position and from the nature of the corresponding anodic peak (stripping peak) which resembles that for dissolution of insoluble species. Peak I<sub>c</sub> was studied by switching the potential before peak II<sub>c</sub> and the cyclic voltammogram appeared as shown in Fig. 4.15. The shape of the voltammogram resembles that for a soluble-soluble couple. It may be observed from Fig. 4.14 that the onset potential for reduction of U(III) ion on Cd pool is close to the onset potential for peak I<sub>c</sub>. Hence peak I<sub>c</sub> is attributed to the underpotential reduction of uranium on cadmium surface. We consider that since the amount of cadmium on the film electrode is limited, initially a peak for underpotential deposition of uranium on cadmium surface occurs and once the surface of the film is saturated with the U-Cd alloy, with no fresh cadmium at the surface, the electrode behaves as an inert electrode. Hence a peak for reduction of U(III) ion to U metal is

observed subsequently. Similar behavior was observed by Murakamiz *et al.* in their study on the electrochemical behavior of zirconium on cadmium film surface [42]. Such behavior was not observed in case of lanthanides, since their redox potentials for RE(III)/RE(0), lie beyond the electrochemical window of the cadmium electrode. Hence from the above discussion it may be inferred that peak I<sub>c</sub> corresponds to under potential deposition of uranium on cadmium.

From the cyclic voltammograms obtained at 10 mVs<sup>-1</sup> on cadmium pool electrode, the number of electrons transferred for the reduction of U(III)/U(Cd) was calculated using Eq. 4.3 applicable for a soluble-soluble redox couple. The value of *n* was close to three. The apparent standard potentials,  $E_{U(III)/U(Cd)}^*$  at different temperatures were estimated using Eq. 4.4 - Eq. 4.7. The potentials thus obtained versus the reference electrode, Ag/AgCl ( $X_{AgCl} = 0.0031$ ), was converted to the scale of Cl<sub>2</sub>/Cl<sup>-</sup> reference electrode using Eq. 3.21 and Eq. 3.22 stated in chapter 3. The apparent standard potential,  $E_{U(III)/U(Cd)}^*$  at different temperatures are shown in Table 7.

Table 4.7 Apparent standard potentials ( $\pm 0.003$  V) for U(III)/U(Cd), estimated from cyclic voltammogram on Cd pool,  $X_{UCl_3} = 0.00267$ ; Ag/AgCl ( $X_{AgCl} = 0.0031$ )

Temperature, K	$E_{U(III)/U(Cd)}^*$ vs. Ag/Ag <sup>+</sup> , V	$E_{U(III)/U(Cd)}^*$ vs. Cl <sub>2</sub> /Cl <sup>-</sup> , V	$E_{1/2,U(III)/U(Cd)}$ vs. Ag/Ag <sup>+</sup> , V [16]
673	-1.323	-2.552	-
698	-1.311	-2.545	-
723	-1.299	-2.538	-1.331
740	-1.293	-2.535	-
773	-1.218	-2.468	-1.320

The values were compared with the apparent standard potential for U(III)/U(0) couple,  $E_{U(III)/U(0)}^*$  which was obtained by emf method discussed in chapter 3. It was expected that the difference in the potentials should correspond to the Gibbs energy formation of the intermetallic, UCd<sub>11</sub>. Fig. 4.16 shows the apparent standard potentials obtained from this study and the standard electrode potentials for U(III)/U(0) and U(III)/U(Cd) couple reported by Shirai *et al.* [23]. Shirai *et al.* had measured the redox potentials for U(III)/U(0) couple at various concentrations at different temperatures by equilibrium measurement. They had obtained the standard reduction potential,  $E_{U(III)/U(0)}^0$  at different temperatures using the Nernst equation. They had derived the half wave potential,  $E_{1/2,U(III)/U(Cd)}$  from the cyclic voltammograms recorded on cadmium pool cathode using the relation for soluble-soluble couple (Eq. 4.3). They had considered the half wave potential,  $E_{1/2,U(III)/U(Cd)}$  as the standard reduction potential for the reduction of U(III) on Cd. The  $E_{1/2,U(III)/U(Cd)}$  reported by them is more negative than their  $E_{U(III)/U(0)}^0$  values for U(III)/U(0) couple as may be seen in Fig. 4.16. Also it may be observed from the figure that the difference between the potentials increases with increase in temperature. As stated earlier, according to the phase diagram of the uranium-cadmium system, UCd<sub>11</sub> is the only intermetallic compound of the system and it decomposes peritectically to liquid +  $\alpha$  U beyond 746 K, whereas in both the studies, that is, study by Shirai *et al.* and this work find underpotential reduction of uranium on the cadmium cathode for temperatures beyond 746 K. But the discrepancy has not been discussed by Shirai *et al.* and no explanation has been given. We also do not know the reason for the behavior.

The apparent standard potentials,  $E_{U(III)/U(Cd)}^*$  are more negative than the apparent standard potentials for U(III)/U(0) couple,  $E_{U(III)/U(0)}^*$ , at temperatures below 746 K in our study similar to the observation made by Shirai *et al.* Their difference,  $\Delta E$ , is less than

those expected from the Gibbs energy formation of  $\text{UCd}_{11}$  reported by Johnson *et al.*[25] and Veleckis *et al.*[26] obtained by galvanic cell emf method and by vapour pressure measurement respectively. However it was observed that the difference in the potentials becomes zero  $\sim 746$  K in our study as expected from the phase diagram unlike in the case of Shirai *et al.* report. In order to know the equilibrium potential of U on cadmium at different temperatures, open circuit potential measurements were carried out.

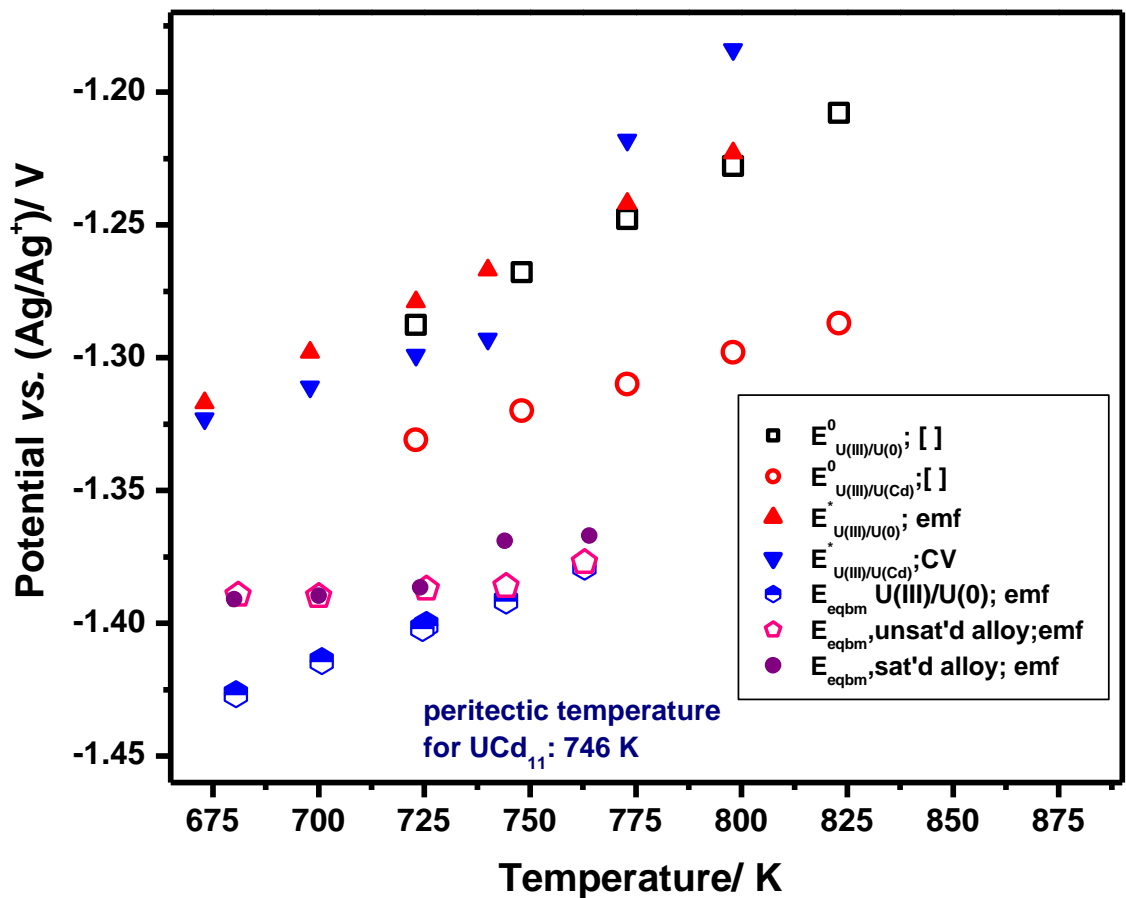


Fig. 4.16 Electrode potentials for U(III)/U(0) and U(III)/U(Cd) couples from cyclic voltammetry and emf method.

#### 4.4.2.2 Open-circuit chronopotentiometry-LiCl-KCl-UCl<sub>3</sub>

Open circuit potential measurements were carried out on cadmium film cathode using LiCl-KCl-UCl<sub>3</sub> melt at different temperatures. The cadmium film was polarized at -1.5 V for a short period (60-120 sec) and the open-circuit potential of the electrode is measured under zero current condition as a function of time. The potential increased towards anodic direction with the evolution of plateau at about -1.4 and -1.22 V. Fig. 4.17 shows the open circuit potential measurements on a cadmium film electrode. The plateau at about -1.4 V, may be attributed to the couple U(III)/U(0) from the potential of the plateau, which is the equilibrium potential of the U(III)/U(0) couple. Since UCd<sub>11</sub> is the only intermetallic of the U-Cd system, we attribute the plateau at about -1.22 V to the coexistence of UCd<sub>11</sub> and Cd. The potential further increases in the anodic direction and stabilizes at the equilibrium potential of Cd(II)/Cd(0) couple. Initially, the potential time transients at various temperatures were obtained by electrodepositing uranium for 300 s at a potential of -1.6 V in the melt LiCl-KCl containing UCl<sub>3</sub> on fresh tungsten electrode at various temperatures. The details were discussed in chapter 3. The potentials measured on cadmium film cathode with respect to the reference electrode, Ag/AgCl ( $X_{AgCl} = 0.0031$ ), was rescaled with reference to that of a U(III)/U(0) electrode. The potential of the plateau on cadmium film electrode referred to the uranium electrode is considered as the emf of the cell represented by Eq.1.

Table 8 shows the equilibrium potential for U(III)/U and those for U(III)/U(Cd) recorded from open circuit potential measurements. The difference between the potential values lie between 187-208 mV in the temperature range 653-743 K. The values are much higher than those reported by Johnson *et al.* [25] for the formation of UCd<sub>11</sub>. Also, we had observed the plateau corresponding to the alloy in the OCP transients for temperatures above

Table 4.8 Equilibrium potentials ( $\pm 0.003$  V),  $E_{U(III)/U(0)}$  and  $E_{U(III)/U(Cd)}$  from open circuit potentials measurement.

Temperature/ K	$E_{U(III)/U(0)}$ / V	$E_{U(III)/U(Cd)}$ / V	$\Delta E$ / V
653	-1.443	-1.256	0.187
670	-1.433	-1.242	0.191
698	-1.417	-1.219	0.198
723	-1.402	-1.199	0.203
743	-1.391	-1.183	0.208

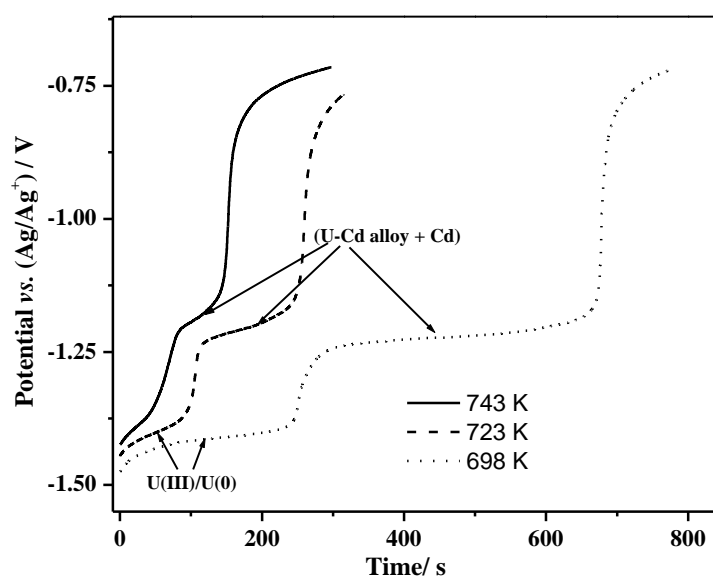


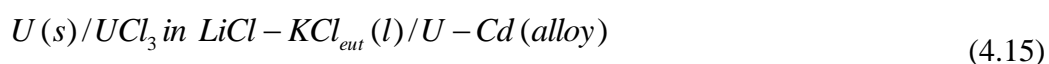
Fig. 4.17 Open circuit potential transient of LiCl-KCl-UCl<sub>3</sub> on Cd film working electrode at different temperatures; Concentration of UCl<sub>3</sub>:  $7.31 \times 10^{-5}$  moles cm<sup>-3</sup>; Applied potential: -1.5 V.

746 K. The same observations were made on repeated measurements. As discussed earlier, we had observed peak for underpotential deposition on cadmium cathode in the cyclic voltammograms recorded beyond 746 K and Shirai *et al.* also have reported  $E_{1/2,U(III)/U(Cd)}$  at 773, 798 and 823 K in their work. These observations are contradictory to the phase diagram, as it may be noted from the phase diagram that  $UCd_{11}$  decomposes to  $U(\alpha) + \text{liquid}$  beyond 746 K.

The anomalous behavior of uranium on cadmium cathode is not well understood. In order to have a better understanding of the uranium-cadmium system, we had studied the uranium cadmium system on the cadmium rich side by galvanic cell emf method.

#### 4.4.2.3 Galvanic cell emf measurement

We had studied the U-Cd system on the cadmium rich side in the temperature range 653 to 764 K by setting up an emf cell as denoted below



Studies were carried out in the region of unsaturated alloy and in the region of saturated alloy. Preparation of the alloy was as discussed in the experimental section. The emf values of the cell are given in Table 9. The emf values were reproducible during the heating and cooling cycles. Variation of the emf with temperature for the saturated alloy is shown in Fig. 4.18. The emf data below 746 K were fitted by a polynomial equation given below

$$emf = 1.4941 - 3.65 * 10^{-3}T + 2.21 * 10^{-6}T^2 \quad (4.16)$$

The Gibbs energy of  $UCd_{11}$  from  $\alpha$ -uranium and pure liquid cadmium is given by

$$\Delta G_{f,UCd_{11}}^o = -zFE + 11RT \ln a_{Cd} \quad (4.17)$$

Where  $z=3$ , the number of electrons participating in the electrode reaction,  $F$ , the Faraday constant and  $a_{Cd}$ , the activity of cadmium in the saturated solution. Assuming

that the solution is ideal with respect to cadmium and from the solubility data [25], the standard Gibbs energy formation of  $UCd_{11}$  was estimated and the values are shown in Table 9.

The Gibbs energy of formation of  $UCd_{11}$  ( $\text{cal mol}^{-1}$ ), obtained by measuring the vapour pressure of cadmium reported by Veleckis *et al.* is given by the following relation in the temperature range 578-650 K [43].



And that by Johnson *et al.* obtained from galvanic cell emf method is given by the following relation in the temperature range 573-746 K [43]

$$\Delta G^{\circ}(UCd_{11}) = -113800 + 151.5T \quad (4.19)$$

We had derived the following relation from the emf data of our measurement

$$\Delta G^{\circ}(UCd_{11}) = -115500 + 154.4T \quad (4.20)$$

Our measurement is very much in agreement with those of Johnson *et al.* whereas those of Veleckis *et al.* not in agreement. However, the three equations extrapolate to  $\Delta G^{\circ} = 0$  at about 746 K which is the peritectic temperature of  $UCd_{11}$  and are consistent with the phase diagram. It shows that the Gibbs energy of formation from all the three studies are in agreement. The enthalpy and entropy values being different are to be explained as they are fit parameters rather than the actual enthalpy and entropy values, as has been discussed by Kubaschwaski *et al.* [44].

The activity of uranium on cadmium was calculated from Eq. 4.21 and the values are given in Table 10.

$$emf = -\frac{RT}{3F} \ln a_{U(Cd)} \quad (4.21)$$

The excess Gibbs energy of U in cadmium is given by,

$$\Delta \bar{G}_U^{xs} = RT \ln \gamma_{U(Cd)} = -3F\Delta E - RT \ln x_{U(Cd)} \quad (4.22)$$

Table 4.9 The emf ( $\pm 0.002$  V) of unsaturated and saturated U-Cd alloy vs. uranium metal.

Temperature/ K	$N_u$ /unsat'd	emf/ V	Temperature/ K	$N_u$ /sat'd	emf / V
680.5	0.006	0.0356	680.5	0.0120	0.0356
681	0.006	0.0323	680.9	0.0120	0.0373
700	0.006	0.0268	699	0.0120	0.0244
743.8	0.006	0.0227	700	0.0120	0.0264
763.9	0.006	0.0113	700.7	0.0120	0.0244
			724	0.0120	0.0121
			724.5	0.0120	0.0128
			725.5	0.0120	0.0133
			744.3	0.0120	0.0051
			762.9	0.0120	-0.0017

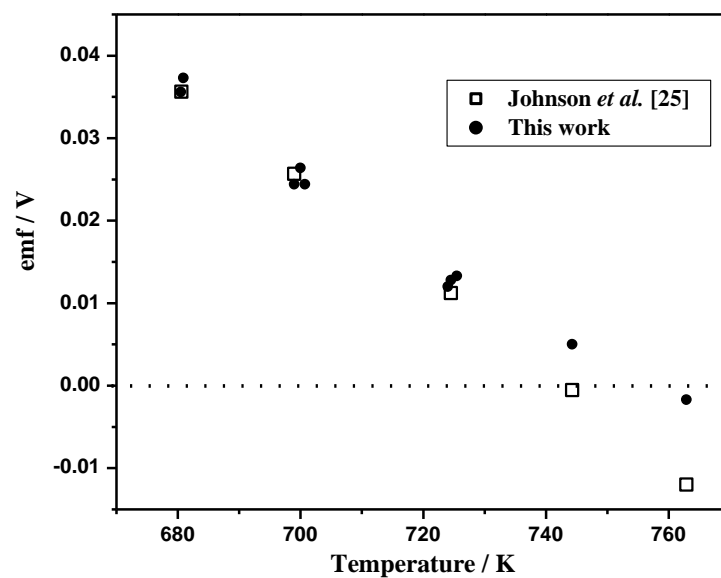


Fig. 4.18: Plot of emf as a function of temperature from galvanic cell emf method.

The activity coefficients of uranium in liquid cadmium was calculated using Eq. 4.22 and are shown in Table 10. The activity coefficient value reported by Johnson *et al.* in the temperature range 671-798 K is 47-100 [25]. The activity coefficient value reported by Sakamura *et al.* in the temperature range 673-773 K is 54-104 [40]. Our values are in very good agreement with the reported values. Roy *et al.* estimated the activity coefficient of uranium in cadmium by studying the distribution coefficient of uranium in salt phase and in cadmium phase at 723 K [45]. They had reported the value as 15. The order of activity coefficient of all the measurement is same.

During the emf measurement, the equilibrium potentials of the uranium electrode and the U-Cd alloy electrode were monitored with respect to the reference electrode, Ag/AgCl ( $X_{AgCl} = 0.0031$ ). Their difference is the emf reported above. The values were compared with the standard potentials reported by Shirai *et al.* [23] and the apparent standard potentials obtained from the cyclic voltammograms in this study as shown in Fig. 4. 16. It may be observed that the equilibrium potentials for the uranium electrode and U-Cd alloy (sat'd) electrode shift to less cathodic values with increase in temperature and intersect at  $\sim 746$  K. The result is in very good agreement with that expected from the reported phase diagram. The equilibrium potentials of the unsaturated alloy are also shown in Fig. 4.16. The values are not much different from the saturated alloy in the concentration range of uranium in cadmium studied.

We had compared the data from the emf study and the cyclic voltammograms to understand the behavior of uranium on cadmium electrode. From Fig. 4.16, it is evident that, there is a change in the slope of the apparent standard potential,  $E_{U(III)/U(Cd)}^*$  for values below 746 K and those above. The trend is similar to that observed for the values of the equilibrium potentials of the saturated alloy. Comparing the values of the emf, from the galvanic cell method and  $\Delta E$  (the difference in the apparent standard potentials,

Table 4.10 Thermodynamic properties of U-Cd system – measurements made by galvanic cell emf method

Temperature/ K	$N_u$	$\Delta_f G_{UCd_{11}}^0 /$ kJmol <sup>-1</sup>	a	$\gamma$
680.9	0.012	-10.4	0.181	15
699	0.012	-7.6	0.325	27
700.7	0.012	-7.3	0.324	28.4
724	0.012	-3.7	0.620	51.7
724.5	0.012	-3.6	0.627	52.2
725.5	0.012	-3.5	0.641	53.4
744.3	0.012	-0.6	0.923	76.9
762.9	0.012		1.213	101.1
680.5	0.006		0.162	29.9
681	0.006		0.192	35.5
700	0.006		0.264	43.8
743.8	0.006		0.346	57.4
763.9	0.006		0.597	99.5

$E_{U(III)/U(0)}^*$  and  $E_{U(III)/U(Cd)}^*$ ), we noted that the value of  $E_{U(III)/U(Cd)}^*$  is more negative by ~ 40 mV. Hence we infer that our measurement by cyclic voltammetry is fairly in agreement with that expected from the emf method.

The appearance of a peak in cyclic voltammograms above 746 K, could be attributed to the large solubility of uranium in liquid cadmium (0.84 - 2.32 wt % in the temperature range 723 - 746 K). The concentration of uranium in cadmium cathode in our experiments could have been in the region of the unsaturated alloy seen in the phase diagram in Fig. 4.12. The peaks in cyclic voltammograms above 746 K may not correspond to  $\text{UCd}_{11}$  as we had presumed. They probably correspond to the unsaturated U-Cd alloy. The large difference in the equilibrium potentials from the OCP measurement, may be due to the above reason.

Fig. 4.21 compares the cyclic voltammograms obtained for LiCl-KCl melt containing  $\text{UCl}_3$ ,  $\text{LaCl}_3$  and  $\text{NdCl}_3$  on cadmium pool cathode. It may be observed that their reduction potentials differ hardly by 150 mV. Hence the separation of actinides from lanthanides cannot be very high on a cadmium cathode.

#### ***4.4.2.4 Potentiostatic electrolysis***

Potentiostatic electrolysis was carried out on the liquid cadmium pool electrode in LiCl-KCl- $\text{UCl}_3$  melt at 723 K for more than 10 hours at a potential of -1.3 V. This potential is more positive than that required for deposition of pure uranium metal on an inert electrode. The amount of uranium deposited on cadmium cathode was estimated from the coulombs passed. The electrolysis was stopped and the cell was cooled, when the amount of uranium in cadmium was in the region of unsaturated alloy. The solidified cathode deposit was retrieved by breaking the alumina container. The deposit was washed with ethylene glycol to remove the adhering salt and subsequently sliced into many pieces to view the cross section. The cross section of the cathode deposit was characterized by XRD analysis. Fig. 4.19 shows the XRD pattern for the top most slice of the cathode deposit. The XRD pattern shows the presence of Cd and the intermetallic,  $\text{UCd}_{11}$  [33]. SEM-EDAX analysis of the samples was carried out to study the morphology and

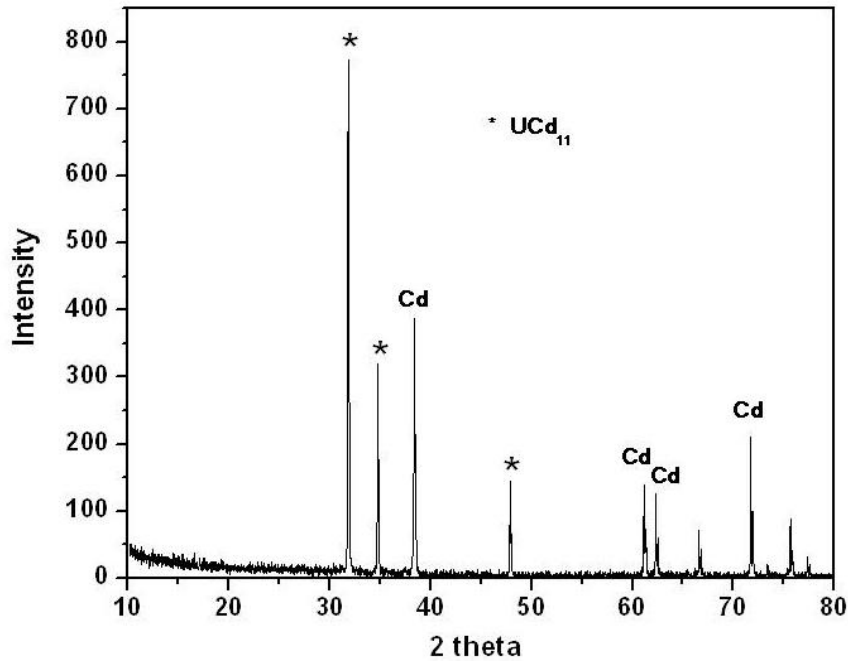


Fig. 4.19 XRD pattern of the cathode deposit of uranium on cadmium pool cathode formed by potentiostatic electrolysis at  $-1.3$  V vs. Ag/AgCl reference electrode at 723 K [46].

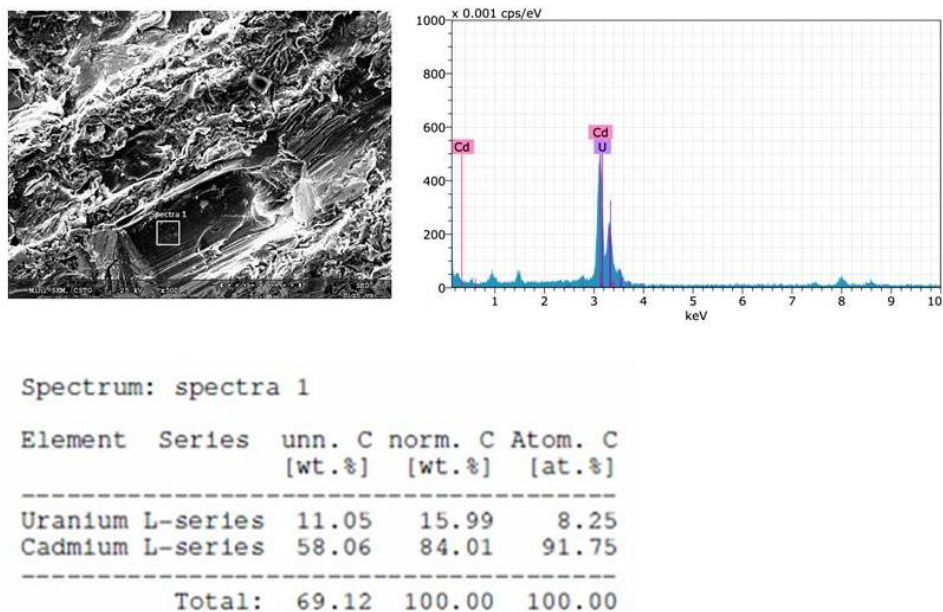


Fig. 4.20 SEM micrograph of the cathode deposit of uranium on cadmium pool cathode formed by potentiostatic electrolysis at  $-1.3$  V vs. AgCl/Ag reference electrode at 723 K and the corresponding EDAX analysis.

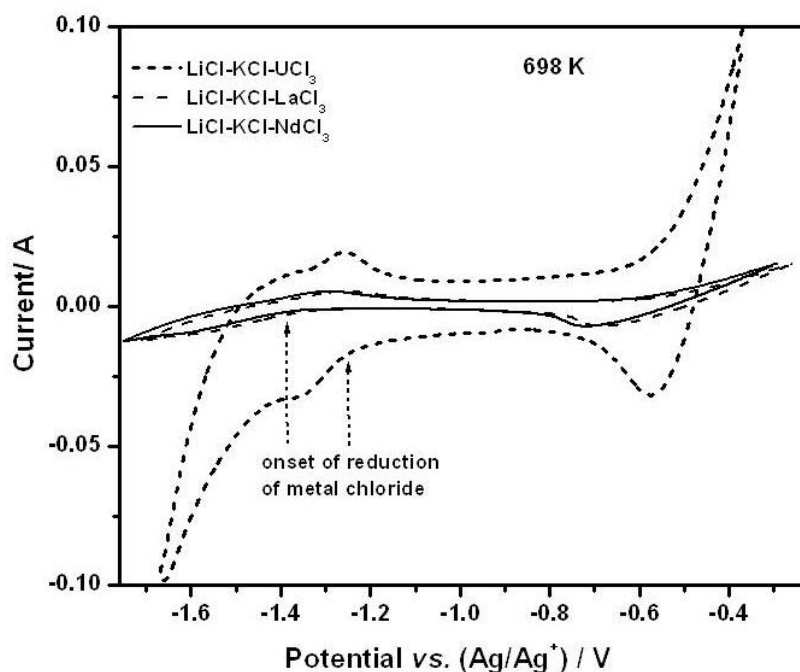


Fig. 4.21 Comparison of cyclic voltammograms for  $\text{UCl}_3$ ,  $\text{LaCl}_3$  and  $\text{NdCl}_3$  in  $\text{LiCl-KCl}$  melt on cadmium pool cathode.

elemental composition. Fig. 4.20 shows the SEM micrographs and EDAX analysis of the same cathode deposit sample. Elemental analysis from EDAX analysis shows the U-Cd ratio as 1:11 corresponding to  $\text{UCd}_{11}$ . The results indicate that underpotential deposition of uranium occurs on cadmium cathode due to formation of U-Cd alloy. On cooling, the liquid alloy solidifies as  $\text{Cd(s)}$  and  $\text{UCd}_{11}$  which is revealed in the XRD pattern [45].

#### 4.5 Summary

The electrode behavior  $\text{LaCl}_3$  and  $\text{NdCl}_3$  in  $\text{LiCl-KCl}$  eutectic melt was studied on liquid cadmium pool and film electrode using cyclic voltammetry. The reduction occurred at more positive potential than that on an inert electrode. The activity of La/Nd is lower on the Cd electrode due to the formation of intermetallic compound. The apparent standard electrode potentials,  $E_{\text{La(III)/La(Cd)}}^*$  and  $E_{\text{Nd(III)/Nd(Cd)}}^*$  were estimated for the temperatures in the range 698-773 K. The equilibrium potentials,  $E_{\text{La(III)/La(Cd)}}$  and

$E_{Nd(III)/Nd(Cd)}$  were obtained from the OCP measurement. The equilibrium potentials thus obtained was converted to emf by comparing the potential against the equilibrium potential of RE(III)/RE(0) obtained from OCP measurement mentioned in chapter 1. This method is used for first time here. The Gibbs energy of formation of the alloys, LaCd<sub>11</sub> and NdCd<sub>11</sub> were obtained from the open circuit potential measurement. The activity of La/Nd in cadmium, the excess Gibbs energy and the activity coefficient of La/Nd in cadmium are reported from the open circuit potential measurement for first time. XRD pattern of the electro-deposit showed the formation of intermetallic compounds LaCd<sub>11</sub> and NdCd<sub>11</sub> on the Cd cathode for La-Cd and Nd-Cd systems respectively. The studies reported on Nd-Cd system in this work is not reported in open literature earlier.

Only one report was found in literature (by Shirai *et al.*) for the redox behavior of UCl<sub>3</sub> on Cd pool electrode. The studies were reported for the temperature range 698-823 K. They had reported the underpotential deposition of uranium on Cd pool electrode due to the formation of UCd<sub>11</sub>. However from the phase diagram, we find that UCd<sub>11</sub> is unstable above 746 K. Also the Gibbs energy formation of UCd<sub>11</sub> reported by them was much higher than those reported by Johnson *et al.* who had studied the U-Cd system by emf method.

Hence, to understand the anomalous behaviour of UCl<sub>3</sub> on cadmium electrode, the reduction mechanism of UCl<sub>3</sub> on cadmium pool and film electrodes was investigated by cyclic voltammetry and open circuit potentiometry in the temperature range 698-798 K. Our studies on the open circuit potential measurement on Cd electrode did not yield any fruitful result. Underpotential deposition of uranium on the cadmium cathode was revealed from the cyclic voltammograms. The shift in potential towards the positive direction was presumed to be due to the formation of the intermetallic compound, UCd<sub>11</sub>. However, the extent of shift in potential did not agree with those reported in literature.

Also we had observed appearance of peak for  $\text{UCd}_{11}$  in the cyclic voltammogram beyond 746 K which is the peritectic temperature of  $\text{UCd}_{11}$ .

The discrepancies were fairly understood from our studies by galvanic cell emf method. . In order to know the equilibrium potential of the U-Cd alloy both in saturated and unsaturated region with respect to the reference electrode, emf measurement was carried out. Apart from measuring the emf between the uranium electrode and the alloy, the potentials of the alloy was monitored against the AgCl/Ag reference electrode over a wide temperature range for the saturated and unsaturated alloy. From the potential values obtained from the cyclic voltammograms and emf studies in this work, we could relate the appearance of peak above 746 K to the underpotential deposition of uranium forming the unsaturated alloy. The large solubility of uranium in cadmium (0.84 -2.32 wt % in the temperature range 723 -746 K) could be the reason for the discrepancies observed. We have not come across any cyclic voltammetry study for such systems with large solubility.

The SEM-EDX analysis and the XRD pattern of the cathode deposit obtained in the region of unsaturated alloy by potentiostatic electrolysis of LiCl-KCl- $\text{UCl}_3$  melt on cadmium pool cathode at 723 K reveal the formation of the intermetallic  $\text{UCd}_{11}$ .

The uranium cadmium system on the cadmium rich side was studied in the temperature range 653 - 764 K by galvanic cell emf method. The Gibbs energies of formation of  $\text{UCd}_{11}$  in the temperature range 680 to 744 K were evaluated and the values were in good agreement with those reported by Johnson *et al.* The peritectic temperature of  $\text{UCd}_{11}$  was evaluated to be 748 K which is consistent with the phase diagram [24] and those reported by Johnson *et al.*[25] , Veleckis *et al.* [26] and Kurata *et al.*[38] are 751 K, 762 K and 748 K respectively. The activity coefficients of uranium in the solvent rich

region were computed in the temperature range 680-764 K were found to be in the range 14-100 and are in good agreement with the literature value.

#### 4.6 References

1. L. Burris, R.K. Steunenberg, W.E. Miller, Proceedings of the AIChE winter annual meeting, Miami, FL, USA, 1986.
2. J. P. Ackerman, *Ind. Eng. Chem. Res.* 30 (1991) 141.
3. J.L. Willit, W.E. Miller, J.E. Battles, *J. Nucl. Mater.* 195 (1992) 229.
4. J. P. Ackerman and T. R. Johnson, Actinides-93 International Conference on Future Nuclear Systems, Washington, September 12-17, 1993.
5. W. H. Hannum, Ed., *Progress in Nuclear Energy*, 31, nos.1/2, Special Issue, 1997.
6. J. P. Ackerman, J. L. Settle, *J. Alloys Compd.* 199 (1993) 77.
7. T. Kato, T. Inoue, T. Iwai, Y. Arai, *J. Nucl. Mater.* 357 (2006) 105.
8. T. Koyama, T. R. Johnson, D. F. Fischer, *J. Alloys Compd.* 189 (1992) 37.
9. L. S. Chow, J. K. Basco, J. P. Ackerman, T. R. Johnson, *Int. Conf. Tech. Exhib.- Global – 93*, Washington, 1993, Conf-950913-30.
10. M. Kurata, Y. Sakamura, T. Matsui, *J. Alloys Compd.* 234 (1996) 83.
11. I. Johnson, ANL-01/16, Contract No. W-31-109-Eng-38, 2001.
12. T. Koyama, K. Kinoshita, T. Inoue, M. Ougier, R. Malmbeck, J. P. Glatz, *Radiochim. Acta* 96 (2008) 311.
13. Y. Castrillejo, M.R. Bermejo, P. Diaz Arocas, A.M. Martinez, E. Barrado, *J. Electroanal. Chem.* 579 (2005) 343.
14. Y. Castrillejo, M.R. Bermejo, A.M. Martneza, E. Barrado, P. Diaz Arocas, *J. Nucl. Mater.* 360 (2007) 32.
15. O. Shirai, A. Uehara, T. Fujii, H. Yamana, *J. Nucl. Mater.* 344 (2005) 147.

16. "Separation by electrolysis in chloride media" – 'PYROREP', Contract No. FIKW-CT- 2000-00049, Project No. FIS5-1999-00199, 2003; Project co-ordinator- H. Boussier.
17. H. Shibata, H. Hayashi, M. Akabori, Y. Arai, M. Kurata, J. Physics and Chemistry of Solids 75 (2014) 972.
18. T. Kobayashi, R. Fujita, H. Nakamura, T. Koyama, M. Iizuka, J. Nucl. Sci. Technol. 36 (3) (1999) 288.
19. K. Uozumi, M. Iizuka, T. Kato, T. Inoue, O. Shirai, T. Iwai, Y. Arai, J. Nucl. Mater. 225 (2004) 34.
20. K. Kinoshita, T. Koyama, T. Inoue, M. Ougier, J. P. Glatz, J. Physics and Chemistry of Solids 66 (2005) 619.
21. O. Shirai, M. Iizuka, T. Iwai, Y. Suzuki, Y. Arai, J. Electroanal. Chem. 490 (2000) 31.
22. M. Iizuka, K. Uozumi, T. Inoue, T. Iwai, O. Shirai, Y. Arai, J. Nucl. Mater. 299 (2001) 32.
23. Osamu Shirai, Koichi Uozumi, Takashi Iwai, Yasuo Arai, Analytical Sciences 2001, vol. 17 Supplement, i959-i962.
24. A. E. Martin, I. Johnson, H. M. Feder, Trans. Metallurg. Soc. AIME 221 (1961) 789.
25. I. Johnson, H. M. Feder, Trans. Met. Soc. AIME, 224 (1962) 468.
26. Veleckis, Feder, Johnson, J. Phys. Chem. 66 (1961) 362.
27. K.A. Gschneidner: Cd-La Phase Diagram, ASM Alloy Phase Diagrams Center, P. Villars, Editor-in-chief; <http://www1.asminternational.org/AsmEnterprise/APD>, ASM International, Materials Park, OH, USA, 2006-2014

28. K.A. Gschneidner: Cd-Nd Phase Diagram, ASM Alloy Phase Diagrams Center, P. Villars, Editor-in-chief; <http://www1.asminternational.org/AsmEnterprise/APD>, ASM International, Materials Park, OH, USA, 2006-2014
29. Y. Castrillejo, M.R. Bermejo, E. Barrado, A.M. Martinez, *Electrochim. Acta* 51 (2006) 1941.
30. Z. Galus, *Fundamentals of Electrochemical Analysis*, Ellis Horwood, London, 1994.
31. A.J. Bard, L.R. Faulkner, *Electrochemical Methods. Fundamentals and Applications*, Wiley New York, 1980, chapter 6.
32. S.A. Kuznetsov, M. Gaune-Escard, *Electrochimica Acta* 46 (2001) 1101.
33. P. Soucek, R. Malmbeck, E. Mendes, C. Nourry, D. Sedmidubsky, J. P. Glatz, J. *Nucl. Mater.* 394 (2009) 26.
34. T. Iida, T. Nohira, Y. Ito, *Electrochim. Acta* 46 (2001) 2537.
35. H. Konishi, T. Nishikiori, T. Nohira, Y. Ito, *Electrochim. Acta* 48 (2003) 1403.
36. P. Taxil, J. Mahenc, *J. Appl. Electrochem.* 17 (1987) 261.
37. I. Johnson, K. E. Anderson, R. A. Bloomquist, *Trans. ASM*, 59 (1966) 352.
38. Masaki Kurata and Yoshiharu Sakamura, *J. Phase Equilibria* 22 (3) (2001) 232.
39. I. Johnson and R. M. Yonco *Met. Trans.*, 1 (1970) 905.
40. Y. Sakamura, T. Inoue, T.S. Storvick, and L.F. Grantham: *Proc. Int. Conf. on Evaluation of Emerging Nuclear Fuel Cycle Systems, Global '95, Versailles, France, Sept. 11–14, 1995, vol. 2, p. 1185.*
41. I. Johnson: *Proc. 2<sup>nd</sup> Conf. on Rare Earth Research*, J. F. Nachman and C. E. Lundin, eds., Gordon and Breach, New York, NY, 1962, p.130.
42. T. Murakamiz, T. Kato, *J. Electrochem. Soc.* 155 (7) (2008) E90.

43. P. Chiotti, V. V. Akhachinskij, I. Ansara, M. H. Rand, "The chemical thermodynamics of actinide elements and compounds, part 5, The Actinide Binary Alloys", p.106.
44. O. Kubaschewski, C.B. Alcock and P.J. Spencer, *Materials Thermochemistry*, 6<sup>th</sup> Edition, Revised of Kubaschewski and Alcock's *Metallurgical Thermochemistry*, Pergamon Press, Oxford, (1993).
45. J. J. Roy, L. F. Grantham, D. L. Grimmett, S. P. Fusselman, C. L. Krueger, T. S. Storvick, T. Inoue, Y. Sakamura, and N. Takahashi, *J. Electrochem. Soc.* 143 (1996) 2487.
46. J. D. Thompson, A. C. Lawson, M. W. McElfresh, A. P. Sattelberger, Z. J. Fisk, *J. Magn. Mater.* (1988) 76/77, 437-438.

## CHAPTER 5

### Electrochemical behavior of La-, Nd- and U-trivalent ions in LiCl-

#### KCl eutectic melt on solid aluminium electrode

##### 5.1 Introduction

The thermodynamic stabilities of the intermetallic compounds formed between the actinides and lanthanides with cadmium are similar. When the concentration of the lanthanides in the electrolyte becomes very high during the electrorefining process, selective deposition of actinides on cadmium cathode without the contamination of lanthanides becomes impossible. Many molten metals (Cd, Bi, Zn, Sn, Ga and Al) have been studied as solvents by extracting the actinides from molten fluoride salts based on the technique of reductive extraction for effecting the actinide- lanthanide separation [1-3]. It is reported in literature that among the molten metal solvents studied aluminium shows better selectivity for actinides than lanthanides, as is also expected from the data on thermodynamic stabilities of the intermetallic compounds of lanthanides and actinides [4]. As mentioned earlier in Chapter 1, there is interest in exploring the suitability of solid aluminium cathode for efficient recovery of actinides over lanthanides in the electrorefining process [5-7]. Investigations are being carried out on elements pertaining to the electrorefining process, to understand the electrode reaction, kinetics, derive the standard potentials and activities of these elements on Al electrode in order to evaluate the efficiency of the electrode [8-10]. In this chapter we have reported a detailed elucidation on the redox behavior of  $\text{LaCl}_3$ ,  $\text{NdCl}_3$  and  $\text{UCl}_3$  on solid aluminium electrode. The thermodynamic properties of the La-Al, Nd-Al and U-Al systems were estimated from the open circuit potential measurement.

## 5.2 Literature survey

The pyrochemical separation technique is being developed at ITU, Karlsruhe, Germany, for selectively reducing the actinides on solid aluminium cathode using molten LiCl-KCl melt [11-13]. Cassayre *et al.* investigated the feasibility of carrying out electrorefining of alloy fuel (U-Zr and U-Pu-Zr) using solid aluminium cathode instead of liquid cadmium cathode [11]. They selectively deposited the actinides, while the lanthanides remained in the salt. Serp *et al.* had determined the An/Ln separation efficiency on simulated spent alloy fuel using aluminium cathode [6, 12]. Soucek *et al.* had investigated the selective reduction of uranium, plutonium and minor actinides on aluminium cathode from simulated An-Ln-Zr alloy fuel followed by their recovery from An-Al alloy through chlorination route [13-15].

Fundamental studies on the reaction of lanthanide and actinide chlorides at the aluminium electrode, their redox mechanism and standard electrode potential for alloy formation have been reported in the literature. Studies related to the electrochemical behavior of some of the lanthanides on aluminium electrode have been carried out extensively by Castrillejo *et al.* [8, 16 -19]. They had obtained the redox potentials for the rare earth metals (La, Ce, Pr, Gd, Er, Ho, Tm) and yttrium on Al electrode. The work of Castrillejo *et al.* and Caravaca *et al.* on the redox behavior of lanthanides on various cathodes has been compiled in the project report PYROREP as mentioned in chapter 4 [20]. The underpotential reduction of lanthanides on Al electrode has been studied by cyclic voltammetry. The Gibbs energy of formation of the various intermetallics of lanthanides with aluminium was estimated from the open circuit potential measurement. Taxil *et al.* have reported the reduction behaviour of lanthanide ions (Ce, Gd, Sm and Nd) on molybdenum electrode and co-reduction of lanthanides and aluminium on the tantalum electrode using LiF-CaF<sub>2</sub>-AlCl<sub>3</sub>-LnCl<sub>3</sub> melt [21-22]. They had investigated the alloy

formed by galvanostatic electrolysis at potentials less cathodic than that required for metal formation.

Studies related to the electrochemical behavior of some of the actinides on aluminium electrode have been carried out at ITU. Cassayre *et al.* had studied the redox behavior of  $\text{UCl}_3$  on Al electrode [10, 11]. Underpotential reduction of uranium on aluminium takes place with formation of the intermetallics,  $\text{UAl}_4$  and  $\text{UAl}_3$ . Mendes *et al.* [23] had investigated the reduction behavior of Pu(III) ions and Soucek *et al.* [24] had investigated that of Np(III) ions on aluminium electrode using cyclic voltammetry. The formation and thermochemical properties of the  $\text{AnAl}_n$  alloys were evaluated by open circuit potentiometry in their study. Cordoba *et al.* had studied the reduction behavior of  $\text{AmCl}_3$  on liquid aluminium cathode and estimated the activity coefficient of Am on aluminium [25].

Other than these studies, there aren't many reports on the electrochemical behaviour of lanthanides and actinides on aluminium electrode to our knowledge. Though the behavior of  $\text{LaCl}_3$  and  $\text{UCl}_3$  are reported, the studies have not been carried out over a range of temperature. Also, the electrode behavior of  $\text{NdCl}_3$  on Al has not been carried out in detail. In order to have a better understanding of the reaction of lanthanides and actinides at the solid aluminium cathode, we had investigated the electrochemical behavior of  $\text{LaCl}_3$ ,  $\text{NdCl}_3$  and  $\text{UCl}_3$  on solid aluminium electrode using cyclic voltammetry and open circuit potentiometry. The reduction potentials of La(III), Nd(III) and U(III) ions on Al electrode were estimated and the formation of  $\text{La}_3\text{Al}_{11}$ ,  $\text{Nd}_3\text{Al}_{11}$  and  $\text{UAl}_n$  alloys were studied. The details are discussed in the chapter.

### **5.3. Experimental**

#### **5.3.1. Chemicals**

High purity aluminium wire and sheets (Alfa Aesar 99.99 %) were used for preparing the aluminium working electrode. The purity of other chemicals used in the study is same as those described in Chapter 3 and 4.

### ***5.3.2. Preparation of the electrolyte salt***

Purification of LiCl-KCl salt mixture was carried out as described earlier in Chapter 2. Preparation of LiCl-KCl-LaCl<sub>3</sub>, LiCl-KCl-NdCl<sub>3</sub> and LiCl-KCl-UCl<sub>3</sub> electrolytes was discussed earlier in Chapter 2.

### ***5.3.3. Electrochemical apparatus and electrodes***

A 1.5 mm diameter Al wire was used as working electrode for the cyclic voltammetry and open circuit potentiometry studies. The working electrode was sheathed with an alumina sleeve exposing 40 mm of the wire and the area of the working electrode was calculated from the depth of immersion. A 5mm thick aluminium sheet was used as working electrode for potentiostatic deposition of the alloys. The reference electrode and the counter electrodes are the same as described in Chapter 2. The cell assembly, experimental procedure and instrumentation are the same as discussed in Chapter 2.

## **5.4 Results and discussion**

### ***5.4.1 Electrochemical reduction behaviour of LaCl<sub>3</sub> & NdCl<sub>3</sub> on solid Al electrode***

#### ***5.4.1.1. Analysis of the cyclic voltammograms***

Cyclic voltammograms obtained on W and Al electrodes in pure LiCl-KCl melt are compared with that obtained with the melt containing LaCl<sub>3</sub> on Al electrode in Fig.5.1. The electroactive domain of pure LiCl-KCl on aluminium electrode is significantly smaller than that on the W electrode. The cathodic limit is shifted to a lesser value due to the formation of Al-Li alloy. The anodic limit is imposed by oxidation of

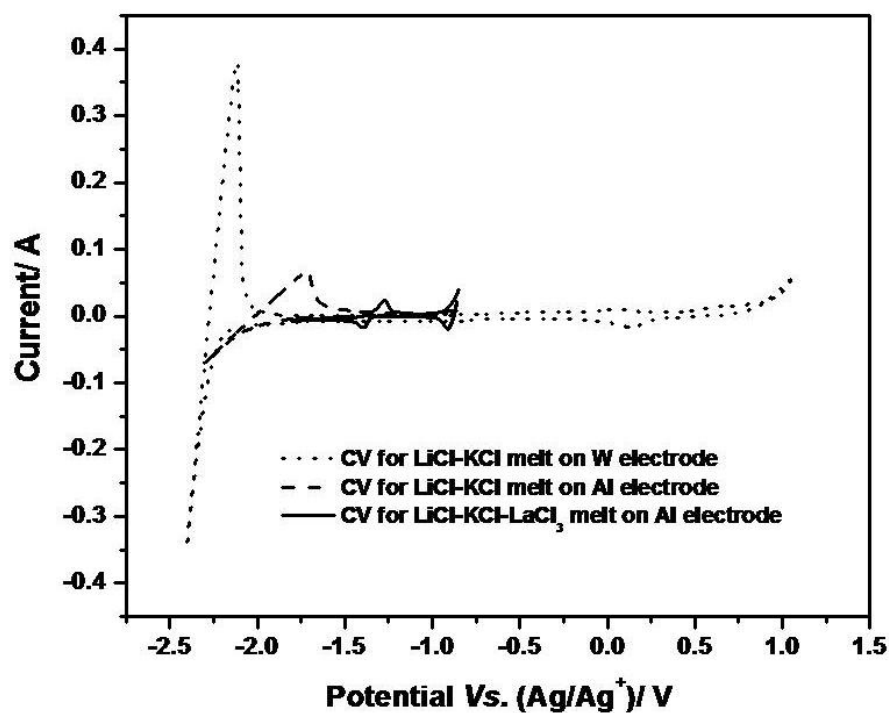


Fig.5.1 Electroactive domain of pure LiCl-KCl on aluminium electrode as compared to that on a W electrode.

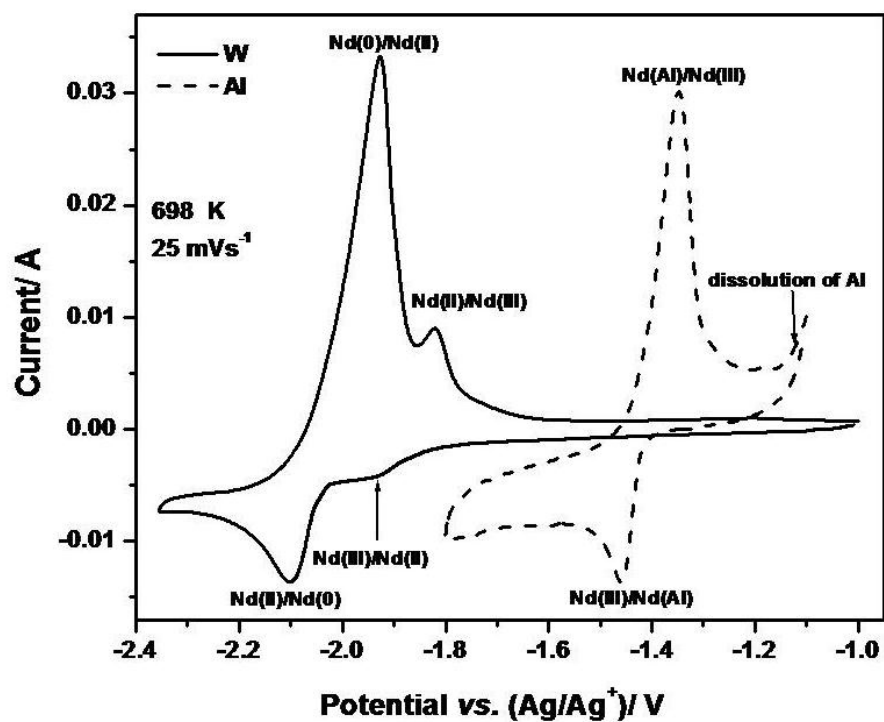


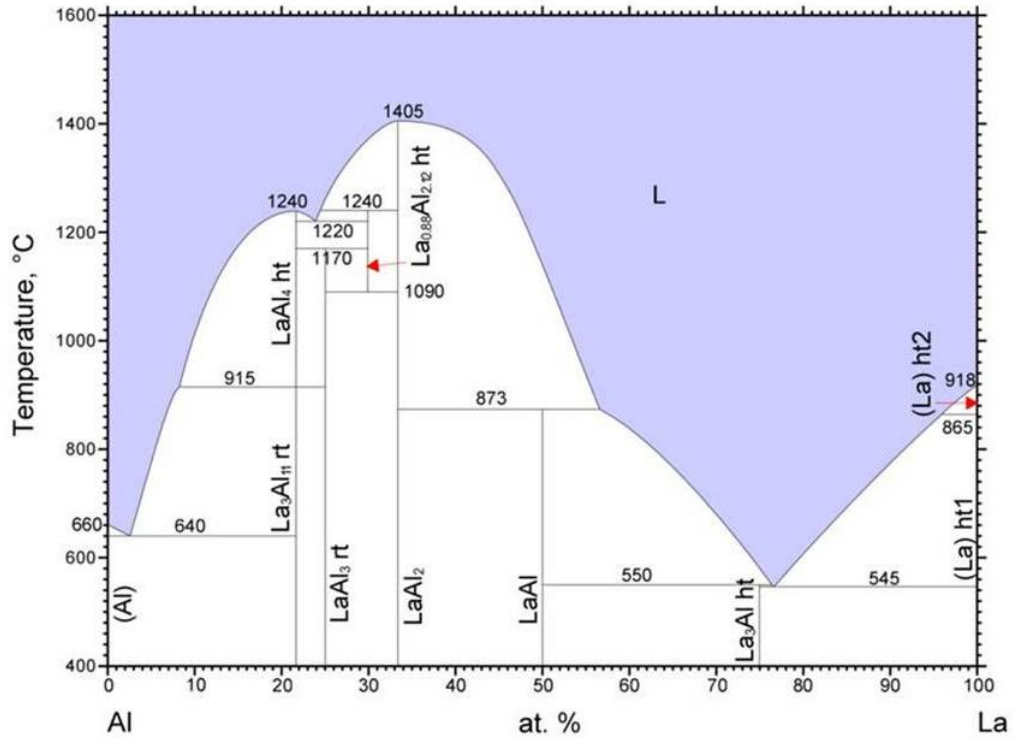
Fig.5.2 Cyclic voltammograms obtained on the tungsten and aluminium electrodes for LiCl-KCl-NdCl<sub>3</sub> melt.

the Al metal. Fig. 5.2 shows the cyclic voltammograms obtained at 698 K on the tungsten and aluminium electrodes at  $25 \text{ mVs}^{-1}$  for LiCl-KCl-NdCl<sub>3</sub> melt. It was observed that the reduction of the rare earth chlorides on Al occurs at a less cathodic potential than that on inert W electrode. Only a single redox couple was observed similar to the RE-Cd system. The redox potentials shift by  $\sim 600 \text{ mV}$  towards the positive direction. The reduction takes place in a single step with three electron transfer on the aluminium electrode forming their respective intermetallic compound during the cathodic cycle and dissolution of the alloy during the anodic cycle. Fig. 5.3 and Fig. 5.4 show the phase diagrams of the La-Al and Nd-Al systems respectively [26, 27]. Lanthanum and neodymium form various intermetallic compounds with aluminium. Based on the reported phase diagrams, the probable reaction on the aluminium rich side could be the formation of the intermetallic rich in aluminium, namely, Al<sub>11</sub>RE<sub>3</sub>.



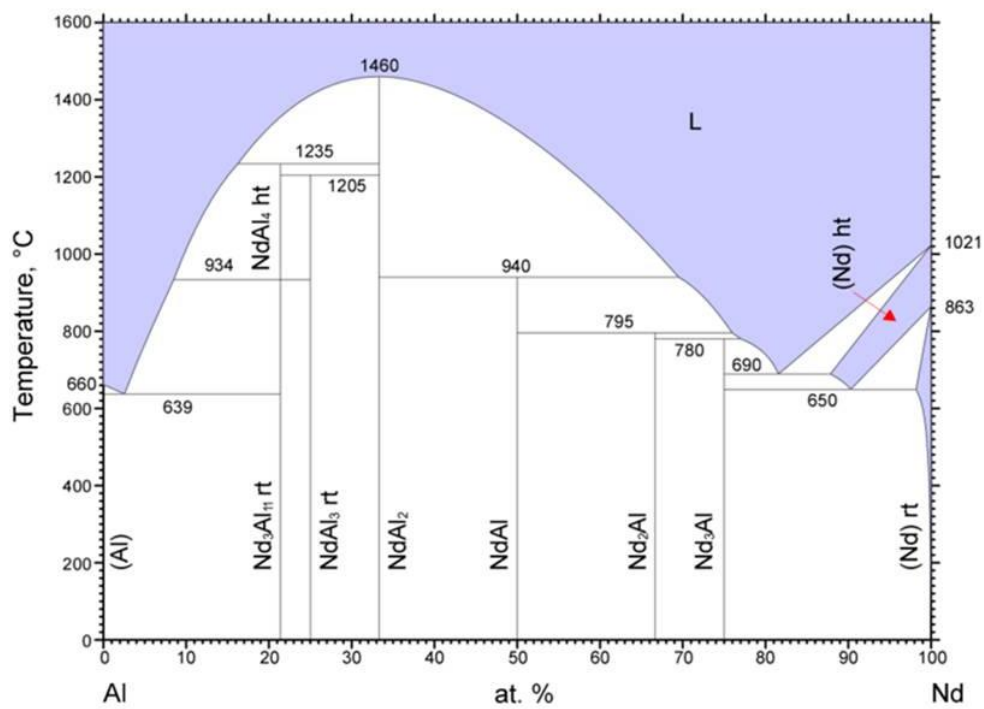
where RE<sup>3+</sup> here refers to La/Nd ions. Similar observations have been made by other authors earlier in case of lanthanum, cerium, praseodymium and erbium [16-18]. Further, the formation of Al<sub>11</sub>RE<sub>3</sub> has been supported by the XRD pattern and SEM-EDX analysis of the electrodeposits, details of which has been discussed in *section 5.4.1.4*.

Fig. 5.5 and Fig. 5.6 show the cyclic voltammograms of LaCl<sub>3</sub> and NdCl<sub>3</sub> in LiCl-KCl melt at 748 K on solid aluminium cathode at various scan rates respectively. The voltammograms show a single reduction wave and its corresponding oxidation wave in the electrochemical domain. The shape of the voltammogram resembles closely that of a soluble-soluble reversible system. It may be observed that the cathodic and anodic peaks for the formation and dissolution of alloy do not vary significantly between sweep rates  $10\text{-}100 \text{ mVs}^{-1}$ . In the cathodic cycle, the magnitude of  $E_{p,c} - E_{p,c/2}$  agrees with the



© ASM International 2006. Diagram No. 900099

Fig. 5.3 Al-La phase diagram



© ASM International 2009. Diagram No. 100290

Fig. 5.4 Al-Nd phase diagram

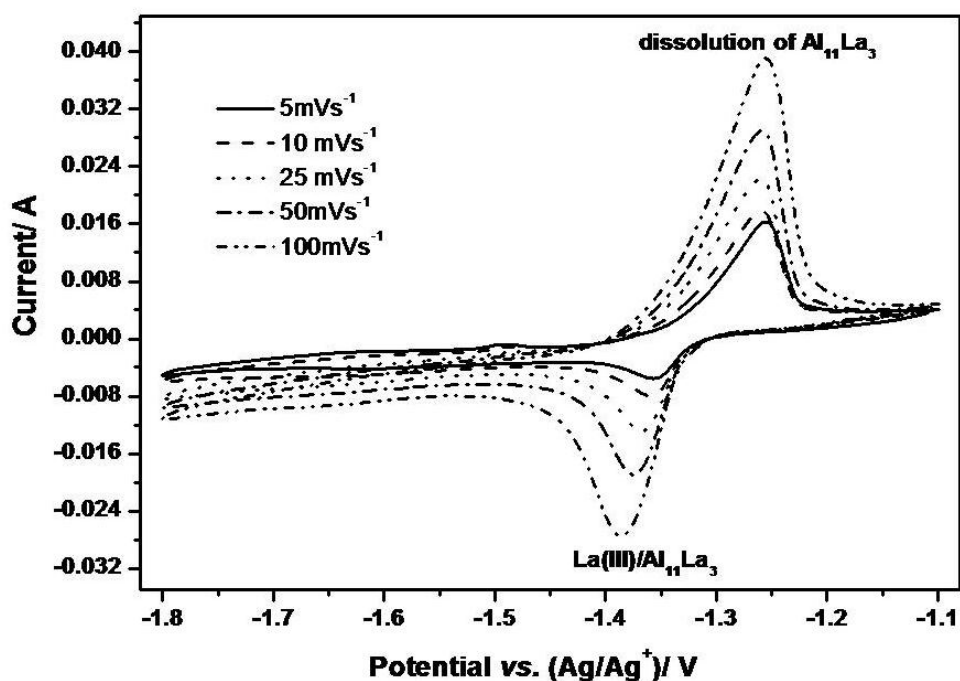


Fig. 5.5 Cyclic voltammograms for  $7.54 \times 10^{-5} \text{ mol cm}^{-3}$   $\text{LaCl}_3$  in  $\text{LiCl-KCl}$  melt on Al electrode at various scan rates. Electrode area:  $0.347 \text{ cm}^2$ . Temperature:  $723 \text{ K}$ .

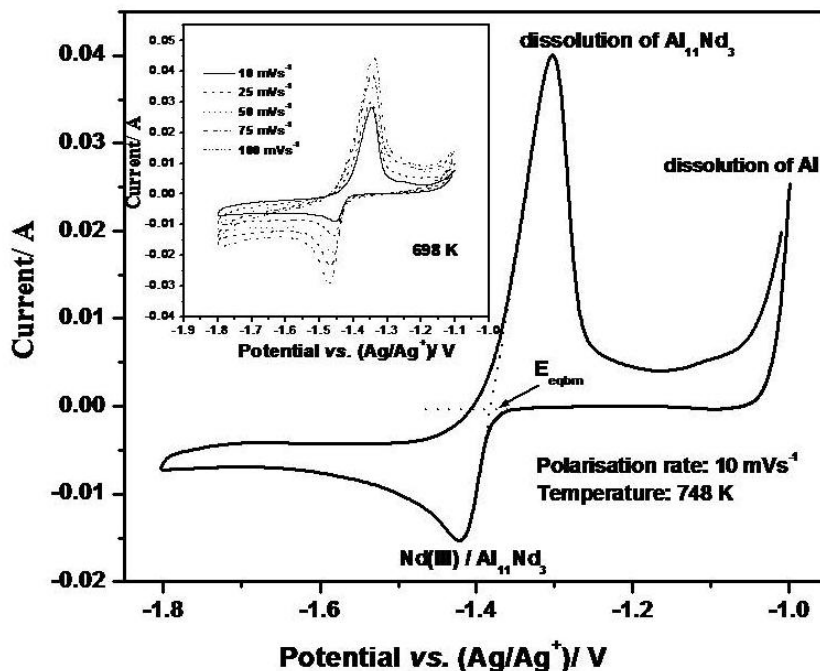


Fig. 5.6 Cyclic voltammogram for  $\text{LiCl-KCl-NdCl}_3$  melt at Al electrode at  $748 \text{ K}$ ; Concentration of  $\text{NdCl}_3$ :  $6.66 \times 10^{-5} \text{ mol cm}^{-3}$ . Inset: Cyclic voltammograms at different scan rates

criteria for soluble-soluble reversible system (Eq. 3.1) yielding the value of  $n$  close to 3. The reduction may be presumed to be close to reversibility at low scan rates and show Nernstian behavior. However, it may not be appropriate to estimate the half wave potentials from the cathodic and anodic peak potentials as was adopted for RE-Cd system using the relation (Eq. 4.2). Eq 4.2 is applicable for soluble-soluble species undergoing reversible exchange. It may not be applicable in this case, since the rate of diffusion of RE(III) ions in salt phase is not comparable to the rate of diffusion of RE in solid aluminium phase. Further, when the concentration of RE exceeds its solubility, precipitation of the solid phase,  $Al_{11}RE_3$  occurs and the electrode surface loses its homogeneity. Hence, we consider it is more appropriate to derive the apparent standard potentials of La/Nd on aluminium electrode using the Nernst equation.

#### 5.4.1.2. Apparent standard potentials of RE(III)/RE(Al) system in LiCl-KCl melt

The equilibrium potential of the redox system RE(III)/RE(Al) is given by the following expression :

$$E_{RE(III)/RE(Al)}^{eq} = E_{RE(III)/RE(0)}^0 + \frac{RT}{3F} \ln \frac{a_{RE(III)}}{a_{RE(Al)}} \quad (5.2)$$

where  $E_{RE(III)/RE(0)}^0$  is the standard potential of RE(III)/RE(0) in LiCl-KCl melt.  $a_{RE(III)}$  and  $a_{RE(Al)}$  are the activities of  $RECl_3$  in salt and that of RE metal in aluminium respectively.

Introducing the expression for apparent standard potential,  $E_{RE(III)/RE(0)}^*$  given in Eq. 5.3,

$$E_{RE(III)/RE(0)}^* = E_{RE(III)/RE(0)}^0 + \frac{RT}{3F} \ln \gamma_{RE(III)} \quad (5.3)$$

Eq. 5.2 is rearranged as

$$E_{RE(III)/RE(Al)}^{eq} = E_{RE(III)/RE(0)}^* + \frac{RT}{3F} \ln X_{RE(III)} - \frac{RT}{3F} \ln a_{RE(Al)} \quad (5.4)$$

The apparent standard potential for reduction of  $RECl_3$  on Al electrode is given as [11]

$$E_{RE(III)/RE(Al)}^* = E_{RE(III)/RE(0)}^* - \frac{RT}{3F} \ln a_{RE(Al)} \quad (5.5)$$

Eq. 5.2 is rewritten as

$$E_{RE(III)/RE(Al)}^{eq} = E_{RE(III)/RE(Al)}^* + \frac{RT}{3F} \ln X_{RE(III)} \quad (5.6)$$

The equilibrium potential,  $E_{RE(III)/RE(Al)}^{eq}$ , was obtained graphically as shown in Fig. 5.6. for cyclic voltammograms obtained at  $25 \text{ mVs}^{-1}$ . The apparent standard potentials for reduction of  $\text{LaCl}_3$  and  $\text{NdCl}_3$  on Al electrode were determined using Eq. 5.6 and the results are listed in Table 1 and Table 2 respectively. The values are compared with those reported by Serp *et al.* [28]. A difference of about 70 mV and 110 mV for  $E_{La(III)/La(Al)}^*$  and  $E_{Nd(III)/Nd(Al)}^*$  respectively, was observed between our value and the reported value. It may be noted that the value of apparent standard potentials for reduction of  $\text{LaCl}_3$  and  $\text{NdCl}_3$  on Al electrode reported by Serp *et al.* were practically the same which is not so in our case.

Table 5.1 Apparent standard potential ( $\pm 0.002 \text{ V}$ ) for La(III)/La(Al) estimated from cyclic voltammogram on Al electrode,  $X_{LaCl_3} = 0.00224$ .

Temperature, K	$E_{La(III)/La(Al)}^*$ vs. Ag/Ag <sup>+</sup> , V*	$E_{La(III)/La(Al)}^*$ vs. Cl <sub>2</sub> /Cl <sup>-</sup> , V	
		This Study	Serp <i>et al.</i> [28]
698	-1.329	-2.564	-
723	-1.305	-2.539	-2.505
748	-1.280	-2.514	-
798	-1.230	-2.465	-

\* Potentials obtained vs. Ag/Ag<sup>+</sup> ( $X_{AgCl} = 0.001$ ) rescaled to Ag/Ag<sup>+</sup> ( $X_{AgCl} = 0.0031$ ) reference electrode

Table 5.2 Apparent standard potential ( $\pm 0.002$  V) for Nd(III)/Nd(Al) estimated from cyclic voltammogram on Al electrode,  $X_{NdCl_3} = 0.00224$ .

Temperature, K	$E_{Nd(III)/Nd(Al)}^*$ vs. Ag/Ag <sup>+</sup> , V	$E_{Nd(III)/Nd(Al)}^*$ vs. Cl <sub>2</sub> /Cl <sup>-</sup> , V	
		This Study	Serp <i>et al.</i> [28]
698	-1.283	-2.517	-
723	-1.257	-2.496	-2.505
748	-1.230	-2.475	-
798	-1.178	-2.432	-

#### 5.4.1.3 Open-circuit chronopotentiometry

Open circuit potential transients were obtained using LiCl-KCl-LaCl<sub>3</sub> and LiCl-KCl-NdCl<sub>3</sub> melt by polarizing the aluminium electrode at different cathodic potentials in the range -1.5 to -1.8 V. Fig. 5.7 shows the open circuit potential transient curves obtained on the aluminium electrode using LiCl-KCl-LaCl<sub>3</sub> at 723 and 753 K exhibiting the formation of a solid phase on the aluminium surface. Even though lanthanum forms several intermetallic compounds with aluminium, only one potential plateau was observed as seen in the figure. From our earlier inference from the cyclic voltammograms, the intermetallic formed is Al<sub>11</sub>La<sub>3</sub> and the potential plateau is due to coexistence of Al<sub>11</sub>La<sub>3</sub> and Al. The potential measured with respect to Ag/ 0.1 mol % AgCl in LiCl-KCl reference electrode was rescaled with reference to that of the La(III)/La electrode, which was obtained earlier as discussed in Chapter 4. Replicate measurements were made to estimate the standard deviation of the measured *emf*. Fig. 5.8 shows the open-circuit chronopotentiograms obtained with a solution of NdCl<sub>3</sub> in LiCl-KCl at Al electrode for a cathodic polarization of -1.8 V for various durations. A significantly distinct plateau was observed at  $\sim -1.4$  V vs. Ag/Ag(I) ( $X_{AgCl} = 0.0031$ ) reference electrode in all the transients, the same potential about which a peak was

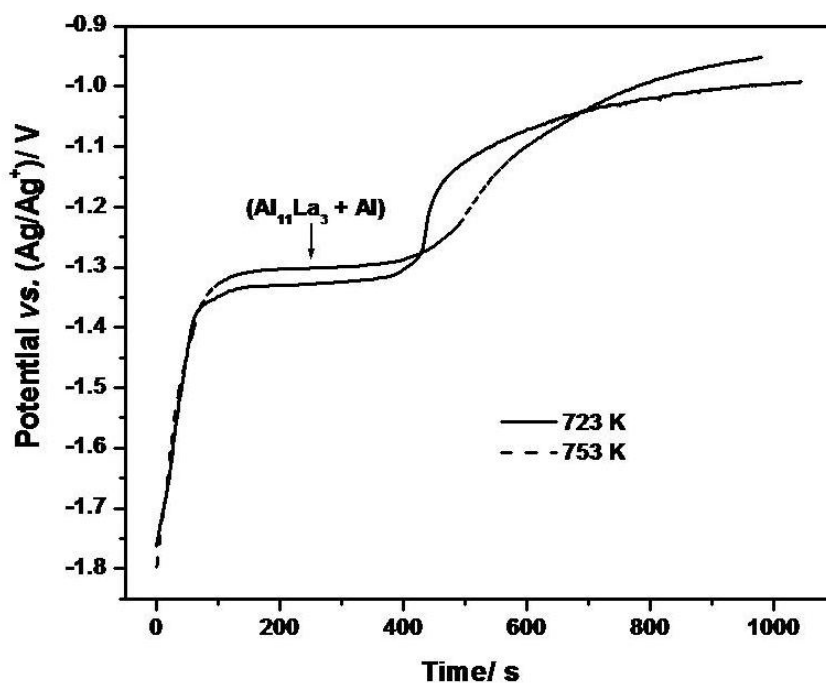


Fig.5.7 OCP transient curve for LiCl-KCl-LaCl<sub>3</sub> melt on Al electrode at different temperatures. Cathodic polarization: -1.8 V vs. (Ag/Ag<sup>+</sup>, X<sub>AgCl</sub> = 0.001) reference electrode.

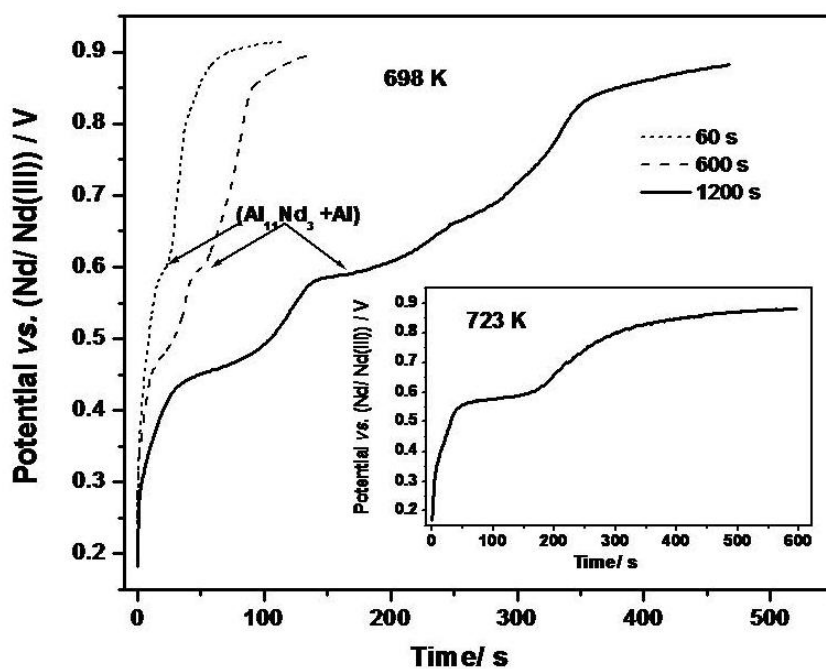
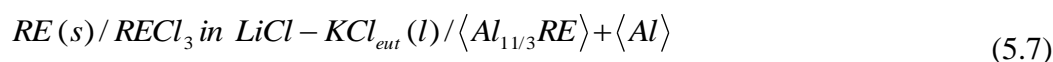


Fig.5.8 OCP transient curve for LiCl-KCl-NdCl<sub>3</sub> melt on Al electrode for different duration. Cathodic polarization: -1.8 V vs. (Ag/Ag<sup>+</sup>) reference electrode. Inset: OCP transient curve at 723 K. Cathodic polarization: -1.8 V for 600 s.

observed in the cyclic voltammograms. The potential shown in Fig. 5.8 is rescaled with respect to Nd(III)/Nd(0) electrode. A plateau  $\sim 0.6$  V vs. Nd(III)/Nd(0) electrode may be seen in the figure. The equilibrium potential of the Nd(III)/Nd(0) couple was obtained earlier as described in chapter 3. Similar to the La-Al system, only one intermetallic was observed for the Nd-Al system under our experimental condition. The plateau corresponds to the coexistence of the phases  $\text{Al}_{11}\text{Nd}_3$  and Al.

The potentials of the plateaus obtained for the La-Al and Nd-Al systems were rescaled to the potentials of the rare earth metal electrode correspond to the emf of the cell represented as:



The Gibbs energy of formation of the intermetallics,  $\text{Al}_{11}\text{La}_3$  and  $\text{Al}_{11}\text{Nd}_3$  were estimated from the emf values at different temperatures. Table 5.3 shows the values of the Gibbs energy of formation of the intermetallic,  $\text{Al}_{11}\text{La}_3$ . Our values are in good agreement with those reported by Castrillejo *et al.* [8] measured using the same technique. Sommer *et al.* [29] had measured the enthalpy of formation of aluminium-lanthanum alloys by solution calorimetry. They had reported the enthalpy of formation of  $\text{Al}_{11}\text{La}_3$  at 1513 K to be  $-41 \pm 2.5$  kJ mol<sup>-1</sup>atom<sup>-1</sup>. Borzone *et al.* had reported the enthalpy of formation of  $\text{Al}_{11}\text{La}_3$  at 298 K to be  $-41 \pm 2.0$  kJ mol<sup>-1</sup>atom<sup>-1</sup> measured by direct calorimetry [30]. In the present work, we had derived the enthalpy of formation of  $\text{Al}_{11}\text{La}_3$  from the slope of the plot of  $\Delta G/T$  vs.  $1/T$  in the temperature range 710-773 K. The heat capacity contribution ( $\Delta C_p$ ) is considered negligible. The enthalpy of formation of  $\text{Al}_{11}\text{La}_3$  at the mid temperature, namely, 742 K was found to be  $-42.92 \pm 1.5$  kJ mol<sup>-1</sup>atom<sup>-1</sup> which is within the experimental uncertainty reported by calorimetric method.

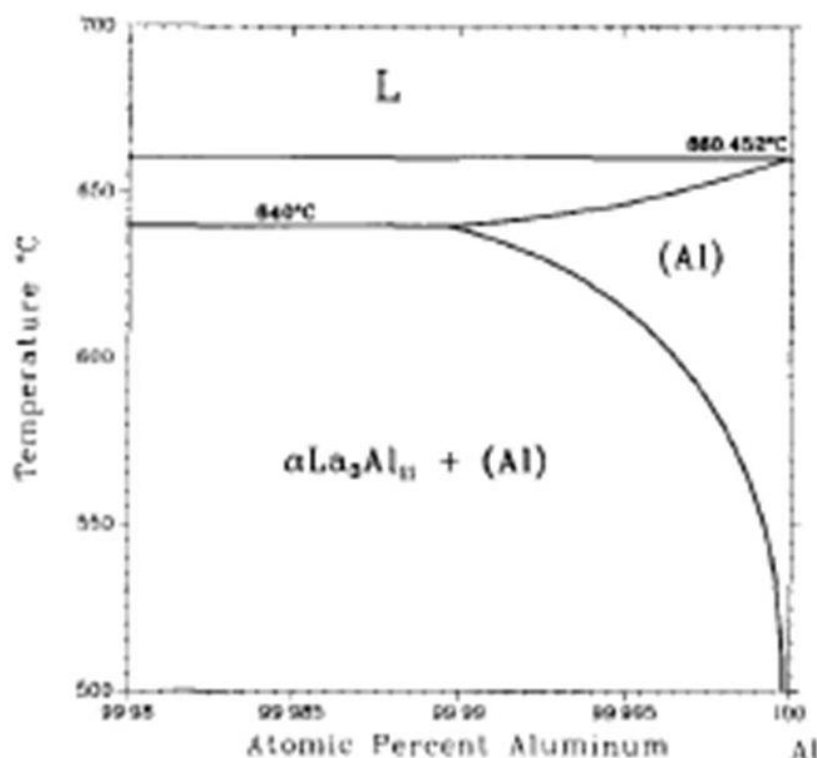


Fig. 5.9 Enlarged view of the aluminium rich region of Al-La phase diagram.

The Gibbs energy of formation of the intermetallic  $\text{Al}_{11}\text{Nd}_3$  at different temperatures were estimated from the emf values and are shown in Table 5.4. Gschneider *et al.* have given an extensive review of the thermodynamic properties of the rare earth alloys [31]. Our values are compared with those obtained by Kober *et al.* by emf measurement taken from the review. The values are fairly in good agreement with those of Kober *et al.* within the uncertainties. The emf value and Gibbs energy formation of  $\text{Nd}_3\text{Al}_{11}$  estimated from OCP measurement reported in “PYROREP” [20] are higher than those of ours. This difference arises from the difference in the equilibrium potentials of  $\text{Nd(III)/Nd(0)}$  obtained in our study and that reported in “PYROREP”.

The activities of the La and Nd in aluminium were calculated from Eq. 5.8 and the values are given in Table 5.5 and Table 5.6 for La-Al and Nd-Al systems respectively.

$$emf = -\frac{RT}{3F} \ln a_{RE(Al)} \quad (5.8)$$

The excess Gibbs energy of RE in aluminium,  $\Delta\bar{G}_{RE}^{xs}$  was evaluated using Eq. 5.9

$$\Delta\bar{G}_{RE}^{xs} = RT \ln \gamma_{RE(Al)} = -3F\Delta E - RT \ln X_{RE(Al)} \quad (5.9)$$

An enlarged view [32] of the aluminium rich region of the La-Al phase diagram is shown in Fig. 5.9. The solid solubility of La in aluminium is reported to be negligible as seen in the figure. Since we did not find any solubility data for La in aluminium, the solubility was taken from the liquidus curve of the phase diagram shown in Fig. 5.9. The solubility of La in aluminium at 823 K from the phase diagram was  $X_{La(Al)} = 1 \times 10^{-5}$  which was used for calculation of the excess Gibbs energy. The values of the excess Gibbs energy of La in aluminium,  $\Delta\bar{G}_{La}^{xs}$  and activity coefficients of lanthanum in solid aluminium calculated using Eq. 5.9 are shown in Table 5.5. The low activity coefficient values show the strong interaction of lanthanum in aluminium. Similarly, the solubility of Nd in solid Al is negligible as reported in literature [33]. Considering the behavior of rare earth elements to be similar, the solubility value was considered as  $X_{Nd(Al)} = 1 \times 10^{-5}$ . The values of the excess Gibbs energy of Nd in aluminium,  $\Delta\bar{G}_{Nd}^{xs}$  and activity coefficients of neodymium in solid aluminium calculated using Eq. 5.9 are shown in Table 5.6.

Table 5.3 Gibbs energy of formation of  $\text{La}_3\text{Al}_{11}$  estimated from OCP measurement on Al electrode

Temperature, K	emf ( $\pm 0.002$ ) V	$\Delta_f G_{\text{La}_3\text{Al}_{11}}$ kJ mol <sup>-1</sup>		
		This study (OCP)	Castrillejo <i>et al.</i> [8] (OCP)	PYROREP [20] (OCP)
723	0.620	-179.5	-180.2	-
753	0.616	-178.2	-179.2	-
773	0.613 0.616 [20]	-177.8	-178.5	-178.2

Table 5.4 Gibbs energy of formation of  $\text{Nd}_3\text{Al}_{11}$  estimated from OCP measurement on Al electrode

Temperature, K	emf ( $\pm 0.002$ ) V	$\Delta_f G_{\text{Nd}_3\text{Al}_{11}}$ kJ mol <sup>-1</sup>		
		This study (OCP)	Kober <i>et al.</i> [30] (emf)	PYROREP [20] (OCP)
698	0.591	-171.0	-176.8	-
723	0.583 0.623 [20]	-168.8	-175.1	-180.4
748	0.575	-166.5	-173.5	-
773	0.567	-164.2	-171.8	-

Table 5.5 Thermodynamic properties of La-Al intermetallic compound estimated from OCP measurement on Al electrode

Temperature, K	$\log a_{\text{La(Al)}}$	$\Delta \bar{G}_{\text{La}}^{xs}$ kJ mol <sup>-1</sup>	$\log \gamma_{\text{La(Al)}}$
723	-12.9	-110.3	-8.0
753	-12.4	-106.2	-7.4
773	-12.0	-103.5	-7.0

Table 5.6 Thermodynamic properties of Nd-Al intermetallic compound estimated from OCP measurement on Al electrode

Temperature, K	$\log a_{Nd(Al)}$	$\Delta \bar{G}_{Nd}^{xs}$ kJ mol <sup>-1</sup>	$\log \gamma_{Nd(Al)}$
698	-12.8	-104.3	-7.8
723	-12.2	-99.6	-7.2
748	-11.6	-94.9	-6.6
773	-11.1	-90.2	-6.1

#### 5.4.1.4 Potentiostatic electrolysis

To confirm the underpotential deposition of La/Nd on aluminium surface and examine the alloy formed at the equilibrium potential measured in OCP measurements, potentiostatic electrolysis was carried out on an aluminium sheet using the LiCl-KCl-LaCl<sub>3</sub> and LiCl-KCl-NdCl<sub>3</sub> melts respectively. The aluminium sheet electrode was polarized at -1.5 V vs. Ag/AgCl reference electrode at 773 K for 4 hrs. The salt adhering to the cathode deposit was scaped and the sheet was washed with ethylene glycol. Fig. 5.10 shows the SEM micrographs and the corresponding EDX analysis of the cathode deposit for LiCl-KCl-LaCl<sub>3</sub> melt. The SEM-EDX analysis reveals the formation of the intermetallic Al<sub>11</sub>La<sub>3</sub>. Fig. 5.11 shows the XRD pattern for electrodeposition of lanthanum on aluminium electrode at -1.5V for 6 hrs at 798 K. The XRD pattern also shows the formation of the intermetallic Al<sub>11</sub>La<sub>3</sub>. Fig. 5.12 shows the SEM micrograph and the corresponding EDX analysis of the cathode deposit for LiCl-KCl-NdCl<sub>3</sub> melt indicating underpotential deposition of Nd on aluminium surface. The XRD analysis of the sample confirms the formation of the intermetallic Al<sub>11</sub>Nd<sub>3</sub> as seen in Fig. 5.13.

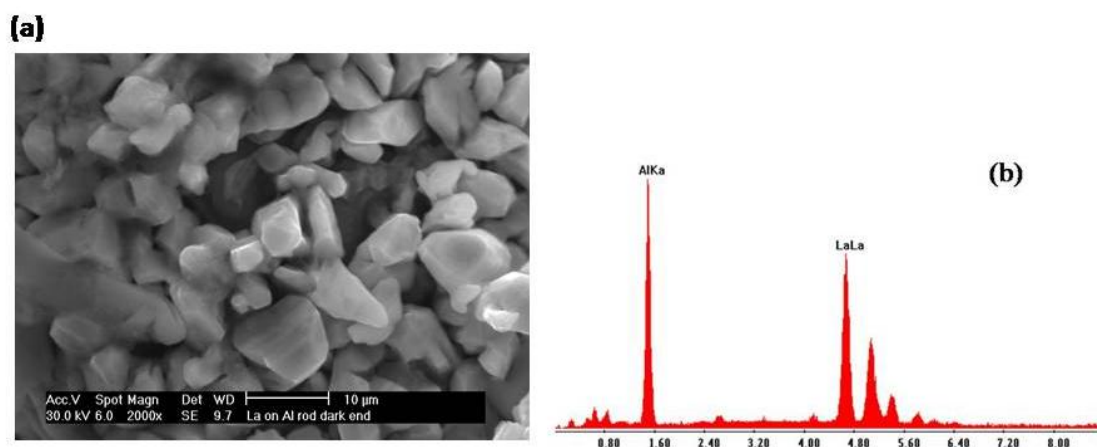


Fig. 5.10 (a) Cross-sectional SEM image of La-Al film formed by potentiostatic electrolysis at 773 K. Cathodic polarization:  $-1.5$  V vs. ( $\text{Ag}/\text{Ag}^+$ ,  $X_{\text{AgCl}} = 0.001$ ) reference electrode (b) corresponding EDX analysis confirming the formation of  $\text{Al}_{11}\text{La}_3$

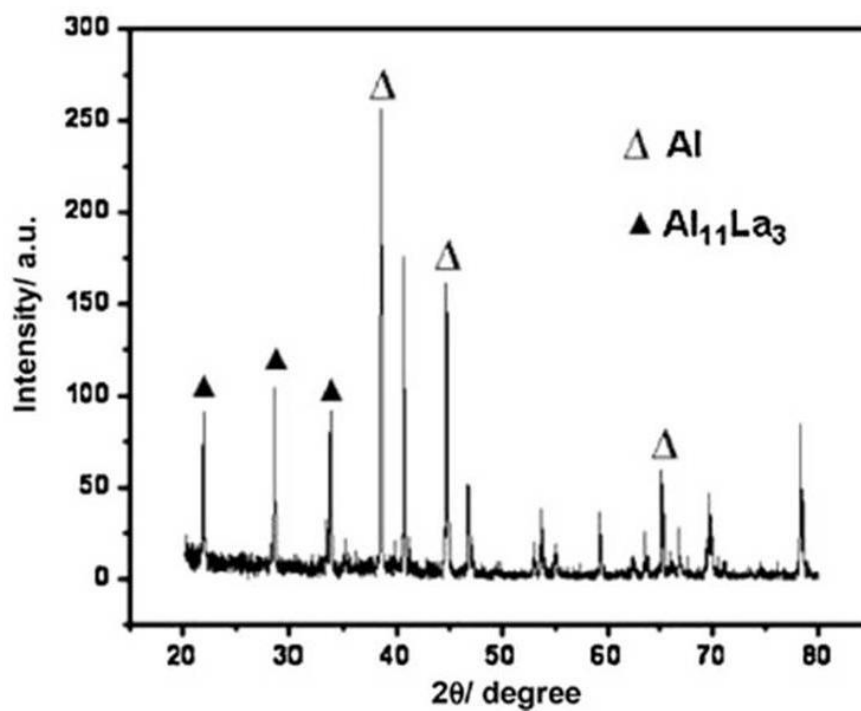


Fig.5.11 XRD pattern of La-Al film formed by potentiostatic electrolysis at 798 K for cathodic polarization of  $-1.5$  V vs. ( $\text{Ag}/\text{Ag}^+$ ,  $X_{\text{AgCl}} = 0.001$ ) reference electrode for 6 hrs.

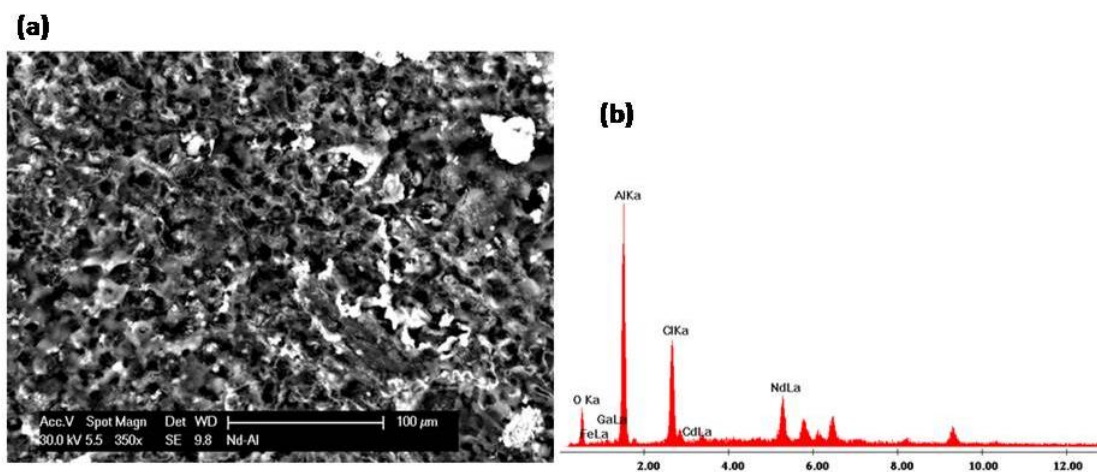


Fig.5.12 (a) Cross-sectional SEM image of Nd–Al film formed by potentiostatic electrolysis at  $-1.5\text{ V vs. (Ag/Ag}^+)$  reference electrode at  $773\text{ K}$  and (b) corresponding EDX analysis confirming the formation of  $\text{Al}_{11}\text{Nd}_3$ .

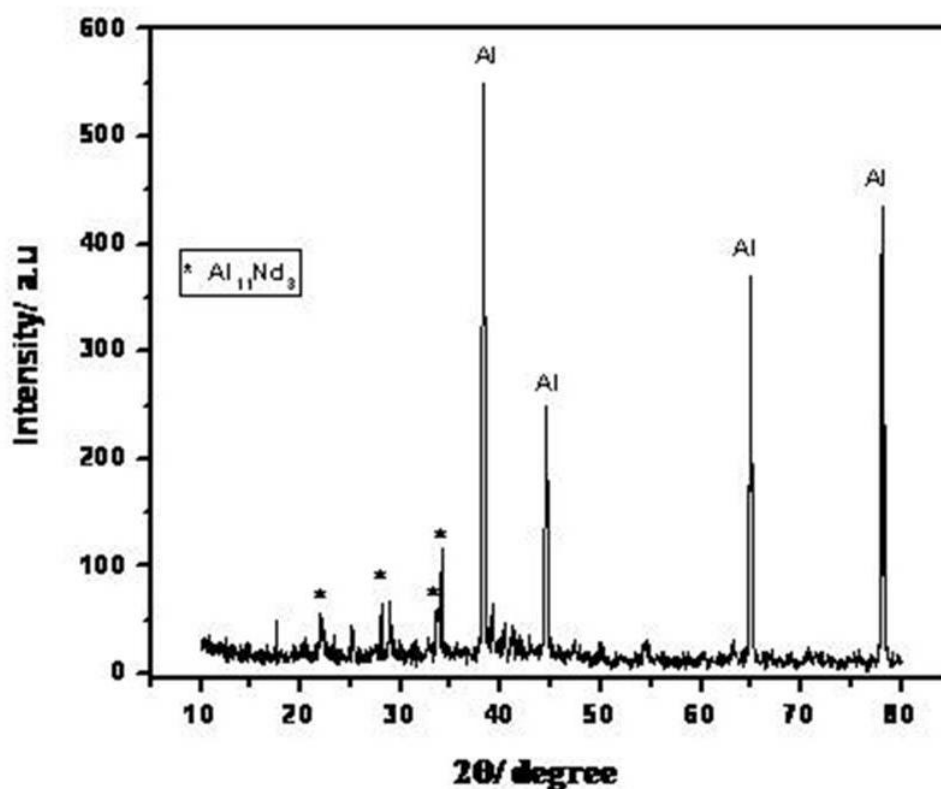


Fig.5.13 XRD pattern of Nd–Al film formed by potentiostatic electrolysis at  $-1.5\text{ V vs. (Ag/Ag}^+)$  reference electrode for 5 hrs at  $773\text{ K}$ .

## 5.4.2 Electrochemical reduction behaviour of $UCl_3$ on solid aluminium electrode

### 5.4.2.1 Analysis of the cyclic voltammograms

The reduction behavior of  $UCl_3$  on aluminium electrode was studied from the cyclic voltammograms obtained at different switching potentials and at different polarization rates. Fig. 5.14 shows the cyclic voltammograms obtained for LiCl-KCl- $UCl_3$  melt on W and Al electrodes at 723 K. The reduction behavior of  $UCl_3$  on W surface was discussed in detail in chapter 3 and we had observed that the peak for the reduction of U(III) ion to U metal appeared  $\sim -1.45$  V. From the peak positions, we attribute peak  $II_c$  in Fig. 5.14 to the reduction of U(III) ion to U metal and peak  $I_c$  at  $\sim -1.1$  V to the underpotential reduction of U(III) ions on the Al surface forming U-Al alloy. It may be observed from the figure that the reduction peak potential for U(III)/U(0) shifted by  $\sim 350$  mV towards the positive direction on the aluminium electrode. Fig. 5.15 shows the cyclic voltammogram obtained for LiCl-KCl- $UCl_3$  melt on Al at 698 K and the inset to those at 723 and 743 K. It may be observed that the redox potentials for U(III)/U(Al) couple is very close to that of the Al electrode. The re-oxidation peak for the U(Al) alloy was not well resolved for all the cyclic voltammograms recorded. This occurred because the re-oxidation peak for the U(Al) alloy was masked by the unlimited current for the dissolution of Al in the anodic cycle. Cyclic voltammograms obtained at low polarization rates alone showed the peaks for formation and dissolution of the U-Al alloy. The nature of the voltammograms was very much dependent on the scan rates and switching potentials. The peak for reduction of Al(III)/Al largely affected the peak position of U(III)/U(Al) couple. The shift in peak potentials with scan rates and the shape of the voltammograms show that the redox couple does not show reversible behavior. Though the peaks for formation and dissolution of the U-Al alloy were not similar to those obtained in the case of the lanthanides, the underpotential reduction of U(III) ion is

revealed from the cyclic voltammograms. The reaction for the reduction of U(III) ions on Al electrode is given as



Our observation is very much similar to the observations made by Cassayre *et al.* [10-11]. Similar studies carried out by Mendes *et al.* and Soucek *et al.* for  $\text{PuCl}_3$  and  $\text{NpCl}_3$ , respectively on aluminium electrode showed reduction peak  $\sim -1.2$  V and re-oxidation peak  $\sim -0.95$  V. They had reported that the re-oxidation of  $\text{An-Al}_n$  alloy was well distinguished from the oxidation of pure Al electrode in contrast to the U-Al alloy [23, 24]. Fig. 5.16 shows the phase diagram of the U-Al system [33]. Though uranium forms three intermetallic compounds with aluminium, only a single redox peak was observed for alloy formation. The formation of U-Al has been investigated further by open circuit potential measurements and potentiostatic electrolysis discussed in the following sections.

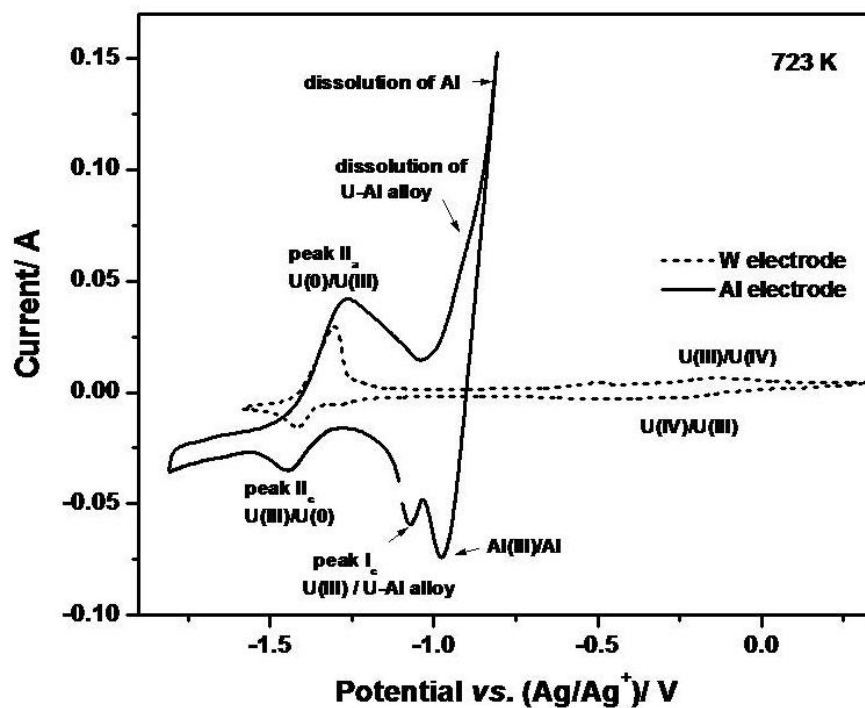


Fig.5.14 Cyclic voltammograms obtained on the tungsten and aluminium electrodes for LiCl-KCl-UCl<sub>3</sub> melt at 723 K.

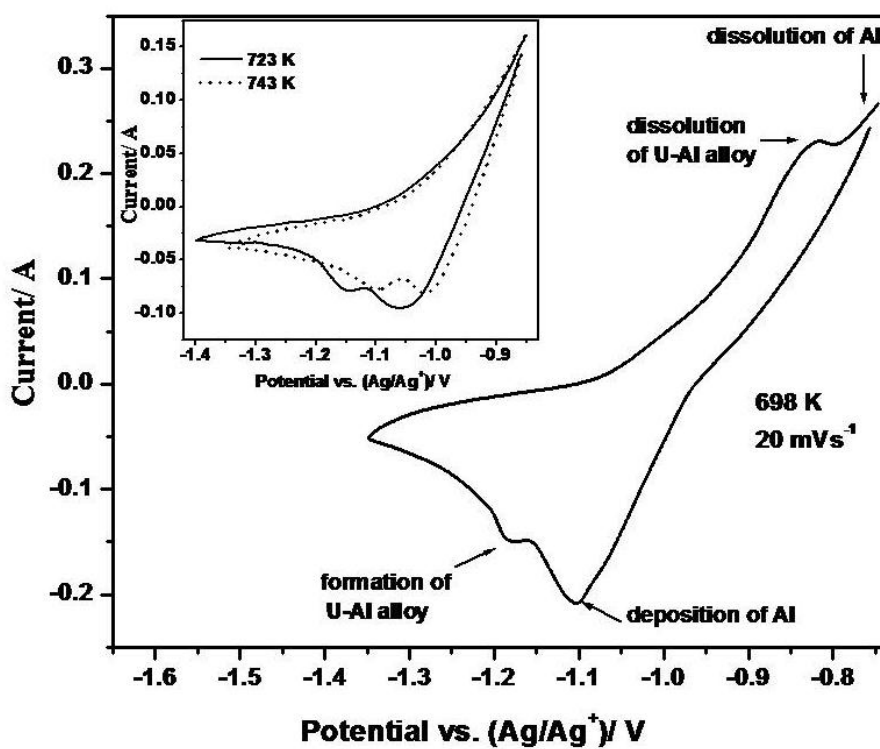


Fig.5.15 Cyclic voltammograms obtained on the aluminium electrode for LiCl-KCl-NdCl<sub>3</sub> melt at different temperatures.

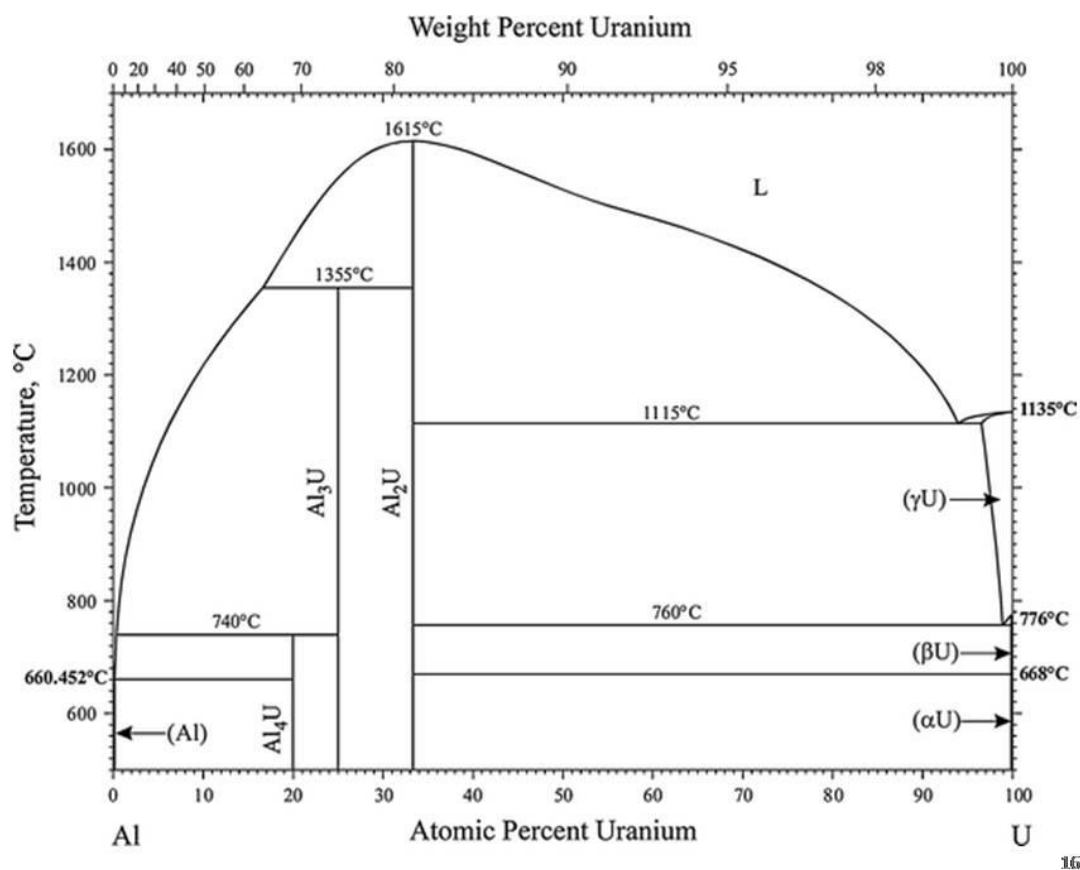


Fig. 5.16 Al-U phase diagram [33].

#### 5.4.2.2 Open-circuit chronopotentiometry

Open circuit potential transients were obtained using LiCl-KCl-UCl<sub>3</sub> melt by polarizing the aluminium electrode at different cathodic potentials. Fig. 5.17 shows the open circuit potential transient curves obtained on the aluminium electrode at 723 K for cathodic polarization at -1.3 V. The plateau for the equilibrium between the U-Al alloy and Al is very close to the rest potential of the aluminium electrode. It is presumed that the plateau for the equilibrium between the U-Al alloy and Al lies between -1.05 and -1V where a change in slope was observed as seen in Fig. 5.17. However Cassayre *et al.* [10] have reported that the potential for the UAl<sub>n</sub> alloy and the rest potential for Al were

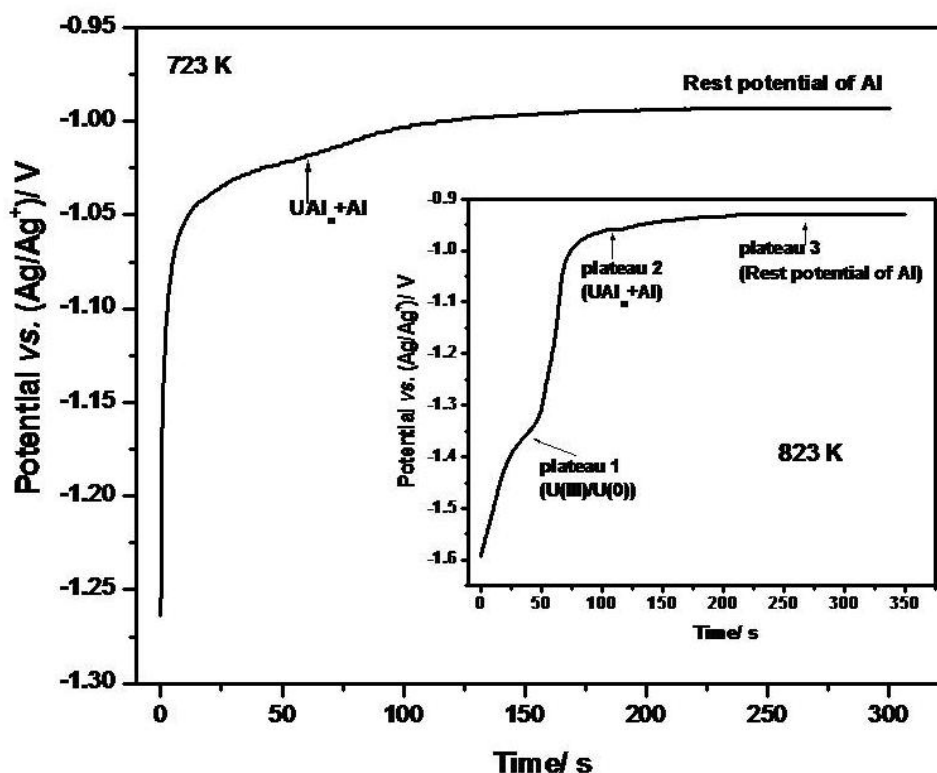


Fig.5.17 Open circuit potential transient curve for  $\text{UCl}_3$  in  $\text{LiCl-KCl}$  melt on Al electrode at different temperatures. Cathodic polarization:  $-1.3 \text{ V vs. (Ag/Ag}^+)$  reference electrode

practically identical. They had considered the rest potential of the Al electrode for estimating the emf and Gibbs energy of formation of the alloy  $\text{UAl}_n$ . One possible reason why they had not observed the change in slope could be due to the long time period of their OCP transient and this could have resulted in poor resolution of the potentials. Inset of Fig.5.17 shows the open circuit transient obtained for a cathodic polarization of  $-1.6 \text{ V}$  at  $823 \text{ K}$ . A plateau corresponding to  $\text{U(III)/U(0)}$  couple is observed  $\sim -1.35 \text{ V}$ . The difference between the potentials of plateau 1 and 2 corresponds to the Gibbs energy of formation of the U-Al alloy. Table 5.7 shows the difference in the potentials of the two plateaus and the Gibbs energy of formation of the intermetallic  $\text{UAl}_n$ . The Standard Gibbs energy of formation of the intermetallics,  $\text{UAl}_4$ ,  $\text{UAl}_3$  and  $\text{UAl}_2$  reported by Chiotti *et al.* from emf measurement are given by the Eq. 5.11, 5.12 and 5.13 respectively [35]. Chiotti

*et al.* have given an extensive review of the thermodynamic properties of actinide binary alloys.

$$\Delta_f G_{UAl_4}^0 (\text{cal / mole}) = -32140 - 7.52T \cdot \ln(T) + 59.07T \quad (5.11)$$

$$\Delta_f G_{UAl_3}^0 (\text{cal / mole}) = -26290 - 1.305T \cdot \ln(T) + 10.5T \quad (5.12)$$

$$\Delta_f G_{UAl_2}^0 (\text{cal / mole}) = -22790 - 2.326T \cdot \ln(T) + 18.37T \quad (5.13)$$

The values of the Gibbs energy of formation of the intermetallics, UAl<sub>4</sub>, UAl<sub>3</sub> and UAl<sub>2</sub> and their corresponding emf values are given in Table 5.8. It may be observed that the Gibbs energy of formation of the intermetallics, UAl<sub>4</sub> and UAl<sub>3</sub> differ merely by 1 kJ mol<sup>-1</sup> and the difference in the corresponding emf is < 10 mV. Taking into consideration of our observation, report by Cassayre *et al.* [10] and emf values of Chiotti *et al.* [35] we may conclude that the compound formed about the plateau region on the Al surface corresponds to the intermetallics, UAl<sub>4</sub> and UAl<sub>3</sub>. The midpoint of the plateau was considered as the equilibrium potential,  $E_{U(III)/U(Al)}^{eqbm}$ . Nagarajan *et al.* had measured the enthalpy of formation of aluminium- uranium alloys by solution calorimetry [36]. They had reported the enthalpy of formation of UAl<sub>4</sub> at 978 K to be  $-126.5 \pm 13.3$  kJ mol<sup>-1</sup> and that of UAl<sub>3</sub> at 1086 K to be  $-118.1 \pm 8.2$  kJ mol<sup>-1</sup>. In the present work, we have derived the enthalpy of formation of UAl<sub>n</sub> from the slope of the plot of  $\Delta G/T$  vs.  $1/T$  in the temperature range 698 - 823 K. The heat capacity contribution is considered negligible. The enthalpy of formation of UAl<sub>n</sub> at the mid temperature, namely, 748 K was found to be  $-139.3 \pm$  kJ mol<sup>-1</sup> and is in agreement with that of Nagarajan *et al.* within the uncertainty reported for UAl<sub>4</sub> by the calorimetric method.

The activity of uranium metal in aluminium was calculated from Eq. 5.14 and the excess Gibbs energy of uranium in aluminium,  $\Delta \bar{G}_U^{xs}$  was evaluated using Eq. 5.15.

$$emf = -\frac{RT}{3F} \ln a_{U(Al)} \quad (5.14)$$

$$\Delta \bar{G}_U^{xs} = RT \ln \gamma_{U(Al)} = -3F\Delta E - RT \ln X_{U(Al)} \quad (5.15)$$

The solid solubility of U in aluminium was given as 1.69 atom % at 913 K (eutectic temperature) in literature [35] and this value was used in the estimation of the excess Gibbs energy of uranium in aluminium,  $\Delta \bar{G}_U^{xs}$ . The activity coefficients of uranium in solid aluminium were calculated using Eq. 5.15. The thermodynamic properties estimated from OCP measurement are shown in Table 5.9. Since the peak potentials for the reduction of U(III)/U(Al) were not reproducible due to the redox peaks for Al(III)/Al, we had estimated the apparent standard potential for reduction of U(III) ion on Al surface from the equilibrium potentials measured by OCP method. The apparent standard potential for reduction of U(III) ion on Al surface,  $E_{U(III)/U(Al)}^*$ , was estimated using Eq. 5.6 and the values are shown in Table 5.10.

Table 5.7 Gibbs energy of formation of  $UAl_n$  estimated from OCP measurement on Al electrode

Temperature, K	emf ( $\pm 0.005$ ) V	$\Delta_f G_{UAl_n}$ kJ mol <sup>-1</sup>	
		This study (OCP)	Cassayre <i>et al.</i> [10] (OCP)
698	0.367	-106.2	-
723	0.363	-105.2	-103.2 $\pm$ 2.1
748	0.360	-104.2	-
773	0.356	-103.1	-102.0 $\pm$ 0.8

Table 5.8 Gibbs energy formation of  $UAl_n$  from emf measurement [35].

Temperature , K	$U(\alpha) + 4Al(c) \leftrightarrow UAl_4(c)$		$U(\alpha) + 3Al(c) \leftrightarrow UAl_3(c)$		$U(\alpha) + 2Al(c) \leftrightarrow UAl_2(c)$	
	emf V	$\Delta_f G_{UAl_4}$ kJ mol <sup>-1</sup>	emf V	$\Delta_f G_{UAl_3}$ kJ mol <sup>-1</sup>	emf V	$\Delta_f G_{UAl_2}$ kJ mol <sup>-1</sup>
698	0.3654	-105.79	0.3593	-104.02	0.2978	-86.21
723	0.3647	-105.57	0.3590	-103.94	0.2975	-86.13
748	0.3639	-105.37	0.3588	-103.87	0.2973	-86.05
773	0.3634	-105.19	0.3686	-103.81	0.2970	-85.99

Table 5.9 Thermodynamic properties of U-Al intermetallic compound estimated from OCP measurement on Al electrode

Temperature, K	$\log a_{U(Al)}$	$\Delta \bar{G}_U^{xs}$ kJ mol <sup>-1</sup>	$\log \gamma_{U(Al)}$
698	-7.9	-82.5	-6.2
723	-7.6	-80.6	-5.8
748	-7.3	-78.8	-5.5
773	-7.0	-76.9	-5.2

Table 5.10 Apparent standard potential ( $\pm 0.005$  V) for U(III)/U(Al) estimated from OCP measurement on Al electrode,  $X_{UCl_3} = 0.00268$ .

Temperature, K	$E_{U(III)/U(Al)}^{eqbm}$ vs. Ag/Ag <sup>+</sup> , V	$E_{U(III)/U(Al)}^*$ vs. Ag/Ag <sup>+</sup> , V	$E_{U(III)/U(Al)}^*$ vs. Cl <sub>2</sub> /Cl <sup>-</sup> , V
698	-1.051	-0.931	-2.165
723	-1.039	-0.916	-2.155
748	-1.028	-0.901	-2.145
798	-1.017	-0.885	-2.135

### 5.4.2.3 Potentiostatic electrolysis

To examine the underpotential reduction of  $\text{UCl}_3$  on aluminium surface at the equilibrium potential measured in OCP measurements, potentiostatic electrolysis was carried out using  $\text{LiCl-KCl-UCl}_3$  melt to electrodeposit uranium on an aluminium sheet. The aluminium sheet electrode was polarized at  $-1.3$  V vs.  $\text{Ag/AgCl}$  reference electrode at  $723$  K for over 8 hrs. The adhering salt was scarped and the sheet was washed with ethylene glycol. Fig. 5.18 shows the XRD pattern for electrodeposition of uranium on aluminium electrode. The XRD analysis of the sample showed the presence of  $\text{UAl}_4$  &  $\text{UAl}_3$ .

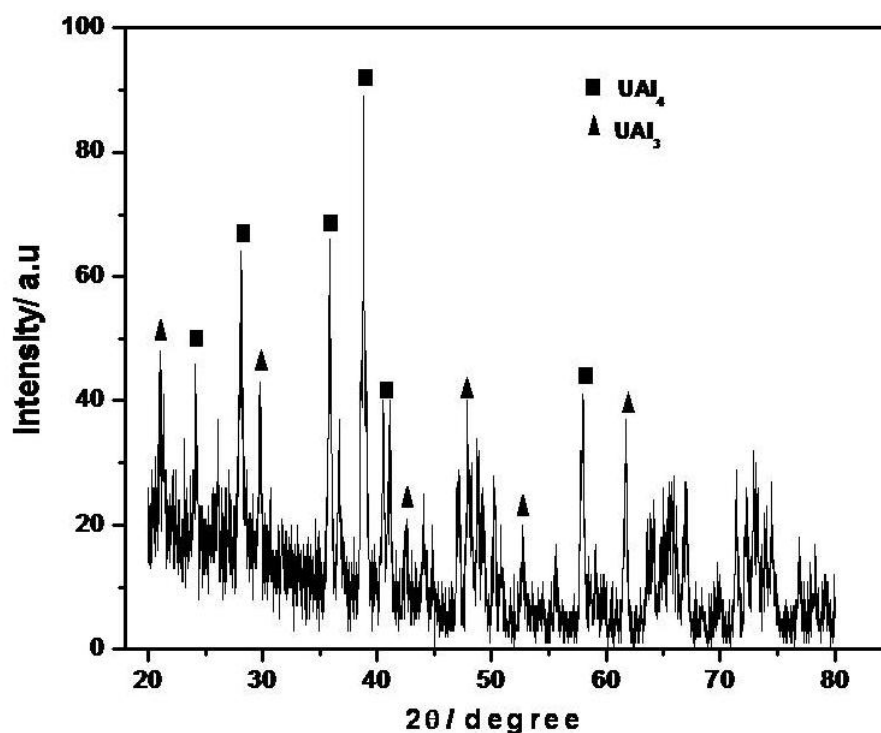


Fig.5.18 XRD pattern of U–Al film formed by potentiostatic electrolysis at  $-1.3$  V vs.  $(\text{Ag/Ag}^+)$  reference electrode for 8 hrs at  $723$  K.

## 5.5 Summary

The electrode reaction of the rare earth ion (RE - La, Nd) on solid aluminium electrode was studied by electrochemical methods. The reduction occurred at more

positive potential than that for pure metal formation. It was thermodynamically analysed to be due to lowering of the activity of the rare earth metal in aluminium due to the formation of intermetallic compound  $\text{Al}_{11}\text{RE}_3$ . The apparent standard electrode potential of  $\text{RE(III)/RE(Al)}$  in the temperature range 698-773 K, was estimated from the cyclic voltammograms. The Gibbs energy of formation of the intermetallics,  $\text{Al}_{11}\text{La}_3$  and  $\text{Al}_{11}\text{Nd}_3$  were obtained from the open circuit potential measurements similar to the method used for the RE-Cd system. The activity of rare earth metal in aluminium, the excess Gibbs energy and the activity coefficient of rare earth metal in aluminium were estimated from the open circuit potential measurement and are reported by this method for the first time here. SEM-EDX analysis and the XRD pattern of the deposit showed the formation of intermetallic compound  $\text{Al}_{11}\text{RE}_3$ . The studies reported on Nd-Al system in this work is not reported in open literature earlier.

The redox behavior of  $\text{UCl}_3$  on solid aluminium electrode was studied by cyclic voltammetry and open circuit potentiometry. The studies showed the underpotential reduction of U(III) ion on aluminium electrode at a potential  $\sim 0.35$  V more anodic than pure uranium metal deposition. The cyclic voltammograms did not show well resolved peaks for the formation and dissolution of the U-Al alloy. The OCP transients showed that the equilibrium potential for the U-Al alloy was very close to the rest potential of the aluminium electrode. The apparent standard electrode potentials of  $\text{U(III)/U(Al)}$ , activity of uranium in aluminium, the excess Gibbs energy and the activity coefficient of uranium in aluminium were estimated from the open circuit potential measurement and are reported by this method for first time.

XRD pattern of the cathode deposit obtained by polarizing the aluminium electrode at -1.3 V showed the formation of the intermetallic compounds,  $\text{UAl}_4$  and  $\text{UAl}_3$ .

## 5.6 References

1. L. M. Ferris, J. C. Mailen, F. J. Smith, J. Inorg. Nuc. Chem. 33 (1971) 1325.
2. H. Morriyama, K. Yajima, Y. Tominaga, K. Moritani, J. Oishi, J. Nuc. Sci. Technol.21 (12) (1984) 949.
3. Masaki Kurata, Yoshiharu Sakamura, Tsuneo Matsui, J. Alloys Comp. 234 (1996) 83.
4. O. Conocar, N. Douyere, J. Lacquement, J. Nucl. Mater. 344 (2005) 136.
5. O. Conocar, N. Douyere, J.P. Glatz, J. Lacquement, R. Malmbeck, J. Serp, Nucl. Sci. Eng. 153 (2006) 253.
6. J. Serp, M. Allibert, A. Le Terrier, R. Malmbeck, M. Ougier, J. Rebizant, J. P. Glatz, J. Electrochem. Soc. 152 (2005) C167.
7. P. Soucek, L. Cassayre, R. Malmbeck, E. Mendes, R. Jardin, J.P. Glatz, Radiochim. Acta 96 (2008) 315.
8. Y. Castrillejo, R. Bermejo, A.M. Martinez, E. Barrado, P. Diaz Arocas, J. Nucl. Mater. 360 (2007) 32.
9. P. Soucek, R. Malmbeck, E. Mendes, C. Nourry, D. Sedmidubsky, J. P. Glatz, J. Nucl. Mater. 394 (2009) 26.
10. L. Cassayre, C. Caravaca, R. Jardin, R. Malmbeck, P. Masset, E. Mendes, J. Serp, P. Soucek, J.P. Glatz, J. Nucl. Mater. 378 (2008) 79.
11. L. Cassayre, R. Malmbeck, P. Masset, J. Rebizant, J. Serp, P. Soucek, J. P. Glatz, J. Nucl. Mater. 360 (2007) 49.
12. J. Serp, R. Malmbeck, C. Schepller, J. P. Glatz, ATALANTE 2004, 21-24 June 2004.
13. P. Soucek, R. Malmbeck, C. Nourry, J. P. Glatz, Energy Procedia 7 (2011) 396.
14. P. Soucek, R. Malmbeck, E. Mendes, C. Nourry, D. Sedmidubsky, J.-P. Glatz, J.

- Nucl. Mater. 394 (2009) 26.
15. L. Cassayre, P. Soucek, E. Mendes, R. Malmbeck, C. Nourry, R. Eloirdi, J. P. Glatz, J. Nucl. Mater. 414 (2011) 12.
  16. Y. Castrillejo, M.R. Bermejo, P. Diaz Arocas, A.M. Martinez, E. Barrado, J. Electroanal. Chem. 575 (2005) 61.
  17. Y. Castrillejo, M. R. Bermejo, P. Diaz arocas, A. M. martinez, E. Barrado, J. Electroanal. Chem. 579 (2005) 343.
  18. Y. Castrillejo, M.R. Bermejo, E. Barrado, A.M. Martinez, Electrochim. Acta 51 (2006) 1941.
  19. Y. Castrillejo, P. Fernandez, M.R. Bermejo, E. Barrado, A.M. Martínez, , Electrochim. Acta 54 (2009) 6212.
  20. “Separation by electrolysis in chloride media” – ‘PYROREP’, Contract No. FIKW-CT-2000-00049, Project No. FIS5-1999-00199, 2003; Project co-coordinator- H. Boussier.
  21. P. Taxil, L. Massot, C. Nourry, M. Gibilaro, P. Chamelot, L. Cassayre, J. Fluorine Chem., 130 (2009) 94.
  22. M. Gibilaro, L. Massot, P. Chamelot, P. Taxil, Electrochim. Acta 55 (2009) 281.
  23. E. Mendes, R. Malmbeck, C. Nourry, P. Soucek, J. P. Glatz, J. Nucl. Mater. 420 (2012) 424.
  24. P. Soucek, R. Malmbeck, E. Mendes, C. Nourry, D. Sedmidubsky, J. P. Glatz, J. Nucl. Mater. 394 (2009) 26.
  25. G. De Córdoba, A. Laplace, O. Conocar, J. Lacquement, J. Nucl. Mater. 393 (2009) 459.
  26. Gschneidner : Al-La Phase Diagram, ASM Alloy Phase Diagrams Center, P. Villars, Editor-in-chief; <http://www1.asminternational.org/AsmEnterprise/APD>, ASM

- International, Materials Park, OH, USA, 2006-2014.
27. H. Okamoto: Al-Nd Phase Diagram, ASM Alloy Phase Diagrams Center, P. Villars, Editor-in-chief; <http://www1.asminternational.org/AsmEnterprise/APD>, ASM International, Materials Park, OH, USA, 2006-2014.
  28. J. Serp, P. Chamelot, S. Fourcaudot, R.J.M. Konings, R. Malmbeck, C. Pernel, J.C. Poignet, J. Rebizant, J.-P. Glatz, *Electrochim. Acta* 51 (19) (2006) 4024.
  29. F. Sommer, M. Keita, H.G. Krull, B. Predel, *J. Less Common Met.* 137 (1988) 267.
  30. G. Borzone, A. Maria Cardinale, N. Parodi, G. Cacciamani, *J. Alloys Compd.* 247 (1997) 141.
  31. K. A. Gschneider, L. Eyring, G. H. Lander and G. R. Choppin, *Handbook on the Physics and Chemistry of Rare Earths*, Vol. 19. , Elsevier Sci. SV, 1994, p.576.
  32. K. A. Gschneider, F. W. Calderwood, *Bull. Alloy Phase Diagrams* Vol.9 No.6 (1988) 686.
  33. Landolt-Börnstein, *Elements and Binary Systems from Ag-Al to Au-Tl - Group IV* *Phy. Chem. Volume 19B1*, 2002, p. 178.
  34. H. Okamoto, *J. Phase Equilibria and Diffusion*, 33 (6) (2012) 489.
  35. P. Chiotti, V. V. Akhachinskij, I. Ansara, M. H. Rand, “The chemical thermodynamics of actinide elements and compounds, Part 5, The Actinide Binary Alloys”, IAEA1981, p. 83.
  36. K. Nagarajan, R. Babu , C.K. Mathews, *J. Nucl. Mater.* 201 (1993) 142.

## CHAPTER 6

### Electrochemical behavior of La-, Nd- and U-trivalent ions in LiCl-KCl eutectic melt on gallium cathode

#### 6.1 Introduction

As mentioned earlier in chapter 5, many molten metals (Cd, Bi, Zn, Sn, Ga and Al) are suitable for actinide-lanthanide separation using pyrochemical separation techniques based on : (a) liquid-liquid reductive extraction; (b) electrodeposition at liquid metal electrode. Not many studies have been reported on the use of gallium metal both by reductive extraction and for electrodeposition in chloride media. In the present work, we have explored the feasibility of using gallium cathode for efficient actinide-lanthanide separation.

#### 6.2 Literature survey

A few studies have been reported on the estimation of activity coefficients of Pu and Ce in liquid gallium by electrochemical methods [1-3]. These studies have been carried out at CEA/ Valduc, France, for developing advanced pyrochemical process for recycling of scrap Pu. Lambertin *et al.* [1] had studied the reduction behavior of  $\text{CeCl}_3$  and  $\text{PuCl}_3$  on gallium cathode in  $\text{CaCl}_2$  and NaCl-KCl melts at 1073 K. The studies showed the feasibility of selective deposition of Pu in gallium cathode. The redox potential of Pu(III) ions and the activity coefficient of Pu in gallium were estimated by chronoamperometry. The activity coefficient of Ce in Ga was estimated by emf method. Bourges *et al.* [2] had reported the redox behavior of  $\text{PuCl}_3$  in NaCl-KCl- $\text{BaCl}_2$  ternary eutectic mixture, equimolar NaCl-KCl and pure  $\text{CaCl}_2$  melts at 1073 K and estimated the formal standard potential of Pu(III)/Pu and Pu(III)/Pu(Ga) using cyclic voltammetry and chronoamperometry. They had deduced the activity coefficient of Pu in liquid gallium from these measurements. Laplace *et al.* [3] had reported the activity coefficient of Pu

and Ce in Cd, Ga, Bi and Zn by cyclic voltammetry and potentiometry. They had compared the values to those reported by Lebedev *et al.* [4] on Al, Bi, Zn and Cd metals. They had ordered the solvents from most selective to the less selective one as Al > Ga > Bi > Zn > Cd. Finne *et al.* had estimated the activity coefficient of Gd in Ga metal by galvanodynamic method using NaCl-CaCl<sub>2</sub> melt [5]. Todd *et al.* had derived the excess thermodynamic quantities (enthalpy and entropy) of Ce, U, Pu and Am in Al, Bi, Cd and Ga metals based on correlations and models [6]. They had compared the separation factors of actinides from Ce in these solvents. Toda *et al.* had reported the distribution coefficients of Am and Ce in LiCl-KCl eutectic and liquid gallium system at 773 K [7]. They had evaluated the separation factor for Am from Ce and compared the values with those in Bi and Cd systems and found that the Ga system was more selective.

No electrochemical study has been reported on U-Ga, La-Ga, Nd-Ga systems in the literature to our knowledge. In the present study, we report the redox behavior of UCl<sub>3</sub>, LaCl<sub>3</sub> and NdCl<sub>3</sub> on Ga surface using cyclic voltammetry and open circuit potentiometry.

## 6.3 Experimental

### 6.3.1 Chemicals

High purity gallium metal (Hindal Co. Industries Ltd. India, 99.99%) was used in the preparation of the electrolyte, LiCl-KCl-GaCl<sub>3</sub>. The purity of other chemicals used in the study is same as those described in Chapter 2.

### 6.3.2. Preparation of the electrolyte salt

Purification of LiCl-KCl salt mixture was as described earlier in Chapter 2. Stock of LiCl-KCl-GaCl<sub>3</sub> electrolyte was prepared by chlorinating the Ga metal taken along with purified LiCl-KCl salt mixture. Chlorine gas was bubbled through the melt at 773 K for over 8 hours in the chlorination facility. The excess chlorine gas was removed from the melt by bubbling high purity argon gas through the melt for about 1 hour. The amount

of Ga in the sample was estimated by ICP-AES. Weighed amounts of LiCl-KCl-GaCl<sub>3</sub> thus prepared were diluted with pure LiCl-KCl salt mixture and weighed amounts of LaCl<sub>3</sub>/ NdCl<sub>3</sub> was added to this mixture for preparing LiCl - KCl – 1 wt% LaCl<sub>3</sub> – 1 wt% GaCl<sub>3</sub> and LiCl - KCl – 1 wt% NdCl<sub>3</sub> – 1 wt% GaCl<sub>3</sub> electrolytes respectively. Preparation of LiCl-KCl-UCl<sub>3</sub> was as described in Chapter 2. Weighed amounts of LiCl-KCl-UCl<sub>3</sub>, LiCl-KCl-GaCl<sub>3</sub> and pure LiCl-KCl salt mixture were used to prepare the electrolyte, LiCl-KCl-1 wt% UCl<sub>3</sub>-1 wt% GaCl<sub>3</sub> for studies on U-Ga system.

### **6.3.3. Electrochemical apparatus and electrodes**

The electrochemical apparatus, electrodes and other experimental procedures are the same as described in Chapter 2.

Cyclic voltammograms were obtained on the W working electrode using LiCl-KCl-1 wt% GaCl<sub>3</sub>, LiCl-KCl-1 wt% GaCl<sub>3</sub>-1 wt% LaCl<sub>3</sub>, LiCl-KCl-1 wt% GaCl<sub>3</sub>-1 wt% NdCl<sub>3</sub> and LiCl-KCl-1 wt% GaCl<sub>3</sub>-1 wt% UCl<sub>3</sub> melts in the temperature range 698-785 K at different scan rates in the potential window -0.3 V to -1.75 V. Open circuit potential measurements were made by polarizing the W electrode at different cathodic potentials for duration 60-300 sec using these electrolytes.

## **6.4 Results and discussion**

### **6.4.1 Reduction behavior of LaCl<sub>3</sub>, NdCl<sub>3</sub> and UCl<sub>3</sub> on the Ga surface from cyclic voltammetry**

Fig.6.1 compares the cyclic voltammograms obtained using pure LiCl-KCl melt and that loaded with GaCl<sub>3</sub>. The cyclic voltammograms obtained in LiCl-KCl in presence of GaCl<sub>3</sub> in this study is similar to those reported by Lambertin *et al.* [1] using NaCl-KCl melt at liquid gallium pool cathode. Lambertin *et al.* had mentioned that the stable state of Ga in chloride media is the tri-chloride and presence of mono-chloride was also observed as a pre-peak. It may be observed in Fig.6.1 that reduction of Ga(III) ion to Ga metal

occurs at about -0.35 V in the cathodic cycle. The Ga film thus formed limits the electrochemical window of the LiCl-KCl melt. Underpotential deposition of Li on Ga surface sets the cathodic limit at about -1.7 V. Similarly dissolution of Ga at about -0.4 V sets the anodic limit for this system. Fig.6.2 compares the cyclic voltammograms obtained using LiCl-KCl-GaCl<sub>3</sub> melt and that containing LaCl<sub>3</sub>. It may be observed that underpotential reduction of La(III) ions occur on the Ga surface. Similar studies were reported by Gibilaro *et al.* in LiF-CaF<sub>2</sub> melt. They had studied the co-reduction of CeF<sub>3</sub>/SmF<sub>3</sub> with AlF<sub>3</sub> [8]. De-Yan *et al.* had reported the electrochemical behavior of Nd(III) ions in LiCl-KCl-AlCl<sub>3</sub> melt [9]. They had studied the Nd-Al intermetallic compounds formed using the LiCl-KCl-AlCl<sub>3</sub>-NdCl<sub>3</sub> melt. Fig. 6.3 and the inset of Fig. 6.4 show the underpotential reduction of UCl<sub>3</sub> and NdCl<sub>3</sub> using the melts LiCl-KCl-GaCl<sub>3</sub>-UCl<sub>3</sub> and LiCl-KCl-GaCl<sub>3</sub>-NdCl<sub>3</sub> respectively.

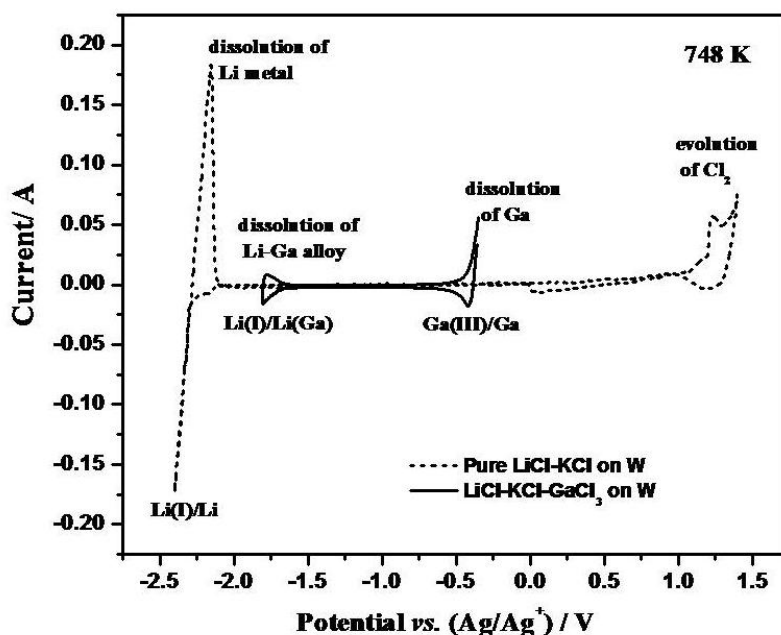


Fig.6.1 Cyclic voltammograms for pure LiCl-KCl melt and LiCl-KCl-GaCl<sub>3</sub> melt on W electrode.

The U(III)/RE(III) ions undergo under-potential reduction on the pre-deposited Ga film surface which was formed at the beginning of the cathodic cycle, thus, resulting in the formation of the respective intermetallic compounds. A single redox couple was observed for all the three systems for formation of the alloy which was similar to the behavior observed earlier on cadmium pool and solid aluminium electrodes.

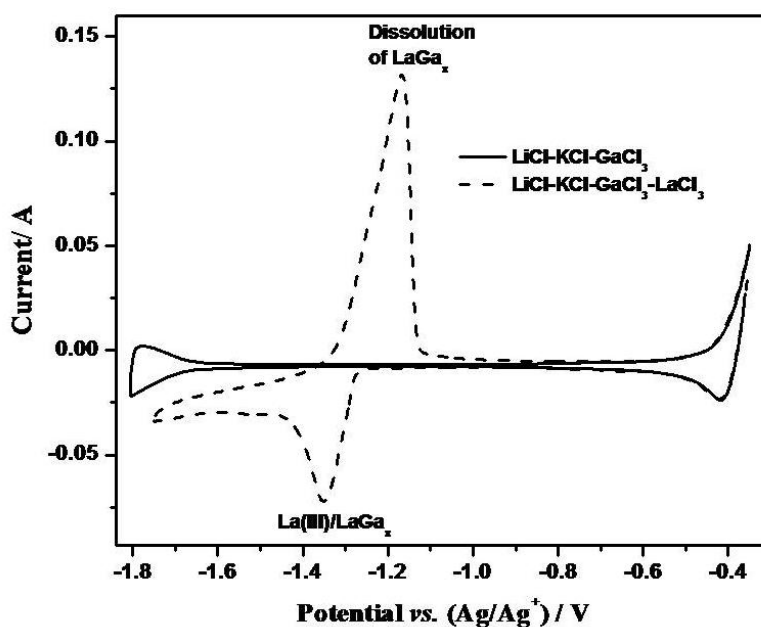


Fig. 6.2 Cyclic voltammograms for LiCl-KCl-GaCl<sub>3</sub> melt in the presence and absence of LaCl<sub>3</sub> at W electrode. Polarization rate: 50 mVs<sup>-1</sup>; Concentration of LaCl<sub>3</sub>: 6.66 x 10<sup>-5</sup> mol cm<sup>-3</sup>.

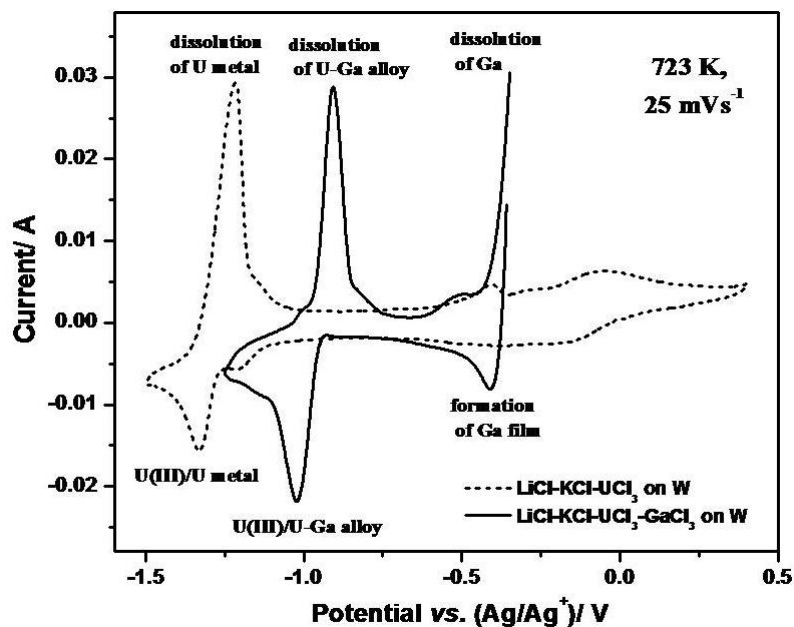


Fig. 6.3 Comparison of cyclic voltammograms for LiCl-KCl-UCl<sub>3</sub> in presence and absence of GaCl<sub>3</sub> on W electrode.

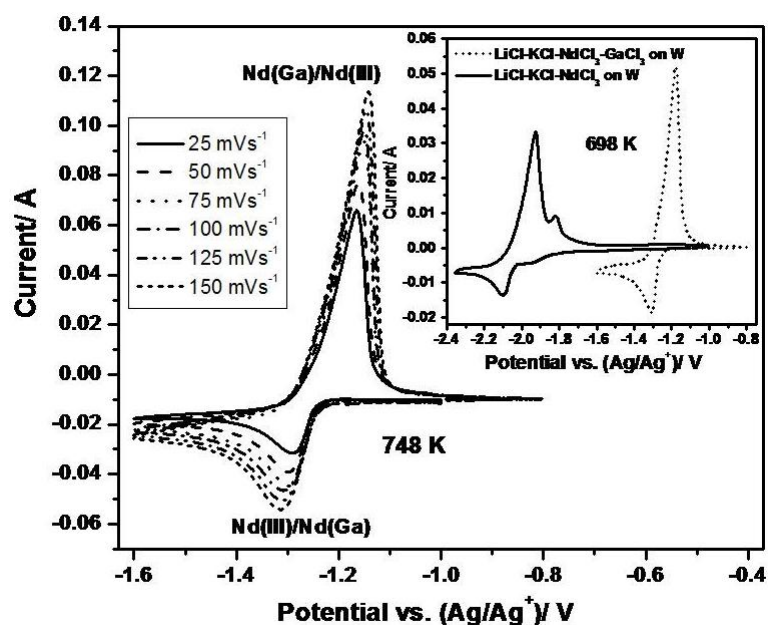


Fig. 6.4 Cyclic voltammograms for NdCl<sub>3</sub> in LiCl-KCl-GaCl<sub>3</sub> melt at W electrode at different scan rates. Temperature: 748 K. Inset: Comparison of cyclic voltammograms for LiCl-KCl-NdCl<sub>3</sub> in presence and absence of GaCl<sub>3</sub> on W electrode.

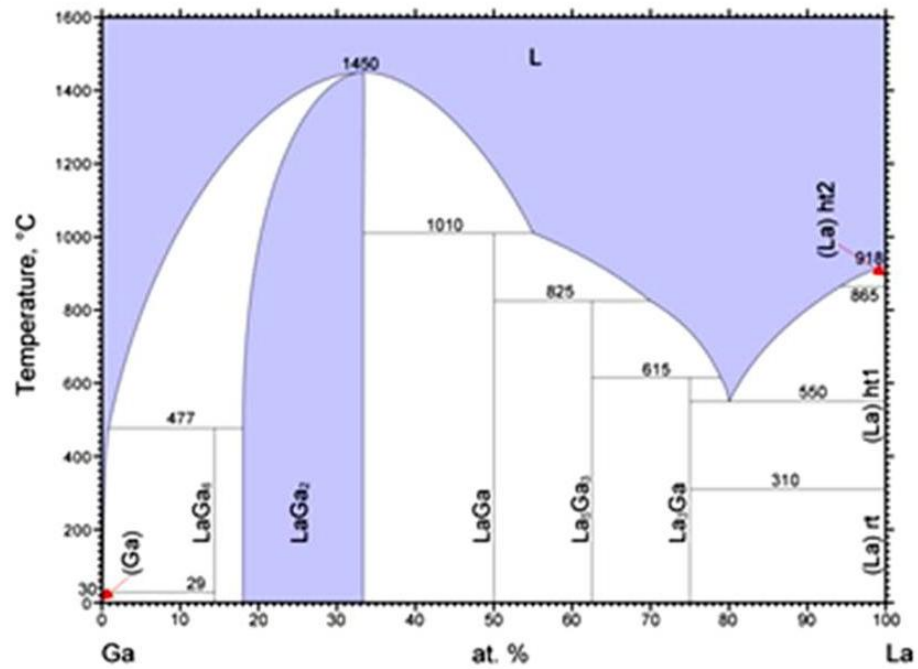
Fig. 6.5, Fig. 6.6 and Fig. 6.7 show the phase diagrams of the La-Ga, Nd-Ga and U-Ga systems respectively [10-12]. Based on the reported phase diagrams, and from our observation from Cd and Al systems, the reaction at the gallium surface may be given as



Fig. 6.4, Fig.6.8 and inset of Fig. 6.9 show the cyclic voltammograms obtained on the W working electrode using LiCl-KCl-GaCl<sub>3</sub>-NdCl<sub>3</sub>, LiCl-KCl-GaCl<sub>3</sub>-LaCl<sub>3</sub>, and LiCl-KCl-GaCl<sub>3</sub>-UCl<sub>3</sub> melts at different scan rates. The nature of the voltammograms is similar to those obtained on cadmium film electrode and those on solid aluminium electrode. The equilibrium potential for reduction of the metal ion on the gallium surface was estimated as done in the case of aluminium electrode. The apparent standard electrode potentials,  $E_{\text{La(III)}/\text{La(Ga)}}^*$ ,  $E_{\text{Nd(III)}/\text{Nd(Ga)}}^*$  and  $E_{\text{U(III)}/\text{U(Ga)}}^*$  were estimated using Eq. 6.3 and the values are shown in Table 6.1, 6.2 and 6.3 respectively.

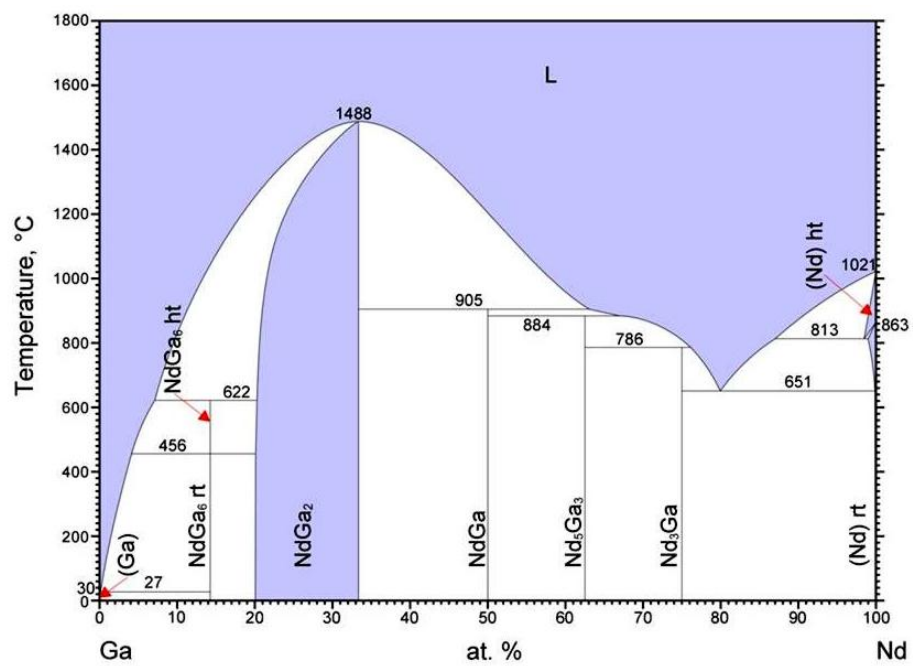
$$E_{M(\text{III})/M(\text{Ga})}^{eq} = E_{M(\text{III})/M(\text{Ga})}^* + \frac{RT}{3F} \ln X_{M(\text{III})} \quad (6.3)$$

M here refers to La, Nd and U. Fig. 6.10 shows the cyclic voltammograms for LaCl<sub>3</sub> on Ga film surface at different temperatures. A single redox peak may be seen in the cyclic voltammograms which is attributed to the Ga rich alloy, LaGa<sub>6</sub> in the temperature range 698- 748 K. The cathodic peaks shift to less cathodic values at higher temperatures as expected. However, the cyclic voltammograms recorded at temperatures 765 and 785 K showed a small shift in the peak potential towards more cathodic direction as seen in the inset of the figure. The observation is consistent with the phase diagram of La-Ga system as LaGa<sub>6</sub> decomposes peritectically to Liq. + LaGa<sub>2</sub> beyond 750 K.



© ASM International 2006 diagram No. 901107

Fig. 6.5 Ga-La phase diagram [10]



© ASM International 2006 diagram No. 901115

Fig. 6.6 Ga-Nd phase diagram [11]

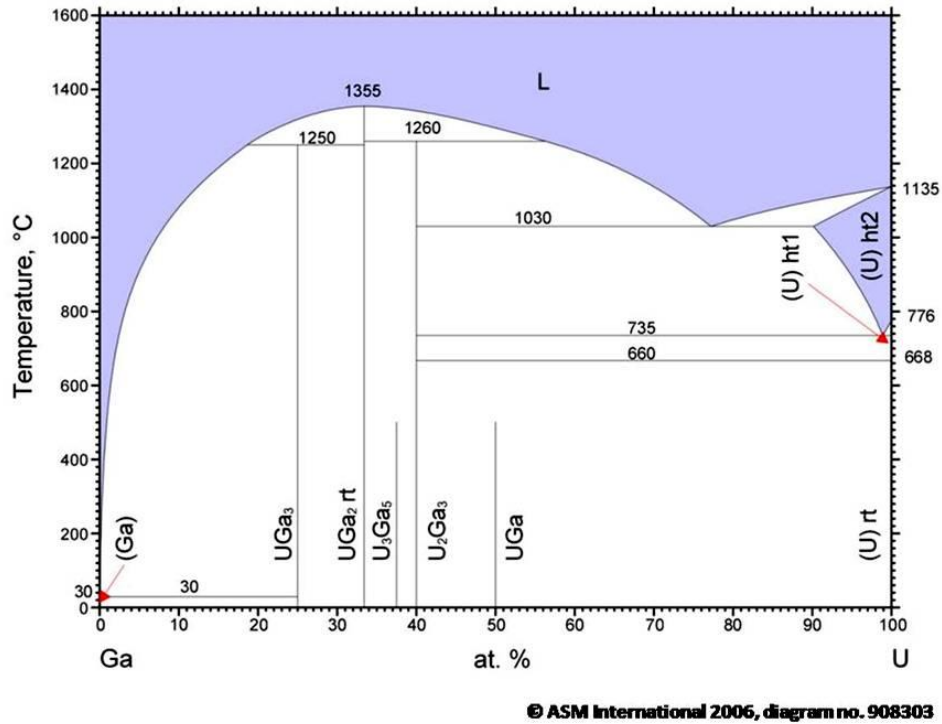


Fig. 6.7 Ga-U phase diagram [12]

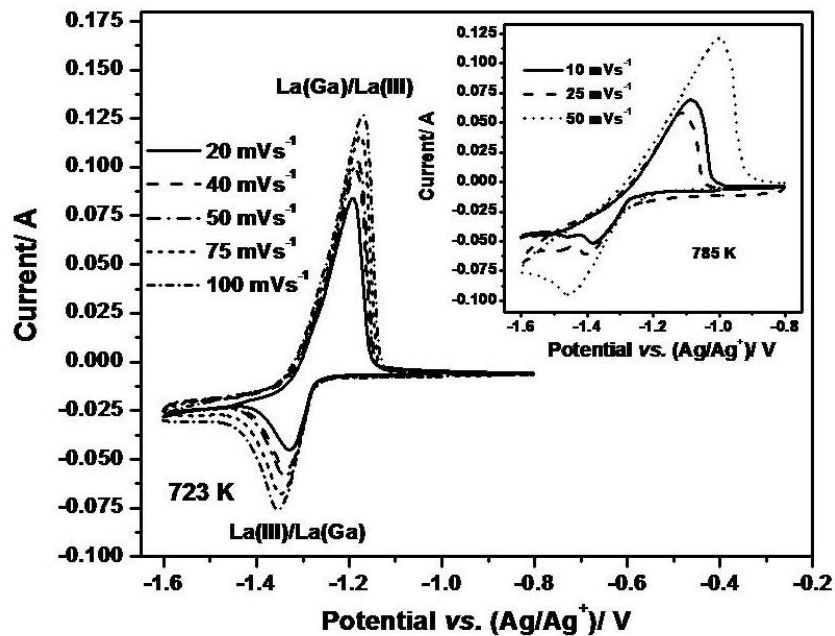


Fig. 6.8 Cyclic voltammograms for  $\text{LaCl}_3$  in  $\text{LiCl-KCl-GaCl}_3$  melt at W electrode at different scan rates at 723 K. Inset: Cyclic voltammograms for the same at different scan rates at 785 K.

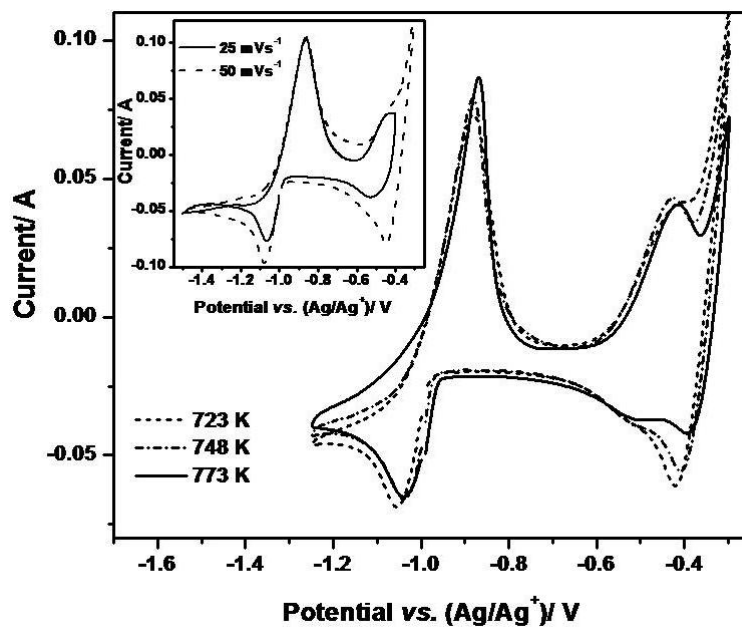


Fig. 6.9 Cyclic voltammograms for  $\text{UCl}_3$  in  $\text{LiCl-KCl-GaCl}_3$  melt at W electrode at different temperatures. Inset: Cyclic voltammograms for the same at different scan rates at 698 K.

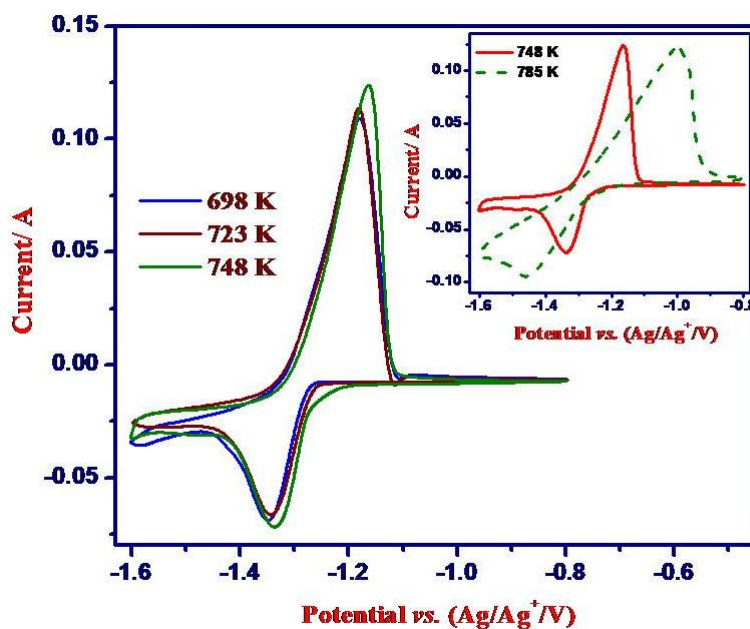


Fig. 6.10 Cyclic voltammograms for  $\text{LaCl}_3$  in  $\text{LiCl-KCl-GaCl}_3$  melt at W electrode at different temperatures. Inset: Cyclic voltammograms for the same comparing at 748 and 785 K.

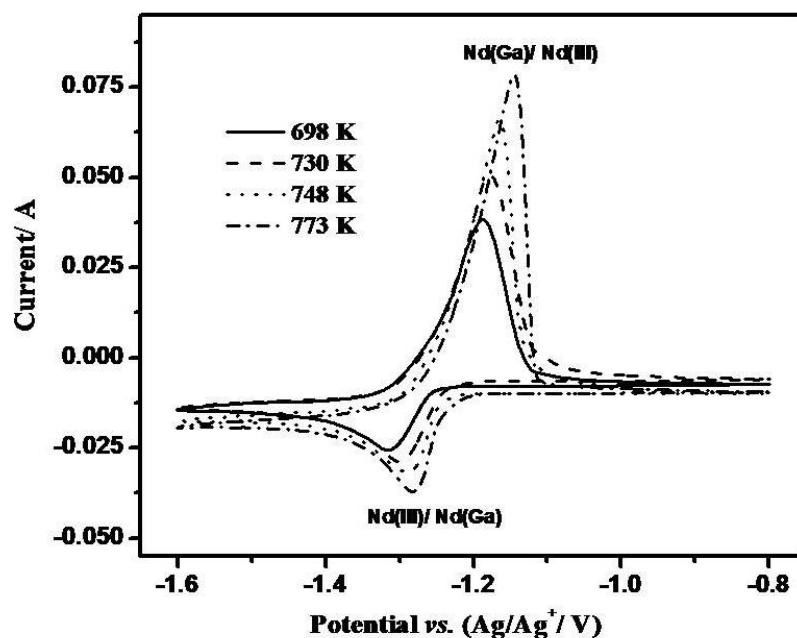


Fig. 6.11 Cyclic voltammograms for  $\text{NdCl}_3$  in  $\text{LiCl-KCl-GaCl}_3$  melt at W electrode at different temperatures.

Fig. 6.9 and Fig. 6.11 show the cyclic voltammograms for  $\text{UCl}_3$  and  $\text{NdCl}_3$  on Ga film surface at different temperatures. The cathodic peaks shift to less cathodic values at higher temperatures as expected in the temperature range studied. No anomalous behavior was seen in the temperature range studied for these two systems.

#### 6.4.2 Open-circuit chronopotentiometry

The formation of RE-Ga alloy was studied using open circuit potential measurement. The W electrode was polarized at  $-1.5$  V for short duration and the open circuit potential was measured under zero current condition. Co-deposition of the lanthanide and Ga metal takes place on the W electrode. Fig. 6.12 and Fig. 6.13 show the open circuit potential transients obtained for La-Ga and Nd-Ga systems. A single potential plateau at  $\sim -1.3$  V corresponding

Table 6.1 Apparent standard potential ( $\pm 0.001$  V) for La(III)/La(Ga) estimated from cyclic voltammogram using LiCl-KCl-LaCl<sub>3</sub>-GaCl<sub>3</sub> melt,  $X_{LaCl_3} = 0.00224$ .

Temperature, K	$E_{La(III)/La(Ga)}^{eqbm}$ vs. Ag/Ag <sup>+</sup> , V	$E_{La(III)/La(Ga)}^*$ vs. Ag/Ag <sup>+</sup> , V	$E_{La(III)/La(Ga)}^*$ vs. Cl <sub>2</sub> /Cl <sup>-</sup> , V
698	-1.284	-1.161	-2.396
723	-1.279	-1.152	-2.392
748	-1.272	-1.141	-2.386
765	-1.277	-1.143	-2.391
785	-1.265	-1.127	-2.379

Table 6.2 Apparent standard potential ( $\pm 0.001$  V) for Nd(III)/Nd(Ga) estimated from cyclic voltammogram using LiCl-KCl-NdCl<sub>3</sub>-GaCl<sub>3</sub> melt,  $X_{NdCl_3} = 0.00224$ .

Temperature, K	$E_{Nd(III)/Nd(Ga)}^{eqbm}$ vs. Ag/Ag <sup>+</sup> , V	$E_{Nd(III)/Nd(Ga)}^*$ vs. Ag/Ag <sup>+</sup> , V	$E_{Nd(III)/Nd(Ga)}^*$ vs. Cl <sub>2</sub> /Cl <sup>-</sup> , V
698	-1.273	-1.149	-2.384
730	-1.262	-1.134	-2.374
748	-1.251	-1.119	-2.364
773	-1.241	-1.105	-2.355

Table 6.3 Apparent standard potential ( $\pm 0.001$  V) for U(III)/U(Ga) estimated from cyclic voltammogram using LiCl-KCl-UCl<sub>3</sub>-GaCl<sub>3</sub> melt,  $X_{UCl_3} = 0.00268$ .

Temperature, K	$E_{U(III)/U(Ga)}^{eqbm}$ vs. Ag/Ag <sup>+</sup> , V	$E_{U(III)/U(Ga)}^*$ vs. Ag/Ag <sup>+</sup> , V	$E_{U(III)/U(Ga)}^*$ vs. Cl <sub>2</sub> /Cl <sup>-</sup> , V
723	-0.967	-0.844	-2.083
735	-0.959	-0.834	-2.076
748	-0.958	-0.831	-2.075
773	-0.946	-0.815	-2.064

to the co-existence of RE-Ga alloy + Ga, was observed for both the La-Ga and Nd-Ga systems. The potentials of the plateaus that were measured with respect to the reference electrode, Ag/AgCl ( $X_{AgCl} = 0.0031$ ), were rescaled to the equilibrium potential of the RE(III)/RE(0) couple obtained earlier as described in Chapter 3. Fig. 6.13 shows the potentials of the OCP transient for Nd-Ga system rescaled to the Nd(III)/Nd(0) electrode. The potential of the plateau referred to the rare earth metal electrode is the emf of the cell represented by



The emf was evaluated for different temperatures for La-Ga and Nd-Ga systems. The inset of Fig.6.12 shows the emf values as a function of temperature. It may be observed that the emf values decreases with increase in temperature from 698 to 748 K. But there is

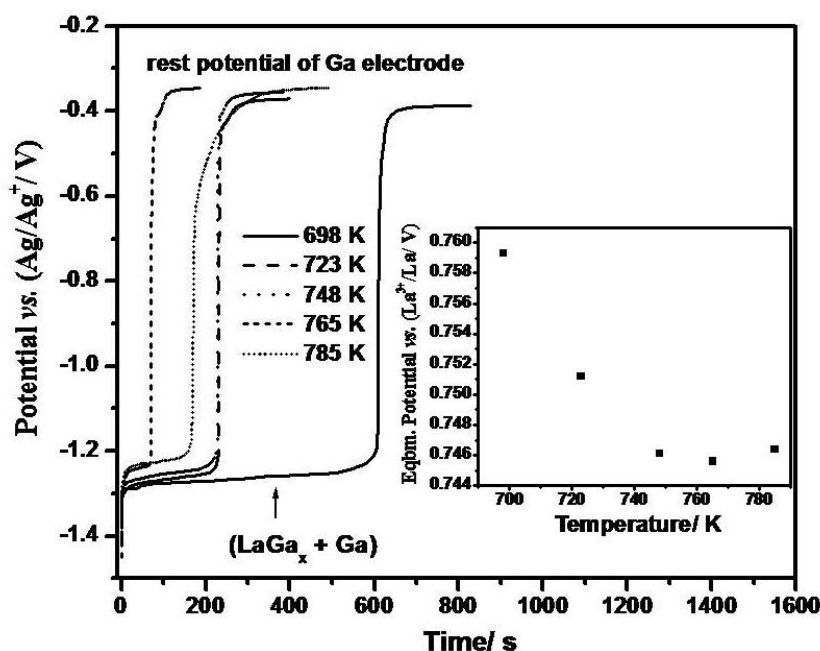


Fig.6.12 Open circuit potential transient curve for LiCl-KCl-LaCl<sub>3</sub>-GaCl<sub>3</sub> melt on W electrode at different temperatures for cathodic polarization: -1.5 V. Inset: Equilibrium potential of La(III)/La(Ga) vs. La(III)/La(0) electrode at different temperatures.

a change in the trend of the emf values for 765 and 785 K. This behavior is similar to the observations made in the cyclic voltammograms. The findings from the open circuit potential measurement strengthen our earlier contention that the intermetallic formed at the Ga surface is  $\text{LaGa}_6$  and it decomposes to  $\text{Liq.} + \text{LaGa}_2$  at 750 K which is the peritectic temperature. Palenzona *et al.* had assessed the Ga-rich side of the Ga-RE systems finding the  $\text{Ga}_6\text{RE}$  compound [14]. This Ga rich compound is formed by the peritectic reaction:  $\text{L} + \text{Ga}_2\text{RE} \leftrightarrow \text{Ga}_6\text{RE}$ .

From Fig.6.13, it may be observed that in the Nd-Ga system, there is no change in the trend of the emf values with increase in temperature in the temperature range studied (698-773 K) as observed in the case of La-Ga system. This is consistent with the phase diagram of the Nd-Ga system as the peritectic temperature for decomposition of  $\text{NdGa}_6$  is 895 K which is beyond the temperature range of this study.

The Gibbs energy of formation of the intermetallic,  $\text{LaGa}_6$  for temperatures below 750 K were estimated from the emf values and are shown in Table 6.4. The Gibbs energy of formation of the intermetallic,  $\text{NdGa}_6$  in the temperature range 698-773 K estimated from the emf values is shown in Table 6.5. We did not find any data in the literature for the thermodynamic properties of the  $\text{REGa}_6$  compound by calorimetry or by emf method, although those for the other intermetallic compounds are reported.

The activity of RE (La, Nd) in gallium was calculated from Eq. 6.5 and the values are given in Table 6.6 and 6.7.

$$emf = -\frac{RT}{3F} \ln a_{RE(Ga)} \quad (6.5)$$

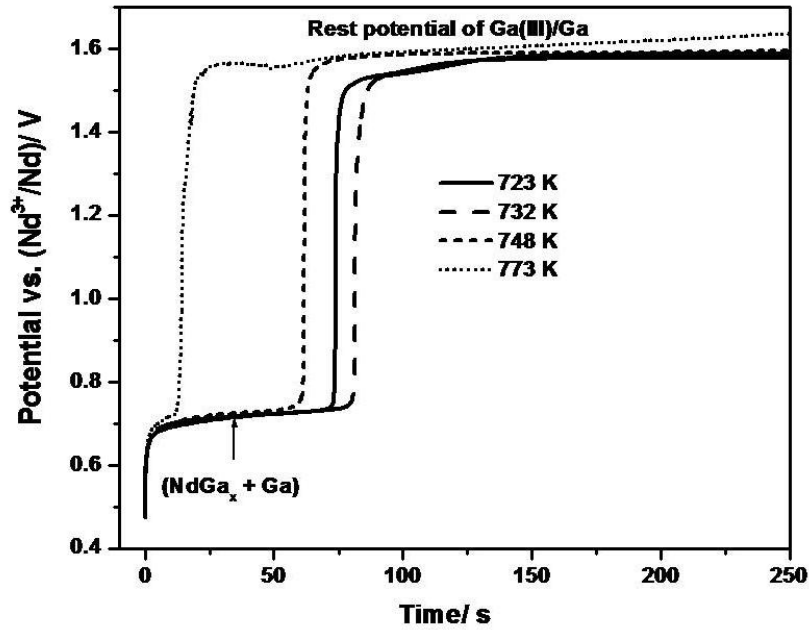


Fig.6.13 Open circuit potential transient curve for LiCl-KCl-NdCl<sub>3</sub>-GaCl<sub>3</sub> melt on W electrode at different temperatures for cathodic polarization: -1.5 V.

The excess Gibbs energy of RE in gallium,  $\overline{\Delta G}_{RE}^{ex}$  was evaluated using Eq. 6.6

$$\overline{\Delta G}_{RE}^{ex} = RT \ln \gamma_{RE(Ga)} = -3F\Delta E - RT \ln X_{RE(Ga)} \quad (6.6)$$

Since we did not find the solubility data for lanthanum and neodymium in Ga, we had taken the solubility value from the liquidus curve in phase diagram. The thermodynamic properties for RE-Ga system estimated from OCP measurements are shown in Table 6.6 and 6.7. The low activity coefficient values show the strong interaction of the rare earth metal with gallium. The excess Gibbs energy of La in gallium is compared with those for Ce in Ga estimated by correlation and models by Toda *et al.* [6] in Table 6.6. The value for La/Nd obtained in this study is comparable with those of Ce reported by Toda *et al.* Since the behavior of rare earth elements are expected to be similar, we consider the present measurement is validated.

Table 6.4 Gibbs energy of formation of LaGa<sub>6</sub> estimated from OCP measurement.

Temperature, K	This study	
	emf(±0.002) V	$\Delta_f G_{LaGa_6}$ kJ mol <sup>-1</sup>
698	0.759	-219.8
723	0.751	-217.5
748	0.746	-215.9
765	0.746	-
785	0.746	-

Table 6.5 Gibbs energy of formation of NdGa<sub>6</sub> estimated from OCP measurement.

Temperature, K	This study	
	emf(±0.002) V	$\Delta_f G_{NdGa_6}$ kJ mol <sup>-1</sup>
723	0.723	-209.3
732	0.720	-208.5
748	0.715	-206.9
773	0.706	-204.3

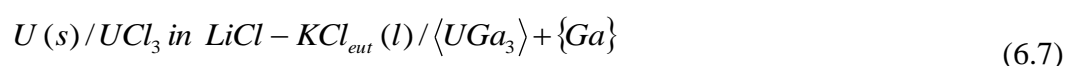
Table 6.6 Thermodynamic properties of La-Ga system estimated from OCP measurement.

Temperature, K	$\log a_{La(Ga)}$	$\Delta \bar{G}_{La}^{xs}$ , kJ mol <sup>-1</sup>	$\log \gamma_{La(Ga)}$	$\Delta \bar{G}_{Ce}^{xs}$ , kJ mol <sup>-1</sup> Todd <i>et al.</i> [6]
698	-16.4	-	-	-179.4
723	-15.7	-188.4	-13.6	-177.8
748	-15.2	-	-	-176.2
765	-14.7	-	-	-175.2
785	-14.3	-186.6	-12.4	-173.9

Table 6.7 Thermodynamic properties of Nd-Ga system estimated from OCP measurement.

Temperature, K	$\log a_{La(Ga)}$	$\overline{\Delta G}_{Nd}^{xs}$ , kJ mol <sup>-1</sup>	$\log \gamma_{La(Ga)}$
723	-15.1	-189.9	-13.7
732	-14.9	-	-
748	-14.5	-	-
773	-13.8	-184.8	-12.5

The electrochemical formation of thin film of U-Ga alloy was studied using the LiCl-KCl-UCl<sub>3</sub>-GaCl<sub>3</sub> melt by open circuit potential measurements. The W electrode was polarized at -1.2 V for different durations in the range 60-300 sec and the open circuit potential was measured under zero current condition. Co-deposition of U and Ga takes place on the W electrode and a potential plateau corresponding to the coexistence of U-Ga alloy + Ga was observed. It was presumed from our previous studies that the alloy is UGa<sub>3</sub>. Fig. 6.14 shows the open circuit potential transient obtained for the U-Ga system. The potential of the plateau that were measured with respect to the reference electrode, Ag/AgCl ( $X_{AgCl} = 0.0031$ ), were rescaled to the equilibrium potential of the U(III)/U(0) couple obtained earlier as described in Chapter 3. The potential of the plateau referred to the uranium metal electrode is the emf of the cell represented by



The emf values and the Gibbs energy of formation of the intermetallic, UGa<sub>3</sub> at different temperatures are shown in Table 6.8 and 6.9. The values are compared with those reported by Reddy *et al.* [16], Johnson *et al.*[17] and Chiotti *et al.*[18] for formation of UGa<sub>3</sub>. Our values are in very good agreement with the literature values' indicating that the intermetallic formed at the Ga surface under our experimental condition was UGa<sub>3</sub>.

The activity of uranium in gallium, the partial molar excess Gibbs energy of U in gallium,  $\Delta\bar{G}_U^{xs}$  and the activity coefficient of uranium in gallium was evaluated and the values are shown in Table 6.10. The solubility of uranium in liquid gallium was taken from the solubility data reported in the literature [19] as:

$$\ln(\text{at.\% U}) = 8.223 - 8803/T \quad (693-922 \text{ K}) \quad (6.8)$$

The activity coefficient of U in gallium estimated in this study was fairly in agreement with those reported by Johnson *et al.* [17] and Chiotti *et al.* [18].

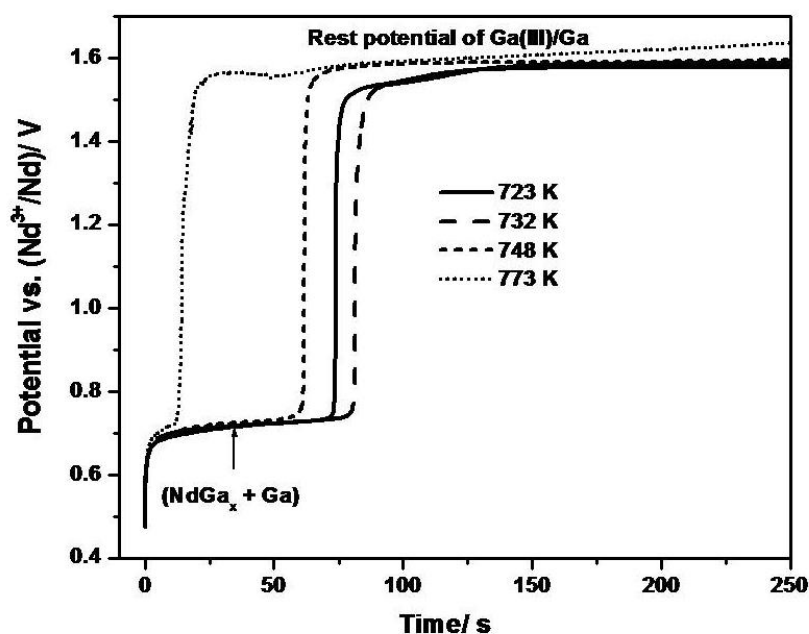


Fig.6.14 Open circuit potential transient curve for LiCl-KCl-UCl<sub>3</sub>-GaCl<sub>3</sub> melt on W electrode at different temperatures for cathodic polarization: -1.2 V.

Table 6.8 Equilibrium potentials ( $\pm 0.002$  V) of U(III) ion on Ga surface from OCP measurement.

Temperature, K	$E_{U(III)/U(0)}^{eqbm}$ vs. Ag/Ag <sup>+</sup> , V	$E_{U(III)/U(Ga)}^{eqbm}$ vs. Ag/Ag <sup>+</sup> , V	emf, V	
			This study	Reddy <i>et al.</i> [16]
687	-1.423	-0.970	0.453	0.458
709	-1.410	-0.961	0.449	0.453
735	-1.395	-0.951	0.445	0.447
748	-1.388	-0.946	0.442	0.444
773	-1.373	-0.936	0.438	0.439

Table 6.9 Gibbs energy of formation of UGa<sub>3</sub> from OCP measurement compared with literature values

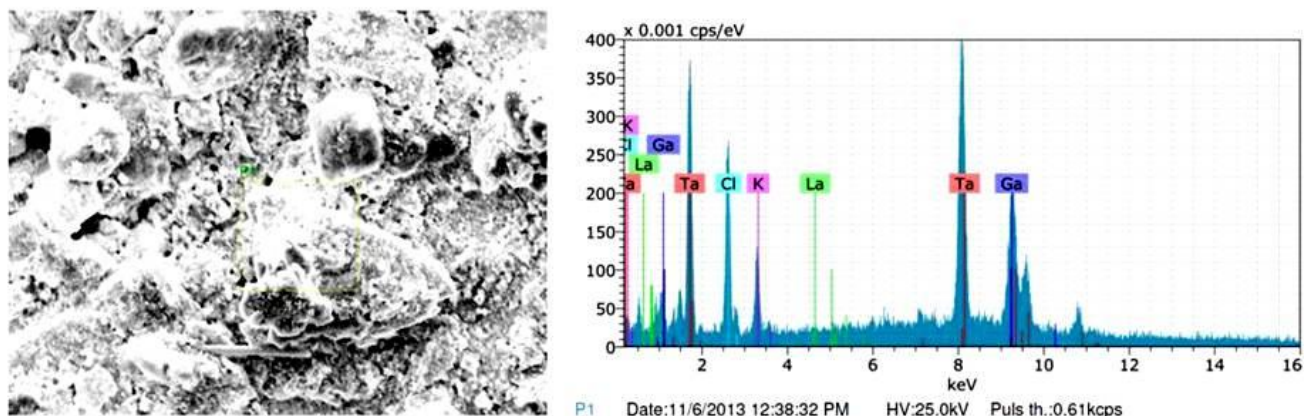
Temperature, K	$\Delta_f G_{UGa_3}$ kJ mol <sup>-1</sup>			
	This study ( $\pm 0.6$ kJ mol <sup>-1</sup> ) OCP	Reddy <i>et al.</i> [16] ( $\pm 0.5$ kJ mol <sup>-1</sup> ) EMF	Johnson <i>et al.</i> [17] EMF	Chiotti <i>et al.</i> [18] Assessment
687	-131.2	-132.4	-131.9	-131.1
709	-130.1	-131.0	-130.7	-129.9
735	-128.7	-129.4	-129.2	-128.4
748	-128.0	-128.5	-128.5	-127.7
773	-126.7	-126.9	-127.1	-126.3

Table 6.10 Thermodynamic properties of U-Ga system estimated from OCP measurement.

Temperature, K	$\log a_{U(Ga)}$	$\overline{\Delta G_U^{xs}}$ , kJ mol <sup>-1</sup>	$\log \gamma_{U(Ga)}$		
			This study	Johnson <i>et al.</i> [17]	Chiotti <i>et al.</i> [18]
687	-10.0	-78.8	-6.0	-6.1	-5.9
709	-9.6	-78.3	-5.8	-5.9	-5.7
735	-9.1	-77.7	-5.5	-5.6	-5.4
748	-8.9	-77.4	-5.4	-5.4	-5.3
773	-8.6	-76.9	-5.2	-5.1	-5.1

### 6.4.3 Electrodeposition

To examine the alloy formed on the cadmium surface, potentiostatic electrolysis was carried out using LiCl-KCl-RECl<sub>3</sub>-GaCl<sub>3</sub> melt. A Ta sheet was polarized at -1.45 V vs. Ag/AgCl reference electrode for 5 hours at 723 K. This potential is slightly cathodic to the potential plateau observed in the OCP measurement for the La-Ga and Nd-Ga system. Co-deposition of Ga and the RE metal was expected to occur on the W surface to form the stable intermetallic compound. However, there was no significant amount of deposit on the Ta sheet. The XRD pattern of the cathode deposit did not show the presence of any intermetallic compound and the peak in the pattern showed the presence of Ta sheet, Ga and KCl. Probably the cathode deposit had fallen down in the melt during electrolysis. The SEM-EDX analysis of the cathode deposit obtained for the La-Ga system is shown in Fig.6.15. The EDX analysis does not show the formation of the LaGa<sub>6</sub> alloy. Further studies have to be carried out to ascertain the formation of the alloy below 750 K.



El	AN	Series	unn. corr.	C [wt.%]	norm. [wt.%]	Atom. [at.%]	C Error	(1 Sigma)	K fact.	Z corr.	A corr.	F
			[wt.%]	[wt.%]	[at.%]	[wt.%]						
Ta	73	L-series	65.16	63.85	30.05	1.82	0.760	0.778	1.000			
Cl	17	K-series	18.14	17.78	42.71	0.77	0.141	1.246	1.000			
Ga	31	K-series	13.25	12.99	15.86	0.48	0.116	1.004	1.000			
K	19	K-series	5.26	5.16	11.24	0.26	0.037	1.362	1.000			
La	57	L-series	0.23	0.22	0.14	0.06	0.002	0.932	1.000			
Total:			102.05	100.00	100.00							

Fig. 6.15 Cross-sectional SEM image of the cathode deposit formed by potentiostatic electrolysis using  $\text{LiCl-KCl-LaCl}_3\text{-GaCl}_3$  melt on Ta sheet at 723 K. Cathodic polarization:  $-1.45$  and the corresponding EDX analysis.

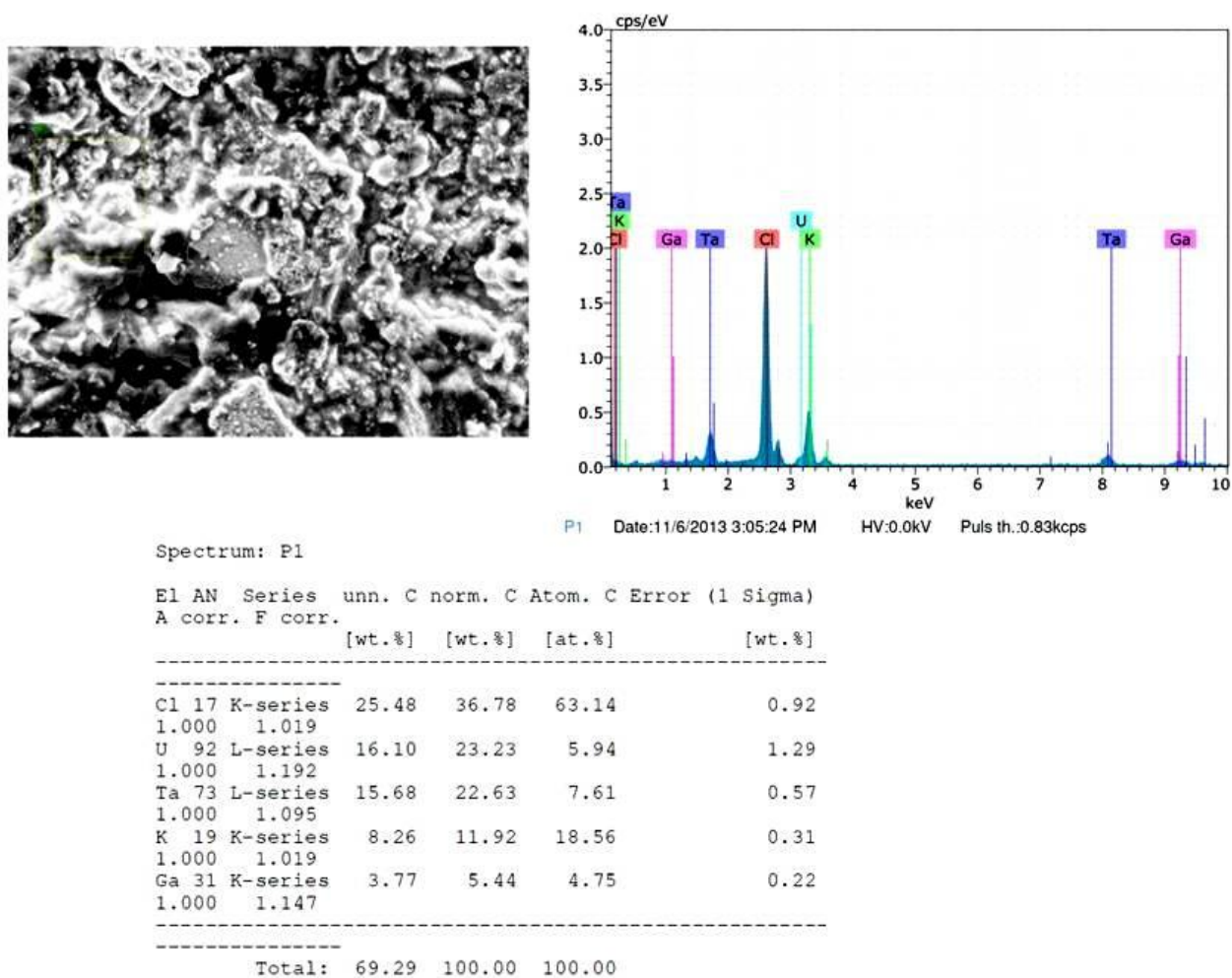


Fig. 6.16 Cross-sectional SEM image of the cathode deposit formed by potentiostatic electrolysis using  $\text{LiCl-KCl-UCl}_3\text{-GaCl}_3$  melt on Ta sheet at 723 K. Cathodic polarization:  $-1.2$  and the corresponding EDX analysis.

Similarly, to confirm the underpotential deposition of U on Ga surface, potentiostatic electrolysis was carried out using LiCl-KCl-UCl<sub>3</sub>-GaCl<sub>3</sub> melt. A Ta sheet was polarized at -1.2 V vs. Ag/AgCl reference electrode for 8 hours at 723 K. The salt adhering to the cathode deposit was scrapped and the deposit was washed with ethylene glycol to remove the salt. The deposit was examined by SEM-EDX analysis. The SEM micrograph and the corresponding EDX analysis are shown in Fig. 6.16. The EDX analysis shows the presence of KCl. Though the EDX analysis shows the presence of U indicating the underpotential reduction of U(III) ion, the compositions of U and Ga does not show the formation of UGa<sub>3</sub>.

### 6.5 Summary

The electrochemical behavior of M(III) ions (M - La, Nd and U) on gallium surface is reported for the first time. The measurements were made using the LiCl-KCl-GaCl<sub>3</sub>-MCl<sub>3</sub> melt in the temperature range 698-785 K at the W electrode using cyclic voltammetry and open circuit potentiometry. The metal ion gets reduced on the pre-deposited gallium surface, at a potential more positive than that required for the pure metal. The shift in the potentials towards the positive direction is interpreted as the formation of the Ga-rich intermetallic compound, LaGa<sub>6</sub>, NdGa<sub>6</sub> and UGa<sub>3</sub> for the La-Ga, Nd-Ga and U-Ga systems respectively. In case of the La-Ga system, there was a change in the trend of the peak potentials in the cyclic voltammograms and the emf values from the OCP transients recorded at temperatures 765 and 785 K. The observation is consistent with the phase diagram of La-Ga system as LaGa<sub>6</sub> decomposes peritectically to Liq. + <LaGa<sub>2</sub>> beyond 750 K. The apparent standard electrode potentials,  $E_{La(III)/La(Ga)}^*$ ,  $E_{Nd(III)/Nd(Ga)}^*$  and  $E_{U(III)/U(Ga)}^*$  were estimated for the temperatures in the range 698-773 K from the cyclic voltammograms. The Gibbs energy formation of the alloys, LaGa<sub>6</sub>, NdGa<sub>6</sub> and UGa<sub>3</sub>, activity of U and lanthanides (La, Nd) in gallium, the excess Gibbs

energy and their activity coefficient were estimated from the open circuit potential measurement. Further studies need to be carried out by potentiostatic electrolysis to ascertain the alloys formed.

## 6.6 References

1. D. Lambertin, S. Chedhomme, G. Bourges, S. Sanchez, G.S. Picard, *J. Nucl. Mater.* 341 (2005) 131.
2. G. Bourges, D. Lambertin, S. Rochefort, S. Delpech, G.S. Picard, *J. Alloys Compd.* 444 (2007) 404.
3. A. Laplace, J. Finne, O. Conocar, S. Delpech, J. Vermeulen, L. Blairat, G. Picard, E. Walle, J. Lacquement, Proc. Ninth Information Exchange Meeting on Actinide and Fission Product Partitioning and Transmutation, Nimes, France, Sep 25-29, 2006, 289.
4. V. A. Lebedev, *Selectivity of Liquid Metal Electrodes in Molten Halides*, Metallurgiya, Chelyabinsk (1993), [in Russian].
5. J. Finne, G. Picard, S. Sanchez, E. Walle, O. conocar, J. Lacquement, J. M. Boursier, D. Noel, *J. Nucl. Mater.* 344 (2008) 165.
6. T. Toda, T. Maruyama, K. Moritani, H. Moriyama, H. Hayashi, *J. Nucl. Sci. Technol.* 46 (1) (2009) 18.
7. T. Toda, T. Maruyama, K. Moritani, H. Moriyama, H. Hayashi, *Electrochem.* 77(8) (2009) 649.
8. M. Gibilaro, L. Massot, P. Chamelot, P. Taxil, *Electrochem. Acta* 54 (2009) 5300.
9. Yong-De Yan, Yan-Lu Xu, Mi-Lin Zhang, Yun Xue, Wei Han, Ying Huang, Qiong Chen, Zhi-Jian Zhang, *J. Nucl. Mater.* 397 (2012) 26.
10. A. Palenzona, Ga-La Phase Diagram, ASM Alloy Phase Diagrams Center, P. Villars, Editor-in-chief; <http://www1.asminternational.org/AsmEnterprise/APD>,

- ASM International, Materials Park, OH, USA, 2006-2014.
11. Okamoto, Ga-Nd Phase Diagram, ASM Alloy Phase Diagrams Center, P. Villars, Editor-in-chief; <http://www1.asminternational.org/AsmEnterprise/APD>, ASM International, Materials Park, OH, USA, 2006-2014.
  12. Okamoto, Ga-U Phase Diagram, ASM Alloy Phase Diagrams Center, P. Villars, Editor-in-chief; <http://www1.asminternational.org/AsmEnterprise/APD>, ASM International, Materials Park, OH, USA, 2006-2014.
  13. A. Palenzona, S. Cirafici, Bull. Alloy Phase Diagrams 11(1) (1990) 72.
  14. V. A. Vnuchkova, A. P. Bayanov, V. V. Serebrennikov, Russ. J. Phy. Chem. 45 (1971) 99.
  15. K. A. Gschneider, L. Eyring, G. H. Lander and G. R. Choppin, Handbook on the Physics and Chemistry of Rare Earths, Volume 19, Elsevier Sci. SV 1994, p. 580.
  16. B. Prabhakara Reddy, R. Kandan, K. Nagarajan, P.R. Vasudeva Rao , Thermochim. Acta 366 (2001) 37.
  17. I. Johnson, H.M. Feder, in: Proc. Symp. Thermodyn. Nucl. Mater., Vienna, IAEA, Vienna, 1962, p. 319.
  18. P. Chiotti, V. V. Akhachinskij, I. Ansara, M. H. Rand, “The chemical thermodynamics of actinide elements and compounds, Part 5, The Actinide Binary Alloys”, IAEA, 1981, p.120.
  19. I. Johnson, M. G. Chasanov, Trans. Am. Soc. Met.56 (1963) 272.

## CHAPTER 7

### **Electrochemical pulse techniques for in-situ monitoring the concentration of uranium in molten LiCl-KCl**

#### **7.1 Introduction**

During the electrorefining of the spent fuel, when uranium is recovered on the steel cathode, the concentration of plutonium chloride in the electrolyte increases. When the concentrations of uranium and plutonium chloride in the electrolyte become comparable, both uranium and plutonium are recovered on the liquid cadmium cathode [1-2]. Since the ratio of U and Pu varies appreciably during the process, it is necessary to have the knowledge of their ratio to decide on switching over to either of the two types of cathodes. Further, after many batches of processing the spent fuel by electrorefining, the electrolyte will undergo waste treatment process for removal of the accumulated fission products. Before this, the actinides are removed from the electrolyte by the actinide drawdown process [3]. More than 99.99 % of the actinides are removed from the electrolyte during the process. Hence it becomes mandatory to observe the actinide composition in the electrolyte to monitor the progress of various stages of the pyrochemical process using a reliable and quick method. As mentioned in chapter 1, electroanalytical pulse techniques are fast and reliable methods for in-situ monitoring of the composition of analyte in multi-component systems [4-5]. These methods are suitable for the estimation of analytes over wide range of concentrations. Some studies are reported on the applicability of the electroanalytical technique to monitor actinide concentration in molten salts [6-7]. In this study we had investigated the suitability of three voltammetric techniques namely, normal pulse voltammetry (NPV), differential pulse voltammetry (DPV) and square wave voltammetry (SWV) for determining the

concentration of uranium in various concentration ranges and in the presence of rare earth chlorides.

## 7.2 Literature survey

Iizuka *et al.* [6] had carried out an exhaustive study on the applicability of normal pulse voltammetry and square wave voltammetry as the on-line monitoring methods for the actinide concentration in molten chloride electrolyte. They had optimized the parameters for determination of the concentration of U and Pu in presence of Gd in the electrolyte. Both the techniques showed the presence of well resolved peaks for U and Pu reduction. They had observed that the dependence of the peak current on concentration was not linear for higher concentrations of actinides in the case of SWV. However, the NPV curves showed that the limiting current for the actinides was linear in the concentration range 0.02-1.7 wt %.

Earlier, in the Argonne National Laboratory, the square wave voltammetry was examined as a process monitoring method for pyrometallurgical treatment [7]. In this study a semi-quantitative analysis of the SWV was carried out in molten chlorides containing Zr, U, Pu & Dy. But there is no discussion on the optimum parameters chosen for the waveform to use this method as an analytical tool for monitoring actinides over wide concentration range. Apart from this we have not come across any other study on electroanalytical techniques used for pyrochemical process.

### 7.3.1 Chemicals

CeCl<sub>3</sub> (Alfa Aesar 99.99 %) and EuCl<sub>3</sub> (Alfa Aesar 99.99%) were used without any treatment. The purity of other chemicals used in the study is same as those described in Chapter 2.

### 7.3.2. Preparation of the electrolyte salt

Purification of LiCl-KCl salt mixture was as described earlier in chapter 2. Stock of LiCl-KCl-11 wt %  $\text{UCl}_3$  electrolyte was prepared earlier. The procedure for loading  $\text{UCl}_3$  in LiCl-KCl salt mixture was as described in chapter 2. This salt was diluted with purified LiCl-KCl salt mixture to prepare the electrolyte with required concentration on  $\text{UCl}_3$ . The amount of uranium in the electrolyte containing  $\text{UCl}_3$  in the concentration range 11 wt. % -0.5 wt. % was estimated by Davis and Gray method described earlier in chapter 2. The concentration of uranium in electrolytes containing less than 0.5 wt. %  $\text{UCl}_3$  was determined by inductively coupled plasma-mass spectrometry (ICP-MS). For simulated studies, weighed amounts of  $\text{CeCl}_3$ ,  $\text{LaCl}_3$  and  $\text{EuCl}_3$  were added to the LiCl-KCl-1 wt. %  $\text{UCl}_3$  electrolyte.

### ***7.3.3. Electrochemical apparatus and electrodes***

As discussed in chapter 2, a 1mm tungsten wire encased in a glass capsule with a known area exposed outside was used as the working electrode. The reference electrode and counter electrode were the same as discussed in chapter 2. The instrumentation, the assembling of cell and other experimental procedures were also the same as described in chapter 2. The normal pulse, differential pulse and square wave voltammograms for various pulse parameters were obtained using AUTOLAB/PGSTAT30 and the data were processed using GPES 4.9. The studies were carried out using LiCl-KCl- $\text{UCl}_3$  electrolyte at 773 K for  $\text{UCl}_3$  in the concentration range 0.08-11 wt. %.

## **7.4 Results and discussion**

### ***7.4.1 Normal pulse voltammograms***

The waveforms for the three techniques were shown in Fig. 2.13 - Fig. 2.15 in chapter 2. The resultant current is a function of the wave form, concentration of analyte, temperature and surface area of the electrode. To optimize the pulse parameters, it becomes necessary to study the dependence of the resultant current with concentration of

the electroactive species, keeping the temperature and the area of the working electrode constant.

Normal pulse voltammograms were recorded for various pulse times ( $t_p$ : 0.05-0.2 s), for different time intervals between two pulses ( $t_m$ : 0.7-3 s) and various pulse heights ( $\Delta E_p$ : 5-10 mV), to arrive at the optimum parameters using LiCl-KCl- 1 wt %  $UCl_3$ . The optimum pulse time was between 50-100 ms and the interval between two pulses was 1-2 sec. A potential increment of 10 mV was found to be optimum. The parameters chosen for this study were-  $t_p$ : 0.1 s;  $t_m$ : 1 s and  $\Delta E_p$ : 10 mV. Fig.7.1a shows the normal pulse voltammogram for LiCl-KCl- $UCl_3$  for different concentrations of  $UCl_3$  at 773 K. The limiting current may be seen at -1.5 V. The reduction current was differentiated with respect to the working electrode potential. Fig. 7.1b shows the differentiated current for the same. The area of the peak corresponds to the reduction current. The optimum parameters were chosen on the basis that a well resolved peak with sufficient current appeared for better selectivity and sensitivity. The area of the differentiate current thus obtained was plotted against the concentration of  $UCl_3$ . A fairly linear dependence on concentration was found in the concentration range 0.1 to 11 wt. % as may be observed in Fig.7.2.

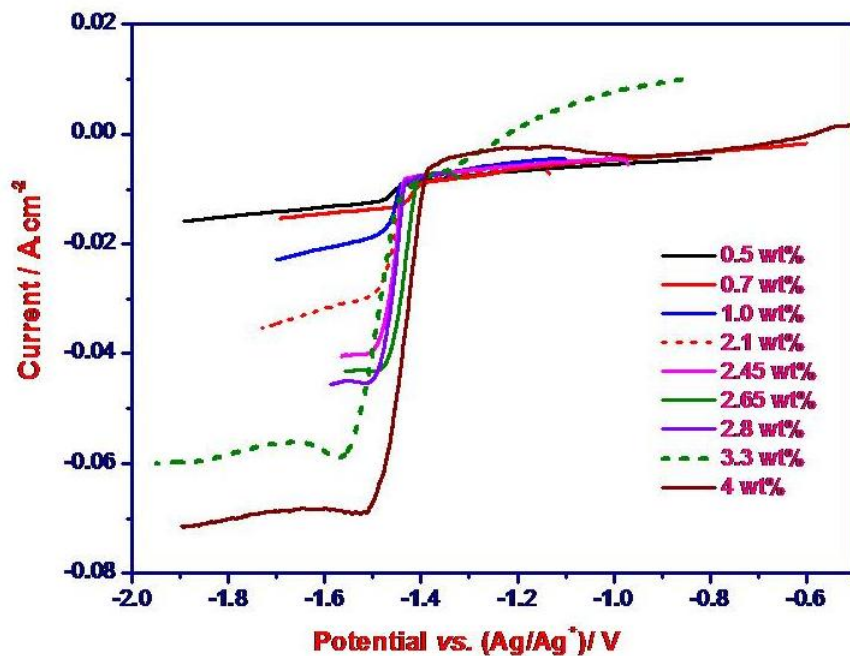


Fig. 7.1a NPV curves for LiCl-KCl-UCl<sub>3</sub> melt at 773 K for different concentrations of UCl<sub>3</sub>. Working electrode: W; area: 0.154 cm<sup>2</sup>.

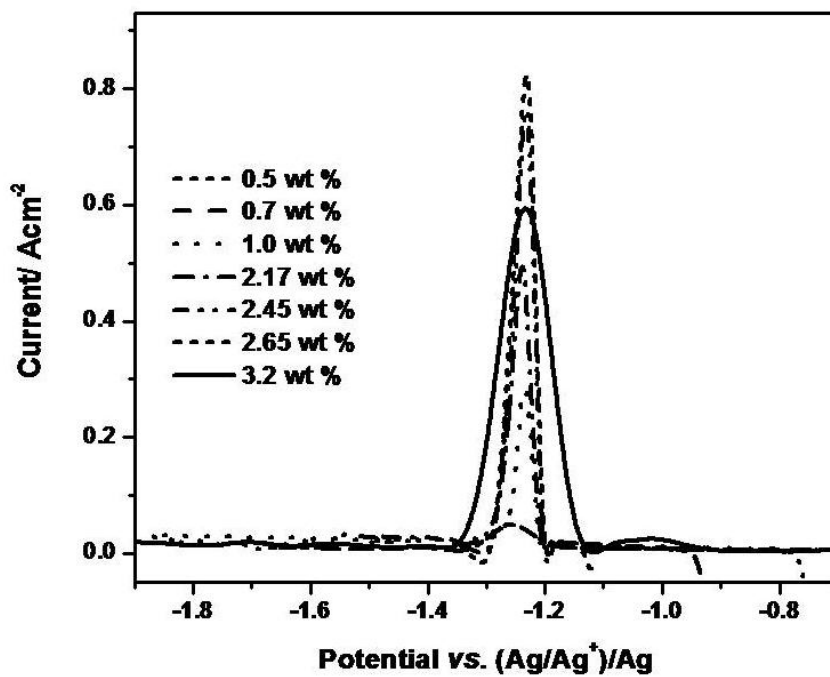


Fig. 7.1b Plot of differentiated current vs. potential for NPV curves in Fig 7.1a.

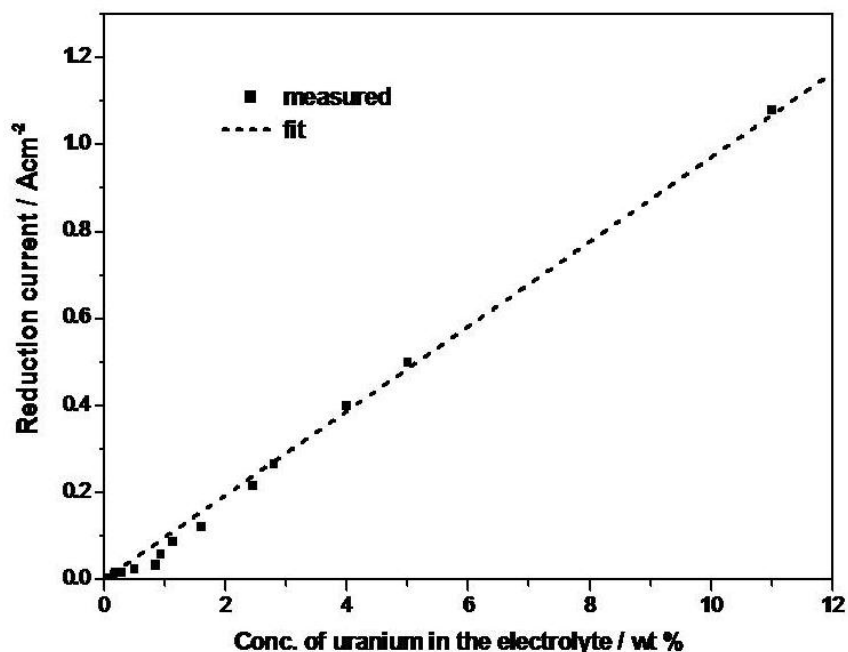


Fig. 7.2 Dependence of reduction current on concentration of  $\text{UCl}_3$  for NPV curves.

#### 7.4.2 Differential pulse voltammograms

Similarly, differential pulse voltammograms were recorded for various pulse times ( $t_p$ : 0.05-0.2 s), for different time interval between two pulses ( $t_m$ : 0.7-3 s) and various pulse heights ( $\Delta E_p$ : 5-75 mV), to arrive at the optimum parameters. Well resolved peaks were obtained for amplitudes between 5-20 mV. The optimum pulse time was between 50-100 ms. The parameters chosen for this study were-  $t_p$ : 0.1 s;  $t_m$ : 1 s and  $\Delta E_p$ : 15 mV. Fig. 7.3 shows the differential pulse voltammograms for different concentrations of  $\text{UCl}_3$ . A peak at -1.25 V appears for the reduction of  $\text{U(III)/U(0)}$ . The peak area was plotted against the concentration of  $\text{UCl}_3$ . A linear dependence of current with concentration of  $\text{UCl}_3$  over the concentration range 0.08 to 4 wt. % was observed as shown in Fig.7.4.

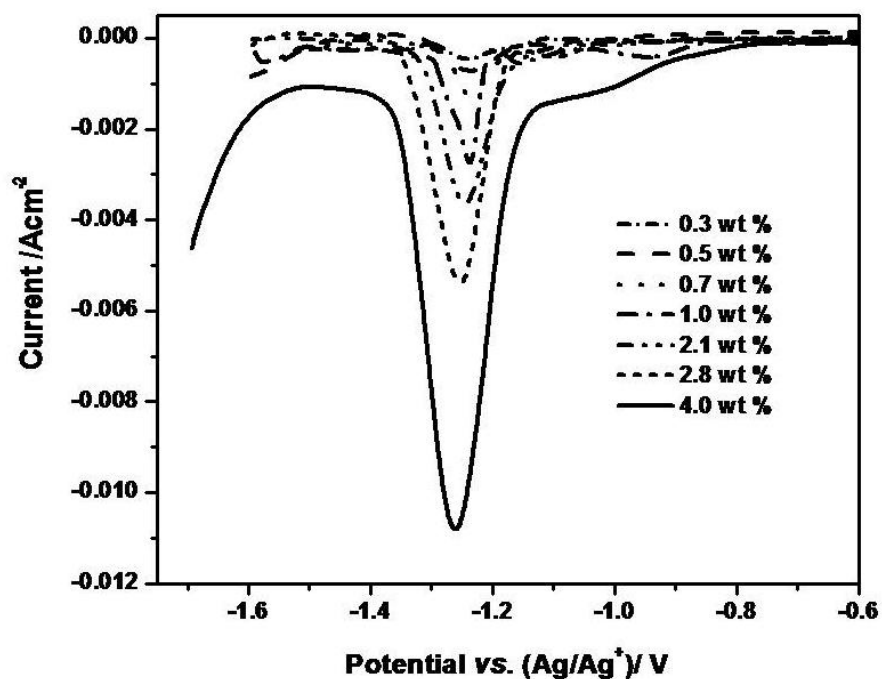


Fig.7.3 DPV curves for LiCl-KCl-UCl<sub>3</sub> melt at 773 K for different concentrations of UCl<sub>3</sub>. Working electrode: W; Area: 0.154 cm<sup>2</sup>; Pulse amplitude: 0.01 V.

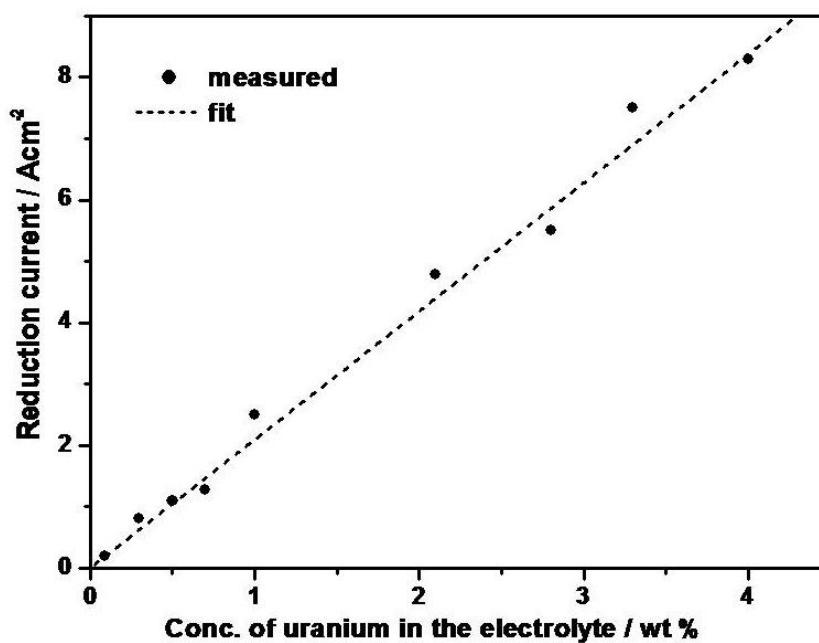


Fig.7.4 Dependence of reduction current on concentration of UCl<sub>3</sub> for DPV curves.

#### 7.4.3 Square wave voltammograms

The effect of pulse amplitude and frequency was studied in the range 2 - 75 mV and 8 - 75 Hz respectively for the square wave voltammograms. Pulse amplitudes of 5- 10 mV and frequency of 5-10 Hz were found to be optimum. Fig. 7.5 shows the square wave voltammograms for different concentrations of  $\text{UCl}_3$ . A peak at -1.25 V appears for the reduction of  $\text{U(III)/U(0)}$ . The peak heights were plotted against the concentration of  $\text{UCl}_3$ . A linear dependence of the reduction current was not observed over the concentration range studied, namely 0.3 to 4.0 wt. % as may be observed in Fig. 7.6. The anomaly may be interpreted from the sampling time for the waveform and the morphology of the uranium deposit. The current is sampled at the end of the forward pulse and at the end of the reverse pulse. The dendritic U deposited in the forward pulse results in increase in surface area of the electrode. The non-linear behavior observed at higher concentrations is due to the fact that the reduction current is not the same as the oxidation current for the forward pulse and the reverse pulse. This behavior has been pointed out in the study of Iizuka et al. [6] also. Although the square wave method has a very low detection limit because of higher sensitivity (output current is higher), the non-linear behaviour at higher concentrations makes it unsuitable for monitoring concentration of uranium over a wide concentration range.

#### ***7.4.4 Influence of the presence of the fission products***

Interference of the peaks for reduction of the fission products with those for  $\text{U(III)/U(0)}$  couple was studied using the melt  $\text{LiCl-KCl-1 wt \% UCl}_3\text{-1 wt \% LaCl}_3\text{-1 wt \% CeCl}_3\text{-0.7 wt \% EuCl}_3$  using NPV, DPV and SWV at 773 K by varying the parameters for the pulse. The potential was scanned from 0 to -2.35 V. The peaks from SWV, DPV and the differentiated peaks of NPV, corresponding to these elements were distinctly different from

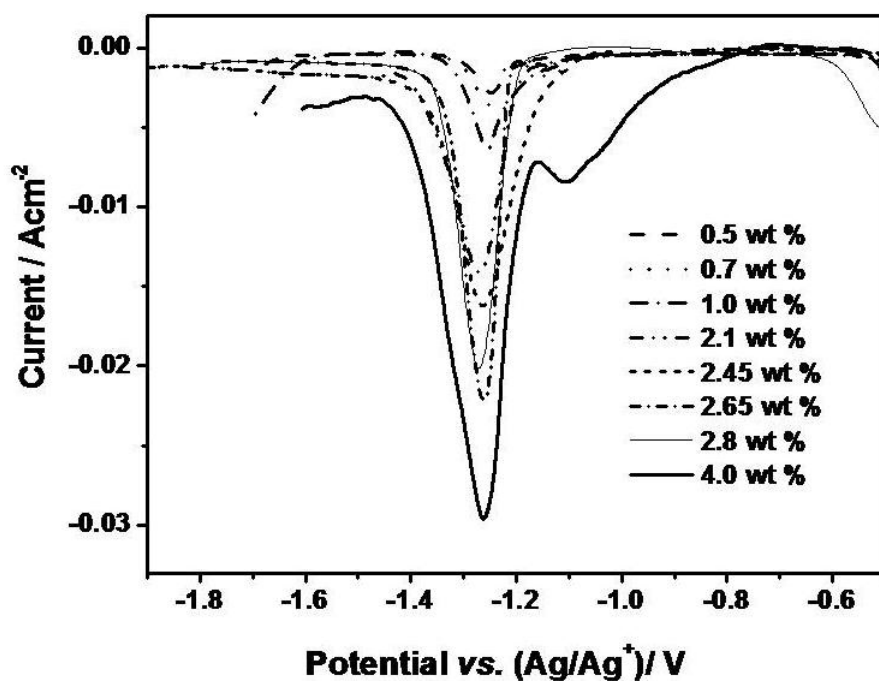


Fig. 7.5 SWV curves for LiCl-KCl-UCl<sub>3</sub> melt at 773 K for different concentrations of UCl<sub>3</sub>. Working electrode: W; Area: 0.154 cm<sup>2</sup>. Pulse amplitude: 0.01 V; Pulse frequency: 10 Hz.

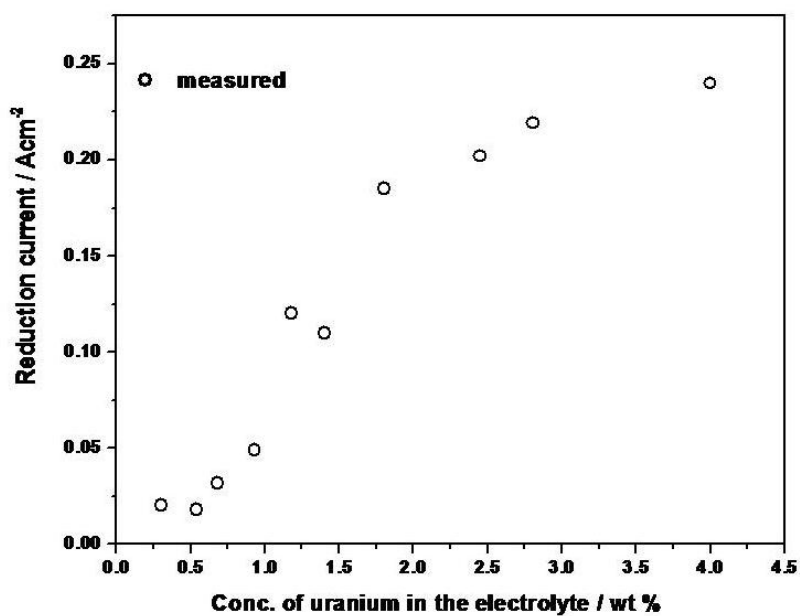


Fig. 7.6 Dependence of reduction current on concentration of UCl<sub>3</sub> for SWV curves.

that of uranium for the parameters discussed above. In case of DPV, at the optimum pulse amplitude, well resolved and distinct peaks were found for each redox couple. At higher pulse amplitudes, the sensitivity was better with increased current but the selectivity was lost due to broad peaks. Similar was the case with SWV. Peak broadening and loss of resolution was observed for higher amplitudes and frequencies. Fig.7.7a shows the normal pulse voltammogram for the simulated melt and Fig. 7.7b shows the differentiated peak for the same. Fig. 7.8 and Fig. 7.9 show the DPV and SWV for the simulated melt. It was observed that all the three techniques gave well resolved peaks for each redox couple. The peaks were assigned to the redox couple based on the potential values from our previous studies and from the literature [8-9]. The preliminary results showed that peak heights for U(III)/U(0), Ce(III)/Ce(0) and La(III)/La(0) were comparable for the NPV and DPV as per the amount of the chlorides taken in the melt whereas they are not so for the SWV. The broad and large peak for U(III)/U(0) couple would result in higher sensitivity but the resolution in multicomponent system would be lost. Similar observation was made in the ANL report [7]. A single large peak for the lanthanides was observed in their study.

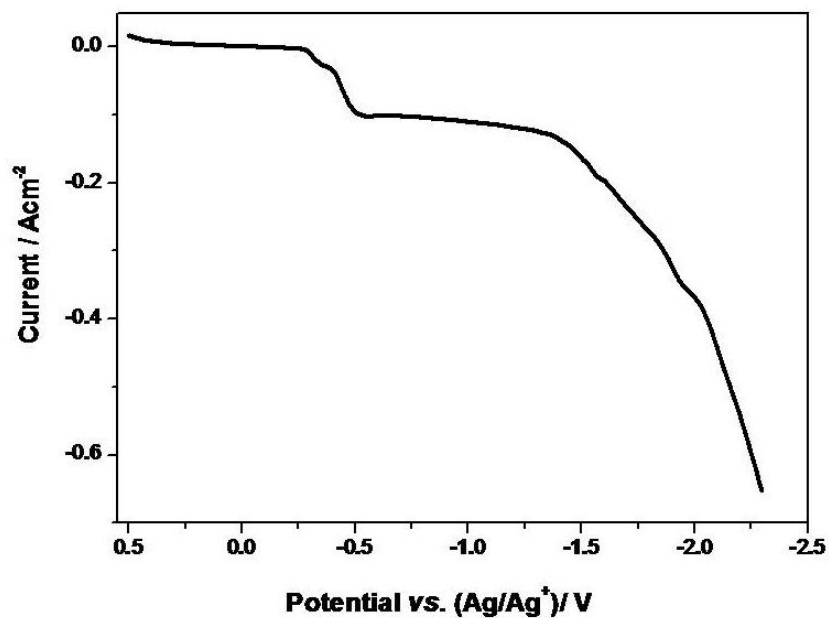


Fig. 7.7a NPV curve for LiCl-KCl-1 wt % UCl<sub>3</sub>-0.7 wt % EuCl<sub>3</sub>-1 wt % CeCl<sub>3</sub>-1 wt % LaCl<sub>3</sub> at 773 K on tungsten electrode. Pulse amplitude: 10 mV.

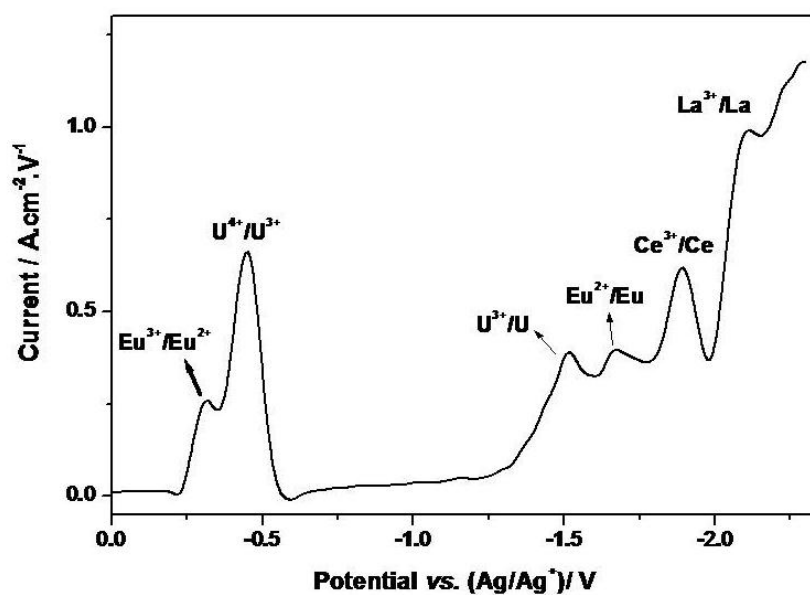


Fig. 7.7b Differentiated current for the NPV curve in Fig. 7.7a.

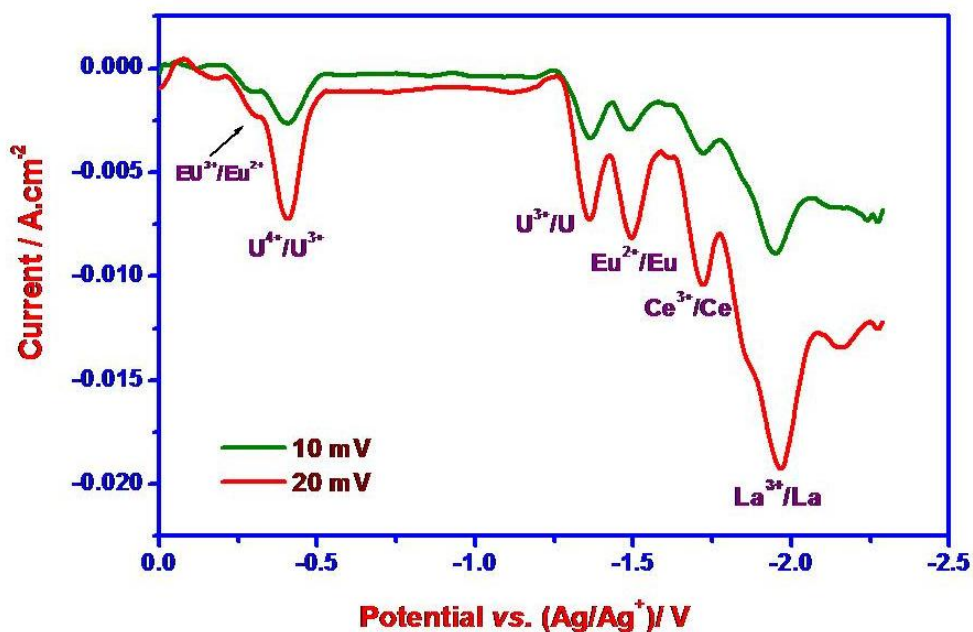


Fig. 7.8 DPV curves for LiCl-KCl-1 wt % UCl<sub>3</sub>-0.7 wt % EuCl<sub>3</sub>-1 wt % CeCl<sub>3</sub>-1 wt % LaCl<sub>3</sub> at 773 K on tungsten electrode for different modulation amplitudes.

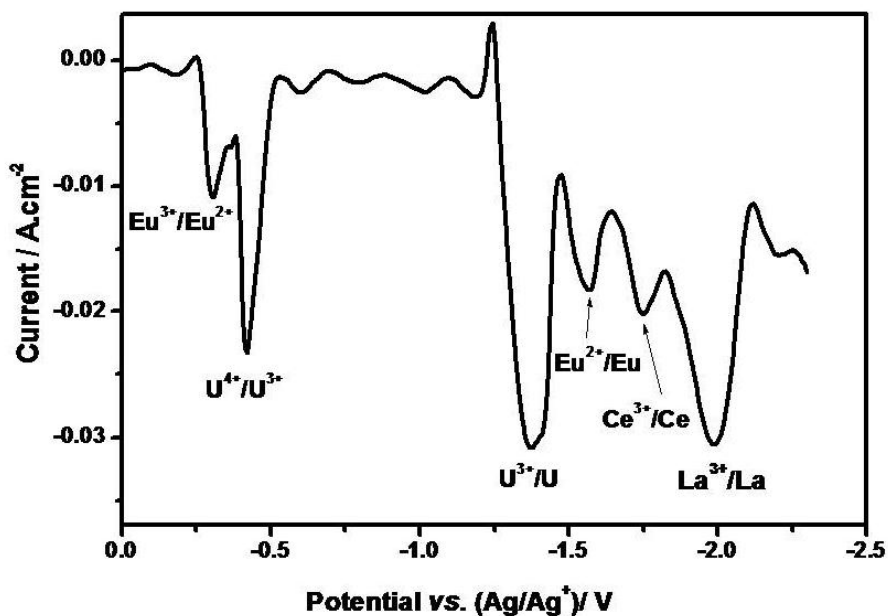


Fig. 7.9 SWV curve for LiCl-KCl-1 wt % UCl<sub>3</sub>-0.7 wt % EuCl<sub>3</sub>-1 wt % CeCl<sub>3</sub>-1 wt % LaCl<sub>3</sub> at 773 K on tungsten electrode. Pulse amplitude: 10 mV; Pulse frequency: 10 Hz.

## 7.5 Summary

It is necessary to monitor the concentration of actinides and lanthanides in the electrolyte salt during the electrorefining process. We had investigated the applicability of electroanalytical pulse techniques for on-line determination of uranium over a wide concentration range. Uranium was estimated by pulse techniques such as normal pulse voltammetry, differential pulse voltammetry and squarewave voltammetry. The three techniques are highly rapid, selective and sensitive and allowed very low detection limit of U. We had studied the effect of various parameter such as time of pulse, pulse interval, pulse amplitude, pulse frequency etc. The parameters were optimized based on appearance of well resolved peak with sufficient height. Linear relationship was observed for the reduction current and the concentration of  $\text{UCl}_3$  in the electrolyte in the concentration range 0.1 -4 wt % for the differential pulse technique and fairly a linear relationship was found in the concentration range 0.1 -11 wt % for the normal pulse technique. The square wave voltammograms showed higher sensitivity but a linear relationship for the reduction current was not observed at higher concentrations of  $\text{UCl}_3$ . Studies using simulated melt showed that the presence fission product does not affect the determination of uranium. In terms of sensitivity and resolution, the DPV may be better than the NPV due to the reduced contribution from the background current. Further studies need to be carried out in presence of Pu and minor actinides to establish the technique as the process monitor.

## 7.6 References

1. Y. I. Chang Nucl. Technol. 88 (1989) 129.
2. T. Koyama, M. Izuka, Y. Shoji, R. Fujita, H. Tanaka, T. Kobayashi, M. Tokiwai, J. Nucl. Sci. Tech. 34 (4) (1997) 384.
3. T. Koyama, T. R. Johnson, D. F. Fischer, J. Alloys Compd., 189 (1992) 37.

4. A.J. Bard, L.R. Faulkner, *Electrochemical Methods. Fundamentals and Applications*, 2<sup>nd</sup> Edition, Wiley New York, 2001, Chapter 7.
5. Samuel P. Kounaves, *Handbook of Instrumental Techniques for Analytical Chemistry*, Frank Settle (ed.), Prentice Hall, New Jersey, 1997, Chapter 37.
6. M. Iizuka, T. Inoue, O. Shirai, T. Iwai, Y. Arai, *J. Nucl. Mater.* 297 (2001) 43.
7. Annual Technical Report for 1994, Chemical Technology Division, Argonne National Laboratory Report; ANL-95/24 (1995) p.88.
8. S. P. Fusselman, J. J. Roy, D. L. Grimmett, I. F. Grantham, C. L. Krueger, C. R. Nabelek, T. S. Storvick, T. Inoue, T. Hijikata, K. Kinoshita, Y. Sakamura, K. Uozumi, T. Kawai, N. Takahashi, *J. Electrochem. Soc.* 146 (7) (1999) 2573
9. Y. Sakamura, T. Hijikata, K. Kinoshita, T. Inoue, T.S. Storvick, C.L. Krueger, J.J. Roy, D.L. Grimmett , S.P. Fusselman , R.L. Gay, *J Alloys Compd.* 271 (1998) 592.

## CHAPTER 8

### Conclusions and scope for further studies

#### 8.1 Conclusions

In the molten salt electrorefining process for reprocessing of spent metal fuel, pure uranium metal is deposited on steel cathode in molten LiCl-KCl medium. The chlorides of the rare earth fission products being more stable than the actinide chlorides, remain in the salt phase. During the recovery of uranium, plutonium and minor actinides remain in the anode and in the electrolyte salt since their chlorides are more stable than that of uranium. The activity of Pu and MA in cadmium is less due to the formation of stable intermetallic compounds. This facilitates their deposition on the cadmium cathode along with uranium metal. However, the cadmium cathode is less selective between actinides and lanthanides. The process variant being developed at Institute of Transuranium Elements (ITU), Karlsruhe, Germany is based on aluminium cathode. Selective recovery of actinides over lanthanides is reported from their studies. This is due to the higher stability of actinide-aluminium alloys than the lanthanide-aluminium alloys. Another promising cathode which is not explored is gallium. Gallium falling in the same group as that of aluminium is expected to show similar behavior.

The objective of the work was to study the redox behavior of actinides and lanthanides on different substrates in order to evaluate them for better actinide-lanthanide separation. Apart from studying the reduction mechanism and the electrode kinetics, the aim was to obtain the standard reduction potentials under identical experimental conditions (such as reference electrode, electrode material, experimental technique etc.). Hence, the electrochemical behavior of three elements (U, La and Nd) was studied on four different electrodes (W, Cd, Al and Ga).

Similar electrochemical studies on actinide and lanthanide chlorides in molten LiCl-KCl are found in the literature. However, the salient features of this study is the investigation of the kinetics for the reduction of La-, Nd- & U- trivalent ions (by convolution method and impedance spectroscopy), estimation of the equilibrium potentials for La(III)/La(0), Nd(III)/Nd(0) and U(III)/U(0) redox couples from the open circuit potential transients and investigation of the reduction behavior of Nd(III) ions on W electrode using various electrochemical techniques. The electrochemical studies on Nd-Cd, Nd-Al, U-Cd, La-Ga, Nd-Ga and U-Ga systems are reported for the first time in this study.

A summary of the studies that were carried out to elucidate the electrochemical behavior of La-, Nd- and U-trivalent ions on different cathodes (W, Cd, Al and Ga) is presented here. The stable oxidation states, reduction potentials of the different elements in LiCl-KCl and the kinetics of the reduction processes were obtained on the W working electrode using various electrochemical transient techniques. Electrochemical transient techniques such as cyclic voltammetry and open circuit potentiometry are fast and reliable methods to study the stable oxidation states and examine the formation of alloys.

The reaction of La-, Nd- and U-trivalent ions on different electrodes (Cd, Al and Ga) were examined. The reduction potentials,  $E_{M(III)/M(Cd)}^*$ ,  $E_{M(III)/M(Al)}^*$  and  $E_{M(III)/M(Ga)}^*$  were obtained from the cyclic voltammograms over a range of temperature between 698-773 K for the metal ions (M-U, La and Nd). The thermodynamic properties of the intermetallic compounds formed were derived from the open circuit potential measurements. The activity coefficients of the metals in Cd, Al and Ga were estimated from the studies.

The reduction of La(III) ions to La metal and that of U(III) ions to U metal on the tungsten electrode were found to take place in a single step with three electron transfer.

On the other hand, reduction of Nd(III) ions to Nd metal takes place in two steps- Nd(III)/Nd(II) and Nd(II)/Nd(0). The kinetics of the reduction process was studied by analyzing the semi-integrals of the cyclic voltammograms. The studies showed that the reduction of La(III)/La(0), Nd(II)/Nd(0) and U(III)/U(0) followed quasi-reversible behavior. The reduction of Nd(III)/Nd(II) showed reversible electrode behavior. The heterogeneous rate constants for the reduction, La(III)/La(0) and Nd(II)/Nd(0) at 798 K were  $4.1 \times 10^{-6}$  and  $7.8 \times 10^{-6} \text{ cm s}^{-1}$  respectively and that for U(III)/U(0) at 773 K was  $1.8 \times 10^{-5} \text{ cm s}^{-1}$ . To validate the values derived from the semi-integrals, the electrode kinetics of La(III)/La(0) couple was examined by impedance spectroscopy. The heterogeneous rate constant obtained from the impedance measurement was of the same order as that obtained from the semi-integrals. The apparent standard electrode potentials,  $E_{La(III)/La(0)}^*$ ,  $E_{Nd(III)/Nd(II)}^*$ ,  $E_{Nd(II)/Nd(0)}^*$ ,  $E_{Nd(III)/Nd(0)}^*$  and  $E_{U(III)/U(0)}^*$  were estimated from the cyclic voltammograms and open circuit potential measurements. In order to validate the measurements using transient techniques, the equilibrium potential of U(III)/U(0) couple was determined using the emf method also. The apparent standard potential values for the redox couple U(III)/U(0) obtained from the three techniques are in agreement with each other within  $\pm 10$  mV and also they lie within the scatter in the reported values. The reduction potentials obtained from this study were used for deriving the thermodynamic properties of different systems examined. We could estimate the apparent standard electrode potential of the Nd(III)/Nd(0) couple from cyclic voltammetry and OCP measurement which is not possible by galvanic cell emf method due to the disproportionation reaction of Nd(II) ion to Nd(III) ion and Nd metal.

Investigation on the reduction behavior of the rare earth chlorides on liquid cadmium pool and film electrodes showed their underpotential reduction forming the solvent rich intermetallic compound,  $\text{LaCd}_{11}$  and  $\text{NdCd}_{11}$ . However, in case of the U-Cd system, the extent of shift in the reduction potential of U(III) ions on cadmium cathode observed in the cyclic voltammograms were much larger than those expected from the Gibbs energy of formation of the intermetallic  $\text{UCd}_{11}$  reported in the literature by molten salt emf measurement. According to the phase diagram of the uranium-cadmium system,  $\text{UCd}_{11}$  is the only intermetallic compound and it decomposes peritectically to liquid +  $\alpha$  U beyond 746 K. But we could observe peak in the cyclic voltammograms at positive potentials beyond 746 K. The discrepancy is attributed to the formation of unsaturated U-Cd alloy rather than  $\text{UCd}_{11}$  at the cadmium surface. The interpretation was arrived at by studying the U-Cd system in the cadmium rich region using the saturated and unsaturated U-Cd alloy by molten salt galvanic cell emf method. The large solubility of uranium in cadmium compared to RE-Cd system could be the reason for this anomalous behavior. The Gibbs energies of formation of  $\text{UCd}_{11}$  in the temperature range 680 to 744 K were evaluated from the emf measurement and the values were in good agreement with the literature value. The peritectic temperature of  $\text{UCd}_{11}$  was evaluated to be 748 K which is consistent with the phase diagram.

Studies on the solid aluminium electrode showed the underpotential reduction of U, La and Nd, forming the solvent rich intermetallic compound,  $\text{Al}_{11}\text{La}_3$ ,  $\text{Al}_{11}\text{Nd}_3$  and  $\text{UAl}_4$  (and  $\text{UAl}_3$ ) respectively. The apparent standard reduction potentials and thermodynamic properties of the La-Al, Nd-Al and U-Al systems were obtained from the studies. The Gibbs energy formation of the intermetallic compounds and the activity of metals in aluminium estimated from open circuit potential measurements are in very good agreement with those estimated from equilibrium measurements and calorimetric

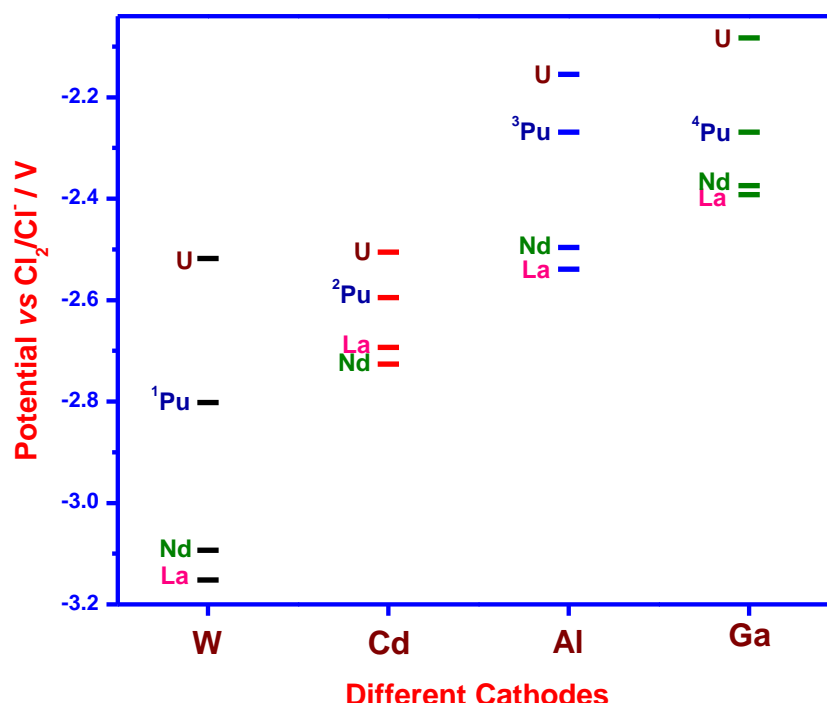
methods. The observations made in this study are similar to those reported from the research at ITU.

The redox behavior of  $\text{LaCl}_3$ ,  $\text{NdCl}_3$  and  $\text{UCl}_3$  on gallium cathode in  $\text{LiCl-KCl}$  medium are reported for the first time. The investigations showed the underpotential reduction of  $\text{La(III)}$ ,  $\text{Nd(III)}$  and  $\text{U(III)}$  ions on Ga surface forming the solvent rich intermetallic compound,  $\text{LaGa}_6$ ,  $\text{NdGa}_6$  and  $\text{UGa}_3$  respectively. The apparent standard reduction potentials and thermodynamic properties of the La-Ga, Nd-Ga and U-Ga systems were obtained from the studies. In the case of the La-Ga system, the change in the trend of the peak potentials in the cyclic voltammograms and the emf values from the OCP transients recorded at temperatures 765 and 785 K are attributed to the decomposition of  $\text{LaGa}_6$  to liquid +  $\text{LaGa}_2$  at its peritectic temperature, 750 K. The observation is consistent with the phase diagram of the La-Ga system.

The apparent standard reduction potentials of uranium and lanthanide ions obtained from the present study on different cathode materials are compared in Fig. 8.1. The values for plutonium shown were taken from the literature to compare the selectivity of different cathode materials. The reduction potentials of the metals become more positive and also the difference ( $\Delta E_{\text{An-Ln}}$ ) between the actinides and lanthanides are reduced on reactive cathodes compared to the inert W cathode as shown in Table 8.1. The actinides can be selectively collected on the reactive cathodes by imposing the appropriate potential during the electrorefining process.

Considering the fact that the difference, ( $\Delta E_{\text{An-Ln}}$ ), plays the major role in the selectivity of actinide-lanthanide separation, the order of selectivity from this study may be given as  $\text{W} > \text{Al} > \text{Ga} > \text{Cd}$  with respect to uranium. However the selectivity for the process can be determined only from the exact values of the reduction potentials of Pu

Fig. 8.1 Comparison of apparent standard reduction potentials of actinides and lanthanides from this study and literature.



1. P. Masset, R.J.M. Konings, R. Malmbeck, J. Serp, J. P. Glatz, *J. Nucl. Mater.* 344 (2005) 173.
2. O. Shirai, M. Iizuka, T. Iwai, Y. Suzuki, Y. Arai, *J. Electroanal. Chem.* 490 (2000) 31.
3. J. Serp, P. Chemelot, S. Fourcaudot, R.J.M. Konings, R. Malmbeck, C. Pernel, J.C. Poignet, J. Rebizant, J.P. Glatz, *Electrochim. Acta* 51 (19) (2006) 4024.
4. T. Toda, T. Maruyama, K. Moritani, H. Moriyama, H. Hayashi, *J. Nucl. Sci. Technol.* 46 (1) (2009) 18. (The values of excess free energy given by Toda et al. for Pu in Al and Ga are comparable, Based on this fact the behavior of Pu on Ga electrode is expected to be same as that on Al and the value of reduction potential of Pu on Ga is considered the same as Pu on Al here).

Table 8. 1 The difference ( $\Delta E_{An-Ln}$ ) in the reduction potentials of actinides with that of Nd.

Electrode	$\Delta E_{U-Nd}$ , V	$\Delta E_{Pu-Nd}$ , V
W	0.575	0.290
Cd	0.220	0.130
Al	0.340	0.235
Ga	0.290	0.115

and minor actinides on Ga cathode, determined from experimental method or estimation from thermodynamic properties.

Although the inert electrode is the most selective, the trans-uranium elements cannot be recovered on the inert electrode in the presence of  $\text{UCl}_3$  in the salt phase. Hence this study shows that aluminium may be a better choice for recovering actinides from the perspective of actinide-lanthanide separation. But the final recovery of actinides from the alloy (cathode product) has to be amenable for plant scale operation.

Electroanalytical pulse techniques serve as quick and reliable method for in-situ monitoring of the composition of actinides in multi-component systems. In this study the feasibility of using three different pulse techniques, namely, normal pulse voltammetry, differential pulse voltammetry and squarewave voltammetry were discussed for determining the concentration of  $\text{UCl}_3$  in the concentration range 0.1 to 11 wt %. Linear relationship was observed for the reduction current with the concentration of  $\text{UCl}_3$  in the concentration range 0.1 -4 wt % for DPV and fairly a linear relationship was found in the concentration range 0.1 -11 wt % for NPV. The SWV showed higher sensitivity, but a linear relationship for the reduction current was not observed throughout the range. Two different linear dependences, one for lower concentration range and the other for the higher concentration range of  $\text{UCl}_3$  was observed. Studies using simulated melt showed that the presence of the lanthanide fission products does not affect the determination of uranium.

### ***8.1.1 Challenges encountered during the study***

The most important challenge of the study was the need for maintaining high pure inert atmosphere for all the unit operations and for the electrochemical measurements. The corrosive nature of the salt and high temperature of operations and the need for chlorinating the salt for purification add to the problems faced. Fouling of the electrodes,

reaction of the actinides/lanthanide chlorides with the container material such as alumina, pyrex glass etc. leading to the formation of oxychlorides was observed, when the same electrolyte was used for repeated measurements or when the experiments were carried out over long periods of time. Heating of the electrochemical cell had to be done carefully and gradually to the required temperature in order to avoid cracking of the crucible material and utmost care had to be taken to avoid braking of the reference electrode material and other electrodes during the course of the experiment. Interpretation of the data for the  $\text{NdCl}_3$  system on inert W cathode, U-Cd and La-Ga systems were quite challenging. Repeated measurements were made to ascertain the observed behavior for the U-Cd system and galvanic cell emf measurement had to be carried out to understand the system.

## 8.2 Scope for further studies

- (1) The studies using different cathodes, namely, W, Cd, Al and Ga can be extended to investigate the redox behavior of the chlorides of Pu and minor actinides and other major fission products so as to have a complete database.
- (2) From the difference in potential values of the actinides and lanthanides, their activity coefficient at different substrate, it is possible to model and evaluate the selectivity of the electrodes.
- (3) Studies on the pulse techniques have to be optimized for U, Pu, minor actinides in the presence of major fission products to simulate the process condition.